



HAL
open science

Image Processing Methods for Dynamical Intracellular Processes Analysis in Quantitative Fluorescence Microscopy

Philippe Roudot

► **To cite this version:**

Philippe Roudot. Image Processing Methods for Dynamical Intracellular Processes Analysis in Quantitative Fluorescence Microscopy. Image Processing [eess.IV]. Université Rennes 1, 2014. English. NNT: . tel-01103887

HAL Id: tel-01103887

<https://theses.hal.science/tel-01103887>

Submitted on 15 Jan 2015

HAL is a multi-disciplinary open access archive for the deposit and dissemination of scientific research documents, whether they are published or not. The documents may come from teaching and research institutions in France or abroad, or from public or private research centers.

L'archive ouverte pluridisciplinaire **HAL**, est destinée au dépôt et à la diffusion de documents scientifiques de niveau recherche, publiés ou non, émanant des établissements d'enseignement et de recherche français ou étrangers, des laboratoires publics ou privés.



THÈSE / UNIVERSITÉ DE RENNES 1
sous le sceau de l'Université Européenne de Bretagne

pour le grade de
DOCTEUR DE L'UNIVERSITÉ DE RENNES 1
Mention : Traitement du Signal et Télécommunications

Ecole doctorale MATISSE

présentée par

Philippe Roudot

Préparée à Inria-Rennes
Centre de Recherche Inria Rennes – Bretagne Atlantique

**Image Processing
Methods for
Dynamical
Intracellular
Processes Analysis
in Quantitative
Fluorescence
Microscopy**

**Thèse soutenue à Inria-Rennes,
le 22 mai 2014**

devant le jury composé de :

Xavier DESCOMBES

Directeur de Recherche Inria-Sophia Antipolis /
rapporteur

Christophe ZIMMER

Directeur de Recherche Institut Pasteur /
rapporteur

Daniel CHOQUET

Directeur de Recherche CNRS Université de
Bordeaux II / *examineur*

Auguste GENOVEZIO

Chercheur Ecole Normale Supérieure /
examineur

Charles KERVRANN

Directeur de Recherche Inria-Rennes /
directeur de thèse

François WAHARTE

Ingénieur de Recherche CNRS Institut Curie /
co-directeur de thèse

UNIVERSITÉ DE RENNES 1
sous le sceau de l'Université Européenne de Bretagne

pour le grade de

DOCTEUR DE L'UNIVERSITÉ DE RENNES 1
Mention : Traitement du Signal et Télécommunications

préparé au Centre de Recherche
Inria Rennes — Bretagne Atlantique
École doctorale Matisse

présenté par

Philippe Roudot

**Image Processing Methods for Dynamical
Intracellular Processes Analysis in Quantitative
Fluorescence Microscopy**

Composition du jury:

Xavier DESCOMBES

Directeur de Recherche Inria, Inria Sophia-Antipolis - Rapporteur

Christophe ZIMMER

Directeur de Recherche, Institut Pasteur Paris - Rapporteur

Daniel CHOQUET

Directeur de Recherche CNRS, Université de Bordeaux II - Examineur

Auguste GENOVESIO

Chercheur, Ecole Normale Supérieure - Examineur

Charles KERVRANN

Directeur de Recherche Inria, Inria Rennes - Directeur de Thèse

François WAHARTE

Ingénieur de Recherche, Institut Curie - Co-Directeur de Thèse

Seeing is not always believing.
(Martin Luther King Jr.)

Je souhaite tout d'abord remercier les membres du Jury qui ont évalué mes contributions lors de ma soutenance. Je remercie tout particulièrement le Pr. Daniel Choquet d'avoir accepté de prendre la présidence de ce jury. Merci aux Dr. Christophe Zimmer et Xavier Descombes pour leurs rapports de thèse perspicaces, instructifs et encourageants. Je remercie spécialement Dr. Auguste Genovesio pour la fructueuse discussion qui a suivi la présentation de mes travaux.

Je remercie chaleureusement Charles Kervrann et François Waharte pour leur encadrement d'une qualité exceptionnelle. Ils m'ont toujours proposé des directions de travail pertinentes tout en m'offrant une réelle liberté d'exploration. Mes encadrants m'ont conseillé jusque dans les moindres détails avec une disponibilité permanente. Enfin, Charles et François m'ont constamment soutenu et encouragé. Je suis très fier de les compter parmi mes mentors.

Je remercie mes collègues et amis de l'Inria de Rennes pour leur soutien sans faille et leurs idées. Merci à Denis d'avoir supporté mon désordre, mes sons et mes désillusions. Merci à Huguette, Antoine, Tristan, Tina, Pierre, Thierry, Ioana, Tudor, Cordelia, Kai, Véronique, Patrick et Cédric. À l'Institut Curie de Paris, merci à Jean Salamero pour son accueil et à Jérôme pour ses précieux conseils. Merci aussi à Vincent, Charles, Périnne, Sylvie, Loïc, Marie, Lucie et Daniel.

Je remercie aussi Charles et François pour avoir encouragé ma mobilité à la Harvard Medical School de Boston. Un grand merci à Gaudenz Danuser pour son excellent accueil et sa confiance. Cette visite a dépassé toutes mes espérances, et si je peux poursuivre aujourd'hui mes travaux au sein du Danuser lab, c'est surtout grâce à l'impulsion initiale de Charles. Je remercie tous les collègues qui ont contribué à faire de cette mobilité une expérience enrichissante et chaleureuse: François, Sangyoon, Marco, Ulrich, Khuloud, Maria, Hunter, Danny, Karen, Christoph, Deepak et Emanuele. Merci aussi à Greg et Luna pour m'avoir accueilli chez eux durant ces trois mois.

Merci à mes amis de Rennes et d'ailleurs : Pedro, Steve, Lionel, Martin, Arthur, Amélie, Alissia, Marianne, JJ, Elisa, François, Caro, Rudi, Gaël, Audrey, Eddie, Tom, Sophie, Clément, Louise, Ben, Lulu, Natalia, Fabien et j'en oublie . . .

Merci à ma famille, pour avoir toujours été là pour moi. Merci tout spécialement à mon père, ma mère, Marie et mes grands-parents.

Enfin, merci à Camille, merci d'avoir bien voulu me suivre dans cette belle aventure, merci pour l'avant et pour l'après.

Philippe

Contents

Notations and Acronyms	8
Résumé en Français	13
1 General introduction	45
1.1 Fluorescence: principles and application to structures labelling	47
1.1.1 Principles of fluorescence	47
1.1.2 Bringing fluorescence to intracellular structures	49
1.1.2.1 Fluorescent staining	50
1.1.3 Fluorescent labelling of <i>in vivo</i> protein	50
1.1.4 Photobleaching and phototoxicity	52
1.2 Live cell fluorescence microscopy techniques	53
1.2.1 Wide-field Microscopy	53
1.2.2 Optical sectioning	54
1.2.2.1 Computational optical sectioning microscopy	54
1.2.2.2 Confocal Microscopy	54
1.2.2.3 Total Internal Reflection fluorescence Microscopy	56
1.2.2.4 Single Plane Illumination Microscopy	56
I Fluorescence lifetime map reconstruction in frequency domain (FD) FLIM	59
2 Fluorescence lifetime and biological application	65
2.1 Fluorescence lifetime theory	65
2.2 Application to biophysical quantities measurement	68
2.2.1 pH sensing	68
2.2.2 Förster Resonance Energy Transfer sensing	68
3 Fluorescence lifetime imaging techniques	71
3.1 Time-correlated single photon counting	72
3.2 Frequency domain FLIM	73
3.2.1 Frequency domain FLIM measurement	74
3.2.2 Fluorescence lifetime estimation in FD FLIM	75

4	Instrumental noise in FD FLIM measurement	81
4.1	Intensified CCD	82
4.2	ICCD Noise modeling	85
4.2.1	Theoretical model	85
4.2.2	Experimental issues and spatial dependency analysis	87
4.2.3	Spatially varying parameter estimation	91
4.2.4	Noise Variance estimation results	92
4.3	Application to parameter estimation in FD FLIM imaging	94
4.3.1	Background lifetime estimation	95
4.3.1.1	Weighted least squares estimator	95
4.3.1.2	Phase estimation on a reference FD FLIM measurement	95
4.3.1.3	Lifetime estimation on a control experimental sample	95
4.3.2	Application to FD FLIM measurement denoising	96
4.3.2.1	Wiener filtering	96
4.3.2.2	Gamma NL-means filter	96
5	Fluorescence lifetime estimation on moving endosomes in FD FLIM	101
5.1	Modeling spatial and temporal variations	103
5.2	Vesicle parameter estimation	104
5.2.1	Iterative minimization procedure	104
5.2.1.1	Sinusoid parameter prediction	104
5.2.1.2	Robust local motion estimation	106
5.2.2	Initialization	106
5.2.2.1	Object detection and initialization	106
5.2.2.2	Trajectory initialization	107
5.3	Lifetime map reconstruction results	108
5.3.1	Lifetime map reconstruction on synthetic data	108
5.3.2	Endosome tracking accuracy in experimental conditions	110
6	Application to protein interaction analysis at the membrane and during endocytosis	113
6.1	Data acquisition	113
6.2	Data analysis	114
6.3	Additional experiments	116
7	Conclusion	119
	Appendices	121
A	Derivation of the phase modulated signal for FD FLIM	122
A.1	The excited signal	122

A.2	Lifetime estimation	123
B	Gamma NL-means and approximate Bayesian Computation	126
B.1	Bayesian interpretation of NL-means	126
B.2	Approximate Bayesian Computation NL-means filtering	127
B.2.1	Principles of ABC rejection method	127
B.2.2	Patch-based ABC method	128
B.2.3	Data-driven density learning	128
B.2.4	Gamma NL-means (GNL-means)	129
II	Tracking heterogeneous transports in a dense intracellular environment	131
8	Quantifying transport heterogeneity in living cells	137
8.1	Dynamical models in living cell	137
8.1.1	Passive transport	137
8.1.2	Active transport	138
8.1.3	Heterogeneous transport	139
8.2	Challenges of intracellular particle transport quantification in fluorescence microscopy	141
8.2.1	Fluorescence microscopy limitations	141
8.2.2	Challenging intracellular phenotypes	142
8.3	A challenging case study: dense intermediate filament network dynamics analysis	143
8.3.1	Intermediate filament network	143
8.3.2	Unit length filament (ULF) dynamics analysis	145
9	Technical review of particle tracking algorithms	149
9.1	Previous review effort	153
9.2	Particle detection	155
9.3	Dynamics modeling	156
9.3.1	Bayesian filtering	156
9.3.2	Kalman Filtering	157
9.3.3	Multiple dynamical model filtering	158
9.3.3.1	Generalized Pseudo Bayesian of order 1	160
9.3.3.2	Interacting multiple model	160
9.3.3.3	Implementations of multiple modeling algorithms	162
9.3.4	Particle filtering	162
9.3.5	Other statistical methods	163
9.3.6	Conclusion	164

9.4	Linking cost optimization	164
9.4.1	Nearest Neighbor assignment	165
9.4.2	Linear programming in a bi-partite detection graph	166
9.4.3	Probabilistic methods	167
9.4.4	Multiple Hypothesis Tracking	167
9.4.5	Three ad-hoc assignment methods	168
9.4.6	Conclusion	169
9.5	Estimation of spatial gating parameter	169
9.6	Similarity measure	170
9.7	Gap closing	172
9.8	Merging and splitting	173
9.9	Conclusion & Table	173
10	Iterative u-track	177
10.1	Iterative Interacting Multiple Model (IIMM) Method	178
10.2	On-line iterative estimation of gating parameter	181
10.3	Tracking performances on synthetic data	182
10.3.1	Tracking performances on heterogeneous dynamics in a dense intracellular environment	185
10.3.2	Evaluation the gating parameter estimation	186
10.3.3	Sensibility to transition speed	187
10.3.4	Sensibility to speed variation	188
10.3.5	Motion type heterogeneity with individual stationarity: non regression test	189
10.3.6	Computational time overhead	189
10.4	Motion quantification results on experimental data	190
10.4.1	Detection method	190
10.4.2	Vimentin is bound to microtubules	191
10.4.3	Robustness against acquisition speed reduction	191
11	Conclusion	195
	Appendices	197
C	Particle detection in experimental conditions	198
C.1	Modeling	198
C.2	Significant local maxima detection	198
C.3	Model fitting	200
C.4	PSF scale estimation	201
12	General conclusion	203

List of figures	217
Bibliography	217

Notations and Acronyms

Mathematical Notations

Image domain

\mathbf{x} Pixel location in \mathbb{R}^2 or \mathbb{R}^3

$I(\mathbf{x})$ Image value in \mathbb{R} at location \mathbf{x}

ξ Read out Gaussian noise and Dark Current (DC)

$G_\gamma(\mathbf{x} - \mathbf{x}_0)$ Gaussian function centered at pixel $\mathbf{x}_0 \in \mathbb{R}^2$

Statistics

$\text{Var}[X]$ Variance of random variable X

$\mathbb{E}[X]$ Mathematical expectation of random variable X

$\hat{\theta}$ Estimator of parameter $\theta \in \Theta$

$\underset{\theta}{\text{argmin}}(f(\theta))$ Argument of the minimum of $f(\theta)$

$\rho_\eta(\cdot)$ Influence function of a M-estimator with scale parameter η

$\underset{z \in D}{\text{med}}(f(z))$ Median value of $f(z)$, $z \in D$

Stochastic filtering

\mathbf{x}_t State parameter at time t

$\mathbf{x}_t^{\theta_t}$ State parameter at time t associated to dynamic model θ_t

$\bar{\mathbf{x}}_t$ Predicted state at time t

$\hat{\mathbf{x}}_t$ Estimated state at time t

$\mathbf{x}_{1:t}$ State parameter sequence $\{\mathbf{x}_1, \dots, \mathbf{x}_t\}$

\mathbf{z}_t Measurement at time t

F Transition matrix

H Observation matrix

K Kalman gain

\mathbf{w}_t Process noise

Q Process noise covariance matrix

μ_t Observation noise

R Observation noise covariance matrix

$p(x|y)$ Probability of x knowing y

Frequency Domain FLIM

τ Fluorescence lifetime (in nanoseconds)

Φ_τ Associated phase in the sinusoidal emission signal

K Modulation phase number

ω_E Excitation frequency

Acronyms

Data description

a.i.u. Arbitrary intensity unit

a.d.u. Arbitrate data unit

3D Three-dimensional

2D Two-dimensional

Modeling and optimization

- PDF** Probability Distribution Function
- HMM** Hidden Markov Model
- KF** Kalman Filter
- IMM** Interacting Multiple Modeling
- JPDA** Joint Probabilistic Data Association
- MHT** Multiple Hypothesis Tracking
- MPT** Multiple Particle Tracking

Microscopy

- SNR** Signal to Noise Ratio
- PSF** Point Spread Function
- RMSE** Root Mean Square Error
- CCD** Charge Coupled Device
- IRF** Instrument Response Function
- FRET** Förster Resonance Energy Transfer
- FLIM** Fluorescence Lifetime Imaging Microscopy
- TIRF** Total Internal Reflection Fluorescence
- TCSPC** Time-Correlated Single-Photon Counting
- SPT** Single Particle Tracking
- MSD** Mean Squared Displacement

Bio-imaging and biology

GFP Green Fluorescence Protein

IF Intermediate Filaments

ULF Unit Length Filament

Résumé en Français

Méthodes numériques pour l'analyse de processus intracellulaires dynamiques en microscopie quantitative.

Depuis la première description de la cellule vivante par Robert Hook, il y a près de 350 ans [[Hooke and Waller, 1705](#)], l'observation à l'aide de microscope a toujours été d'une grande fécondité dans l'étude de la cellule vivante. La dernière évolution majeure dans ce domaine est sans conteste le développement des techniques de marquage par fluorescence. Il est ainsi possible aujourd'hui, grâce aux techniques de marquage par ingénierie génétique, couplées à la vidéo-microscopie optique de haute résolution, d'observer avec précision les molécules régissant les fonctions de l'organisation intracellulaire. A l'opposé des expérimentations en biochimie ou en génétique, la microscopie de fluorescence permet des observations dynamiques *in vivo* capables de restituer l'hétérogénéité inhérente à la complexité des interactions intracellulaires [[Tinoco and Gonzalez, 2011](#)].

Dans ce contexte, les méthodes numériques ont un rôle important à jouer. En traitement d'image, les méthodes de reconstruction du signal permettent de corriger les artefacts induits par l'instrumentation optique (diffraction, bruit de mesure) mais aussi induits par le signal d'intérêt (bruit photonique, mouvement). Ensuite, en vision par ordinateur, les phénotypes observés doivent être quantifiés et interprétés. Nous décrivons dans ce manuscrit deux études représentatives des développements méthodologiques menés en traitement d'image et en vision par ordinateur nécessaires pour l'étude du vivant.

Dans première partie du document, nous présentons une étude portant sur l'imagerie de temps de vie de fluorescence sur structures dynamiques dans le domaine de fréquence (FD FLIM). Une mesure en FD FLIM est définie par une série d'images présentant une variation d'intensité sinusoïdale. La variation d'un temps de vie se traduit par une variation dans la phase de la sinusoïde décrite par l'intensité. Sur cette thématique, notre étude comporte deux contributions principales. Le processus de formation de l'image est d'abord étudié afin de prendre en compte les bruits hétérogènes causés par l'instrumentation et la nature photonique du signal. Nous démontrons la nécessité d'une correction du modèle théorique et nous proposons une méthode d'estimation de ces

paramètres. Un algorithme de débruitage tire parti du modèle de bruit pour améliorer les séquences obtenues. Ensuite, l'estimation du temps de vie sur des molécules mobiles est rendu possible grâce à une procédure d'estimation conjointe du temps de vie et du mouvement des vésicules intracellulaires. L'algorithme de reconstruction de cartes de temps de vie est finalement testé sur des séquences expérimentales. Des résultats préliminaires sont présentés.

Dans la seconde partie du document, Nous présentons une étude portant sur la quantification du transport hétérogène dans un environnement intracellulaire dense. Les transitions entre la diffusion Brownienne dans le cytoplasme et les transports actifs supportés par le cytosquelette sont en effet des scénarios très couramment observés dans des cellules vivantes. La complexité de la quantification de ces mouvements est due au caractère imprévisible des transitions et nous montrons que les algorithmes proposés dans la littérature ne sont pas conçus pour les détecter. De plus, accroître artificiellement le rayon de recherche n'est pas une solution efficace car ce choix conduit à une augmentation du nombre de faux positifs dans des conditions denses. Notre proposition d'algorithme exploite certains principes de l'algorithme de suivi u-track [Jaqaman et al., 2008]. Nous proposons ainsi d'effectuer plusieurs filtrages de Kalman qui évaluent plusieurs types de transport (Brownien, dirigé ...) [Genovesio et al., 2006] indépendamment pour chaque particule. Par ailleurs, nous tirons parti de multiples balayages de suivi pour effectuer un lissage de Kalman dit "forward-backward". Nous obtenons ainsi une estimation convergente de la vitesse à chaque point de temps et nous tenons compte de la nature locale du mouvement. A notre connaissance, c'est la première fois qu'une telle approche est proposée dans la littérature. Nous montrons, sur différents scénarios simulés, la supériorité de notre approche face aux approches compétitives reposant sur une modélisation des dynamiques multiples. Nous illustrons sur séquences expérimentales l'aptitude de notre algorithme à détecter des mouvements dirigés rares dans une population dense de vimentine. Nous montrons aussi la robustesse de notre méthode sur des séquences réelles (virus) échantillonnées temporellement avec des fréquences variables pour modifier l'amplitude des déplacements apparents.

Ce résumé en français est structuré comme suit. Nous présentons d'abord brièvement le contexte général de notre étude en décrivant la révolution apportée par la microscopie de fluorescence puis le rôle grandissant de la communauté du traitement et de l'analyse d'image en microscopie de fluorescence. Nous présentons ensuite les résultats obtenus dans deux études: la reconstruction de cartes de temps de vie sur molécule dynamique d'une part, et la quantification de transport hétérogène dans une population dense de particules d'autre part. Nous concluons ce résumé par quelques lignes directrices qui doivent orienter nos futures investigations.

1 Contexte: Analyse de données en microscopie de fluorescence pour l'étude du vivant

La révolution du marquage par fluorescence

Aujourd'hui, les méthodes biochimiques et génétiques telles que la reconstruction de processus cellulaires *in vitro* ou la détermination de la structure des protéines permettent de mettre à jour, de façon extrêmement détaillée, les interactions moléculaires et lipidiques régissant l'organisation intracellulaire et ses fonctions. Pourtant, ces méthodes présentent plusieurs désavantages: elle ne permettent qu'une observation statique de la cellule, ainsi qu'une projection moyennée et homogène de phénotypes potentiellement nombreux. Par ailleurs, les expériences sont effectuées *ex-vivo*. Depuis l'avènement de l'imagerie microscopique de fluorescence, l'étude de la cellule vivante est entrée dans une nouvelle ère [Vonesch et al., 2006]. Grâce au marquage fluorescent des protéines d'intérêt, les chercheurs en biologie peuvent observer les processus intracellulaires avec une grande précision, parfois en temps réel. L'hétérogénéité des comportements inhérents à la cellule vivante peut être désormais analysée et les expériences sont, dans une certaine mesure, réalisées *in vivo* [Tinoco and Gonzalez, 2011].

La révolution de l'imagerie de fluorescence a été possible grâce à des avancées dans deux domaines différents. C'est tout d'abord la purification de la GFP (Protéine Fluorescente Verte) [Shimomura et al., 1962], son clonage [Prasher et al., 1992] et la diversification de son expression [Tsien, 1998] qui ont ouvert la voie au marquage par protéine fluorescente (Figure 0.1). Exploitant les propriétés du phénomène de fluorescence et plus précisément le décalage de Stokes, le marquage permet d'observer plusieurs types de protéines d'intérêt simultanément alors que le milieu cellulaire est uniformément excité. Ce marquage est effectué par recombinaison génétique et transfection dans la cellule hôte. Ainsi, depuis le séquençage de l'intégralité du génome humain achevé en 2004, toutes les protéines d'intérêt peuvent être marquées avant d'être observées en microscopie [Lippincott-Schwartz, 2003]. Comme nous le verrons dans notre première étude, la fluorescence n'a pas pour autant pour seule vocation de révéler la présence d'une molécule d'intérêt. Ses propriétés physiques sont très précieuses pour quantifier les interactions entre protéines à l'échelle de quelques nanomètres, et par conséquent jouent un rôle essentiel dans la mesure de l'activité moléculaire.

Deux phénomènes limitant sont néanmoins à considérer lors de l'acquisition d'images de fluorescence: le photoblanchiment et la phototoxicité. Le premier correspond à la perte de fluorescence du fluorophore induite par des dommages chimiques liés à un excès de photons. Le second correspond aux dommages causés à l'échelle des structures intracellulaires générant des radicaux libres d'oxygène, libérés par réaction à la fluorescence. En cherchant à réduire autant que possible la quantité d'excitation nécessaire pour acquérir une image de fluorescence, les progrès réalisés dans ce domaine (optique, capteurs de lumière) ont permis de contrôler davantage ces deux phénomènes. A titre d'exemple, la microscopie

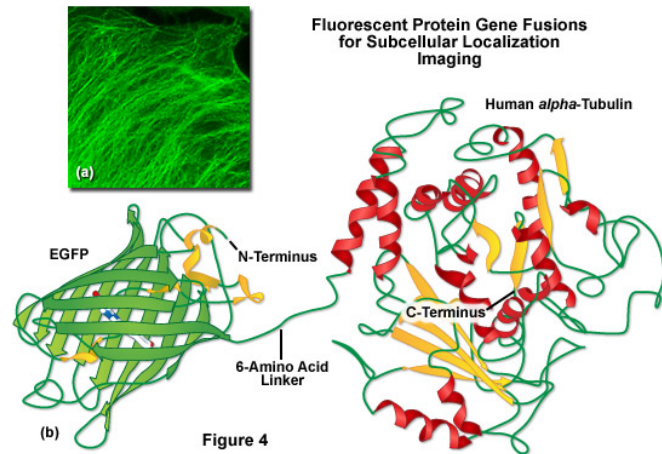


Figure 0.1: α -tubuline marqué par la EGFP (GFP amélioré). **a)** cette chimère localise les microtubules **(b)** la EGFP est attaché au N-terminus de la α -tubuline. La partie intérieur de la structure cylindrique de la GFP est responsable du phénomène de fluorescence (source: Zeiss).

confocale (Figure 0.2) a permis de n'exciter que la zone d'intérêt dans une section optique de la cellule. Par la suite, l'utilisation de capteurs à amplificateur (EMCCD) a facilité le développement de l'imagerie à haute fréquence à faibles doses d'illumination. D'autres avancées significatives sont à l'origine de progrès importants qui conduisent à des images de très haute qualité et de séries temporelles finement résolues spatialement (en 2D et 3D) et temporellement [Stephens and Allan, 2003; Lippincott-Schwartz et al., 2001]. L'acquisition dite 3D+temps s'est ainsi progressivement répandue grâce à la microscopie confocale. De plus, les événements membranaires peuvent être observés très finement grâce à la technologie TIRF. La limite de diffraction optique (~ 200 nm) a finalement été brisée grâce aux récents progrès en microscopie de super-résolution.

Traitement et analyse d'image en microscopie de fluorescence

Le traitement et l'analyse d'image participent également aux avancées technologiques en imagerie biologique.

Tout d'abord, la modélisation du processus de formation de l'image permet la reconstruction du signal émis par l'échantillon expérimental. Ces algorithmes de traitement d'image peuvent aider à réduire le bruit [Boulanger et al., 2010] ou à déconvoluer les signaux [Hom et al., 2007]. Ils répondent également à des besoins spécifiques tels que la mesure du temps de vie de fluorescence comme nous l'abordons dans la première partie de ce document. Si le processus de formation des images est parfaitement connu et l'optique est bien maîtrisé, les algorithmes numériques concourent aussi à la mise en oeuvre de nouvelles pratiques d'acquisition. Par exemple, la super-résolution

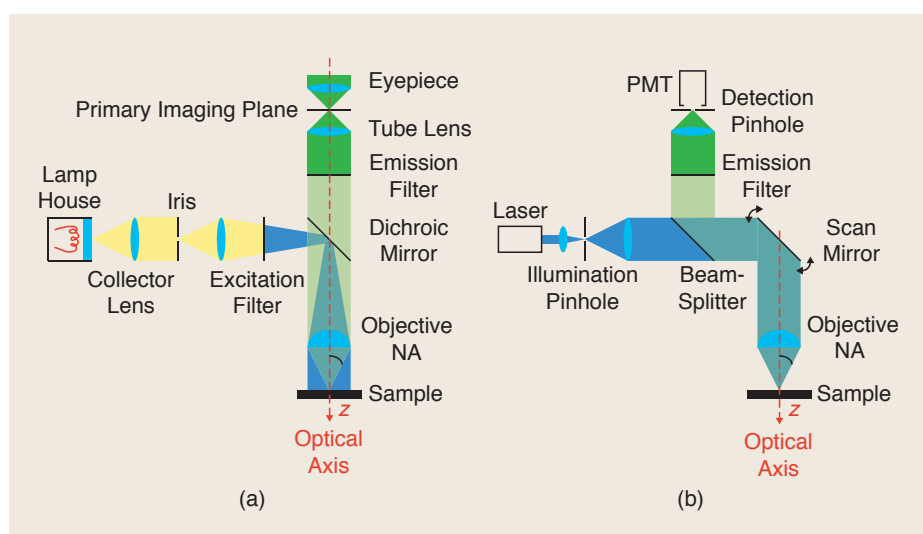


Figure 0.2: Comparaison schématique des microscopies à champ large et confocale typiquement utilisées pour l'étude du vivant (source [Vonesch et al., 2006]).

par localisation de molécules uniques [Kechkar et al., 2013; Henriques et al., 2010] ou l'illumination structurée [Gustafsson, 2005; Kner et al., 2009] sont des illustrations parfaites de cette coopération.

Ensuite, le traitement d'image joue un rôle prépondérant pour la quantification et la classification automatique de phénotypes observés. A cet égard, les apports des méthodes d'analyse d'image peuvent être classés en quatre catégories. Premièrement, l'essor de la vidéo-microscopie et les résolutions toujours plus hautes nécessitent le développement de méthodes automatisées. Il est devenu impossible pour un opérateur humain de quantifier l'intégralité des événements présents dans une image dans un temps raisonnable, avec une précision constante [Meijering et al., 2006]. Deuxièmement, en considérant l'intégralité des objets observables, les algorithmes peuvent identifier des événements rares et hétérogènes que l'opérateur peut manquer dans une population dense d'événements homogènes [Danuser, 2011]. On peut citer la localisation de cellules et des structures intracellulaires [Smal et al., 2010; Zimmer, 2012], le suivi d'objets [Meijering et al., 2006; Genovesio et al., 2006; Jaqaman et al., 2008; Chenouard et al., 2014; Zimmer, 2012], la détermination et la classification automatique de phénotypes [Walter et al., 2010; Kim et al., 2013] etc ... La troisième apport des méthodes de traitement d'image est la révélation d'informations invisibles à l'expérimentateur. Les paramètres contrôlant les processus sous-jacents peuvent être estimés en modélisant leurs relations avec les événements mesurés sur l'image. Les travaux pionniers de [Sprague et al., 2003] sur la dynamique des kinétochores assurant la liaison chromosomes-microtubules durant la métaphase en est un exemple. A cause des limites de résolution en microscopie optique, la position des kinétochores ne

peut pas être précisément estimée. C’est la dynamique des microtubules, plus facilement mesurable, qui a permis d’inférer le mouvement des kinétochores. Le procédé a été nommé “la convolution de modèle” par les auteurs. De nombreux travaux s’inspirant du principe de la “convolution de modèle”, ont été menés depuis [Vilela et al., 2013; Machacek et al., 2009]. Enfin, les méthodes de traitement d’image permettent de rationaliser et d’optimiser au mieux les efforts d’acquisition des données. Dans nos travaux de thèse, nous montrons qu’un algorithme de suivi de particules suffisamment robuste permet de réduire notablement la fréquence d’acquisition d’un échantillon tout en maintenant la qualité pour des opérations de quantification. Ainsi, en exposant faiblement l’échantillon à la lumière, nous pouvons limiter le photoblanchiment et la phototoxicité. Un algorithme de suivi robuste au bruit et aux grands déplacements est alors capable de quantifier des mouvements sur de longues périodes d’acquisition sans artefacts biologiques.

Néanmoins, un problème récurrent est la validation de la qualité des mesures issues de l’algorithme et la validation des modèles supposés [Zimmer, 2012]. Pour cela, trois tâches doivent être effectuées. Une vérification visuelle est d’abord indispensable pour contrôler les erreurs importantes et ajuster les paramètres. Une simulation aussi précise que possible doit être aussi mise en oeuvre pour évaluer les performances de l’algorithme et les erreurs d’estimation. Enfin, puisqu’il est extrêmement difficile, voire parfois impossible, de simuler parfaitement une image expérimentale, une dernière opération consiste à exploiter des données expérimentales de référence pour lesquelles on dispose d’une “vérité-terrain”, c’est à dire d’une mesure connue sur le phénotype d’intérêt.

Dans ce contexte, mes travaux de thèse portent sur deux aspects du traitement et de l’analyse d’image en microscopie optique. Une première contribution vise à reconstruire des cartes de temps de vie de fluorescence mesurées dans le domaine de fréquence sur des structures intracellulaires en mouvement. Une deuxième contribution a pour objet de quantifier le transport intracellulaire avec des algorithmes de suivi de cibles. Dans ces deux situations, nous analysons finement les dynamiques observées afin de répondre au mieux aux exigences requises pour des applications en biologie.

2 Reconstruction de cartes de temps vie de fluorescence mesurés dans le domaine fréquentiel

Lorsqu’une molécule fluorescente absorbe un photon, elle atteint un état d’énergie excité. De multiples voies de désexcitation sont alors possibles pour revenir à l’état de repos. L’émission quasi immédiate d’un photon en est une; c’est ce qu’on appelle la fluorescence. Le temps de vie de fluorescence est le temps moyen de résidence d’une molécule dans état excité avant que celle-ci éventuellement relâche un photon. Cette grandeur dépend de la probabilité des autres voies de désexcitation. Typiquement, la proximité d’une molécule fluorescente du spectre d’absorption adéquat peut créer un transfert d’énergie non radiatif entre le “donneur” et l’“accepteur” provoquant une baisse immédiate du temps de vie de

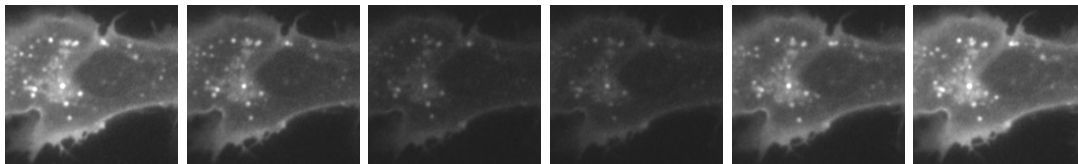


Figure 0.3: Un exemple de mesure FD FLIM pour $K = 6$ signaux de modulation. Le contraste a été augmenté artificiellement pour améliorer la visualisation. Les molécules fluorescentes permettent de localiser le récepteur IFNAR1 marqué en GFP sur des cellules épithéliales (RPE1).

fluorescence. Ce phénomène, appelé FRET (pour Förster Resonance Energy Transfer), est un des nombreuses avantages de l'étude du temps de vie de fluorescence. La mesure de FRET est notamment recommandée pour quantifier l'activité de bio-capteurs ainsi que les interactions entre protéines distantes de quelques nanomètres. Dans le cadre d'une expérimentation effectuée à l'Institut Curie en collaboration l'équipe Inria Serpico, nous avons étudié la mesure de FRET sur des récepteurs *in vivo* non fixés. Pour cela, nous avons choisi l'unique technique compatible avec la quantification de temps de vie sur structures dynamiques: l'imagerie de temps de vie de fluorescence en domaine de fréquence (FD FLIM).

Imagerie de temps de vie de fluorescence en domaine de fréquence

En FD FLIM, le signal d'excitation et le signal émis par l'échantillon sont sinusoïdaux. Les variations de temps de vie présentées par l'échantillon correspondent à des variations dans la phase du signal émis. Afin de rendre mesurables ces variations qui ont lieu à très hautes fréquences (> 40 Mhz), le signal est modulé en phase par K signaux. Au final, à une mesure FD FLIM à un seul pas de temps, correspond une série de K images présentant une variation d'intensité sinusoïdale (voir Figures 0.3 et 3.4). L'image $S_\theta(k)$ d'indice $k \in [1, K]$ est définie comme suit

$$S_\theta(k) = C_S + A_S \cos\left(\frac{2\pi k}{K} + \Phi_{M_0} - \Phi_E + \arctan(\omega_E \tau)\right) \quad (0.1)$$

où Φ_E représente la phase du signal initial, Φ_{M_0} le signal de modulation, ω_E la fréquence d'excitation et τ le temps de vie de fluorescence. Par la suite, nous notons $\theta = (C_S, A_S, \Phi_\tau)^T$ le vecteur des paramètres associés.

Après calibration du déphasage, il est établi que le temps de vie peut être déduit de (0.1). Généralement, le calcul de la phase en FD FLIM s'effectue point à point dans le domaine de Fourier selon la formule suivante:

$$\hat{\Phi}_\tau = -\arctan\left(\frac{\sum_k I(k) \cos\left(\frac{2\pi k}{K}\right)}{\sum_k I(k) \sin\left(\frac{2\pi k}{K}\right)}\right) + \frac{\pi}{2}.$$

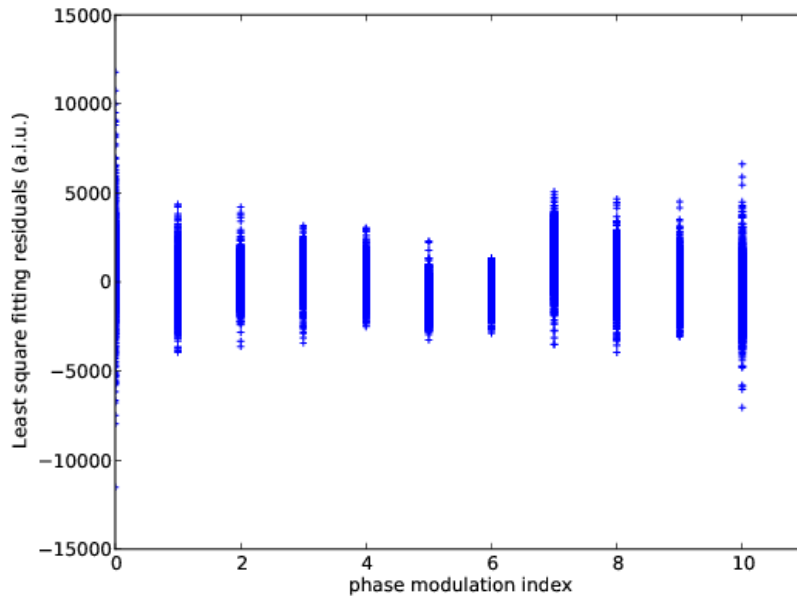


Figure 0.4: Résidus obtenus au sens des moindres carrés après estimation du modèle paramétrique décrivant le comportement sinusoïdal de la modulation de phase (voir (0.1)). Les résidus sont tracés pour l’ensemble de la mesure (Figure 3.4). La variation d’amplitude des résidus met en évidence une forte hétéroscédasticité. Estimation effectuée sur un microscope confocal “spinning disk” avec un intensifieur II18MD (Lambert Instruments).

La grande majorité des contributions en FD FLIM exploite cette formule, équivalente à une estimation des paramètres de la sinusoïde au sens des moindres carrés [Holub, 2003; van Munster and Gadella Jr, 2004; Spring and Clegg, 2009; Hutchinson et al., 1995]. Néanmoins, on suppose bien souvent que le bruit est homogène et que les structures sont stationnaires, des hypothèses qui méritent toute notre attention.

D’emblée, on peut faire remarquer que la variance du bruit photonique dépend de l’intensité du signal, ce qui devrait se traduire par un comportement hétéroscédastique des erreurs d’estimation. Nous verrons que cette caractéristique est encore accrue en FD FLIM (voir Figure 0.4). En outre, nous verrons que les aléas expérimentaux doivent être rigoureusement pris en compte si on s’intéresse à la caractérisation du bruit d’acquisition.

Par la suite, nous traitons les artefacts liés aux mouvements endosomaux et visibles sur les images acquises en FD FLIM. Malgré la rapidité des acquisitions (de dix à quelques centaines de millisecondes), les structures intracellulaires peuvent encore se déplacer lors de la mesure. Ces mouvements résultent de l’expression d’un “effet Doppler” sur la carte

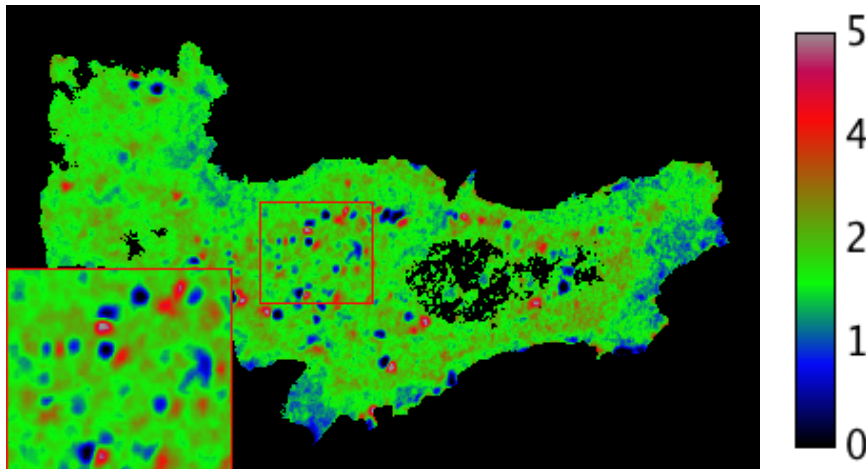


Figure 0.5: “Effet Doppler” induit par le mouvement des endosomes sur les mesures de temps de vie de l’ordre de quelques nanosecondes (séquence 0.3).

de temps de vie (voir Figure 0.5). Ils ne facilitent pas la mesure de temps de vie *in vivo* d’une manière générale.

Nous proposons donc de traiter ces deux questions et d’améliorer les performances de quantification en FD FLIM, une technologie prometteuse aux multiples applications.

Etude du bruit instrumental en FD FLIM

Modélisation du bruit de mesure de l’intensificateur

En raison du caractère sinusoïdal du mode d’acquisition, un intensificateur est généralement requis en FD FLIM pour mesurer des signaux les plus faibles. De plus, la variation de tension au borne l’intensificateur permet la modulation de phase du signal émis. L’ensemble formé par l’intensificateur et le capteur CCD est communément appelé ICCD (voir Figure 0.6).

Afin d’estimer le bruit localement causé par l’instrumentation, nous proposons une dérivation originale pour identifier le modèle de variance du bruit Poisson-Gaussien généré par le capteur ICCD, fonction de l’espérance locale de l’intensité:

$$\text{Var}[I(\mathbf{x})] = \frac{\text{Var}[g_{\text{INT}}]}{\mathbb{E}^2[g_{\text{INT}}]} (\mathbb{E}[I(\mathbf{x})] - m_\xi)^2 + g_{\text{CCD}} \left(\mathbb{E}[g_{\text{INT}}] + \frac{\text{Var}[g_{\text{INT}}]}{\mathbb{E}[g_{\text{INT}}]} \right) (\mathbb{E}[I(\mathbf{x})] - m_\xi) + \sigma_\xi^2$$

où $\mathbf{x} = (x, y) \in \mathbb{R}^2$ désigne la position d’un pixel dans l’image. Nous obtenons ainsi une relation quadratique pour un capteur ICCD, alors qu’un capteur CCD présente théoriquement une relation linéaire. Cette différence est liée aux variations stochastiques non négligeables du gain dans l’intensificateur.

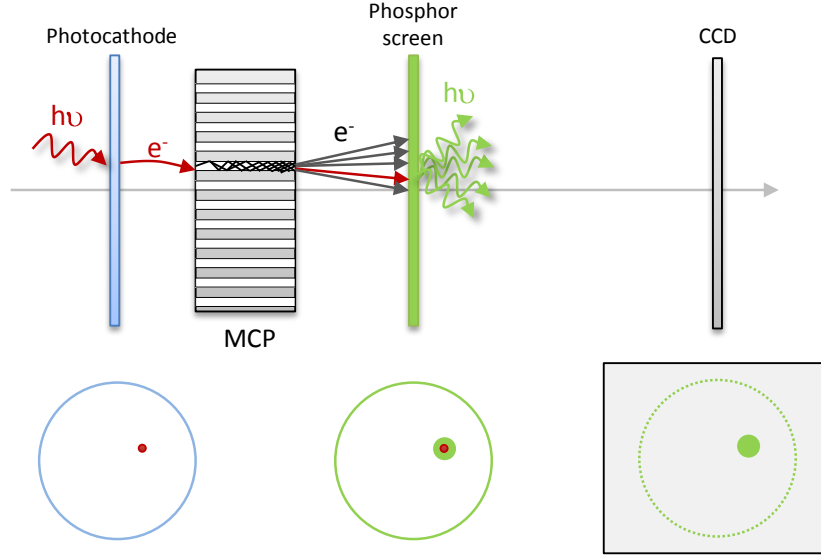


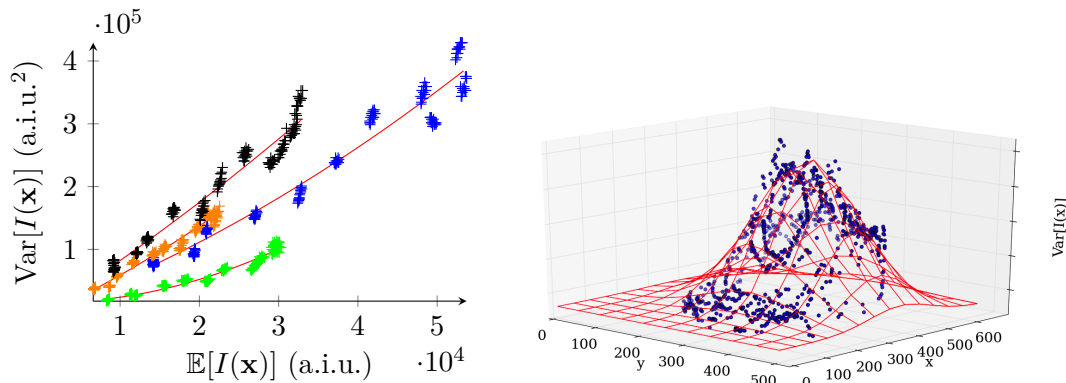
Figure 0.6: Processus de formation de l'image formation dans un CCD intensificateur de troisième génération.

En testant notre modèle théorique en conditions expérimentales, nous observons bien localement un comportement quadratique. Néanmoins, nous observons aussi une forte instabilité du gain qui n'est pas pris en compte par notre modèle (voir Figure 0.7(a)). Après quelques investigations, nous avons identifié une déformation supplémentaire, probablement induite par le relais optique du capteur ICCD, qui perturbe spatialement les variances mesurées. Pour vérifier cela, nous avons tracé les variances estimées localement en fonction de leurs coordonnées spatiales (axes x et y), pour un plusieurs valeurs d'intensité λ avec une tolérance de plus ou moins 0.0005% (voir Figure 0.7(b)) pour une valeur donnée $\lambda = 2000 \pm 10$).

Nous proposons un nouveau modèle ainsi qu'une méthode d'estimation pour corriger cette variation:

$$\text{Var}[I(\mathbf{x})] = (a\mathbb{E}[I(\mathbf{x})]^2 + b\mathbb{E}[I(\mathbf{x})] + c) \left(e^{-\frac{(x-x_0)^2}{2\sigma_x^2} - \frac{(y-y_0)^2}{2\sigma_y^2}} + o \right) \quad (0.2)$$

où a, b and c sont les paramètres dérivés de (0.2) et $x_0, y_0, \sigma_x, \sigma_y$ et o sont les paramètres contrôlant le terme de correction. La forme Gaussienne a été choisie pour des raisons de stabilité numérique durant la phase d'estimation qui ne sera pas détaillée ici. Le modèle et l'estimation ont été validés en microscopie confocale et en microscopie champ large.



(a) Quatre gains quadratiques différents mesurés dans quatre régions différentes. Les croix d'intensité $\lambda = 20000 \pm 10$ a.i.u., tracées en noir, orange, bleu et vert, représentent les variances mesurées, les courbes rouges représentent la fonction (0.2) contrôlée par les paramètres estimés localement. (b) Variance locale mesurée pour une valeur d'intensité $\lambda = 20000 \pm 10$ a.i.u., tracée en rouge, fonction des positions spatiales. En théorie les variances mesurées devraient former un plan horizontal.

Figure 0.7: Gain expérimental non-stationnaire en FD FLIM. Représentation de la variance calculée sur une mesure de référence FD FLIM de 12 images acquises avec un microscope confocal.

Sur les images de référence nous mesurons une division par deux de l'erreur de prédiction de la variance du bruit par rapport à un modèle théorique. Nous envisageons désormais d'effectuer ces mêmes expériences avec un ICCD fibré.

Application aux mesures FD FLIM

Nous exploitons notre modèle de bruit pour estimer les paramètres de correction, au sens des moindres carrés pondérés:

$$\hat{\theta}_b = \underset{\theta_b}{\operatorname{argmin}} \sum_{k \in [1, K]} \frac{(I(k)(\mathbf{x}) - S_{\theta_b}(k)(\mathbf{x}))^2}{\text{Var}[I(k)(\mathbf{x})]} \quad (0.3)$$

où $\text{Var}[I(k)(\mathbf{x})]$ est la variance obtenue à partir de (0.2) au pixel \mathbf{x} et d'intensité $I(k)(\mathbf{x})$. La figure 0.8 présente la distribution de phase estimée à partir d'une mesure FD FLIM en microscopie champ large et sur un échantillon uniforme de fluorescéine qui a la bonne propriété de présenter un temps de vie unique. Nous comparons les résultats obtenus avec une méthode de Fourier conventionnelle et avec notre approche hétéroscédastique. Il ressort qu'un déplacement significatif du mode de la distribution est observé. Par ailleurs, notre correction présente clairement un gain de 10% en kurtosis, ce qui est attendu pour un échantillon homogène [Spring and Clegg, 2009].

Nous proposons d'intégrer notre modèle de bruit dans un schéma de débruitage de séquences expérimentales FD FLIM. Deux filtres de Wiener élaborés sur la base du

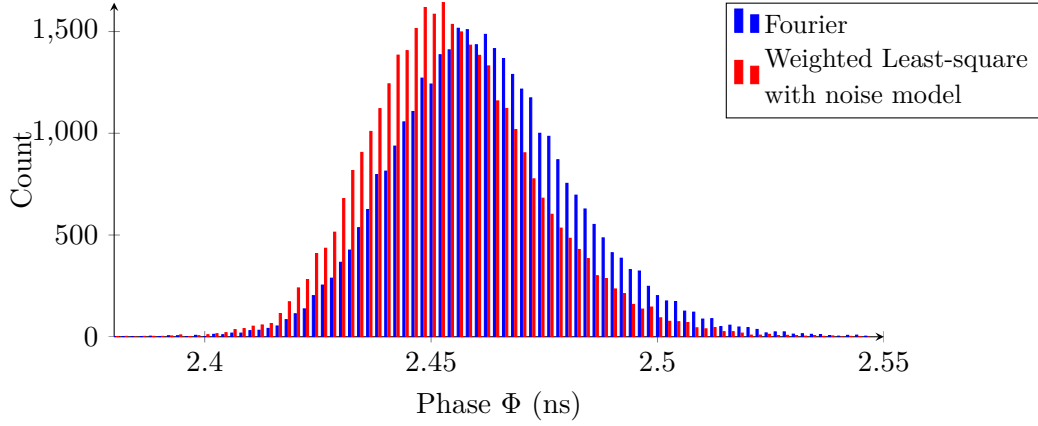


Figure 0.8: Histogrammes de phase comparant les résultats obtenus avec la méthode de Fourier et la méthode des moindres carrés pondérés par l’échelle du bruit estimée.

modèle théorique et du modèle corrigé sont d’abord étudiés (voir Figure 4.11 page 98). Nous avons ensuite considéré un algorithme plus sophistiqué, basé sur le principe des moyennes non-locales (filtre “NL-means”) [Buades et al., 2005]. Le filtre “NL-means” calcule une moyenne pondérée des valeurs d’intensité en identifiant à chaque position spatiale les patches les plus similaires au patch central. Nous adoptons la formulation Bayésienne décrite dans [Kervrann et al., 2007] pour élaborer un filtre approprié à la nature du bruit observé. Nous considérons toujours une distance Euclidienne entre patches ($\sqrt{n} \times \sqrt{n}$) afin d’identifier empiriquement une loi de probabilité adaptée. Sous des hypothèses de bruit blanc Gaussien, la distance entre patches non-recouvrants, suit une distribution du χ^2 avec n degrés de liberté [Kervrann et al., 2007]. Dans notre contexte de bruit Poisson-Gaussien, nous recourons à une distribution Gamma, plus flexible que la distribution du χ^2 . Ces considérations, également détaillées dans une annexe du manuscrit, conduisent au filtre suivant de débruitage:

$$\hat{I}_{GNL}(\mathbf{x}) = \frac{\sum_{\mathbf{y} \sim U_r(\mathbf{x})} \left(\frac{\|S_I(\mathbf{y}) - S_I(\mathbf{x})\|^2}{2 \text{Var}[I(\mathbf{x})]} \right)^{k-1} e^{-\frac{\|S_I(\mathbf{y}) - S_I(\mathbf{x})\|^2}{2\beta \text{Var}[I(\mathbf{x})]}} I(\mathbf{y})}{\sum_{\mathbf{y} \sim U_r(\mathbf{x})} \left(\frac{\|S_I(\mathbf{y}) - S_I(\mathbf{x})\|^2}{2 \text{Var}[I(\mathbf{x})]} \right)^{k-1} e^{-\frac{\|S_I(\mathbf{y}) - S_I(\mathbf{x})\|^2}{2\beta \text{Var}[I(\mathbf{x})]}}} \quad (0.4)$$

où les positions $\mathbf{y} \sim U_r(\mathbf{x})$ sont uniformément tirés dans une boule de rayon r . Les paramètres k et β , caractéristiques de la distribution Gamma, sont estimés sur l’image. Les performances de cet algorithme de débruitage sont illustrés sur la figure 4.12 (voir page 100).

Estimation de temps vie sur les structures intracellulaires dynamiques

Estimation conjointe des paramètres de temps de vie et de mouvement

Les artefacts induits par les mouvements des structures cellulaires ont été précédemment diagnostiqués par Hanley et al. [2001], puis finement analysés dans [Lajevardipour and Clayton, 2013]. Pourtant, à notre connaissance, aucune méthode n'a été proposée pour estimer le temps de vie sur ces objets. La mesure de FRET sur structures dynamiques (pas de fixation) est pourtant d'une importance capitale. Dans le contexte d'une étude menée à l'Institut Curie, nous nous sommes intéressés à la variation de temps de vie de fluorescence sur des endosomes précoces. Nous proposons ici une modélisation des variations spatiales et temporelles d'un endosome acquis en FD FLIM et une méthode d'estimation de temps de vie conçue spécifiquement pour les endosomes en mouvement.

Soit $\mathbf{x}_0(k)$ la position dans \mathbb{R}^2 d'un endosome dans l'image d'indice k . Nous proposons le modèle suivant pour décrire le comportement des valeurs d'intensité d'un endosome:

$$\begin{aligned} I(k)(\mathbf{x}) &= S_{\theta_b}(k)(\mathbf{x}) + S_{\theta_0}(k)G_\gamma(\mathbf{x} - \mathbf{x}_0) + \varepsilon(k)(\mathbf{x}) \\ &= S_{\theta_b}(k)(\mathbf{x}) + \left[C_{S_0} + A_{S_0} \cos\left(\frac{2\pi k}{K} + \Phi_{\tau_0}\right) \right] G_\gamma(\mathbf{x} - \mathbf{x}_0(k)) + \varepsilon(k)(\mathbf{x}) \end{aligned} \quad (0.5)$$

où $S_{\theta_0}(k)$ est l'intensité moyenne de la vésicule paramétrée par $\theta_0 = (C_{S_0}, A_{S_0}, \Phi_{\tau_0})^T$ (voir (0.1)), $S_{\theta_b}(k)(\mathbf{x})$ est le signal du fond avec la même signature, $G_\gamma(\cdot)$ est une fonction Gaussienne de variance γ^2 décrivant la forme de la vésicule et ε est le bruit introduit par le capteur ICCD, étudié précédemment.

Pour chaque particule détectée sur la première image, nous proposons une estimation alternée des paramètres de temps de vie (régissant la sinusoïde) et ceux des mouvements comme suit. Soit une trajectoire initialisée par estimation locale des paramètres du spot Gaussien image-après-image. Soit une fenêtre $W(\mathbf{x}_0^n(k))$ de 7×7 pixels autour de la position $\hat{\mathbf{x}}_0^n(k)$. Les paramètres de temps de vie d'une particule sont estimés à partir des intensités mesuré aux l'emplacement estimé:

$$\hat{\theta}_0^n = \underset{\theta_0}{\operatorname{argmin}} \sum_{k \in [1, K]} \sum_{\mathbf{x} \in W(\hat{\mathbf{x}}_0^n(k))} \frac{(I(k)(\mathbf{x}) - S_{\theta_0}(k)G_{\gamma^n}(\mathbf{x} - \hat{\mathbf{x}}_0^n(k)))^2}{\operatorname{Var}[I(k)(\mathbf{x})]}. \quad (0.6)$$

Dans une seconde étape, les paramètres de mouvement sont re-estimés en exploitant le modèle sinusoidale d'intensité grâce à une méthode de M-estimation qui calcule la position et les paramètres du spot Gaussien sur chaque image:

$$(\hat{\mathbf{x}}_0^{n+1}(k), \hat{\gamma}^{n+1}) = \underset{(\mathbf{x}_0(k), \gamma)}{\operatorname{argmin}} \sum_{\mathbf{x} \in W(\mathbf{x}_0(k))} \rho_\eta \left(I(k)(\mathbf{x}) - S_{\hat{\theta}_0^n}(k)G_\gamma(\mathbf{x} - \mathbf{x}_0(k)) \right).$$

Les deux étapes sont itérées jusqu'à convergence des paramètres et ce indépendamment pour chaque vesicle détecté sur la première image. Quatre itérations sont généralement

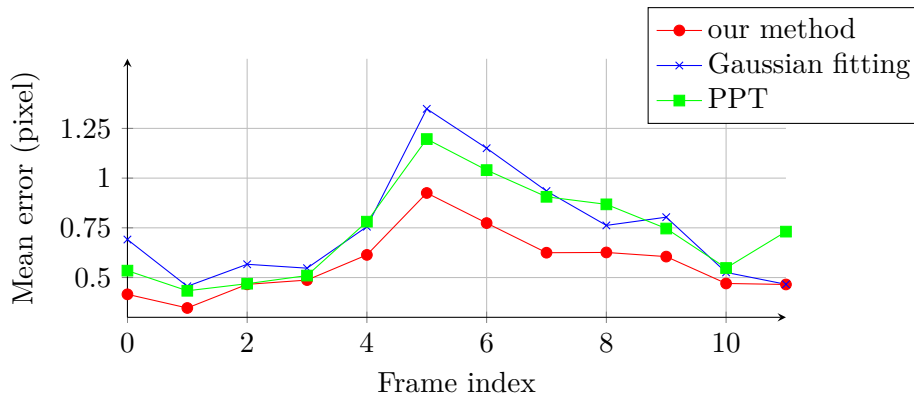


Figure 0.9: Erreurs moyennes de localisation. La méthode “Gaussian Fitting” [Anderson et al., 1992] est analogue à notre méthode, mais sans prise en compte de modèle d’intensité sinusoïdale. La méthode PPT est une méthode plus avancée combinant détection, puis calcul des trajectoires selon le principe du filtrage stochastique [Genovesio et al., 2006]. Les résultats sont obtenus sur des protéines RX marquées GFP et suivies manuellement (cellules épithéliales).

suffisantes en pratique. Les détails décrivant le processus d’initialisation peuvent être consultés au Chapitre 5.2.2.

Résultats expérimentaux

Evaluer la qualité de l’estimation de temps de vie sur des endosomes en conditions expérimentales est une tâche complexe. Néanmoins, il est tout à fait possible de générer une “vérité-terrain” des déplacements de la structure. Comme la précision de l’estimation de temps de vie dépend avant tout de la qualité de l’estimation du mouvement, nous adoptons cette procédure en deux étapes pour traiter les séquences expérimentales. Nous comparons les performances d’estimation des déplacements avec deux autres méthodes de suivi d’objets (voir Figure 0.9). Le fait de modéliser spécifiquement les variations d’intensité, donne un net avantage à notre méthode qui gère mieux les images le plus sombres, présentant un rapport signal sur bruit très faible. Notre méthode a aussi été évaluée sur des séquences synthétiques.

Dans le cadre du challenge portant sur le suivi de particules organisé par E. Meijering et J.-C. Olivo-Marin et publié récemment [Chenouard et al., 2014], nous avons également proposé un M-estimateur très similaire pour le suivi de protéines fluorescentes. Le modèle d’intensité sinusoïdale n’a pas d’intérêt dans ce contexte et n’a donc pas été utilisé ici. Notre méthode est locale spatialement et temporellement, elle ne prend pas en compte l’ensemble des protéines pour effectuer l’appariement. Malgré cela, notre méthode de M-estimation s’est bien comportée puisqu’elle fut classée 2^{ème}/14 en terme de précision de localisation.

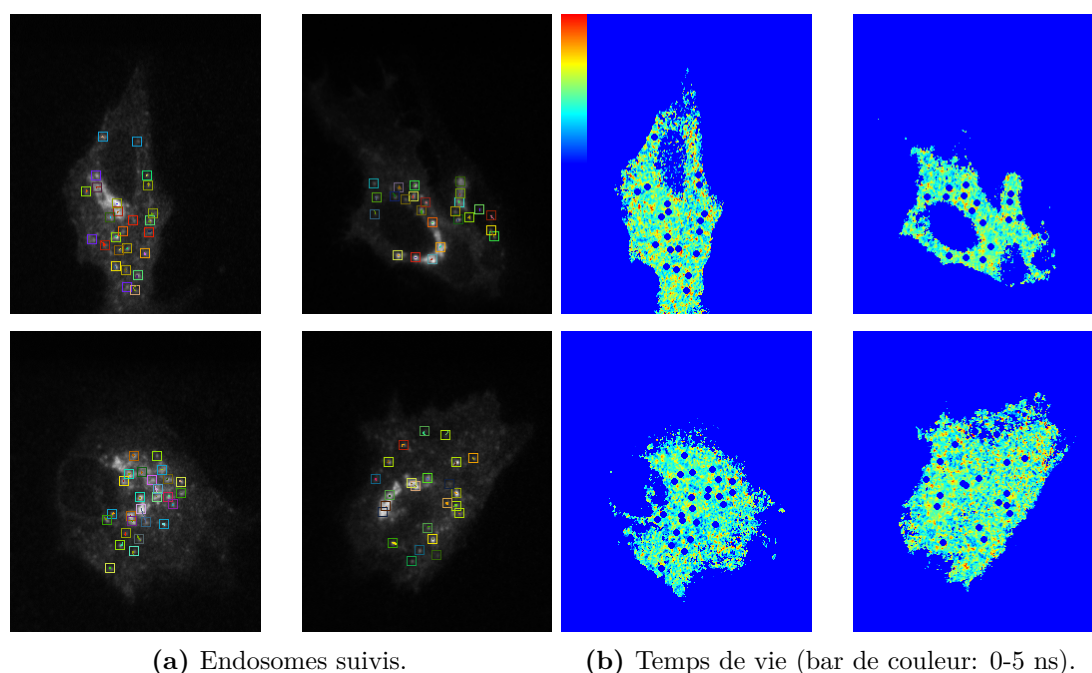


Figure 0.10: RX protéine marquée GFP sur les endosomes (gauche) et temps de vie à la membrane (droite) en l'absence d'accepteur.

Analyse des interactions entre protéines à la membrane au cours de l'endocytose

Nos collaborateurs de l'équipe de Ludger Johannes à l'Institut Curie (UMR 144) sont intéressés par l'étude des interactions par mesure de FRET entre un récepteur de cytokine RX et sa kynase KX¹ à la membrane au cours de l'endocytose *in vivo*. Les cellules ne sont pas fixées chimiquement. Leurs dynamiques internes nécessitent donc l'usage de l'imagerie FD FLIM couplée à notre méthode numérique.

Pour différencier les temps de vie estimés au niveau des endosomes mobiles et au niveau de la membrane, nous exploitons d'une part les objets suivis, et d'autre part le fond de la cellule automatiquement segmentée (voir Figure 0.10). Quelques résultats préliminaires sont présentés sur la figure 0.11. Les résultats obtenus semblent suggérer une différence d'efficacité de FRET entre la membrane et au niveau des endosomes, en réponse à une augmentation de l'ajout de l'accepteur. L'interaction serait donc plus importante au niveau des endosomes. Nous avons prévu de mener d'autres expérimentations afin d'accroître le nombre d'endosomes et d'améliorer la significativité statistique de ces résultats.

¹Les molécules sont anonymes pour des raisons de confidentialité.

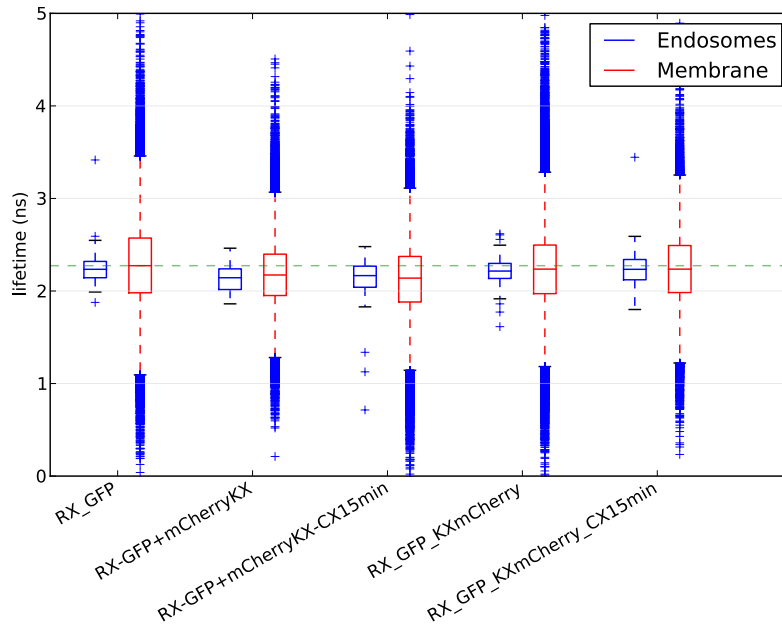


Figure 0.11: Distribution de temps de vie estimés au niveau des endosomes et à la membranes (voir détails Section 6.1 à la page 113).

Conclusion

Dans cette première partie, nous avons proposé une nouvelle étude rigoureuse du bruit de mesure en FD FLIM et une nouvelle méthode pour compenser les mouvements des structures intracellulaires. L'exploitation de ces méthodes dans le cadre d'une expérience de biologie est toujours en cours et les résultats sont prometteurs.

De nouvelles investigations devront être menées pour poursuivre ce projet. Le bruit issu de capteurs ICCD fibrés doit être étudié dans un premier temps pour tester notre hypothèse quant à l'origine de la déformation observée. Ensuite, nous souhaitons porter nos efforts sur les aspects opérationnels de l'algorithme d'estimation de temps de vie de fluorescence, dans des contextes biologiques variés. Pour cela, il est question de coupler notre estimateur de temps de vie à des méthodes de suivi de protéines plus sophistiqués. Dans la suite du manuscrit, nous présentons un algorithme qui répond bien à ce besoin. D'autres pistes de travail devront être étudiées pour caractériser le temps de vie sur des structures non-endosomales.

Résumé des contributions:

- Analyse et modélisation du bruit issu d'un intensificateur CCD
 - Un modèle de variance de bruit pre en compte les aberrations optiques induites par le ICCD.
 - Un estimateur des paramètres du modèle de variance.
 - Application de notre modèle au débruitage de mesures FD FLIM.
 - Une dérivation originale pour le bruit de capteur.
- Reconstruction de carte de temps de vie mesurée en domaine de fréquence
 - La prise en compte du modèle de bruit améliore l'estimation du temps de vie sur échantillon statique.
 - Estimation conjointe du temps de vie et du déplacement des endosomes mobiles.
- Une dérivation nouvelle pour le modèle de mesure FD FLIM (Annexe A).

3 Etude d'un algorithme de suivi de particules à dynamiques hétérogènes dans un environnement intracellulaire dense

J'ai eu la chance d'effectuer trois mois de mobilité internationale au sein du laboratoire de Gaudenz Danuser, professeur à Harvard Medical School, grâce au soutien du GDR 2588, d'Inria et de l'École Doctorale MATISSE. Le projet initial concernait alors le suivi de molécules de vimentine marquées en fluorescence, alternant mouvements diffusifs dans le cytoplasme et transports actifs. Très rapidement, le défi bien plus large de la quantification de trajectoires hétérogènes dans un environnement dense, s'est posé. Par trajectoires hétérogènes, nous entendons qu'il existe parmi ces trajectoires des transitions d'un type de transport à l'autre qui sont imprévisibles, dans l'espace et dans le temps. C'est la combinaison des facteurs de densité de particules et d'hétérogénéité qui est à l'origine de l'ambiguïté des associations. Ce problème, abordé depuis longtemps en vision par ordinateur, reste néanmoins encore ouvert et aucune solution complète n'a été publiée dans la littérature. L'ambition du projet a donc été de dépasser le problème de la vimentine, pour proposer un algorithme de suivi performant dans le cas de populations denses de particules présentant une hétérogénéité importante de mouvement. Nous avons également souhaité conserver d'excellentes performances sur des scénarios plus simples, sans surcoût en complexité algorithmique.

Quantifier l'hétérogénéité de transport dans la cellule vivante

Les transports intracellulaires peuvent être classés en trois grandes catégories: les transports diffusifs dans le cytoplasme, les transports actifs le long du cytosquelette et les transports hétérogènes. Ces derniers sont de diverses natures, mais nous nous intéressons ici aux variations instantanées de régimes de transport alternant diffusion et transport actif. Ce comportement s'applique à de nombreux phénotypes comme le transport axonale, les infections virales ou encore le transport de filaments unitaires de vimentine.

La quantification de ces mouvements est complexe lorsque, à la densité, s'ajoute l'hétérogénéité des mouvements des particules. Par densité intracellulaire, nous entendons densité spatio-temporelle liée à la fréquence d'acquisition. C'est le rapport entre la vitesse de déplacement et la vitesse d'acquisition qui va définir la difficulté des associations entre les différentes molécules détectées. La détection de transitions brutales entre deux types de transport n'est pas un problème s'il n'y a pas d'autres protéines dans le voisinage immédiat. Par contre, la densité locale peut générer des appariements ambigus. Enfin, la densité complique la tâche de détection d'initialisations et de terminaisons qui dépendent des apparitions et des disparitions d'objets, fréquentes en bio-imagerie.

Les acquisitions de vimentine sont exemplaires à cet égard. La vimentine est une protéine qui compose les filaments intermédiaires. Le support à leur formation, qui dure quelques secondes, est encore mal connu et l'étude de leurs dynamiques devrait apporter quelques réponses dans ce domaine. Les mouvements que nous observons et que nous souhaitons quantifier sont rapides, de nature instable, transitant d'un état Brownien à un état confiné ou dirigé. Ils doivent être détectés dans une population très dense de protéines.

Etat de l'art des algorithmes de suivi de particules multiples

De nombreux algorithmes ont été proposés pour répondre aux défis très spécifiques posés par le suivi de particules multiples en microscopie de fluorescence. Dans la littérature, la grande majorité des méthodes repose sur une phase de détection, suivie d'une phase de calcul des trajectoires. La détection, déjà largement étudiée [Smal et al., 2010], n'est pas discutée dans nos travaux. Dans cette seconde partie, nous proposons une classification des algorithmes en fonction de six critères: la modélisation de la dynamique, l'optimisation des associations, le calcul du rayon de recherche, la mesure de la similarité entre les objets, la détection de points manquants dans les trajectoires et la capacité à détecter la fusion ou la séparation de particules. Dans ce résumé, nous portons notre attention sur le premier point (modélisation de la dynamique), le plus important dans notre étude.

Deux approches ont été proposées pour modéliser les trajectoires hétérogènes [Genovesio et al., 2006; Jaqaman et al., 2008]. Ces deux approches s'appuient sur de multiples filtres

de Kalman pour évaluer autant de dynamiques possibles. Les matrices de transition peuvent représenter un mouvement “Brownien”, “dirigé” ou “dirigé inversé”. De par les mécanismes de filtrage, ces algorithmes ne peuvent détecter que des transitions lentes entre les différents types de déplacement. Nous montrons que les mécanismes de l’algorithme u-track [Jaqaman et al., 2008], qui ne comprend qu’un seul vecteur d’état, a pour caractéristique de maintenir une certaine inertie lors de l’estimation de la vitesse et d’orienter la convergence vers un seul vecteur par trajectoire. D’autre part, nous montrons que les algorithmes de type IMM sont plus flexibles à cet égard.

En imagerie biologique la transition instantanée entre un transport Brownien et dirigé est un phénotype fréquent, pourtant, aucun algorithme de l’état de l’art ne semble cibler ce problème particulier.

Lissages multiples et estimation adaptative du rayon de recherche

Nous proposons deux contributions pour améliorer le suivi de particules avec des mouvements hétérogènes dans un environnement dense. La première contribution vise à prédire les transitions entre différents modèles de mouvement en considérant les dynamiques passées et futures et en probabilisant les associations. La seconde contribution a pour objet d’adapter localement et itérativement le rayon de recherche propre à chaque objet/particule suivi, ceci afin d’améliorer la détection de terminaisons et d’initialisations de trajectoires.

Interaction de modèles multiples itératifs

Afin de prendre en compte les dynamiques passées et futures de chaque trajectoire avec une complexité algorithmique raisonnable, nous proposons l’utilisation d’un lissage de type “forward-backward” [Fraser and Potter, 1969]. Plusieurs balayages de filtrage stochastique sont appliqués itérativement en inversant la séquence temporellement. Ainsi, chaque prédiction est mise en compétition avec la prédiction issue de l’état estimé au balayage précédent. Nous appliquons ce principe à un filtrage de type IMM. Nous avons ainsi implémenté un filtre IMM itératif permettant d’obtenir une estimation convergente de la vitesse et du type de transport à chaque point de temps. La figure 0.12 illustre l’effet de trois balayages temporels restreints sur une séquence expérimentale de vimentine. L’équation (0.7) permet de calculer la probabilité *a posteriori* qui tient compte des probabilités associées aux différents types de transports et de la probabilité évaluée à l’itération précédente:

$$p(\mathbf{x}_{t+1,k+1}, \mathbf{z}_{1:T}) \approx \sum_{\theta_{t+1,k+1} \in \{1 \dots N\}} p(\theta_{t+1,k+1} | \mathbf{z}_{1:t+1}) p(\mathbf{x}_{t+1,k+1} | \theta_{t+1,k+1}, \mathbf{z}_{1:t+1}) \quad (0.7)$$

$$+ p(\hat{\theta}_{t+1,k} | \mathbf{z}_{t+1:T}) p((2\mathbf{H} - I)\mathbf{x}_{t+1,k} | \hat{\theta}_{t+1,k}, \mathbf{x}^{\mathbf{z}_{t+1:T}})$$

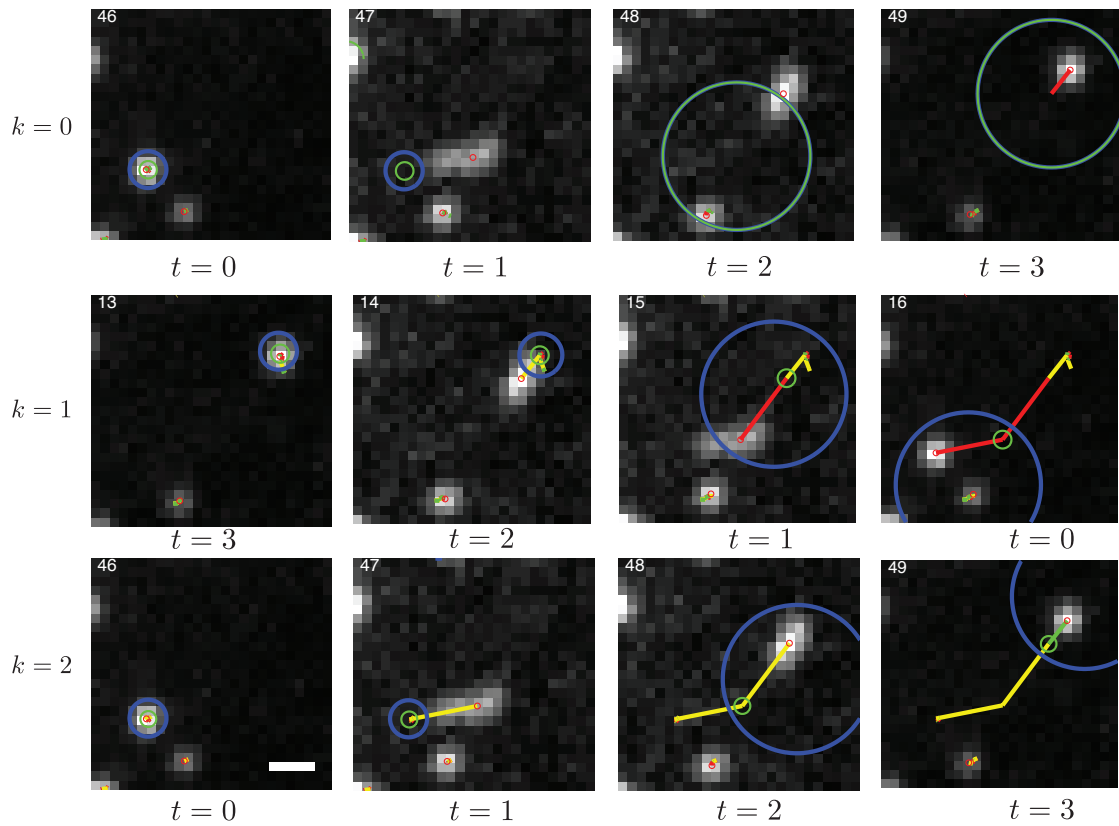


Figure 0.12: Convergence des estimations de vitesse à l'échelle du point de temps lors d'un changement de brutal dynamique. Avant l'image # 46, la particule de vimentine présente un mouvement Brownien confiné prolongé. Elle se déplace brutalement le long du cytosquelette pour retrouver un état Brownien confiné prolongé dès l'image # 49. Les traits rouges représentent la détection de déplacement dirigés, les traits verts représente la détection d'un mouvement Brownien et les traits jaunes représentent la prédiction issue du calcul à l'itération précédente.

Estimation en ligne adaptative du rayon de recherche

Nous avons également amélioré l'estimation de la variance du bruit de processus. Cette estimation est utile pour définir la zone d'appariement et permet de détecter automatiquement la terminaison d'une trajectoire et, par conséquent, de réduire le nombre de fausses trajectoires. Nous avons privilégié un calcul en ligne récursif permettant d'appréhender les mesures d'erreur issues du précédent balayage temporel. Les filtres de Kalman indépendants permettent également d'estimer le bruit de modèle pour chaque type de mouvement et de s'adapter aux mouvements détectés (Brownien ou direct). Nous ne détaillerons pas cet aspect de notre travail ici. La figure 0.13 illustre les performances de notre nouvel estimateur.

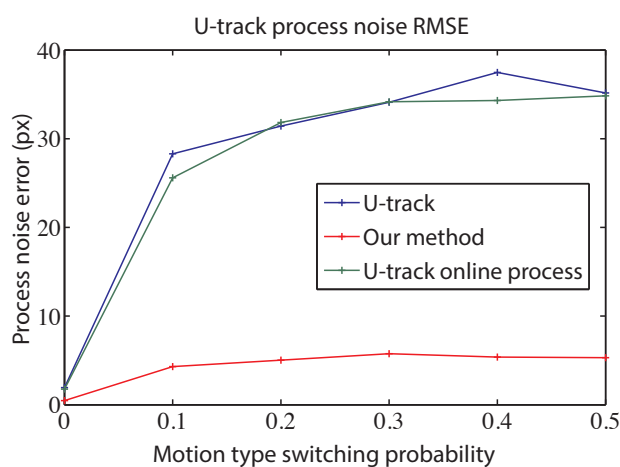


Figure 0.13: Erreurs d'estimation de la variance du bruit caractérisant le processus mesuré sur simulations en fonction de la probabilité de changement de type de transport (0 indique un déplacement purement Brownien confiné, 0.5 indique une chance sur deux de transiter vers un mouvement dirigé à chaque point de temps). Notre méthode (en rouge) est sept fois plus précise que l'estimateur u-track (en bleu). De plus, une simple estimation récursive de la variance, prenant en compte les mesures d'erreur issues du calcul à l'itération précédente, met en évidence l'intérêt de notre méthode basée sur l'algorithme u-track (en vert). L'adaptivité et l'agilité de l'algorithme de suivi sont assurées par la mise en place de plusieurs filtres.

Résultats sur séquences synthétiques

La figure 0.14 illustre les performances de notre filtre IMM itératif sur simulations. De plus, nous mettons en évidence que notre méthode se comporte mieux que les algorithmes concurrents [Genovesio et al., 2006; Jaqaman et al., 2008] pour traiter des situations variées telles que le transport actif à vitesse variable ou une vitesse de transition variable entre états de transport. L'algorithme présente de meilleures performances que u-track pour calculer les trajectoires avec un sur-coût de complexité algorithmique négligeable.

Résultats sur séquences expérimentales

Quantification du transport hétérogène de vimentine

Selon l'hypothèse du professeur Gelfand (North Northeastern University, collaborateur de G. Danuser), les filaments intermédiaires unitaires se déplacent le long des microtubules. Afin de tester cette hypothèse, les cellules sont traitées au nocodazole, un agent biologique qui provoque la dépolymérisation des microtubules. Si le traitement affecte les mouvements dirigés de la vimentine, alors cela favorise l'hypothèse selon laquelle la vimentine se déplace le long des microtubules. L'étude de la dynamique des protéines est

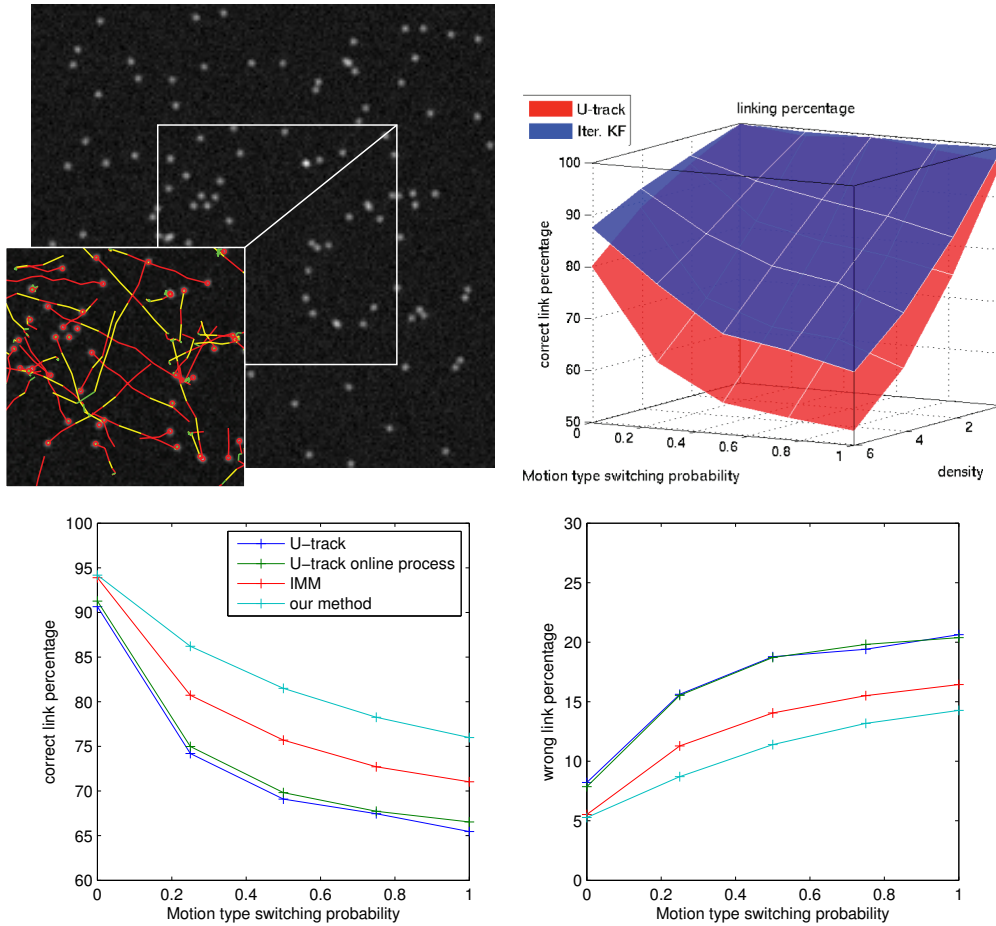


Figure 0.14: Pourcentage de vrais positifs (et faux positifs sur le graphique de droite) sur données simulées en fonction de la densité et de la probabilité de changement de type de transport (0 indique un déplacement purement Brownien confiné, 0.5 indique une chance sur deux de transiter vers un mouvement dirigé à chaque point de temps). Comparaison des performances avec notre méthode u-track et avec un filtrage IMM. La densité est fixé à 3 spots par micromètre carré sur l'exemple à gauche et sur les résultats à droite. Notre approche présente une amélioration de 15% par rapport à u-track sur le scénario le plus complexe.

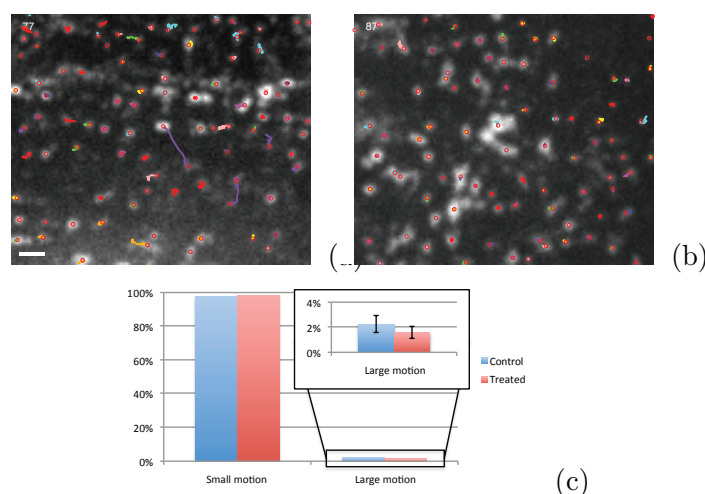


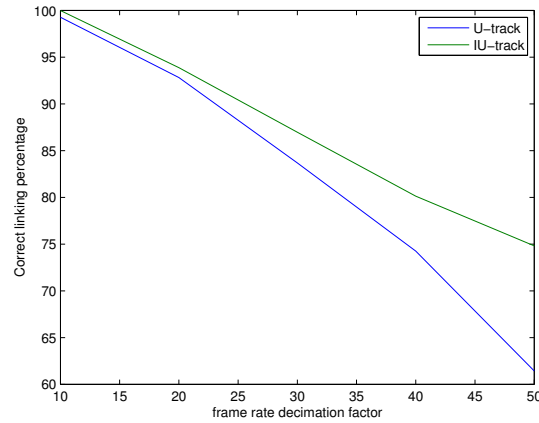
Figure 0.15: (a) & (b) Exemple de suivi de filaments unitaires de vimentine sur une cellule témoin (à gauche) et traitée au nocodazole. (c) Proportion de mouvement d’amplitude importante avant et après traitement au nocodazole. Un mouvement d’amplitude importante est défini comme le 99,9 percentile de la vitesse estimée localement par le filtre de Kalman. L’évaluation de la dynamique sur 6 cellules de contrôle et 6 cellules traitées (séquences de 100 images) met en évidence une différence significative pour une p -valeur de 0.0088 (t -test).

effectuée par microscopie confocale à disques rotatifs après transfection cellulaire pour marquer la vimentine par GFP. Le problème rencontré était de quantifier les dynamiques des particules avant et après traitement (voir Figure 0.15(a)-(b)). La faible différence est due au taux variable de pénétration du traitement au nocodazole. Pourtant, notre méthode met en évidence une différence significative sur la figure 0.15(c). Ces résultats confirment l’hypothèse initiale selon laquelle les filaments unitaires se déplacent bien le long du réseau de microtubules.

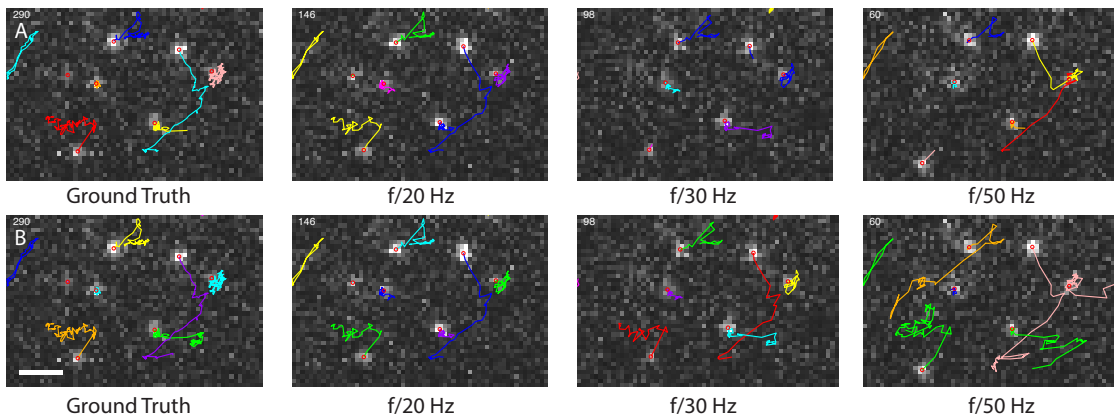
Robustesse face à la baisse de la fréquence d’acquisition

Comme expliqué plus haut, une méthode fiable pour tester un algorithme de quantification en biologie consiste à utiliser une séquence expérimentale pour un phénotype connu. Dans ce cadre, les séquences exceptionnelles de virus issues des travaux présentés dans [Burckhardt et al., 2011] ont pu être exploitées. En effet, la fréquence d’acquisition rapide, rendue possible grâce à une abondance de marquage, permet une quantification aisée du déplacement des virus. Nous proposons alors d’utiliser cette quantification comme “vérité-terrain” et de tester la robustesse de notre approche pour faire face à différents échantillonnages d’acquisition temporels (voir Figure 0.16). Avec un niveau croissant de décimation temporelle, notre algorithme présente une décroissance linéaire de ses

performances, alors que u-track présente plutôt une décroissance quadratique.



(a) Pourcentage de vrais positifs obtenus avec u-track et notre méthode en fonction de la décimation temporelle de la séquence d'origine.



(b) u-track échoue à partir d'un facteur de décimation égal à 30 tandis que notre approche présente une seule erreur pour un facteur de décimation égal à 50 (les trajectoires les plus longues sont liées des fréquences faibles d'échantillonnage).

Figure 0.16: Suivi automatique de virus dans la cellule [Burckhardt et al., 2011]. La fréquence d'acquisition est artificiellement réduite pour tester la robustesse de l'algorithme.

Conclusion

Nous avons identifié un problème de quantification de trajectoires relativement fréquent en imagerie du vivant: la quantification de dynamique hétérogène dans un environnement dense. Nous avons mis en évidence que l'état de l'art ne permettait pas de répondre

à cette problématique complètement. Partant de ce constat, nous avons proposé des innovations ciblées et une méthode originale de suivi. Notre approche présente d'excellentes performances pour une large gamme de scénarios biologiques ainsi qu'une complexité algorithmique comparable aux algorithmes usuels de la littérature.

Notre approche peut être couplée aux techniques MHT qui ont été très récemment expérimentées dans le domaine du suivi d'entités biologiques [Chenouard et al., 2014]. La prochaine étape, d'un point de vue méthodologique, est donc très clairement de proposer une fenêtre d'analyse temporelle plus importante pour effectuer l'optimisation des appariements. Cela dit, les innovations, pour être fécondes et robustes, doivent être effectuées avec un objectif applicatif précis. Il est important de mettre d'abord l'expérience acquise au service des problématiques biologiques, afin d'optimiser la qualité et la quantité des données obtenues, de mieux comprendre les prochains défis de l'analyse dynamique en biologie quantitative et de proposer des méthodes robustes qui auront un impact fort dans de nombreuses communautés.

Résumé des contributions:

- Revue des méthodes de suivi de particules
 - Description de la modélisation de dynamiques multiples dans l'algorithme u-track, un algorithme de suivi très répandu en bio-imagerie.
 - Discussion des capacités des algorithmes de suivi de particules selon six caractéristiques techniques.
- Un nouvel algorithme conçu pour le suivi individuel de population dense de particules à dynamiques hétérogènes
 - Un lisseur IMM (Interacting Multiple Modeling en anglais) de type "forward-backward" permet la détection de transitions brutales.
 - Estimation adaptative et itérative du rayon de recherche.
 - Faible surcoût algorithmique.
- Validation expérimentale
 - Notre méthode propose de meilleures performances que les algorithmes connus sur données synthétiques simulant la problématique cible.
 - Notre méthode propose de meilleures performances que les algorithmes connus sur données synthétiques simulant une variété de scénarios moins sophistiqués.
 - L'étude du trafic de la vimentine met en avant des transitions rares et brutales dans leur dynamiques.

- Nous montrons que notre méthode est plus robuste face à la réduction de la vitesse d’acquisition sur des séquences de virus.

4 Conclusion Générale

Nous avons présenté deux projets qui répondent aux défis actuels en biologie et en bio-imagerie. La dynamique et l’hétérogénéité inhérente à tout processus bio-physique est désormais observable par les techniques de fluorescence. Nous avons proposé des solutions originales qui modélisent ces phénomènes et permettent d’estimer les paramètres sous-jacents.

Une première contribution visait à améliorer la précision et la fiabilité de la mesure de temps de vie sur des structures dynamiques en FD FLIM. Une seconde contribution méthodologique a porté sur le suivi de particules afin d’améliorer la quantification des dynamiques intra-cellulaires. Ces deux contributions sont au coeur des problématiques abordées par la communauté spécialiste des méthodes numériques en microscope de fluorescence: la modélisation de processus de formation des images de microscopie d’une part, et d’autre part la modélisation et la quantification des phénotypes dynamiques. A court terme, nous souhaitons valoriser ces travaux dans des études variées en biologie et mettre ces approches numériques à disposition d’un grand nombre d’utilisateurs.

En conclusion, je suis maintenant convaincu qu’un numéricien peut jouer un rôle décisif dans la biologie moderne. La collaboration des différentes expertises en bio-chimie, microscopie et analyse de données permettra de conduire des projets ambitieux en microscopie. On peut s’attendre à l’émergence de nouvelles techniques d’imagerie qui donneront une place importante au modèle mathématique et à la modélisation. A titre d’exemple, en microscopie de “speckle”, la modélisation est prise en compte dès la phase de marquage fluorescent. Cette stratégie permettra de rationaliser les acquisitions de données également. Le développement de méthodes de traitement de données synchrones avec les problématiques biologiques est bénéfique pour la communauté des biologistes tout comme pour la communauté des numériciens. Il assurera la qualité et la complétude des données à analyser. Une meilleure coordination et une meilleure concertation devraient assurer une exploitation plus rapide des données et une optimisation des efforts. Les défis dans le domaine de l’imagerie biologique sont nombreux et ils ne sont pas encore tous identifiés. C’est dans cet état d’esprit que je vais continuer mes recherches post-doctorales au sein du laboratoire de Gaudenz Danuser, un laboratoire de biologie cellulaire dirigé par un expert en vision par ordinateur et en traitement du signal.

Organization of the thesis

In this section, we detail the organization of the thesis. The two main contributions are presented in two separate parts. The biological backgrounds related to these two contributions are given the first chapter of each part.

Chapter 1: General introduction

In the first chapter, we place the present work in the more general context of fluorescence microscopy and its application to the study of living cell. We briefly describe the fundamental biophysical principles and experimental instruments that are required to image dynamical intracellular processes.

Part I : Fluorescence lifetime map reconstruction in frequency domain (FD) FLIM

This part detail is devoted to the estimation of fluorescence lifetime maps corrupted by instrumental noise and motion in frequency domain FLIM.

Chapter 2: Fluorescence lifetime and biological application

We first describe the physical basis for fluorescence lifetime imaging. We describe the competing des-excitation processes that influence magnitude. Finally, we present the application to the measurement of various biophysical quantities, most notably the Förster resonance energy transfer (FRET) between interacting molecules.

Chapter 3: Fluorescence lifetime imaging techniques

We present the fluorescence lifetime imaging instrumentation both in time and frequency domain. Due to its speed of acquisition, the frequency domain approach is more suitable for *in vivo* and/or dynamical acquisitions. We describe the computational approaches proposed in the literature to estimate fluorescence lifetime out of a FD FLIM measurement.

Chapter 4: Instrumental noise in FD FLIM measurement

Our main contributions in FD FLIM are presented in this chapter. We describe a study of the noise variance introduced by the intensifier CCD required in FD FLIM. A model

correction and associated parameter estimation are proposed to take optical aberrations into account. We apply this modeling to fluorescence lifetime estimation. We also highlight the relevance of our model thanks to FD FLIM measurement denoising. We use a simple Wiener filter to compare the influence of our adaptive model to a usual constant noise variance model. A more advanced denoising algorithm (Non-local means) is also introduced to produce better results.

Chapter 5: Fluorescence lifetime estimation on moving endosomes in FD FLIM

This chapter focuses on the estimation of fluorescence lifetime on non-fixed endosomes. We propose a robust statistical framework for the joint estimation of the fluorescence lifetime and diffusive motion of particles. Our approach is tested on simulations and experimental samples.

Chapter 6: Application to protein interaction analysis at the membrane and during endocytosis

Our lifetime reconstruction framework is applied to an on-going study of the signaling pathway triggered by a cytokine. In this chapter, we focus on the FRET-based detection of interactions between the cytokine receptor and its kinesin. Our collaborators wished to evaluate the level of interaction at the membrane or on the early endosomes. The application of our fluorescence lifetime reconstruction framework on *in vivo* acquisition hints for a stronger interaction on the endosomes. Our results guided the design of new acquisitions for a better statistical significance in future work.

Conclusion

Part II : Tracking heterogeneous transports in a dense intracellular environment

In the second part of the thesis, we present a more general study of the quantification of a very frequent phenotype in living cells: the heterogeneous transport of vesicles or molecules in dense cellular environments. This study has been carried out within the Danuser lab in Harvard Medical School and supported by the GDR 2588, Inria and MATISSE doctoral school.

Chapter 8: Quantifying transport heterogeneity in living cells

In this introductory chapter, we first present the variety of intracellular transports involved in the living cell functions. In this non-exhaustive review, we classify those transports into

three types : diffusion, active transport and heterogeneous transport. We then present the possible pitfalls in the quantification of those phenotypes in fluorescence microscopy. We finally focus on the challenging, yet frequent scenario, of unpredictable transitions between diffusion inside the cytoplasm and active transport along the cytoskeleton in the cluttered environment of the living cell. We introduce the vimentin dynamics study that have been the starting point of our work.

Chapter 9: Technical review of particle tracking algorithms

We propose a study and a classification of the related works in the field of multiple particle tracking. We classified fifteen algorithms chosen for their impact and originality in the literature. We classify their strategies with respect to six key criteria: dynamic modeling, linking cost optimization, spatial gating strategy, similarity distance, gap closing ability and particle merging and splitting detection. Although we focus on a specific case study, our tracking approach can be used for a large set of biological problems. In a nutshell, we show that the related effort in modeling multiple motions such as interacting multiple models is not designed to estimate abrupt changes in the transportation model.

Chapter 10: Iterative u-track

Building over the u-track algorithm, we propose a new, interacting multiple model smoother that exploits recursive tracking in multiple rounds in forward and backward temporal directions in order to achieve convergence of the instantaneous speed estimate time-point-by-time-point instead of the average speed over a track. This allows us to recover fast transitions from freely or confined diffusive to directed motion. To avoid false positives we improved the recursive tracking with a robust in-line estimator of the adaptive search radius for assignment (a.k.a. gating).

We tested our method on simulations to measure the influence of density and motion switching probability. Our method is demonstrated to outperform competing methods that model multiple transport types such as interacting multiple models and General Bayesian problem of order 1 (GP1). We also highlight the good performance of our approach with respect to active transport speed in heterogeneous motion. We finally show that our method outperforms competing methods in more homogeneous scenarios such as varying speed in active transport or a mixed population of diffuse particles and actively transported particle. The measured computation time show a 10% with respect to the U-track algorithm.

On biological applications, our algorithm allows us to quantify the extremely small percentage of motor-driven movements of intermediate filament precursor particles along microtubules in a dense field of unbound molecules of vimentin. We also show in experimental data sets of virus trafficking that our algorithm can cope with a high reduction in recording frame rate without losing tracking performance relatively to

methods relying on fast sampling.

Conclusion

General conclusion

1 General introduction

Since the first description of the living cell by Robert Hook some 350 years ago [[Hooke and Waller, 1705](#)], microscope-aided observation has been a fruitful mean of investigation in cell biology. The last major evolution in microscopy is probably the discovery of the fluorescent tagging technique. It is now possible thanks to genetic engineering coupled with time lapse microscopy, to observe with molecular precision the events controlling the function and organization of the living cell.

Microscopy is not the only approach available to probe the mechanisms and processes in cell biology. Biochemical and genetic methods are also playing a major role in this field. By measuring physical quantities on millions of molecules in a single experiment, those techniques have been unfolding thousands of phenotypes. The experiments provide homogeneous projections that average the behavior of an ensemble of molecules. While efficient and statistically significant, those techniques cannot measure the dynamics of cells, the spatiotemporal distribution of subcellular components, and the transient processes that involve intracellular molecules [[Tinoco and Gonzalez, 2011](#)]. Fluorescence microscopy fills this need by allowing *in vivo* dynamical observations that render the heterogeneity inherent to complex intracellular interactions.

Nowadays, thanks to time-lapse imaging in fluorescence microscopy, biologists can study this heterogeneity of processes and structures in space and time [[Lippincott-Schwartz, 2003](#)]. In this first chapter, we will describe several technical breakthroughs that made dynamical intracellular processes observation possible. First, fluorescence tagging opened the way to single molecule detection. Now that the genome sequence of a variety of organisms has been completed, the structures of interest can be precisely labeled and studied. Secondly, the development of dedicated optical microscopes and light sensors have permitted the acquisition of high-quality image datasets with increasing temporal and spatial resolution. Modern microscopy allows an ever reducing amount of sample excitation to reduce the light induced damages to the sample.

All these targeted innovations in genetics, optics and light sensing instruments allow the observation of thousands of proteins and as many behaviours in the same sequence. In this context, data processing and analysis have a major role to play. A dedicated effort has recently emerged from the community in signal processing and image analysis to master and interpret the ever increasing amounts of data produced in fluorescence microscopy [[Danuser, 2011](#); [Zimmer, 2012](#)]. This effort is two-fold. First, the method for signal reconstruction model the signal and the instrumentation to push the envelope in data acquisition by compensating artifacts (diffraction,noise...). Secondly, the computer

vision and data analysis methods model, quantify and compare the biological phenotypes described by the measured intensities.

We describe in this manuscript two representative studies for which efforts in signal processing and computer vision were required for the study of the cell *in vivo*.

In the first part, we introduce a statistical method for the reconstruction of fluorescence lifetime map corrupted by instrumental noise and dynamical events. The fluorescence lifetime is defined as the nanosecond-scale delay between excitation and emission of fluorescence. Lifetime measurement yields numerous indications on cellular environmental quantities, as much as interprotein and intraprotein mechanisms through fluorescent tagging. We propose in this manuscript a study of the instrumentation required for the quantification in frequency domain fluorescence lifetime imaging microscopy (FD FLIM). Adapting to this specific instrumentation, we propose a statistical framework for noise estimation and compensation. We also enable for the first time the measurement of fluorescence lifetime on moving endosomes.

The second part presents a contribution to the tracking of multiple particles presenting heterogeneous transports in dense conditions. Heterogeneous transports are ubiquitous in the cell. We focus here on the switching between confined diffusion in the cytosol and motor-mediated active transport in random directions. In time lapse fluorescence microscopy, the current state-of-the-art in tracking of sub-resolved particles handles correctly those types of transport on spatially sparse scenarios or high frequency acquisitions. However, when the particle population densifies, the acquisition rate cannot be increased endlessly because of photodamages and the signal-to-noise ratios required for detection. This is the typical scenario we faced while studying the dynamics of vimentin filaments formation. In this context, current multiple model filtering and gating strategies fail at estimating unpredictable transitions between Brownian and directed displacements. We propose in this manuscript a study and a classification of the related works in the field. Upon this study, we propose two improvements on dynamical modeling and search radius estimation to improve the tracking of heterogeneous types of motion in challenging conditions. Our approach has been evaluated on simulated data, we show that our method outperforms competing methods in the targeted scenario, but also on more homogeneous types of dynamics challenged by density. On experimental sequences we manage to quantify the challenging vimentin dynamics. We also highlight the resistance of our method toward a reduction in temporal resolution.

Hence, the first part of this work describes a signal processing method that models an instrumentation to enable its potential for quantification of dynamical processes. The second part describes a data analysis method that models a phenotype to push the boundaries in quantification of intracellular dynamics.

In this general introduction, we first describe the context of fluorescence microscopy. We describe the principle and application of fluorescence structure labelling in Section 1.1. We then propose a brief overview of optical microscopy techniques used for live cell imaging in Section 1.2.

1.1 Fluorescence: principles and application to structures labelling

1.1.1 Principles of fluorescence

The fluorescence phenomena has been discovered in 1852 by George G. Stokes [Stokes, 1852]. In this paper, the author reported light emission from a mineral (the fluospar that gave its name to fluorescence) during its excitation with an ultra-violet light. He noted that the emitted wavelength was longer than the the incident wavelength, a phenomenon now known as the Stokes shift.

To understand this discovery, the electronic energy of fluorescent molecules must be modeled. The electron energy depends on its orbital, and the energy of the whole electronic configuration depends on the total electron energy and the symmetry of the electron spin states. Due to the quantum nature of electronic energy, the molecular energy is quantized. For each molecule, the lowest energy level is the so-called ground state \mathbf{S}_0 , followed by discrete excited states \mathbf{S}_1 , \mathbf{S}_2 , \mathbf{S}_3 or more. When a photon hits a molecule in its ground energy state \mathbf{S}_0 , some of its electrons undergo an orbital leap. If the photon has sufficient energy, it can reach an excited quantum of higher energy \mathbf{S}_1 (or less probably \mathbf{S}_2). This phenomenon known as absorption is illustrated on the simplified Jablonsky diagram Figure 1.1. In order to return to the stable ground state \mathbf{S}_0 , one possible de-excitation pathway is the immediate emission of a photon. This rapid light emission that happens within nanoseconds (10^{-9} to 10^{-10} seconds) is the fluorescence.

The wavelength shift observed by Stokes is due to the energy lost by the fluorescent molecule before the photon emission (see Figure 1.1). This energy loss can have several causes, but the main ones are the vibrational relaxation (\mathbf{S}_1 to \mathbf{S}_1) and internal conversion (\mathbf{S}_2 to \mathbf{S}_1) to its lowest vibrational energy level. The two phenomena consist in a very fast (10^{-14} - 10^{-11} seconds) non-radiative process where the electronic energy is transformed into kinetic energy absorbed by neighboring molecules. Due to its time scale this energetic transition is very likely to happen before photon emission. The Planck equation

$$E = \frac{hc}{\lambda} \quad (1.1)$$

where c is the speed of light and h is the Planck's constant, makes the link between this energy loss in a quantum E and the longer wavelength λ .

As depicted in Figure 1.1, multiple possible energetic transitions between vibrational states are possible for absorption as well as emission. Depending on the electronic configuration of the molecule, those transitions occur with different probabilities. As a result, each fluorescent molecule presents a characteristic absorption and emission spectrum (see Figure 1.2). Due to the vibrational relaxation, the emission spectrum is independent of the excitation wavelength.

The average time for a molecule to stay in an excited state before emitting a photon is called the fluorescence lifetime. Lifetime is dependent on the multiple other de-excitation

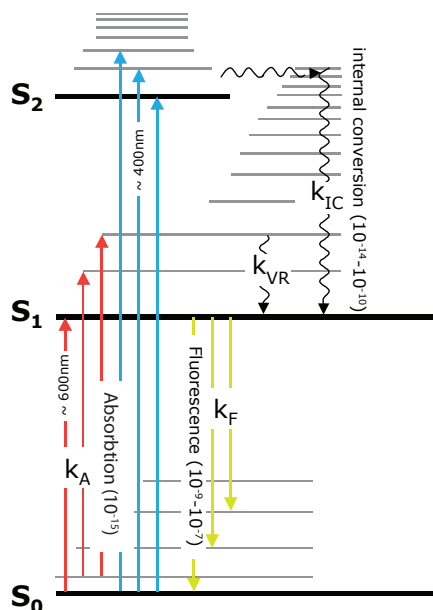


Figure 1.1: Simplified Jablonsky diagram. The thick horizontal lines denote electronic energy levels. The thinner grey lines represents the various vibrational energy states. Straight arrows are associated with absorption or emission of a photon. Wavy arrows illustrate molecular internal conversions or non-radiative relaxation processes. Vertical upward arrows indicate the instantaneous nature of excitation processes.

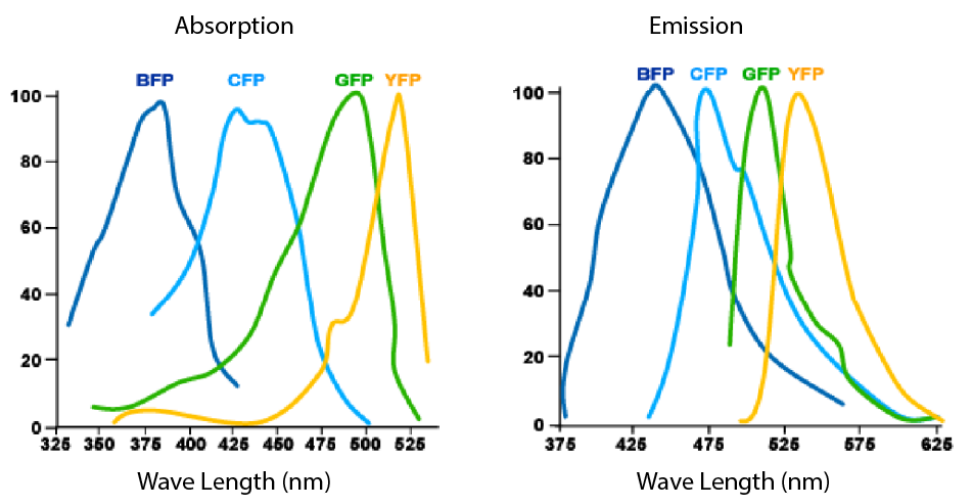


Figure 1.2: Stokes shift for different species of GFP and some GFP mutation (adapted courtesy of Damien Maurel)

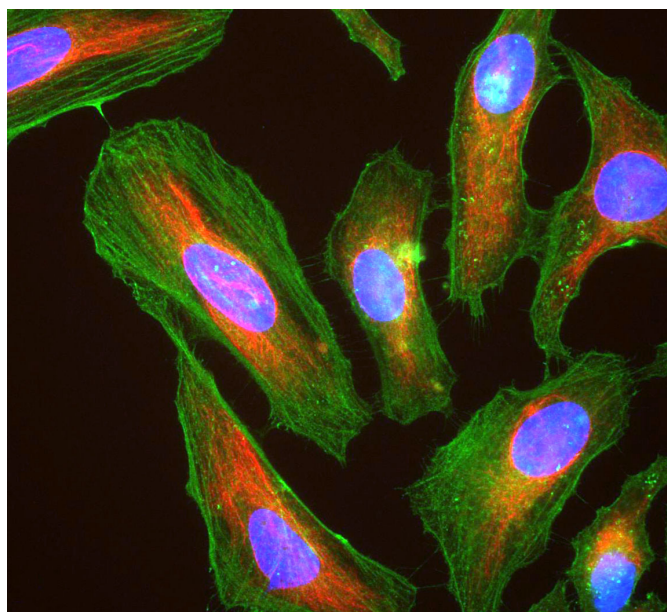


Figure 1.3: HeLa cells stained with antibody to actin (green), vimentin (red) and DNA (blue) (courtesy of EnCor Biotechnology)

pathways that compete with photon emission for the molecule to return to its ground state. So, there is numerous biological applications to the measurement of fluorescence lifetime such as pH sensing and proximity measurement between fluorophores. We will detail the physical origin, modeling and application in Part I which is dedicated to lifetime estimation.

1.1.2 Bringing fluorescence to intracellular structures

The difference between excitation and emission wavelength is actually what makes fluorochrome an invaluable tool in the study of the living cell. Combined with optical microscopy using barrier filters that selectively transmit a wavelength of choice, the fluorochrome can be localized with unprecedented precision within a larger sample that is uniformly excited. Furthermore, the specific emission spectrum of each fluorophore allows the decorrelation of the signal emitted by different fluorophores in a same sample at the same time. In order to exploit those properties at the cellular or subcellular structure levels, fluorescence staining or labelling consists in highlighting structures in biological tissues thanks to fluorochromes chemically or genetically attached to molecules. In this Section we present the two main approaches exploited in cell biology to bring the fluorescence to the biomolecule.

1.1.2.1 Fluorescent staining

Fluorescence staining consists in the injection inside the cell of a fluorescent probe. This probe is introduced in the form of a fluorochrome chemically linked to a biological vector molecule that binds the protein targeted for visualization. Various methods for fluorescence staining have been discovered, generally classified by the vector molecule of choice.

Immunofluorescence exploits antibodies to bind to their respective antigens associated to the molecule of interest [Miller and Shakes, 1995]. If antibodies are used by the immune system to neutralized biological objects from the external environment (“non-self”), antigens also originate from within the body (“self”). Accordingly the immunofluorescence can tag any biomolecule in the living cell. Two methods, direct and indirect, are widely used for immunofluorescence staining. The first method directly uses a fluorochrome-labelled antibody as a probe. In the indirect method, the primary antibody that binds the antigen is not fluorescently labeled, the fluorophore is attached to a secondary antibody that in turn binds the primary antibodies. The second approach presents several advantages: the use of multiple secondary antibody enhances signal quality and this method provide much more flexibility as a large number of secondary antibody can bind to a given antibody and *vice-versa*. For the antibodies to efficiently penetrate the cell, the plasma membrane must be permeabilized or the cell sectioned. Consequently, the technique generally requires the fixation procedure of tissues and cells prior to the staining and is unsuitable for live-imaging.

Fluorescence in situ hybridization (FISH) is used to identify a specific gene or sequence within a gene in DNA or RNA. Hence this technique allows the detection of gene expression in the cell and localization in the chromosomes. To design the probe, fluorochrome are chemically attached to specific genetic regions of microbes that will differentiate them from other groups. Once injected, the fluorescent-labeled probes hybridize with the complementary RNA or DNA molecules. Fixation and permeabilization are also necessary.

Chemical fluorescent probe are yet an other category of fluorescent staining agent. They can bind to biomolecules specific to the targeted structures in the Cell such as actin fiber (FITC-Phalloidin, Rhodamine-Phalloidin), mitochondria (mitoTracker®, Rhodamine 123), chromosomes/nucleus (DAPI), Endoplasmic Reticulum (ERTracker®), lysosome (LysoTrackers®) or Golgi apparatus. Except the actin fiber binder, all the pre-cited agent are suitable for live cell imaging.

1.1.3 Fluorescent labelling of *in vivo* protein

The purification [Shimomura et al., 1962], cloning [Prasher et al., 1992] and heterogeneous expression [Tsien, 1998] of the Green Fluorescent Protein (GFP) opened the way to the synthesis of labelled proteins inside the cell. GFP has become a major tool for biologists

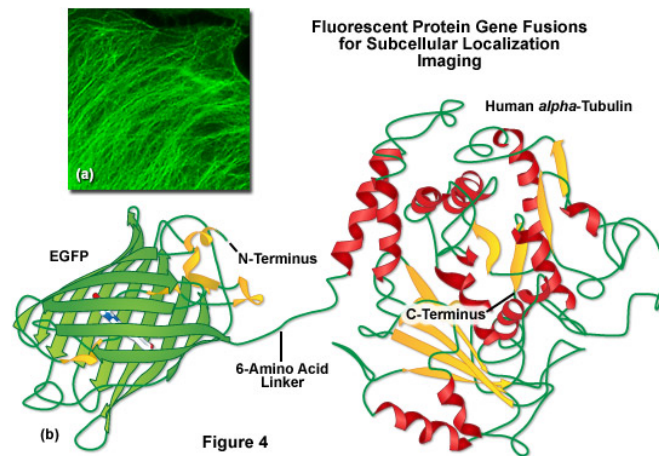


Figure 1.4: α -tubulin labeled with GFP. **a)** this chimera localizes to microtubules **b)** the EGFP is tagged on the N-terminus of the α -tubulin. The interior part of the barrel shape structure is responsible for the fluorescent phenomena (copyright Zeiss).

to tag specific target proteins *in vivo* and track the localization and dynamics of proteins, organelles, and other cellular compartments [Giepmans et al., 2006].

The fluorescently labeled protein (or chimera) is a protein of which the gene is composed by two distinct protein genes. The location for the fluorochrome on the original protein must be carefully chosen in order not to conflict with the protein function under study. While producing a biosensor, the pair of fluorophores must be located to trigger the FRET effect (see Section 2.2.2) on protein activation. When too few information on the optimal tagging locus is available, different tagging sites must be experimented (see Chapter 6). In order to produce the chimera, the two genes are fused together using genetic recombination technique forming a recombinant DNA.

The recombinant DNA is then transfected into the cell using a plasmid or a viral vector (in this second case, the process is called transduction). Multiple reagents are commercially available with variable efficiency to facilitate vectors uptake by the living cell, but none of them necessitates permeabilization of the cell membrane. There are two types of transfection depending on the persistency of the chimera inside the host cell. In stable transfection the genetic material (DNA or mRNA) is integrated into the host genome and sustains transgene expression even after host cells replicate. In the case of transient transfection, the gene does not integrate into the chromosomes, and can be expressed in the cytoplasm for a short period of time (72 to 96 hours after introduction) [Kim and Eberwine, 2010].

Inside the cell, the recombinant DNA is translated by the ribosome to produce a specific amino-acid chain that will later fold into a fluorescent protein. This genetic tagging technique avoids the problem of purifying, tagging, and introducing labeled proteins into

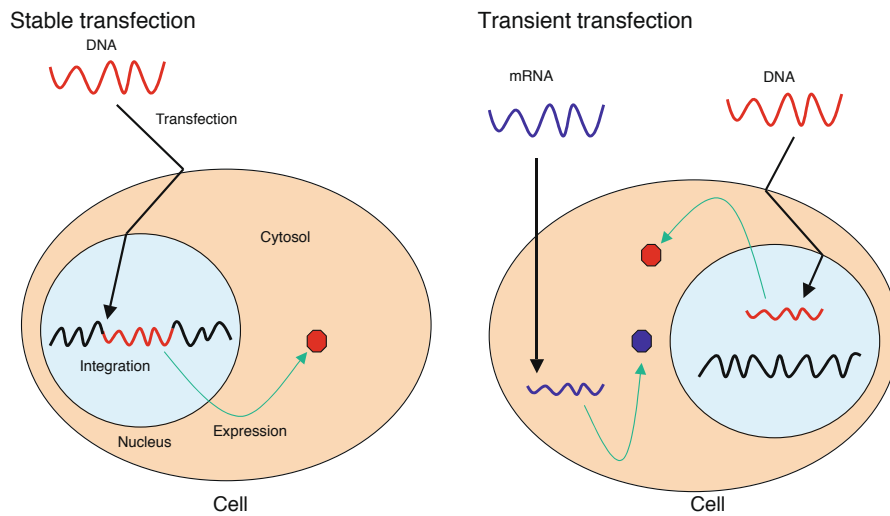


Figure 1.5: In stable transfection the vector DNA (red wave) pass through the cell and nuclear membranes and integrated into the host genome (black wave) where it is expressed sustainably. In transient transfection, the vector DNA is delivered into the nucleus but is not integrated into the genome. (adapted from [Kim and Eberwine, 2010])

cells or the task of producing specific antibodies for surface or internal antigens.

1.1.4 Photobleaching and phototoxicity

Two main limitations in the image acquisition process in fluorescence microscopy are photobleaching and phototoxicity.

Photobleaching (or fading) is a permanent loss of fluorescence of a fluorophore. A fluorescent molecule in the excited state presents a varying probability of interaction with an other molecule, a reaction that will cause irreversible covalent modifications. This probability will depend on the fluorophore and on the molecular environment. As a result, photobleaching can occur after a few photons emission as well as millions of fluorescence cycles depending on the fluorophore robustness and experimental conditions. Even if various reagents can reduce bleaching rate, photobleaching is an issue that seriously hinder the acquisition of strong signal or time lapse acquisition in fluorescence microscopy. It is thus very important to manage the fluorescent capacity by controlling the sample excitation during acquisition.

The photobleaching effect can also be exploited to measure biophysical quantities in fluorescence microscopy. For example, in fluorescence recovery after photobleaching (FRAP) experiments [Axelrod et al., 1976], the fluorophores are intentionally bleached in a selected area using excessive illumination. The dynamic of non-bleached fluorophore molecules diffusing into the bleached area can then be measured. Using this technique,

the local dynamics of fluorescently labeled molecules can be assessed with a spatial resolution of 2 to 5 micrometers.

The other important limitation is phototoxicity due to the interaction between the excited fluorophore and another molecule, especially with oxygen. This reaction causes the release of free radical oxygens in the living cells that can damage chemically destroy other structures in the cell in addition to the fluorescent molecule. Phototoxicity often occurs upon repeated laser exposures of fluorescently labeled cells.

1.2 Live cell fluorescence microscopy techniques

The fluorescence signal emitted by the fluorophores inside the cell is imaged thanks to modern microscopy. A wide range of single molecule microscopy methods have been proposed to adapt to specific structures, dynamics or intracellular location under study.

Microscopical methods should be chosen considering various factors: the sample under study, the phenotype under study and the trade off between the resulting signal-to-noise ratio and damage on the sample during observation [Stephens and Allan \[2003\]](#). Thickness of the sample will guide the decision to wide-field or optical sectioning. The speed of the process under study will have an impact on the acquisition speed. The spatiotemporal scale of the entire phenotype under study can restrain the spatiotemporal resolution, *via* depth resolution in 3D or acquisition speed, of the acquisition to harness photodamaging effect.

Furthermore, the choice of the microscopical setup should be done in parallel with the whole experiment design, considering diverse fluorescent tagging technologies and data processing and analysis methods to optimize the quality of the resulting quantification. Indeed, the quantum efficiency of the fluorescently labelled protein will also define the illumination needed for signal detectability. Another important factor is the amount of signal and acquisition speed actually needed for object detection or quantification of dynamics.

In this chapter we briefly present the main technologies that are relevant to the field of dynamical process analysis.

1.2.1 Wide-field Microscopy

Wide-field microscopy allows for vesicle localization with a resolution of 200 nm in the whole cell by illuminating the whole sample with a single light source. A lens focuses the illumination field on the sample. The technique is schematically described Figure 1.6. This setup provides fast imaging and flexibility at low cost. As a result, it is the most widely used imaging technique in biology. However, wide-field microscopy presents some limitations. Using this technique, the blurred intensity stemming from out-of-focus structures will be integrated as much as the focal plane in CCD sensor. This can reduce the contrast on the structure of interest if the sample is not thin enough. Additionally,

the plain illumination of the sample can cause unnecessary photodamages. Confocal microscopy can address those restrictions by minimizing the out-of-focus interferences.

1.2.2 Optical sectioning

1.2.2.1 Computational optical sectioning microscopy

Computational optical sectioning microscopy (COSM) combines wide-field imaging with deconvolution algorithms to remove out-of-focus light blurring [Conchello and Lichtman, 2005]. Deconvolution is based on the knowledge of the image formation process. The algorithm use this information to solve an inverse problem and retrieve the original optical section. Multiple two-dimensional images are acquired at different focus depths and are post-processed to obtain a three-dimensional view of the sample. Because of the use of multiple plain sample illumination for a single time step, this method is sensitive to photodamages as well as cellular motility.

1.2.2.2 Confocal Microscopy

Confocal microscopy uses a convergent laser beam to focus on a single point on the focal plane [Minsky, 1988]. A pinhole aperture is placed at the detection end to reduce the impact of out-of-focus fluorescence, thus providing an optical sectioning effect. By reducing the size of that pinhole below the size of the central airy disc pattern, the resolution of the confocal microscope can be enhanced by a factor 1.4 when compared with the wide-field microscope resolution [Conchello and Lichtman, 2005]. The precision of this technique is limited by the diffraction of laser focal point.

The signal quality is obtained at the expense of its quantity. Two approaches have been proposed to face this problem. Laser-scanning confocal microscopy consists in a raster scan of the focal plane to image a two-dimensional slice of the sample. The sample can be thus excited with high precision. Photobleaching experiments are possible with a local raster scanning of the area of interest. A faster method is the spinning (a.k.a. Nipkow) disk setup. This multifocal imaging technique allows the acquisition of multiple points on the CCD at the same time (see Figure 1.6). The spinning disk setup is more affordable than the instrumentation required for laser-scanning and offers higher sensitivity due to CCD detector, thus reducing phototoxicity. However, controlled localization of the excitation is not possible and optical resolution is usually lower.

Three-dimensional images can be acquired with confocal microscopy by sequential movement of the objective or the sample. However, acquisition time and photodamage limit the axial resolution.

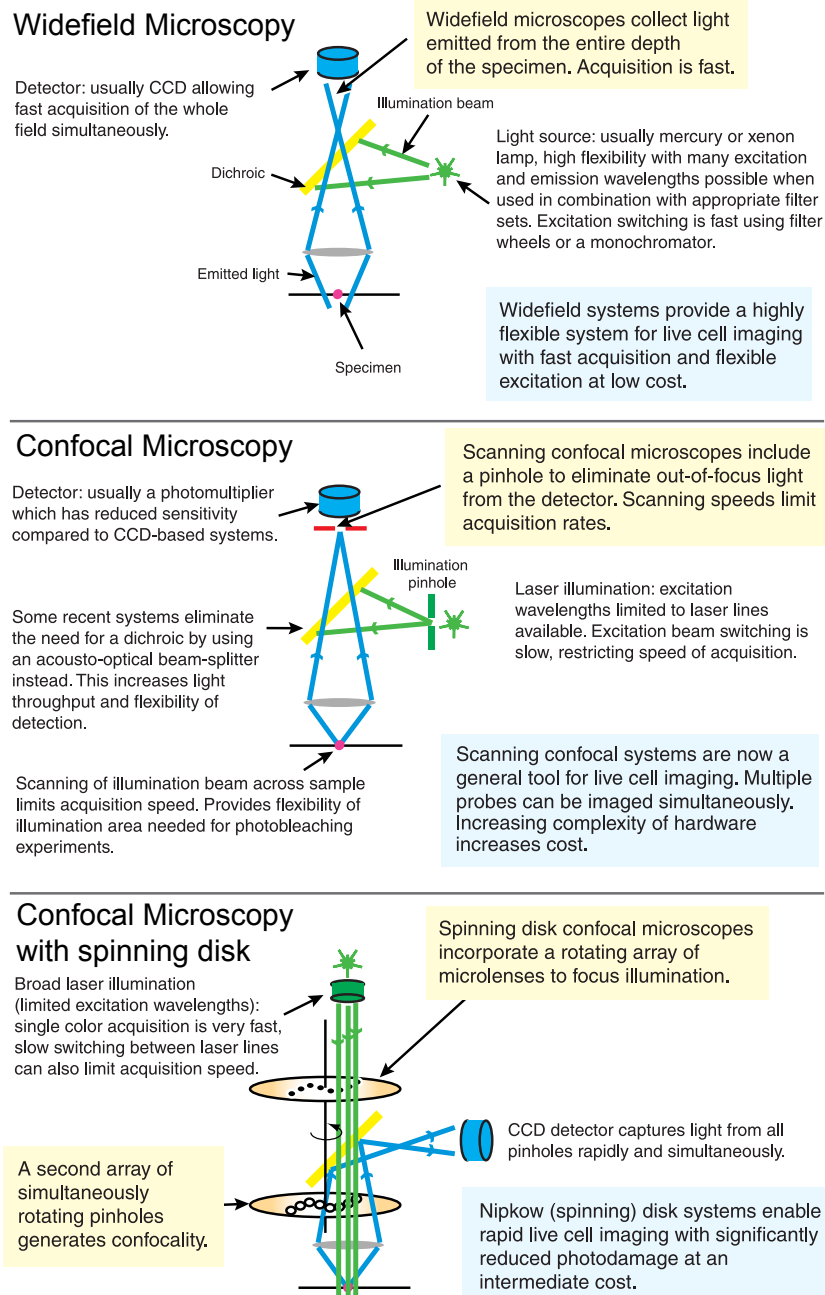


Figure 1.6: Comparison of wide-field, scanning confocal and spinning disk confocal systems, with schematics for each. All systems are capable of being equipped for 3D and 4D data acquisition. Excitation beams are shown in green; emission beams, in blue. The differences between these systems mean that no single system is suited for every experiment. Typical system configurations are shown, and user modification and options allow great flexibility (source: from [Stephens and Allan, 2003]).

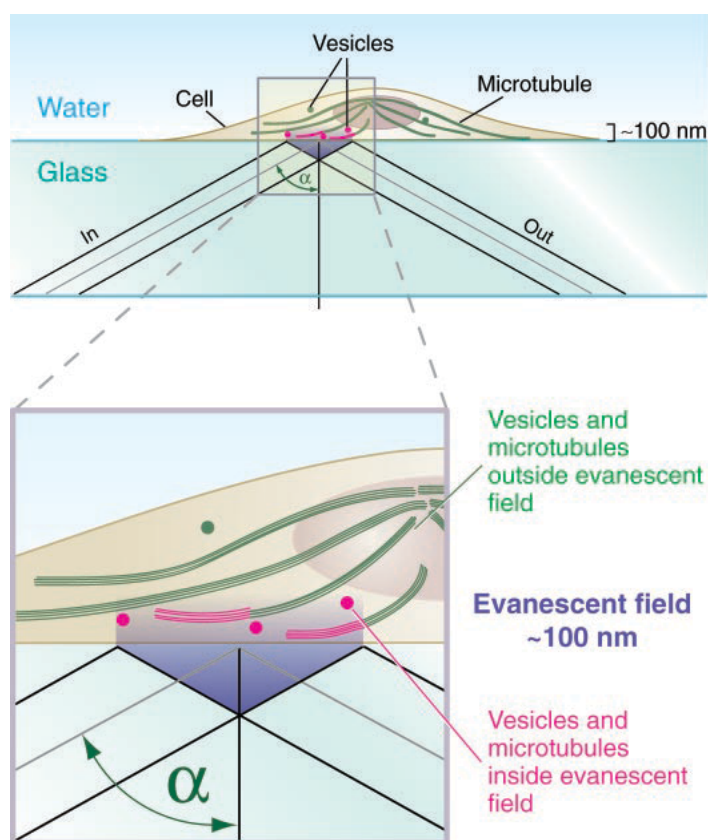


Figure 1.7: TIRF technique exploits the evanescent field to measure fluorescence at the plasma membrane (source: from [Stephens and Allan, 2003]).

1.2.2.3 Total Internal Reflection fluorescence Microscopy

Total internal reflection fluorescence microscopy (TIRF) is better resolved than the previous techniques both spatially (in axial direction) and temporally. Yet, this technique is limited to a small sample region, near the coverslip, like the plasma membrane, for example used to study selective exocytosis and endocytosis events at the plasma membrane. Excitation at a critical angle generates an evanescent field of excitation light which intensity decays rapidly (exponentially) with distance from the coverslip, limiting the depth of excitation to a distance in a range of 50 to 200 nm (see Figure 1.7).

1.2.2.4 Single Plane Illumination Microscopy

Single plane illumination microscopy (SPIM) has recently made important progress and combines the advantages of wide-field and confocal microscopy: the light sheet-based

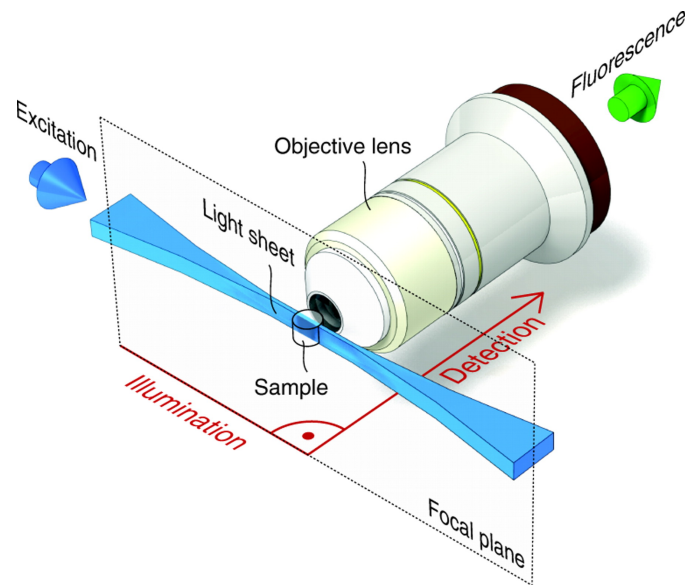


Figure 1.8: Schematic representation of SPIM principle (source: from a scheme by Jan Krieger)

illumination reduces photobleaching while illuminating the whole sample uniformly without the need for scanning. Thanks to the high acquisition speed and low photodamage, SPIM is widely used for long term *in toto* time-lapse imaging of developing biological specimens with cellular resolution, such as developing embryos. Its limitations are the lowest axial resolution (thickness of the light sheet), the lack of spatial control of illumination (compared to raster scanned systems) and the usually huge size of datasets that requires image registration for 3D reconstruction.

Part I

Fluorescence lifetime map reconstruction in frequency domain (FD) FLIM

Introduction

Fluorescence Lifetime Imaging Microscopy (FLIM) is now a widely spread, minimally invasive, technique for sensing fluorophore environment in a living biological sample (pH, ions, temperature ...). Fluorescence lifetime is also particularly useful to detect Förster resonance energy transfer (FRET) between molecules in close proximity [[Jares-Erijman and Jovin, 2003](#); [Lakowicz and Masters, 2008](#)].

The numerous FLIM techniques proposed in the literature can be classified into two main categories: time domain method and frequency domain method. Time domain methods such as the Time-Correlated Single-Photon Counting (TCSPC) technique measure the mean delay between a photon emission and a pulsed excitation. Those methods are well established, propose a high temporal resolution for lifetime estimation and provide a visually intuitive fluorescence decay with well established Poisson statistics [[Birch and Imhof, 1999](#)] (see Figure 3.2). However, one drawback of time domain methods is the time step required between each laser pulse for the fluorescence to decay completely. Accordingly, an acquisition typically takes several seconds for conventional techniques [[Becker et al., 2009](#)]. Frequency domain methods, on the other hand, do not present such a limitation [[Suhling et al., 2005](#)]. A FLIM measurement in the frequency domain (FD FLIM measurement) is a short image sequence presenting a sinusoidal intensity footprint that reflects the sinusoidal excitation of the sample followed by the phase modulation of the emitted signal. A fluorescence lifetime variation is reflected as a phase variation in the measurement. This acquisition process results in 10-fold to 500-fold faster acquisition times than temporal approaches [[Lajevardipour and Clayton, 2013](#); [P. C. Schneider, 1997](#); [Holub et al., 2001](#)]. The FD FLIM method is thus more suitable for the study of dynamical processes and more generally for the study of the cell *in vivo*.

In the literature, the Fourier transform or equivalently the least mean squares fitting of a sine function is the estimator of choice to compute the lifetime map from FD FLIM measurement [[Spring and Clegg \[2009\]](#); [Lakowicz and Masters \[2008\]](#)]. This estimator, though efficient, presents several issues. First, it implicitly makes a stationary Gaussian assumption on instrumental noise. This is not a realistic assumption due to the photonic nature of the emitted signal and the property of the acquisition instrument. Additionally, those methods consider the sample to be static during the measurement acquisition. Though, if those methods are faster than time domain approaches, transient motions of intracellular structures can still happen during the FD FLIM measurement acquisition and corrupt the estimated lifetime map [[Lajevardipour and Clayton \[2013\]](#); [Hanley et al. \[2001\]](#)].

In this study we propose two contributions that enable the potential for *in vivo* and dynamical experiments in FD FLIM. A thorough analysis of the noise induced by the specific FD FLIM instrumentation is first carried out. We show that a theoretical model for the local noise variance is not sufficient to describe this noise footprint accurately on non-fibered FD FLIM setup. Thereby, we propose a model correction and a statistical framework for parameter estimation. This noise model is first exploited for lifetime estimation in the case of still background. A denoising algorithm that takes advantage of this model has also been designed. We then exploit the FD FLIM intensity model and the noise model to estimate fluorescence lifetime on vesicles that underwent non-negligible motions during the acquisition. We propose a statistical framework that combines weighted least squares based lifetime estimation and robust M-estimator-based tracking to alternatively and iteratively estimate lifetimes and motions of vesicles.

Each of those contributions are calibrated and tested using experimental acquisitions with controlled fluorophores, simulated measurement or visual inspection (for the denoising method). Our noise model accuracy is tested on a plain FD FLIM reference measurement. The impact of this modeling on phase and lifetime estimation is demonstrated on controlled real samples presenting an homogeneous fluorescence lifetime. Our lifetime estimator for moving structures is tested on both simulated and experimental sample. On experimental data, it is extremely difficult to obtain a ground truth for the fluorescence lifetime of moving vesicles. The accuracy of our method is thus tested *via* the motion estimation results that are compared against competitive particle trackers.

Finally, the complete lifetime map reconstruction framework is applied to the *in vivo* study of receptor-kinase¹ interactions in epithelial cells. The fluorescence lifetime is measured on both membrane and moving endosomes to sense for the spatial distribution of FRET efficiency. The preliminary results of this on-going experiment are laid out. From those data, we were able to point out some weakness in statistical significance and propose the design of future acquisitions.

The remainder of Part I is organized as follows. The physical concepts behind fluorescence lifetime and its application to biology are described in Chapter . Chapter 3 presents fluorescence lifetime imaging techniques, first briefly in the time domain with TCSPC and then more extensively in the frequency domain (FD FLIM). The conventional method for lifetime estimation in FD FLIM are described in the same chapter. Chapter 4.2 describes the instrumental noise modeling in FD FLIM. We describe our model correction and the results of its application to fluorescence lifetime estimation and denoising. Chapter 5 describes our lifetime estimation approach on dynamical structures, presenting our results on both simulated and experimental FD FLIM measurements. Finally, Chapter 6 presents our on-going experiments on receptor-kinase interaction measurement.

¹The name of the protein involved in this experiment and its biological background cannot be disclose due to editorial conflicts.

Contributions:

- Intensified CCD noise analysis and modeling.
 - An original derivation for the ICCD theoretical noise model.
 - A noise variance model correction taking experimental issues such as optical aberration into account.
 - A two-step estimation framework for the noise model parameters.
 - Application to image denoising using an original patch-based Gamma NL-means filter.
- FD FLIM lifetime map reconstruction algorithm.
 - Weighted least squares make use of our experimental noise modeling to improve static lifetime estimation.
 - Joint estimation of vesicles lifetime and displacement.
- A new complete derivation for the FD FLIM signal model in appendix A.

2 Fluorescence lifetime and biological application

2.1 Fluorescence lifetime theory

We define the fluorescence lifetime τ of a given fluorescent species as the average time during which the fluorophore stays in excited state before relaxing to its ground state and possibly emitting a photon. Let $N(t)$ be the number of particles in an excited state at time t among a population of fluorophores, the lifetime is defined as:

$$\tau = \frac{\int_0^{+\infty} tN(t)dt}{\int_0^{+\infty} N(t)dt}. \quad (2.1)$$

Although an excited state can be the product of light absorption, mechanical friction or chemical reaction, we will focus on the photon-induced excitation in this chapter. As described in the general introduction of this work, the absorption of a photon by a molecule is an all-or-nothing phenomena that can trigger the transition of the fluorophore energy to different quanta (denoted S_0 , S_1 and S_2 on the Jablonsky diagram Figure 2.1). Accordingly, a fluorophore excitation by a photon that presents insufficient energy to reach a higher electronic state will not produce excitation and the fluorescent molecule will remain in its ground state. On the contrary, an incident photon that presents too much energy with respect to a given quantum might be absorbed (if not too energetic) and the molecule will have this excess of energy converted into vibrational and rotational energy (gray lines in Figure 2.1). This photonic radiation energy is inversely proportional to the incident light wavelength as stated by Planck's law. Therefore, a blue incident light will result in higher energy quantum than a red one.

While the photon absorption process occurs in femtoseconds, the de-excitation processes are much slower. After internal relaxation in a picosecond or less, the fluorophore energy can be relaxed to its ground state through various de-excitation pathways (see Figure 2.1). The excited state energy can be dissipated non-radiatively by collision with another molecule in its ground state. The energy is then dissipated by heat. When an excited fluorophore is in close proximity with another molecule (1 to 10 nm) the Förster Resonance Energy Transfer (FRET) can be an other non-radiative de-excitation pathway. This phenomenon depends on distance between the an excited fluorophore (donor) and a molecule in its ground state (acceptor), their spectral overlapping and the orientation of the dipole-dipole association formed by both molecules. A relatively rare

phenomenon known as inter-system crossing to the lowest excited triplet state is yet another de-excitation pathway. Inter-system crossing results either in a photon emission through phosphorescence, a slow process that can take one thousandth to hundreds of seconds, or a transition back to the excited singlet state that yields delayed fluorescence. Finally, a fluorophore can return to its ground state through photon emission in a few to a hundreds nanoseconds, a phenomenon known as fluorescence. Consequently, there are many de-excitation pathways, and their contributions must be taken into account to provide a model for fluorescence lifetime.

Each of those de-excitation pathways can be modeled as kinetic reactions that compete with each other to deactivate the excited state [Lakowicz and Masters, 2008]. Therefore, each process is associated to a reaction rate. Accordingly, the higher the sum of reaction rates in a population of fluorophores, the shorter the fluorescence lifetime is. Regrouping the de-excitation rate as radiative fluorescent k_f and non-radiative rates k_{nr} , a population of $N(t)$ identical molecules excited at $t = 0$ will follow a first-order kinetics:

$$\frac{dN(t)}{dt} = -(k_r + k_{nr})N(t) \quad (2.2)$$

and then

$$N(t) = N(0)e^{-t/\tau} \quad (2.3)$$

with the lifetime τ defined as:

$$\tau = \frac{1}{k_f + k_{nr}} \quad (2.4)$$

It is usually not possible to determine the number $N(t)$ of excited molecules at a given time. However, it is possible to measure the number of fluorescent molecules at a given time thanks to photonic sensors. Given the quantum yield defined as:

$$\Phi = \frac{N_{\text{emitted photon}}}{N_{\text{absorbed photon}}} = \frac{k_f}{k_f + k_{nr}}, \quad (2.5)$$

the number of photons emitted by a sample $N_p(t)$ is proportional to the exponential decay:

$$N_p(t) = \Phi N(0)e^{-t/\tau}. \quad (2.6)$$

Following (9.11), we can infer that a modification in de-excitation pathways will impact both the measured intensity decay time and amplitude.

Finally, in experimental conditions, there can be several populations of molecules with different lifetimes at a given point. As the ordinary differential equation above is linear, the expected number of excited molecules will be the sum of negative exponentials of which the rates are assumed to be constant:

$$N_p(t) = \sum_{i=0}^{K-1} A_i e^{-t/\tau_i} \quad (2.7)$$

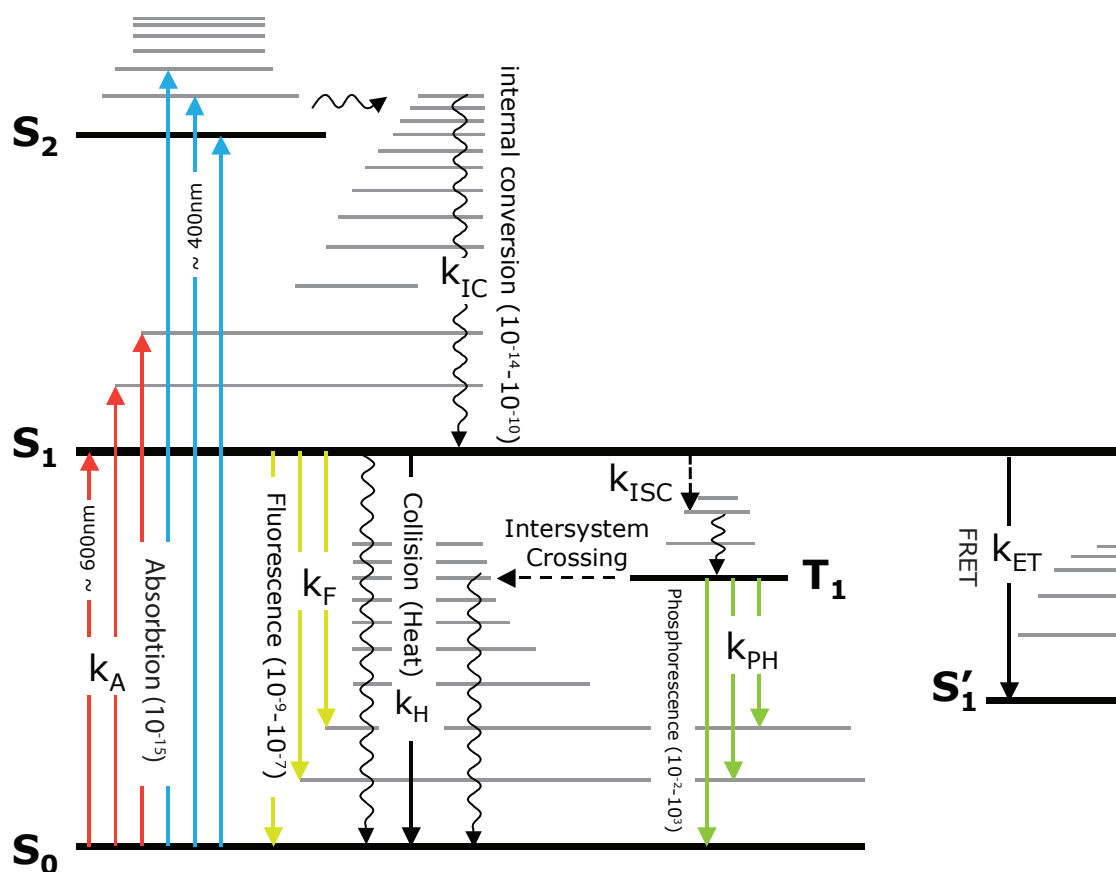


Figure 2.1: Jablonsky diagram: the thicker lines represent electronic energy levels and the thinner lines denote the various vibrational energy states. A timescale for the transition or a color is given as an example when physically meaningful.

where K is the number of fluorescent species and A_i and τ_i denote the associated initial photon counts and lifetime respectively.

2.2 Application to biophysical quantities measurement

Beyond the localization abilities offered by fluorescence tagging combined with modern microscopy, fluorescence lifetime analysis allows the sensing of various physical quantities such as pH, refractive index or viscosity. In contrast with intensity-based sensing for fluorescence lifetime [Han and Burgess, 2010; Grynkiewicz et al., 1985], direct fluorescence lifetime measurement can sense the living cell independently of fluorophores concentration, illumination intensity variation, light optical path or cellular leakage without the need for ratiometric methods [Suhling et al., 2005]. In this section, we focus on two widespread usages of fluorescence lifetime measurement: pH sensing and FRET efficiency measurement.

2.2.1 pH sensing

Fluorescence lifetime enables the measurement of intracellular pH with spatial and temporal resolution through the use of fluorescent sensors [Lin et al., 2003; Lakowicz and Szmacinski, 1993]. Similarly to other potential ions of interest, the bounding probability between hydrogen ions and fluorescent dyes will raise with the concentration of the former. The resulting impact on fluorescent lifetime can be directly quantified through fluorescence lifetime imaging.

2.2.2 Förster Resonance Energy Transfer sensing

An other widespread application of fluorescence lifetime measurements is the Förster Resonance Energy Transfer (FRET) phenomenon [Jares-Erijman and Jovin, 2003; Hink et al., 2002]. To probe for interactions between two types of proteins (see Figure 2.3.a), each type of molecules are tagged with a distinct fluorophore, both fluorophores having overlapping emission and absorption spectra. On protein proximity (< 10 nm), the excited fluorophore takes the role of the donor and presents a fluorescence lifetime decrease caused by a non-radiative energy transfer. Simultaneously, a lifetime increase will be measured on the population of acceptors. The acceptor molecule does not need to be a fluorophore, it can be a chromophore (a molecule that transmits or reflects visible light after absorption of part of its spectrum) but fluorophores are generally used for both donors and acceptors in practice. The FRET theory establishes that the energy transfer decreases with the distance between the donor and the acceptor following:

$$E_{\text{FRET}}(r) = \frac{1}{1 + (r/R_0)^6} \quad (2.8)$$

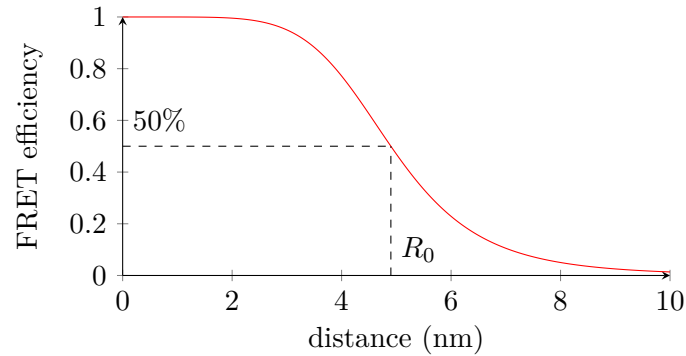
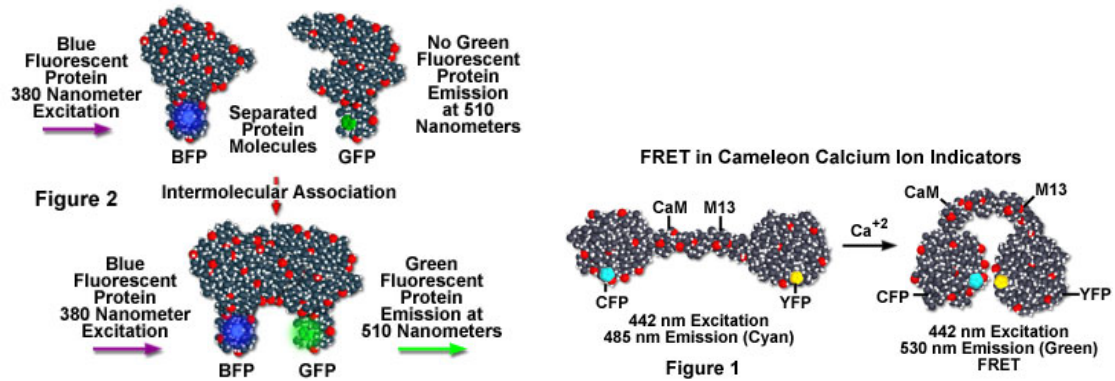


Figure 2.2: FRET efficiency evolution with the distance r between fluorophores ECFP and EYFP ($R_0=4.9$ nm).

FRET Detection of *in vivo* Protein-Protein Interactions



(a) Intermolecular interaction can be detected and quantified by measuring FRET efficiency (source: from [Olympus America Inc., 2012]). (b) Conformational changes and structural clivage are detected through FRET measurement in a biosensor (source: from [Olympus America Inc., 2012]).

Figure 2.3: FRET allows the measurement of structural dynamical events *in vivo*.

where R_0 is the Förster distance, at which there is a 50% FRET efficiency (see Figure 2.2). Fluorescent protein biosensor is an other widespread application of the FRET effect [Machacek et al., 2009]. To form a biosensor, two different parts of the protein are fused with a donor and an acceptor respectively (see Figure 2.3.b). Fluorescence lifetime variations will thus allow the detection on structural modification such as proteolysis or conformational change.

3 Fluorescence lifetime imaging techniques

The aim of FLIM microscopy is to measure the fluorescence lifetime τ at each location in space and time. The values taken by τ typically range from 10 picoseconds to 100 nanoseconds, needing highly specialized instruments that we will be detailed in this chapter.

The first class of methods are the techniques that operate in the time domain. Those approaches require repeated laser pulses to measure the mean delay between photon emissions and instantaneous excitations of the sample. In Time-Correlated Single Photon Counting (TCSPC) [O'Connor, 1984], each photon emission delay is explicitly measured. The collected distribution of photon emission delays is then fitted with the exponential decay described Section 2.1 (see left panel in Figure 3.1). In time-gated FLIM [Dowling et al., 1997], various very short acquisitions are carried out at multiple nanoseconds delay after excitations. This process results in a photon emission delay histogram that can also be easily fitted.

A second class of methods are the frequency domain techniques. A modulated excitation (i.e. sinusoidal) is imposed on the sample, fluorescence lifetime is retrieved from the phase delay of the response [Gaviola, 1927, 1926] (see right panel in Figure 3.1).

The two approaches have been experimentally proven equivalent with respect to measurement precision on fixed samples [Hedstrom et al., 1988]. However, for some applications, the frequency domain instrumentation is considered easier to implement since ultra-short pulsed laser sources are not required, especially for longer lifetimes [Suhling et al., 2005]. Frequency domain techniques also present a better photon efficiency and require no deconvolution of the instrumental response. On the other hand, the time domain measurements have been shown to present a better SNR [Philip and Carlsson, 2003]. They also more suitable to resolve two very different lifetimes on a same sample [Suhling et al., 2005]. Finally, lifetime measurements in the time domain require a delay between each excitation pulse for the fluorescent sample to completely decay and need several excitation pulses for an accurate lifetime estimation [Lakowicz and Masters, 2008]. This an important issue while dealing with the quantification of dynamical processes. Frequency domain methods do not present such a requirement and the lifetime measurement is only limited by the time taken for the phase modulation. As a result, we will focus on this method which is intrinsically more suitable for dynamical process analysis. We nevertheless briefly describe the analysis principles used in TCSPC in this

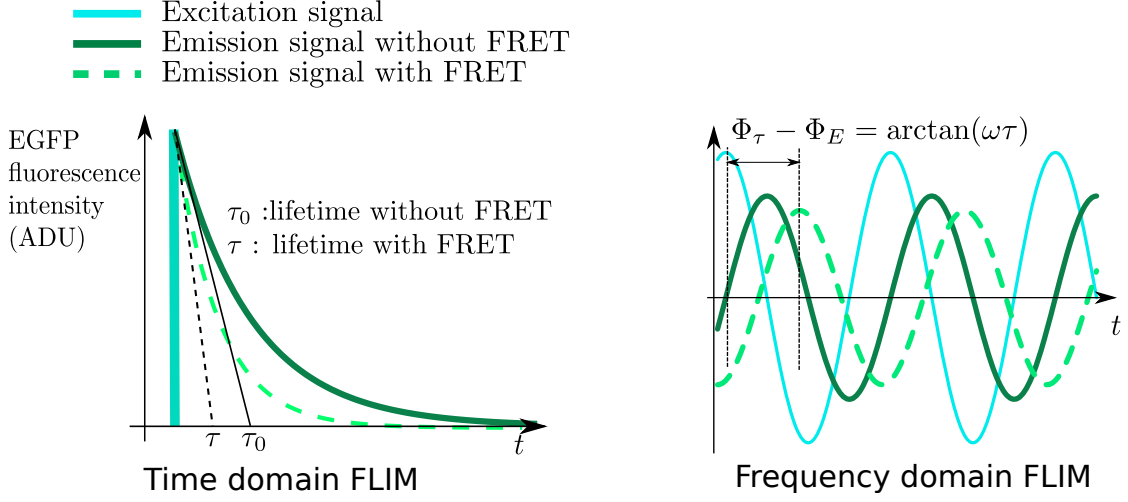


Figure 3.1: Representation of lifetime measurement and effect of a fluorescence lifetime loss in the time domain and frequency domain.

chapter based on previous work in our lab [Chessel et al., 2013].

For the sake of clarity, we will restrain in this section to the description of the main theoretical and instrumental concept put forward in two widespread technique for fluorescence lifetime measurement: TCSPC and FD FLIM. For a historical perspective on fluorescence lifetime imaging techniques and a detailed description of techniques, refer to [Lakowicz and Masters, 2008].

3.1 Time-correlated single photon counting

In TCSPC imaging, each emitted photon is counted individually. This technology generally uses confocal scanning for excitation and photon multiplier tube for photon detection. A laser pulse is fired repeatedly, then for each pulse either one or zero photon is received and the arrival time after the laser pulse is recorded. Depending on the sample, this operation is repeated for a variable duration and photon arrival times accumulated until the whole decrease can be recovered. An acquisition can take up to several minutes (for 128×128 or 256×256 images) to accumulate enough photons on each pixel to derive a fluorescence lifetime map (see Fig. 3.2).

Depending on the detector used, and given the very small time scale, the arrival time is recorded with a finite accuracy. This will lead to a convolution of the data with the Instrument Response Function (IRF) f_{IRF} . Thus, taking into account a constant additive background noise b , the full model of the measured intensity is defined as

$$I(t) = \int f_{IRF}(t' - \delta) N_p(t - t') dt' + b \quad (3.1)$$

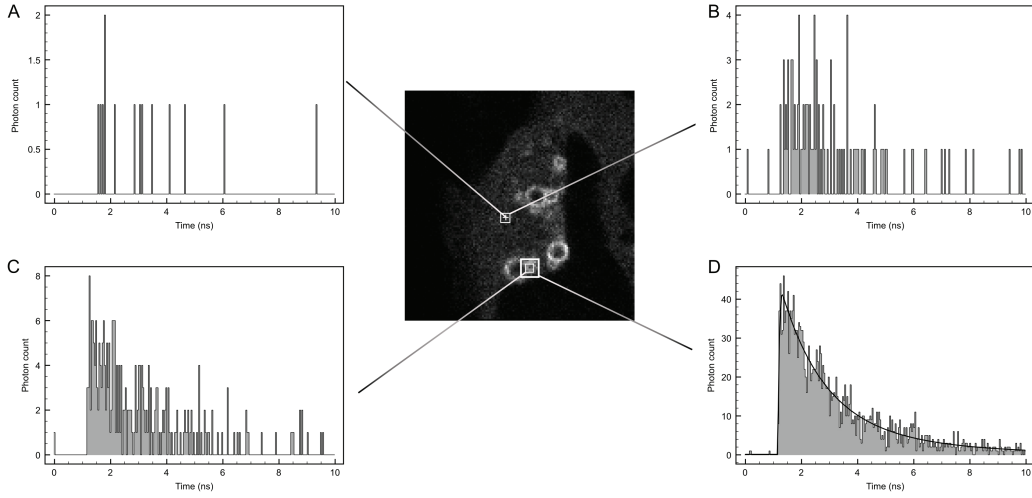


Figure 3.2: Example of typical TCSPC FLIM data. Total fluorescence intensity is shown in the center and corresponds to the sum of photon counts along the time axis at each pixel. The four side graphs correspond to time dependent photon counts in four different regions with variable sizes. By considering large regions, we observe an exponential fluorescence decay (see D). A: one pixel region; B and C: 3×3 patches at different locations; D: 15×15 patch and lifetime estimation by least mean squares fitting (commercial software).

where δ is a zero-time shift to be estimated and $N_p(t)$ is the fluorescent decay as described in Section 2.1. In the literature, the intensity $I(t)$ is assumed to follow a pure Poisson process. Least mean squares estimation is often carried out to estimate the lifetime parameter of the intensity decay [Lakowicz and Masters, 2008], even though the photon counts can be too low to assume the Gaussian distribution. In [Chessel et al., 2013], the authors proposed a maximum likelihood estimator to take into account Poisson noise. It turns out the corresponding algorithm performs better than least mean squares estimation especially for low photon-counts.

If the sample being studied is a living cell, the movements of proteins introduce some blur in the acquired data. The longer the acquisition takes, the more important this effect is. This problem justified our focus on the lifetime measurement in frequency which is known to be faster and allows a more accurate and efficient handling of motion-induced artifacts.

3.2 Frequency domain FLIM

This section presents the basis for lifetime measurement in FD FLIM by homodyne detection. For the sake of clarity, we propose here a high level description of the signal transformation involved in the FD FLIM measurement production and then the lifetime

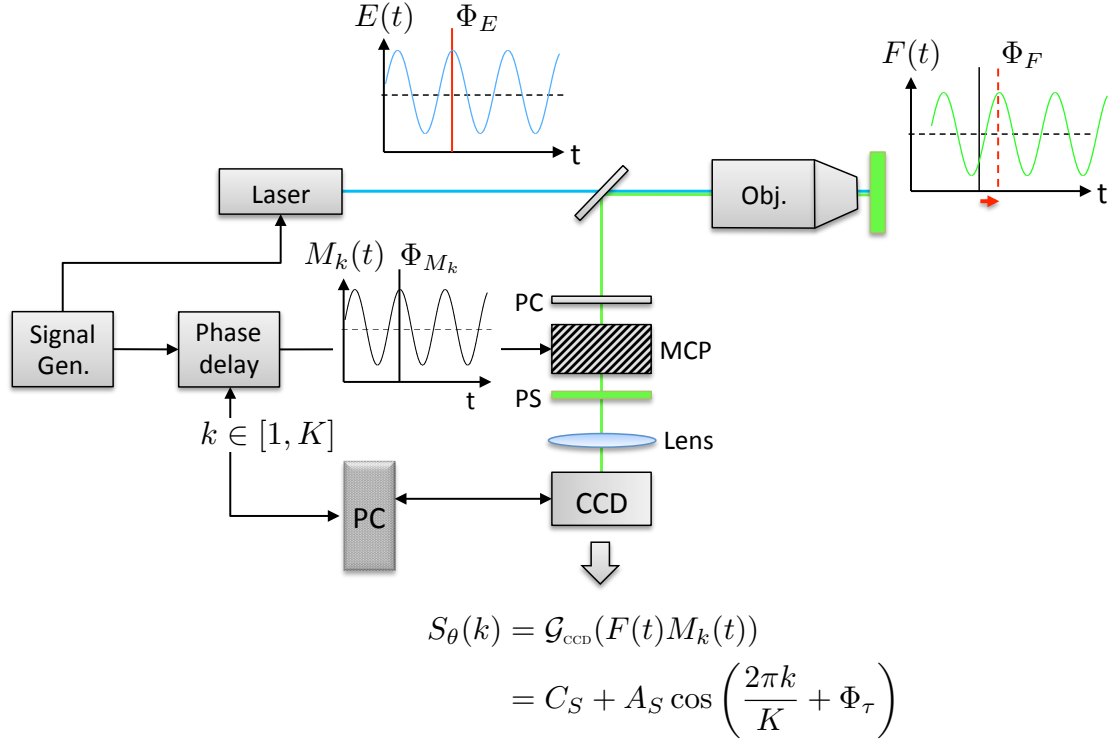


Figure 3.3: Instrumental setup showing the different elements of the system and the corresponding signals for FD FLIM. $E(t)$ denotes the excitation light, $F(t)$ the fluorescence signal, $M_k(t)$ the detection modulation signal and S_{θ} is the resulting FD FLIM measurement.

estimate. A detailed and original mathematical derivation for the fluorescent signal expression and the phase modulation can be found in Appendix A.

3.2.1 Frequency domain FLIM measurement

Instead of the pulsed laser excitation that characterizes time-domain methods, the FD FLIM excitation source is a sinusoidally modulated signal $E(t)$ (blue ray in Figure 3.3) defined as:

$$E(t) = C_E + A_E \sin(\omega_E t + \Phi_E) \quad (3.2)$$

where ω_E denotes the radial frequency of the excitation signal, C_E the offset, A_E the amplitude and Φ_E is the phase delay. This excitation can be operated in both wide-field or confocal microscopy. The signal emitted by the sample $F(t)$ (Green ray in Figure 3.3)

is defined as :

$$\begin{aligned} F(t) &= E(t) * I(t) \\ &= C_F + A_F \sin(\omega_E t + \Phi_E - \arctan(\omega_E \tau)) \end{aligned} \quad (3.3)$$

where $*$ denotes the convolution operator. Accordingly, the phase delay $\Phi_E - \arctan(\omega_E \tau)$ of $F(t)$ allows us to recover τ (see Figure 3.1). In an experimental setup, the frequency ω_E is too high (> 1 MHz) to be compatible with the frame rate of a CCD sensor. Therefore the signal $F(t)$ is phase-modulated with K sinusoidal signals $M_k(t)$, $k \in [1, K]$ (black signal in Figure 3.3) at the same frequency ω_E (homodyne detection):

$$M_k(t) = C_M + A_M \sin\left(\omega_E t + \Phi_{M_0} + \frac{2\pi k}{K}\right). \quad (3.4)$$

This modulation is operated by applying a time-varying voltage to the photocathode terminal in the intensified CCD. As we shall see in the Chapter 4, the intensified CCD is in turn required to acquire the lowest intensity images resulting from modulation. Thanks to the low pass effect of the CCD detector, the higher frequencies of the phase modulated-signal $F(t)M_k(t)$ are negligible. After phase-modulation, the K time-independent signals described as a function of $k \in [1, K]$:

$$\begin{aligned} S_\theta(k) &= \mathcal{G}_{\text{ccd}}(F(t)M_k(t)) \\ &= C_S + A_S \cos\left(\frac{2\pi k}{K} + \Phi_\tau\right) \end{aligned} \quad (3.5)$$

where $C_S = C_F C_M$, $A_S = A_F A_M$ and Φ_τ is the phase. In what follows, we denote $\theta = (C_S, A_S, \Phi_\tau)^T$. Equation (9.34) describes the FD FLIM measurement. It thus consists in K images presenting a sinusoidal footprint (see Figure 3.4). For each pixel, the phase Φ_τ combined with proper calibration yields the lifetime estimate. The next section discusses the brief state of the art in this domain.

3.2.2 Fluorescence lifetime estimation in FD FLIM

Estimating the fluorescence lifetime described by the FD FLIM measurement amounts to estimating the parameters that control the sinusoidal footprint (see Figure 3.5.B). These parameters, most notably the phase $\Phi_\tau = (\Phi_{M_0} - \Phi_E + \arctan(\omega_E \tau))$, can be recovered using conventional least mean squares-based sine fitting or the equivalent Fourier decomposition. The phase delay $(\Phi_{M_0} - \Phi_E)$ of the system must be calibrated by recording a reference frame sequence of a fluorescent sample with known lifetime. Finally, as we monitor the frequency ω_E , the lifetime τ comes straightforwardly. It is also possible to recover the fluorescence lifetime using the relative modulation amplitude A_s as detailed in Appendix A. The latter approach has been shown less precise than the phase-based

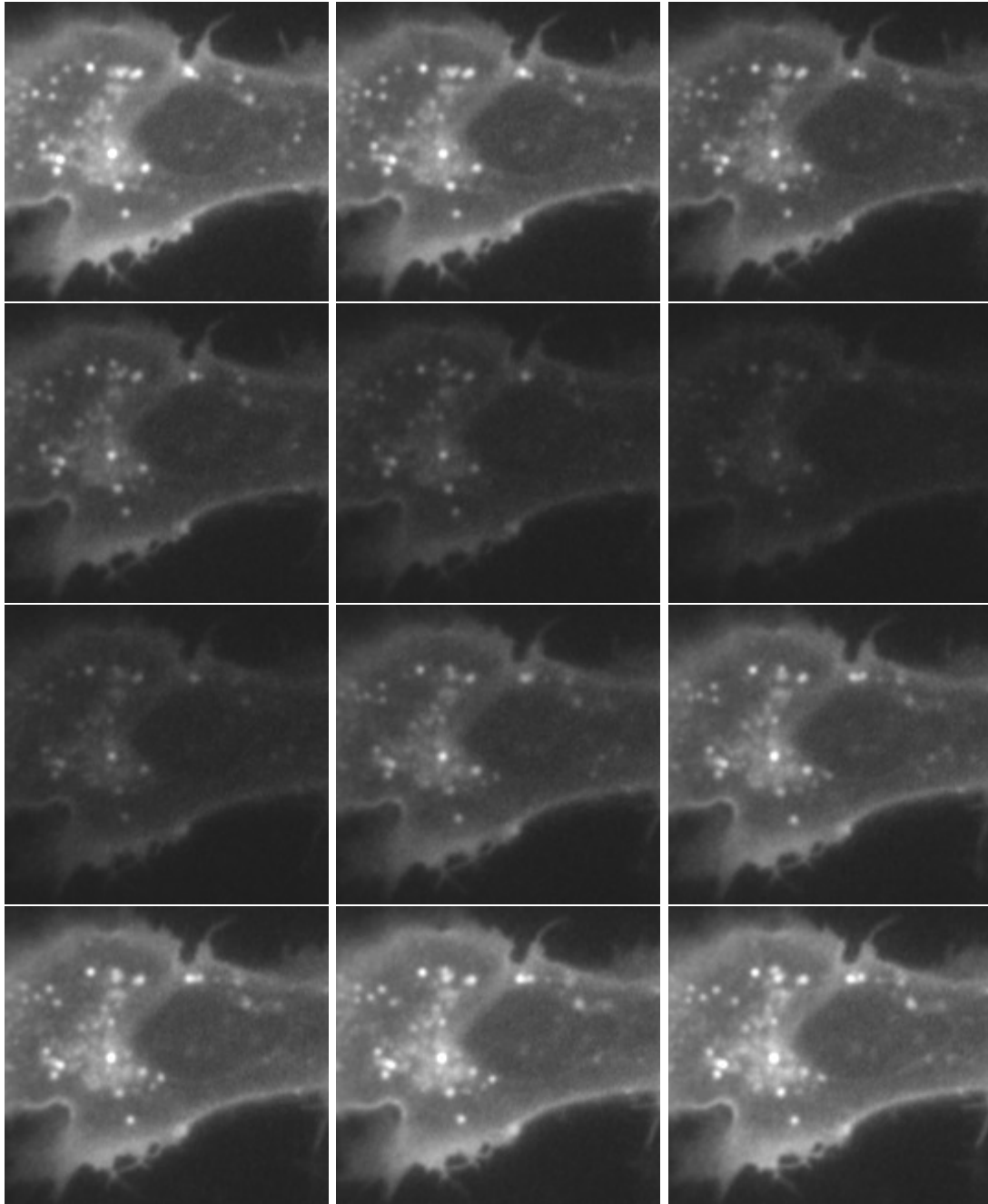


Figure 3.4: An example of FD FLIM measurement with $K = 12$ phase-modulation signals. The sequence must read from the upper left to the lower right. Fluorescent structures localize receptors tagged with GFP in epithelial cells (RPE1). Contrast has been artificially enhanced on the image presenting low intensity for visualization purpose.

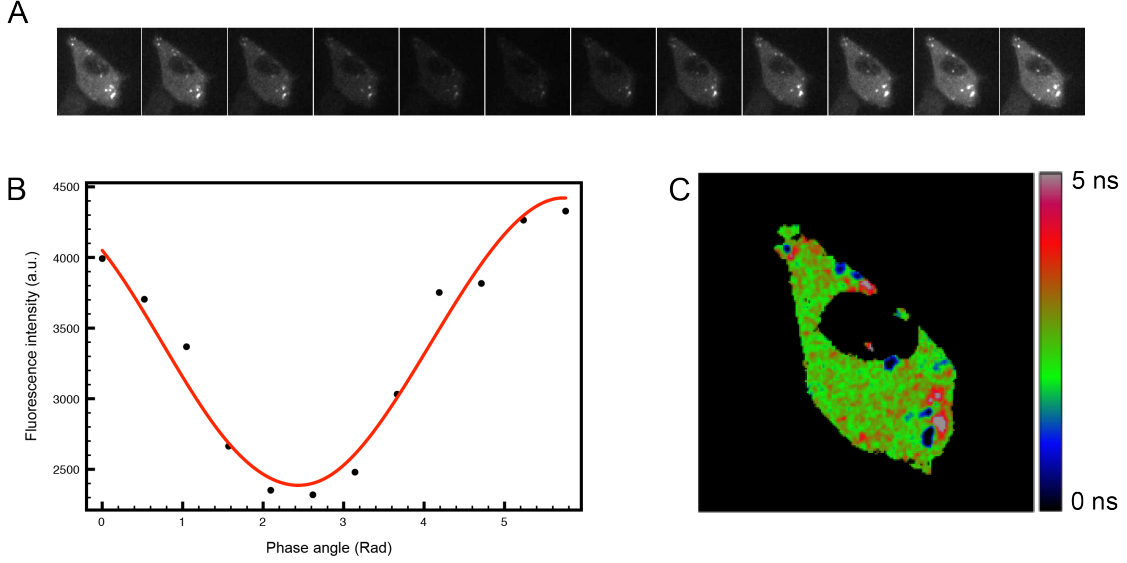


Figure 3.5: Principle of FD FLIM measurement post-processing A: Example of an image sequence showing the intensity variation (S_θ) at different phase shift values ($K=12$ values distributed on 2π radians). B: Example of signal S_θ observed at a given pixel (black dots) with a sine fitting curve (red). C: Fluorescence lifetime image reconstructed from the image sequence in B.

method on short lifetime [Hanley et al., 2001]. For that reason, the amplitude based lifetime estimation will not be detailed in the present work.

As noted above, the classical method used in FD FLIM to estimate the phase of the signal $S_\theta(k)$ is based on the Fourier transform. It consists in computing the signal phase pixel-by-pixel using:

$$\hat{\Phi}_\tau = -\arctan\left(\frac{\sum_k I(k) \cos(\frac{2\pi k}{K})}{\sum_k I(k) \sin(\frac{2\pi k}{K})}\right) + \frac{\pi}{2} \quad (3.6)$$

where $I(k)$ is the measured intensity in the phase-modulated image k . The large majority of contributions in FD FLIM exploits this estimator [Holub, 2003; van Munster and Gadella Jr, 2004; Spring and Clegg, 2009; Hutchinson et al., 1995] as much as commercial softwares such as Li-FLIM® by Lambert Instrument. In order to handle the impact of photobleaching, van Munster and Gadella Jr [2004] proposed to randomize the order of phase modulation. The noise induced by photobleaching is thus shown to be mixed into the uncorrelated measurement noise.

Very few works have been focusing in further improving or characterizing the phase estimator. In [Gadella et al., 1994; Clegg et al., 1994], the authors proposed a linearization

of the problem which is equivalent to the Fourier expression above:

$$\begin{aligned}
 \hat{\theta}_b &= \underset{\theta_b}{\operatorname{argmin}} \sum_k (I(k) - S_{\theta_b}(k))^2 & (3.7) \\
 &= \underset{\theta_b}{\operatorname{argmin}} \sum_k \left(I(k) - \left(C_S + A_S \cos \left(\frac{2\pi k}{K} + \Phi_\tau \right) \right) \right)^2 \\
 &= \underset{\theta_b}{\operatorname{argmin}} \sum_k \left(I(k) - \left(C_S + A_S \sin(\Phi_\tau) \cos \left(\frac{2\pi k}{K} \right) + A_s \cos(\Phi_\tau) \sin \left(\frac{2\pi k}{K} \right) \right) \right)^2.
 \end{aligned}$$

The vector of parameter $(A_s \sin(\Phi_\tau), A_s \cos(\Phi_\tau), C_s)^T$ can thus be solved using an ordinary linear least mean squares estimator:

$$\begin{pmatrix} A_s \sin(\Phi_\tau) \\ A_s \cos(\Phi_\tau) \\ C_s \end{pmatrix} = \begin{pmatrix} \sum_k \sin \left(\frac{2\pi k}{K} \right)^2 & \frac{1}{2} \sum_k \sin \left(\frac{4\pi k}{K} \right) & \sum_k \sin \left(\frac{2\pi k}{K} \right) \\ \frac{1}{2} \sum_k \sin \left(\frac{4\pi k}{K} \right) & \sum_k \cos \left(\frac{2\pi k}{K} \right)^2 & \sum_k \cos \left(\frac{2\pi k}{K} \right) \\ \sum_k \sin \left(\frac{2\pi k}{K} \right) & \sum_k \cos \left(\frac{2\pi k}{K} \right) & K \end{pmatrix}^{-1} \begin{pmatrix} \sum_k I(k) \sin \left(\frac{2\pi k}{K} \right) \\ \sum_k I(k) \cos \left(\frac{2\pi k}{K} \right) \\ \sum_k I(k) \end{pmatrix} \quad (3.8)$$

In [Boddeke, 1998], the author discussed the use of the Newton algorithm to solve the least mean squares problem, showing that the Fourier-based estimator presents a lower residual variance, that is closer to the Cramér-Rao lower bound.

A major issue with the methods cited above is that the least mean squares estimator (see (3.7)), assumes the measurement noise to be homoscedastic and uncorrelated for consistency and optimality in the class of linear unbiased estimators. This assumption does not hold in FD FLIM measurement due to photonic noise and specific FD FLIM instrumentation (see Figure 3.6 and Chapter 4). Furthermore, a large number of image-based signal processing methods (denoising, optical flow, object detection ...) depends on the same assumption of homoscedasticity. In Chapter 4, we propose a thorough study of instrument-induced noise taking both theoretical and experimental factors in consideration to compensate noise heterogeneity.

An other issue that presents pixel-by-pixel estimation is the underlying assumption of spatial stationary of the sample. Yet, if the FD FLIM method is faster than the TCSPC technique, the acquisition still takes up to hundreds of milliseconds [Lajevardipour and Clayton, 2013; P. C. Schneider, 1997; Holub et al., 2001], as a result intracellular structure can move between phase modulation image acquisition (see Figure 3.7 below and Figure 5.1 in Chapter 5). In this work we propose a joint estimation framework for fluorescence lifetime and motion on moving vesicles.

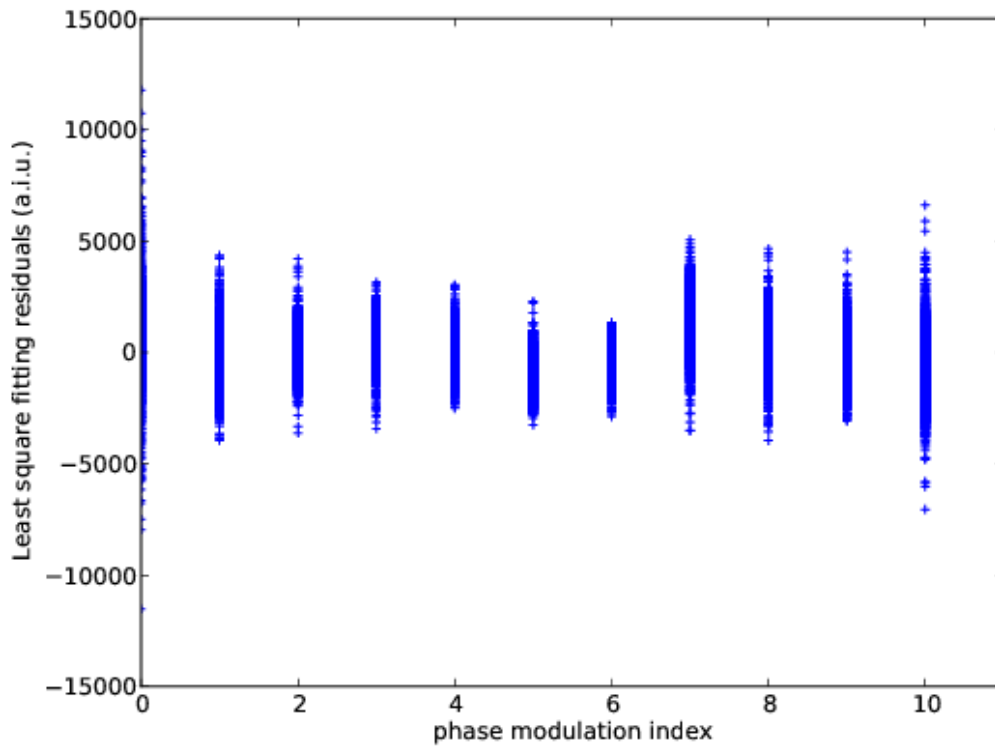


Figure 3.6: Residuals of least-squares estimates of the parameters controlling the sinusoidal described by the phase modulation images (see (9.34)). The residuals associated to each pixel in the whole stack presented Figure 3.4 are plotted. The residual amplitude variability highlights a strong heteroscedasticity (Spinning disk and an intensifier II18MD from Lambert Instruments).

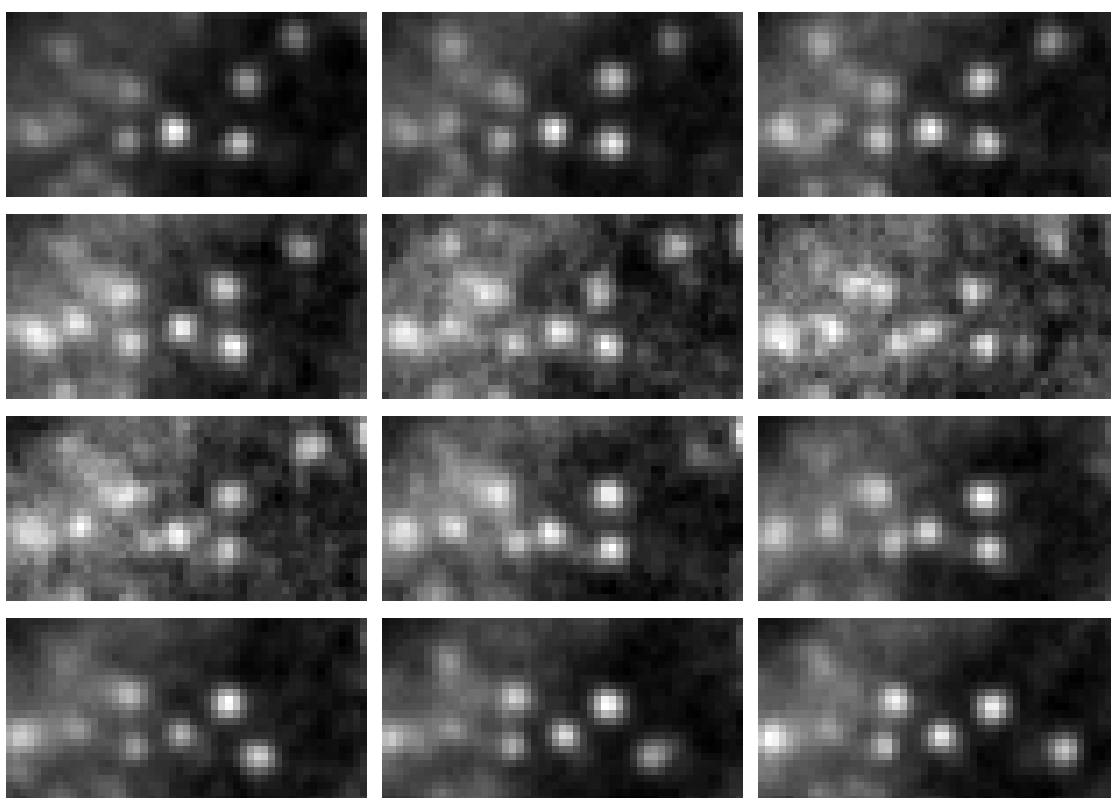


Figure 3.7: Dynamical structures in FD FLIM (normalized details from Figure 3.4).

4 Instrumental noise in FD FLIM measurement

In FD FLIM as in numerous imaging applications, a CCD (charge-coupled device) transforms a light pattern into a discrete spatial distribution of photo-electrons trapped in potential wells. Modeled as the realization of a random variable, the measured intensity on a CCD follows a mixture of Poisson and Gaussian statistics. Those two noise processes are respectively due to the photonic nature of light and the readout and dark current noise of the CCD instrument. Let $\aleph(\mathbf{x})$ be the incident photon number on the CCD following a Poisson law of parameter $\lambda(\mathbf{x})$. The measured intensity $I(\mathbf{x})$ at location $\mathbf{x} = (x, y, k) \in \Omega \subset \mathbb{R}^3$ follows:

$$I(\mathbf{x}) = g_{\text{ccd}}\aleph(\mathbf{x}) + \xi \quad (4.1)$$

where ξ is the CCD readout Gaussian noise such as $\xi \sim \mathcal{N}(m_\xi, \sigma_\xi^2)$, g_{ccd} is the gain of the CCD sensor. Given an estimation problem where this intensity is the dependent variable, a common approximation consists in modelling the intensity as Gaussian and stationary across the measured sample. This approximation is also made in previous work in phase-shift estimation in FD FLIM (see Section 3.2.2). However, the phase modulation of the emitted signal in FD FLIM causes an important dynamic range across the K phase-modulated images. As a result the approximation of homoscedasticity does not hold in the phase estimation problem (see Figure 3.6 in the previous chapter). Controlling heteroscedasticity is not only important to control parameters estimation. Indeed, numerous techniques rely on homoscedasticity of the residuals of the estimator such as parameters covariance estimation or robust estimation techniques.

As opposed to common biological imaging techniques, the specific intensity footprint of FD FLIM imposes the use of an image sensor that is efficient in a broad range of intensity values. Consequently, an image intensifier is placed before the CCD in order to increase low-level signal above the readout noise of the CCD [Lakowicz and Masters, 2008]. The resulting sensor is called an ICCD for intensified CCD. Because of the physical properties of this intensifier, intensified measurements present a different noise spectrum than a classical scientific CCD acquisitions as described by (9.29). Accordingly, the study of the dependent variable heteroscedasticity in the lifetime estimation problem calls for a thorough study of the ICCD characteristic noise. While the performances of this class of instruments has been studied in the past in the field of experimental physics

[Boddeke, 1998; Frenkel et al., 1997], very few works have been dedicated to local noise estimation and its application. A notable exception is the work of Spring and Clegg [2009], where a theoretical noise model is derived and applied for noise stabilization. In our work, we first present an original derivation for this theoretical noise model. We then show that such a theoretical model is not sufficient to describe the noise measured on non-fibered ICCD-image-formation, a widespread type of ICCD setup and the kind we used for our experimental fluorescence lifetime measurements. Accordingly, we propose a corrected model that takes non-stationary blurring into account. A robust estimation framework for the parameters controlling this model is also proposed.

Thanks to this precise modeling, we can take instrumental noise into account in our fluorescence lifetime estimation using a weighted least squares estimator for phase-modulated signal phase estimation. To our knowledge, no previous method have been taking heteroscedasticity into account for frequency domain fluorescence imaging. The lifetime estimation results are compared with the widespread Fourier decomposition. The comparison is carried out against FD FLIM acquisitions of plain reference fluorescein sample and controlled living cell sample that both present a single fluorescence lifetime.

Exploiting further this experimental noise model, we apply it to two denoising algorithms for FD FLIM measurements. We first highlight the advantages of a careful modeling of noise heteroscedasticity with Wiener filtering. We compare the impact of our noise model with a spatially uniform variance estimate. We also propose a more advanced patch-based method based on the *NL-means filter* [Buades et al., 2005]. Our denoising approach does not require a variance stabilizing transformation and we do not assume the noise to be Gaussian. We have been testing this method on FD FLIM measurement, but this method is suitable to any kind of imaging technique provided that a noise model is available. Our approach has been compared against BM3D [Dabov et al., 2007] and ND-SAFIR [Boulanger et al., 2010]. Visual inspection highlights that our denoising algorithm presents a better noise reduction than the former while presenting less artifact than the latter.

The remainder of this chapter is organized as follows. The ICCD is first described in more details Section 4.1. We then present our theoretical noise model derivation and the proposed correction presented in Section 4.2.1 and 4.2.2 along with parameter estimation framework Section 4.2.3. Finally, Sections 5.3 and 4.3 presents experimental results on both lifetime estimation and denoising in real FD FLIM sequences.

4.1 Intensified CCD

To image low-light signal using a scientific CCD, it is common practice to increase the exposure time so as to integrate more photo-electrons in the sensor wells. To do so, the thermal noise (causing dark current) can be controlled by exploiting the Peltier cooling

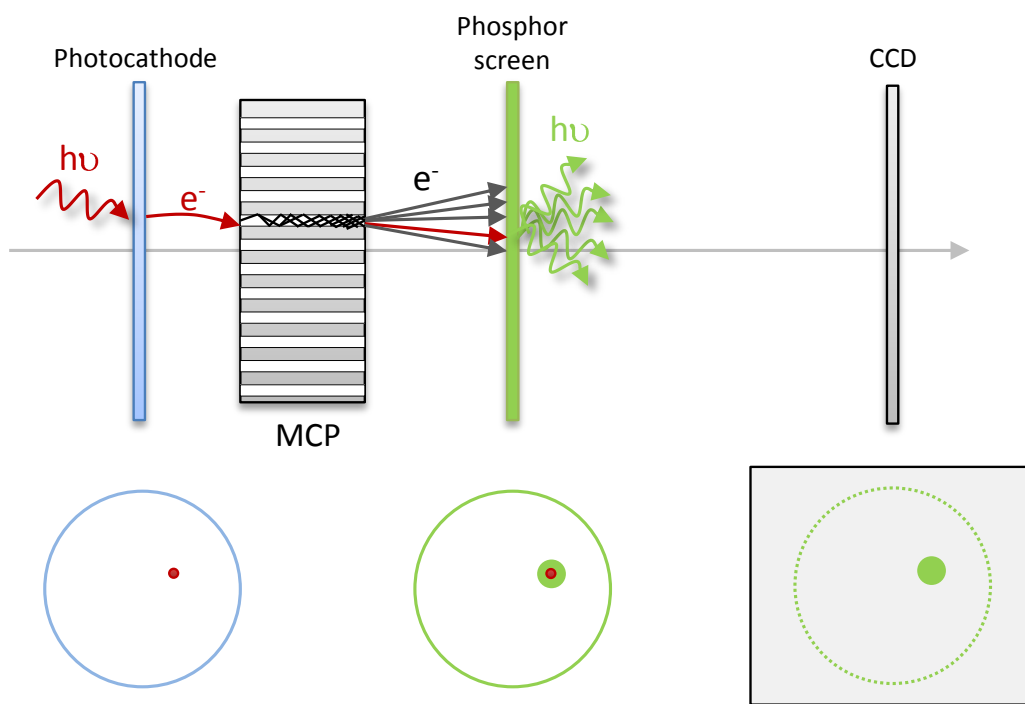


Figure 4.1: Image formation process in a third generation Intensified CCD.

effect. However, in live cell microscopy, the exposure time is typically limited by biological phenomena such as photo-bleaching, photo-toxicity or the dynamic of the object under study. In such a case, an intensifier can amplify the signal before the CCD recording process and thus allowing for shorter exposure time. Due to ICCD performances in low-light conditions, it is used in a large variety of domains such as military, astronomy or biological applications. Thanks to the high sensitivity of the phosphor screen, the ICCD can even be used for photons counting [Bergamini et al., 2000]. This amplification comes at the cost of other noise sources such as stronger spatial correlation and gain variability. To better understand and model the amplified signal, we will shortly describe the different components of the common ICCD (see Figure 4.1).

The signal amplification takes place in the electronic domain. After a window typically made of anti-vailing glass, a photocathode transforms incoming photons into electrons. The intensification process consists in adding energy to the newly transformed electrons, then transforming the electrons back into photons thanks to a phosphor screen. The latter will translate this higher energy into a higher number of photons. To avoid

additional electrons caused by ionization, the intensifier operate in a vacuum. In the first generation of intensifier, this energy was induced by electrons acceleration controlled by an electrical field. The space between the photocathode and the phosphor screen is limited in order to reduce the effect of random electron motions that cause a loss in spatial resolution. To improve further the gain of the instrument, a microchannel plate (MCP) is placed between the photocathode and the phosphor screen in the second generation of instrument (see Figure 4.1). A MCP is a very thin (0.5 mm) disc built as a honeycomb of glass tubes with very small diameter (6 to 10 nm) and a resistive coating. An incident electron with sufficient energy will trigger secondary electrons on contact with a tube wall. This will trigger a snow ball effect that will result in a burst of electrons at the tube output. Two to three MCPs can be put in cascade resulting in even higher gain. As illustrated in Figure 4.1, a single electron out of a MCP tube will result in a burst of photons on the phosphor screen. The phosphor screen is a thin ($< 10 \mu\text{m}$), very sensitive, layer of phosphor particles that are crystalline compounds of Zinc Sulfide impured with Silver atoms (1 to 5 μm). Finally, the output photons are brought to the CCD wells via relay optics such as a lens or fiber optic.

In order to summarize the impact of each component, the ICCD can be described by four characteristics:

- The **Photon-to-photon gain** describes best the purpose of the intensifier. The gain is controlled by the voltage over the MCP. Modulating the gain allow short exposure time (nanoseconds), or high frequency (Mhz) sinusoidal modulation as in FD FLIM acquisition. The phosphor screen can present a variable gain that will hinder the overall gain stationarity.
- The **Spectral sensitivity** or quantum efficiency is the probability that a photon of a given wavelength is detected. It relies on the photocathode material. The third generation of intensifier replaces the multi-alkali photocathode of the second generation by a Gallium-Arsenide (GaAs) photocathode resulting in quantum efficiency extension to ultraviolet and infrared.
- An ICCD will also present a **spectral conversion** ability due to the spectrum of the phosphor screen. An important characteristic while picking for the right CCD sensor.
- The tube diameter in the micro channel plate and the phosphor screen has an important impact on the **spatial resolution** of the intensifier. The photons resulting from a single burst on the phosphor screen output will be spread out on various CCD resulting in spatial smoothing.

In what follows, we will focus on the characterization of the noise footprint of the ICCD induced by its different components. Thanks to this model, we will be able to better compensate the heteroscedastic measurement noise within our lifetime estimator.

4.2 ICCD Noise modeling

In this section we derive a theoretical model describing the noise induced by a third generation ICCD. We present an original and alternative approach to the derivation described in [Spring and Clegg, 2009] where the CCD gain is supposed to vary among other approximations. We also propose a noise variance model correction for applications in experimental conditions.

FD FLIM measurements are always coupled with a reference stack to calibrate the excitation signal phase. This reference stack typically corresponds to the acquisition of a plain fluorescein sample that will be imaged in conditions that are strictly identical to the acquisition process of the sample of interest. The reference stack thus presents a large range of locally uniform intensity. This makes reference FD FLIM measurement attractive for modeling the noise induced by the instrumentation and for estimating the noise variance that vary with intensity in living cells. After the calibration of our noise model on this reference stack, our aim is to be able to estimate the noise at each location in space and time on experimental samples.

4.2.1 Theoretical model

Let $I(\mathbf{x})$ be the ICCD response at location $\mathbf{x} = (x, y, k) \in \Omega \subset \mathbb{R}^3$ where k describes the frame index, the intensification and sensing processes can be approximated by a linear relation [Boddeke, 1998]:

$$I(\mathbf{x}) = g_{\text{ccd}}g_{\text{int}}\aleph(\mathbf{x}) + \xi \quad (4.2)$$

where $\aleph(\mathbf{x})$ is the incident photon number on the ICCD which follows a Poisson law of parameter $\lambda(\mathbf{x})$, ξ is the CCD readout Gaussian noise such as $\xi \sim \mathcal{N}(m_\xi, \sigma_\xi^2)$, g_{ccd} is the gain of the CCD sensor and g_{int} is the gain of the intensifier assumed to be a realization of a random variable. The goal is to estimate the parameters that control the instrumental-induced noise variance of $I(\mathbf{x})$ assumed to be a realization of a random variable. Due to the quantum nature of light, this variance theoretically depends on the expected number of photons $\lambda(\mathbf{x})$. Accordingly, we first propose a robust regression between the local expected intensity value $\mathbb{E}[I(x)]$ and the local variance $\text{Var}[I(\mathbf{x})]$. This method has already first been proposed for bare CCD sensors in [Ramani et al., 2008; Delpretti et al., 2008] using least mean squares estimation and later enhanced in a robust framework in [Boulanger et al., 2010].

While CCD gain is considered constant throughout the whole sensor surface, it has been experimentally showed in [Boddeke, 1998] that the uncontrolled photon bursts in the phosphor screen result in a noisy gain that cannot be considered stationary. Figure 4.2 illustrates such a lack of stationarity with a so-called background image. The background image is recorded without any illumination to calibrate the measurement with respect to the readout and dark current noise of the CCD and the intensity offset due to the phosphor screen. In this image, one can observe the constant Gaussian noise footprint

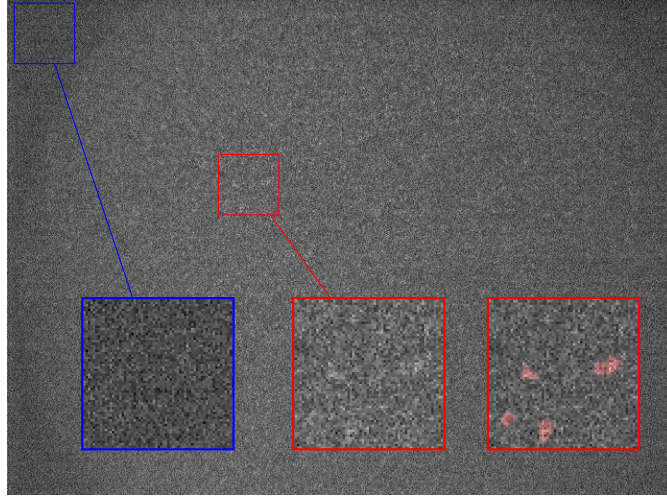


Figure 4.2: Spatial non-stationarity induced by the ICCD on a background image (an acquisition in the absence of excitation on ICCD input). Spontaneous burst of photon in the intensified area highlights the sensitivity of the device (raw intensity is presented on the middle magnification and automatically highlighted in red in the right magnification)). The blue-squared area is not intensified and describe a much more stationary intensity footprint for the CCD.

of the CCD on the non-intensified area while the intensified area presents a much more unstable gain due to stochastic burst of photons. By modeling this noisy gain and under the proper assumptions of independence, the intensity variance is given by:

$$\begin{aligned} \text{Var}[I(\mathbf{x})] &= g_{\text{CCD}}^2 \text{Var}[g_{\text{INT}}\aleph(\mathbf{x})] + \sigma_{\xi}^2 \\ &= g_{\text{CCD}}^2 \text{Var}[g_{\text{INT}}] \text{Var}^2[\aleph(\mathbf{x})] + g_{\text{CCD}}^2 (\mathbb{E}^2[g_{\text{INT}}] + \text{Var}[g_{\text{INT}}]) \text{Var}[\aleph(\mathbf{x})] + \sigma_{\xi}^2. \end{aligned} \quad (4.3)$$

Taking the expectation of (9.29) we also obtain:

$$\mathbb{E}[I(\mathbf{x})] = g_{\text{CCD}}\mathbb{E}[g_{\text{INT}}]\mathbb{E}[\aleph(\mathbf{x})] + m_{\xi}. \quad (4.4)$$

As the properties of the Poisson process yields:

$$\text{Var}[\aleph(\mathbf{x})] = \lambda(\mathbf{x}) = \mathbb{E}[\aleph(\mathbf{x})], \quad (4.5)$$

it follows a quadratic relationship between the local expectation and variance:

$$\text{Var}[I(\mathbf{x})] = \frac{\text{Var}[g_{\text{INT}}]}{\mathbb{E}^2[g_{\text{INT}}]} (\mathbb{E}[I(\mathbf{x})] - m_{\xi})^2 + g_{\text{CCD}} (\mathbb{E}[g_{\text{INT}}] + \frac{\text{Var}[g_{\text{INT}}]}{\mathbb{E}[g_{\text{INT}}]}) (\mathbb{E}[I(\mathbf{x})] - m_{\xi}) + \sigma_{\xi}^2,$$

while a similar derivation with a scientific CCD straightforwardly yields:

$$\text{Var}[I(\mathbf{x})] = g_{\text{CCD}} (\mathbb{E}[I(\mathbf{x})] - m_{\xi}) + \sigma_{\xi}^2. \quad (4.6)$$

To estimate the parameters ruling this quadratic relation, we propose a robust regression method. The values $\mathbb{E}[I(\mathbf{x})]$ are approximated by the median values taken in a 30×30 pixels squared neighborhood centered at pixel \mathbf{x} . The values of $\text{Var}[I(\mathbf{x})]$ are obtained using least-trimmed squares estimation on the pseudo-residuals¹ computed over the same neighborhood. Those measurements are carried on FD FLIM plain reference stack measurement. Thanks to local uniformity, the empirical measures of expectation and variance are not over-estimated by local structure in the images. Additionally they present a very wide intensity amplitude (see Figure 4.3.a).

Inspired by Boulanger et al. [2010], we used an M-estimator with a Leclerc's influence function to obtain a robust fit for the model (9.40). The M-estimator will automatically sorts out the outlier values that describe the non-intensified area and impurity. The M-estimator scale is set using the median of absolute deviation. Figure 4.3.b shows an example of such a robust fit on a phase calibration stack. To avoid undesirable effects described in the next section and highlight the theoretical noise model, the FD FLIM measurement have been cropped in the center.

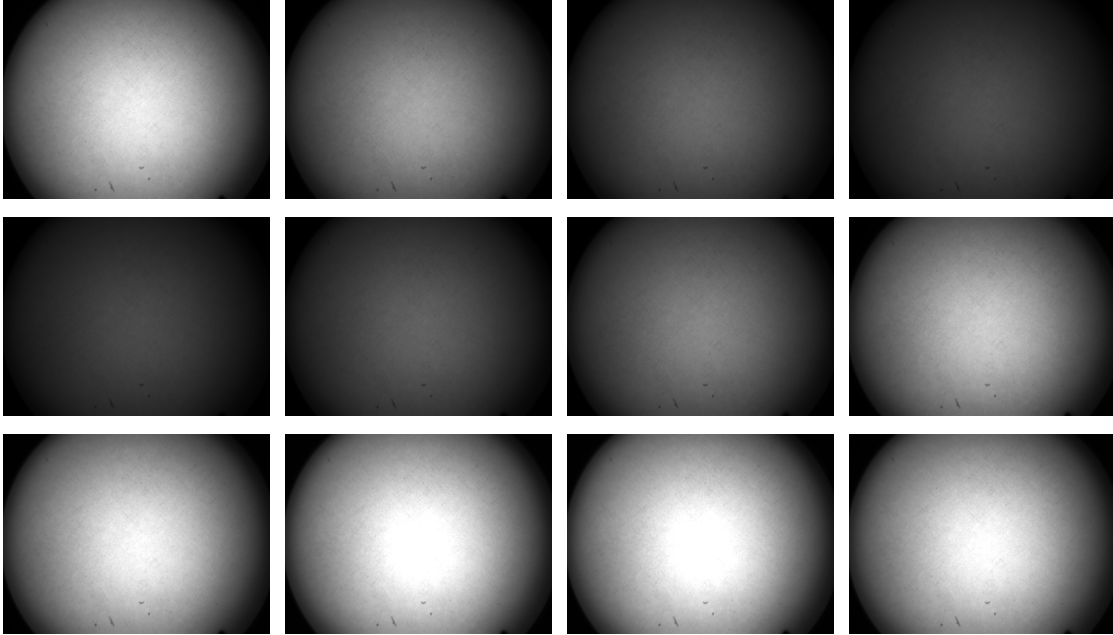
4.2.2 Experimental issues and spatial dependency analysis

When analyzing the images recorded by specialists in daily experimental conditions, we noticed unexpected asymmetric blurriness on the sample. To investigate that problem further we measured the local variance estimated on a plain reference stack. As illustrated in Figure 4.4, the spatial distribution of measured variances differs from the theory. Indeed, on a simulated reference, the variances highlight the same symmetry as the intensity (see Figure 4.4.a), a property that is dictated by the theoretical quadratic relationship between intensity and variance. However, on experimental sequences, the asymmetry in the measured variance does not cope with a stationary gain throughout the whole image. This property has been observed on both wide-field and confocal microscopes.

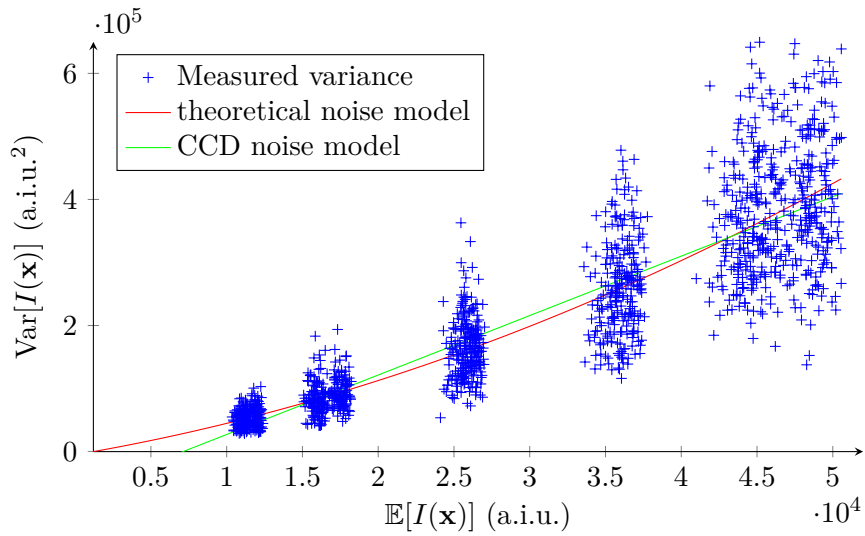
Taking a different angle on the data, Figure 4.5 shows that the noise footprint locally follows the noise model in the whole image. Yet, there is an important gain variation depending on the pixel location whereas a perfect ICCD and microscope should present a single quadratic gain as depicted in Figure 4.3.

Such differences with the expected constant theoretical gain could come from monochromatic aberrations. This can typically be due to the relay optics between the phosphor screen and the CCD. To test this hypothesis, experimentations with a fibered ICCD are currently planned. The most frequent aberration is the spherical aberration which causes non-stationary blur on the recorded image. This blurring effect increases with the distance from the center. Figure 4.6 illustrates the spatial dependency

¹Assume $I(\mathbf{x})$ is corrupted by a zero-mean white Gaussian noise with variance σ^2 . We define image pseudo-residuals as $e(\mathbf{x}) = e(x, y) = \frac{1}{\sqrt{20}}(4I((x, y) - (I(x-1, y) + I(x+1, y) + I(x, y-1) + I(x, y+1)))$. It follows that $\mathbb{E}[e(x, y)^2] = \sigma^2$ if the true image is constant in the neighborhood of (x, y) .

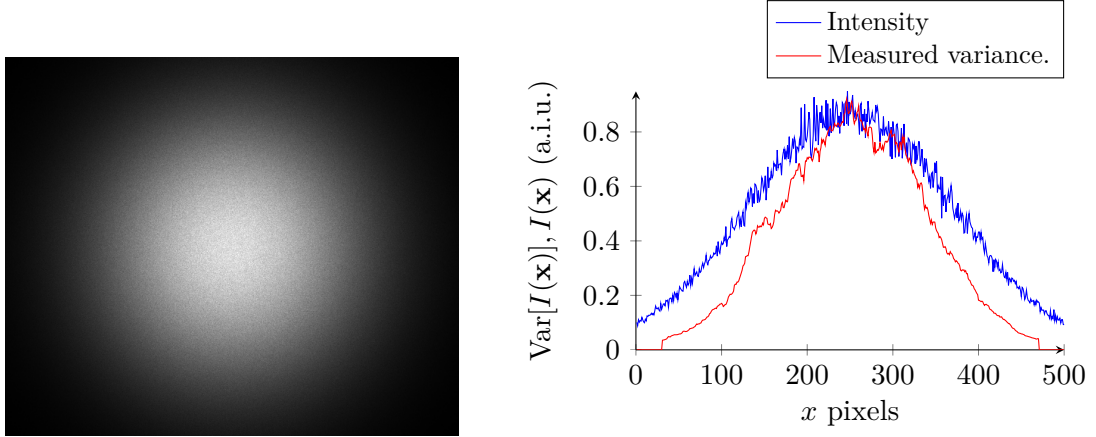


(a) Plain reference stack used for noise calibration.

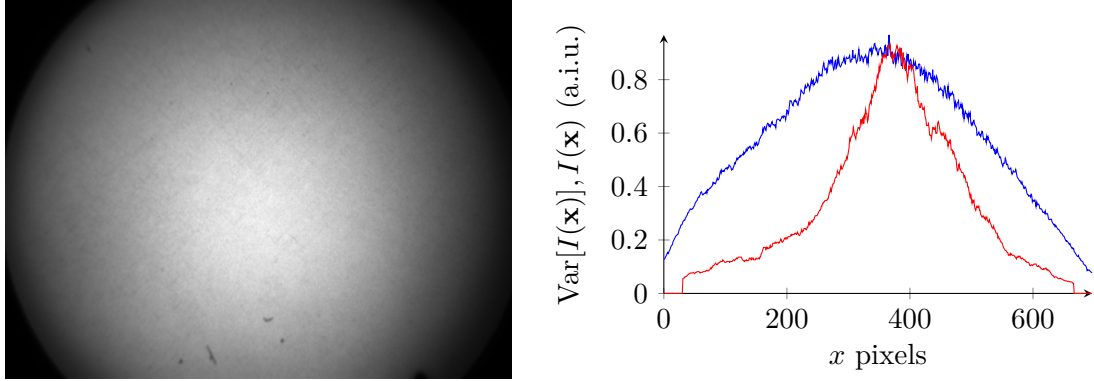


(b) Robust fit from local estimation of $\mathbb{E}[I(\mathbf{x})]$ and $\text{Var}[I(\mathbf{x})]$ computed from a FD FLIM reference stack (a.i.u. (arbitrary intensity unit)).

Figure 4.3: Confirmation of the validity of the quadratic model from experimental measurements in a given local area of the II18MD from Lambert Instruments.



(a) Simulated reference stack.



(b) Experimental reference stack of fluorescein.

Figure 4.4: Horizontal profiles (after normalization) of noise variance and intensity on a single image. **a)** A simulated reference stack respecting the theoretical image formation highlights the expected equivalent symmetry between intensity and variance. **b)** On an experimental wide-field stack the curve highlights a dis-symmetry that is not compatible with a constant gain between intensity and variance. The variance is estimated using the median of absolute deviation on a 30×30 pixels square window.

of image variance for a given intensity value of $\lambda = 20000$ (a.i.u.). This demonstrates that the gain variation is significant and must be taken into account.

As illustrated in Fig. 4.6, we propose to model this monochromatic aberration by a parametric Gaussian function that describes the additional blurring (9.9). The resulting corrected variance model is of the following form:

$$\text{Var}[I(\mathbf{x})] = (a\mathbb{E}[I(\mathbf{x})]^2 + b\mathbb{E}[I(\mathbf{x})] + c) \left(e^{-\frac{(x-x_0)^2}{2\sigma_x^2} - \frac{(y-y_0)^2}{2\sigma_y^2}} + o \right) \quad (4.7)$$

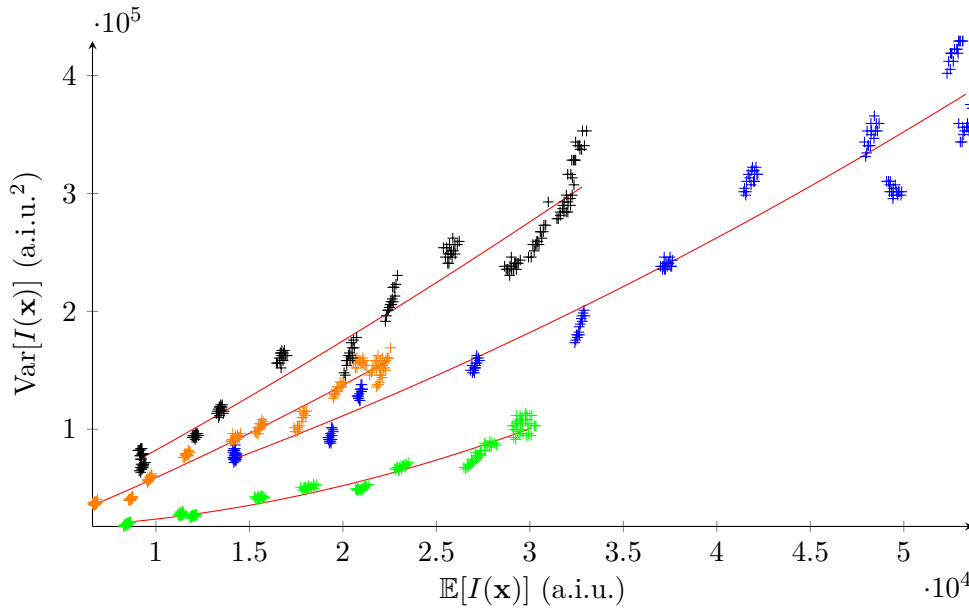
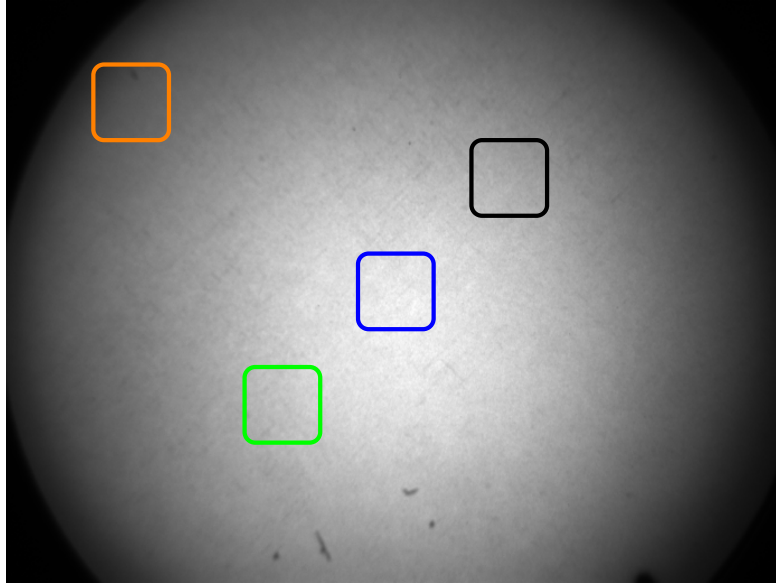


Figure 4.5: Four different gains at four different locations computed from a FD FLIM reference stack of 13 frames acquired with a confocal setup (crosses represent measured variances, lines represent the theoretical noise model).

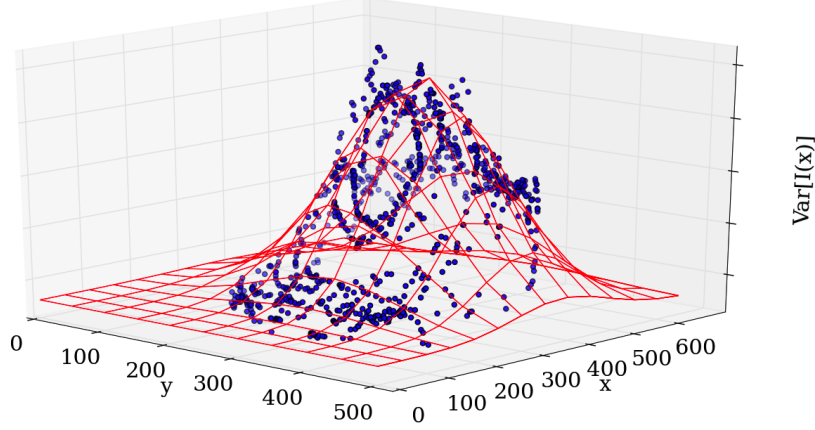


Figure 4.6: Variance vs spatial coordinates for $\lambda = 20000$ and $\epsilon = 10$ (a.i.u.) from a reference stack of 13 frames (FD FLIM confocal). In theory, the measured variance should form a horizontal plane with constant estimates.

when a, b and c are the parameters derived from (9.40) and $x_0, y_0, \sigma_x, \sigma_y$ and o are the parameters of the correction term. A Zernike polynomial would probably be more accurate in the case of a spherical aberration, we though choose the close Gaussian correction for numerical stability at the estimation step.

4.2.3 Spatially varying parameter estimation

In order to solve the estimation problem, we propose a two-step computational approach since global optimization of eight parameters did not produce satisfying results. Let

$$\lambda \in \Lambda = \{I_{min} \cdots I_{max}\} \quad (4.8)$$

be a given intensity value. Let us consider the parameter

$$\theta_\lambda = (A^\lambda, O^\lambda, x_0^\lambda, y_0^\lambda, \sigma_x^\lambda, \sigma_y^\lambda)^T \quad (4.9)$$

controlling the spatially-varying variance for a given intensity value λ such that:

$$\text{Var}[I(\mathbf{x})] = A^\lambda e^{-\frac{(x-x_0^\lambda)^2}{2\sigma_x^{\lambda^2}} - \frac{(y-y_0^\lambda)^2}{2\sigma_y^{\lambda^2}}} + O^\lambda, \quad (4.10)$$

$\forall \mathbf{x} \in \Omega_\lambda = \{\mathbf{x} : |\mathbb{E}[I(\mathbf{x})] - \lambda| < \epsilon\}$ where Ω_λ is the level set λ . Furthermore, we consider a subset $\Lambda_M = \{\lambda_1 \cdots \lambda_M\}$ of intensity values. An estimator of θ_λ for a given $\lambda \in \Lambda_M$ is then defined as:

$$\hat{\theta}_\lambda = \underset{\theta_\lambda}{\operatorname{argmin}} \sum_{\mathbf{x} \in \Omega_\lambda} \left(\text{Var}[I(\mathbf{x})] - A^\lambda e^{-\frac{(x-x_0^\lambda)^2}{2\sigma_x^{\lambda^2}} - \frac{(y-y_0^\lambda)^2}{2\sigma_y^{\lambda^2}}} - O^\lambda \right)^2. \quad (4.11)$$

Figure 4.6 illustrates the estimation results for $\lambda = 20000$ and $\epsilon = 10$. Given the set of estimates $\{\hat{\theta}^\lambda | \lambda \in \Lambda_M\}$, we use a M-estimator to compute the remaining parameters a, b and c as:

$$(\hat{a}, \hat{b}, \hat{c}) = \operatorname{argmin}_{a,b,c} \sum_{\lambda \in \Lambda_M} \rho_\tau \left(A^\lambda - (a\lambda^2 + b\lambda + c) \right). \quad (4.12)$$

The function ρ is a Leclerc's influence function from the M-estimator family and τ is a scale parameter used to weight down outliers. The scale parameter is defined as $\tau = 3\varsigma$ [Rousseeuw et al., 1987]:

$$\varsigma = 1.4826 \operatorname{med} \left(|r_\lambda - \operatorname{med}_{\lambda \in \Lambda_M}(r_\lambda)| \right) \quad (4.13)$$

where $\{r_\lambda\}$ is the set of residuals when using the L^2 -norm as influence function, which is equivalent to a least mean squares fit.

In order to estimate robustly the remaining parameters, the median estimator is preferred to the mean (see Fig. 4.7):

$$\begin{aligned} \hat{\sigma}_x &= \operatorname{med}_{\lambda \in \Lambda_M}(\sigma_x^\lambda), & \hat{\sigma}_y &= \operatorname{med}_{\lambda \in \Lambda_M}(\sigma_y^\lambda), & \hat{o} &= \operatorname{med}_{\lambda \in \Lambda_M} \left(\frac{O^\lambda}{A^\lambda} \right), \\ \hat{x}_0 &= \operatorname{med}_{\lambda \in \Lambda_M}(x_0^\lambda), & \hat{y}_0 &= \operatorname{med}_{\lambda \in \Lambda_M}(y_0^\lambda) \end{aligned} \quad (4.14)$$

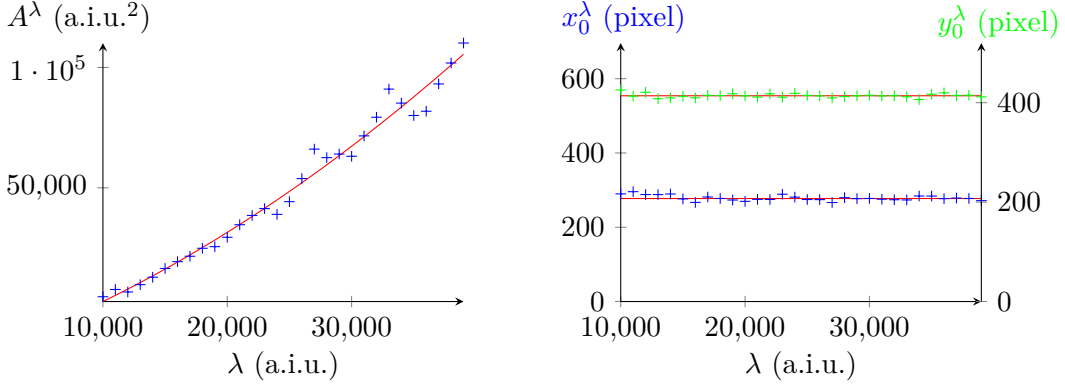
4.2.4 Noise Variance estimation results

The noise variance estimation procedure has been tested on FD FLIM stacks depicting living cells using confocal and wide-field setups (UMR 144 CNRS-PICT Institut Curie). The ICCD is the third generation device built by Lambert Instruments (model II18MD).

We demonstrate the potential of our noise variance model using a plain fluorescein FD FLIM reference stack acquired with a wide-field microscope. Figure 4.7 plots the parameters $\hat{\theta}_\lambda$ resulting from the estimation (9.14) controlling the Gaussian model for λ ranging from 10000 to 35000 a.i.u. Figure 4.7 shows that the height of the Gaussian model and the offset is conform to the theoretical quadratic evolution. Also, the estimated center and scale for our spatial correction are stationary although estimated independently. This experiment demonstrates that our proposed correction solve satisfyingly the problem of spatial dependency.

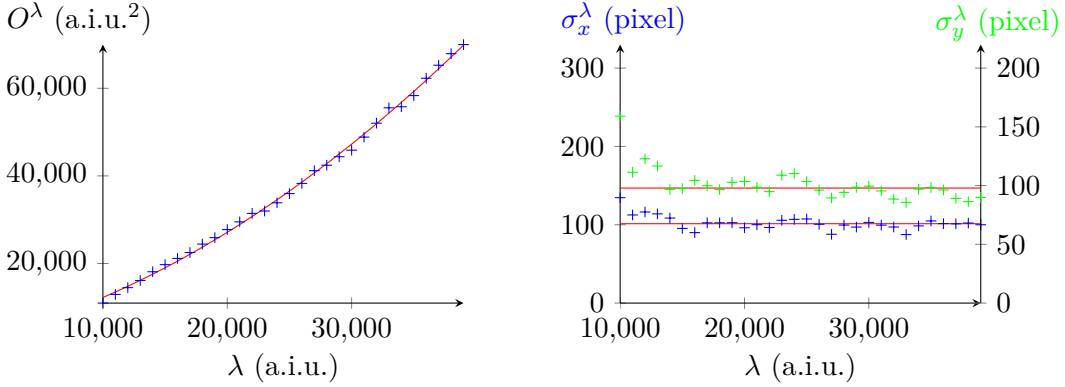
Figure 4.8 plots (in red) our predicted noise map described by (4.15) for a given intensity value λ on each location of the image. The blue spots correspond to the set $\{\operatorname{Var}[I(\mathbf{x})] | x \in \Omega_\lambda\}$ of measured noise variances computed from the reference stack with $\lambda = 20000$ and $\epsilon = 10$. Table 4.1 gives the performances of the correction term that reduce the average RMSE by a factor 2 while compared with the theoretical model.

We evaluate this estimation procedure in the next section.



(a) The estimated amplitude for each intensity level λ follows the theoretical ICCD noise model.

(b) Even though estimated independently the centers of our deformation model show a strictly stationary distribution.



(c) The deformation offset also conforms with ICCD quadratic model.

(d) The sigma estimation highlights a more correlated output, this is due to our Gaussian approximation.

Figure 4.7: Global parameter estimation from a wide-field FD FLIM sequence.

	Quadratic model	Our model
$\ \widehat{\text{Var}}[I(\mathbf{x})] - \text{Var}[I(\mathbf{x})]\ $	63039	27259

Table 4.1: Mean RMSE between the predicted variance and the measured variance from five experimental reference stacks using confocal and wide-field setups.

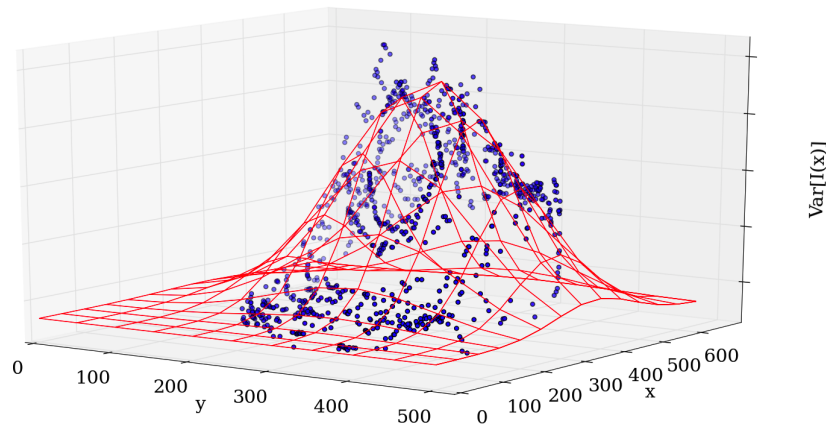


Figure 4.8: Variance prediction with added correction (red: noise variance model; blue: measured noise variance).

4.3 Application to parameter estimation in FD FLIM imaging

In this Section, we propose to exploit the noise modeling to improve static sample lifetime estimation and to adaptively reduce noise in images.

Most of state-of-the-art algorithms used for parameters estimation in photon-limited imaging rely on variance stabilization to transform the heteroscedastic noise footprint into a stationary Gaussian process. The main methods are dedicated to image denoising [Makitalo and Foi, 2013; Dabov et al., 2007; Boulanger et al., 2010; Spring and Clegg, 2009]. When the parameter of interest is not the intensity value, denoising is considered as a pre-processing step before parameter estimation such as particle localization [Smal et al., 2010] or fluorescence lifetime estimation in FD FLIM [Spring and Clegg, 2009].

Denoising techniques that use Variance Stabilization Transform (VST) present two issues. First the process of VST, denoising and inverse VST requires *ad-hoc* assumption on the image statistics and the quality of the denoising. In [Makitalo and Foi, 2013] the residual error is supposed to be symmetric and unimodal in order to control the inverse Anscombe transform bias. In [Spring and Clegg, 2009], variance stabilization is also applied but the denoising error is neglected leading to a biased inversed transform. Secondly, if those techniques can efficiently reduce the noise before parameter estimation [Spring and Clegg, 2009], non-stationarity of the noise can still be present during estimation and will not be taken into account in a homoscedastic regression procedure.

In this section, we apply our noise modeling to enhance the estimation of two parameters described by FD FLIM measurement without the use of variance stabilization transform. We first focus on the main objective of this work by estimating fluorescence lifetime using a weighted least squares estimator. We then apply the heteroscedastic noise modeling for

image denoising. We first combine our noise model to the well-known Wiener filtering. We compare the performances with an assumed constant variance model estimated over the whole image support. We then propose a more sophisticated patch-based *Gamma NL-means* denoising method. In this approach, the noise model is exploited to normalize the inter-patch distances. The empirical distribution of distances is approximated by a Gamma distribution to cope with non-Gaussian noise and overlapping patches.

4.3.1 Background lifetime estimation

4.3.1.1 Weighted least squares estimator

Due to the high number of photons on the ICCD output we can model the Poisson-Gaussian noise as a locally Gaussian process with variance $\text{Var}[I(k)(x)]$. Thanks to the model derived and tested above, we can weight the residuals of the phase least squares estimator with the locally estimated standard deviation to cope with non-stationary noise. Accordingly, the background lifetime parameters are estimated by minimizing the following least mean squares criterion:

$$\hat{\theta}_b = \underset{\theta_b}{\operatorname{argmin}} \sum_{k=1}^K \frac{(I(k)(\mathbf{x}) - S_{\theta_b}(k)(\mathbf{x}))^2}{\text{Var}[I(k)(\mathbf{x})]} \quad (4.15)$$

where $\text{Var}[I(k)(\mathbf{x})]$ is given by (9.38) at frame k and pixel \mathbf{x} .

4.3.1.2 Phase estimation on a reference FD FLIM measurement

Figure 4.9 shows the phase distribution estimated on a FD FLIM acquisition of a sample of fluorescein presenting a single fluorescence lifetime that is constant throughout the sample. As a result, a single mode is expected for the estimated phase distribution. The fluorescence sample has been acquired with a wide-field setup with a third generation intensifier from Lambert Instruments (model II18MD) (see Figure 4.3.a). On this graph, we compared the Fourier decomposition used in the literature (or equivalently, the least mean squares estimator) and our heteroscedastic modeling approach. Those results highlights the significant shift caused by the weighting of least squares residuals. Also, our correction results in a 10% gain in kurtosis which is expected for a plain fluorescein sample [Spring and Clegg, 2009].

4.3.1.3 Lifetime estimation on a control experimental sample

Figure 4.10 presents the lifetime distribution estimated on an epithelial cell membrane (RPE1) using the Fourier decomposition and our weighted least squares method on a control sample. Experimental data are a subset of the acquisition carried out in the context of the experiment described Chapter 6. In this experiment, receptors on

the membrane and early endosomes are tagged with GFP in the absence of a donor. Experiments were conducted using a confocal microscope with spinning disk setup and the same intensifier as above (UMR 144 CNRS-PICT Institut Curie).

Our method estimates a narrower distribution, highlighting a standard deviation 0.27 ns while the Fourier decomposition estimates a standard decomposition of 0.48 ns. It is hard to assess the quality of a lifetime distribution in experimental conditions. However, the sample under study cannot present any transfer of energy and should thus present a single lifetime distribution. It follows that a narrow lifetime distribution with a single mode is expected by experts.

4.3.2 Application to FD FLIM measurement denoising

We tested our modeling approach by comparing two denoising methods. We tested those methods on a living epithelial cell image acquired in FD FLIM coupled with a confocal setup. Figure 4.11.a depicts the sample presenting fluorescently tagged caveolin proteins. This image presents the lowest SNR value in the FD FLIM measurement since its average intensity is the lowest among all the K frames.

4.3.2.1 Wiener filtering

First, we applied a spatial Wiener filter to highlight the advantages of a spatially varying intensity-dependent noise model. Let $m(I(\mathbf{x})) \in \mathbb{R}$ and $s(I(\mathbf{x}))^2 \in \mathbb{R}$ be respectively the mean and variance estimated locally over a 3×3 pixels square window centered at pixel \mathbf{x} . The denoised image $\hat{I}(\mathbf{x})$ at location x is given by [Lee, 1981]:

$$\hat{I}(x) = m(I(\mathbf{x})) + \frac{s(I(\mathbf{x}))^2}{s(I(\mathbf{x}))^2 + \sigma^2} (I(\mathbf{x}) - m(I(\mathbf{x}))) \quad (4.16)$$

where σ^2 is the noise variance to be estimated. Figure 4.11.b shows the effect of the Wiener filter using an assumed constant noise variance. We used the least-trimmed squares variance estimate computed from image pseudo-residuals. Figure 4.11.c highlights the use of our noise model $\sigma^2 = \text{Var}[I(x)]$. We can see that the stationary estimation results in noisy artifacts around bright spots. The spatially varying noise variance model combined with Wiener filtering overcomes these issues.

4.3.2.2 Gamma NL-means filter

We considered also more sophisticated denoisers and one of the most recent examples is the patch-based *NL-means filter* [Buades et al., 2005]. The denoised intensity of a given pixel is obtained with the weighted average of the intensities of all pixels in the image. The weights are proportional to the similarities between local neighborhoods (or patches) and the central patch to be restored. We briefly describe in this Section a new approach based on the same principle, more detail can be found in Appendix B.

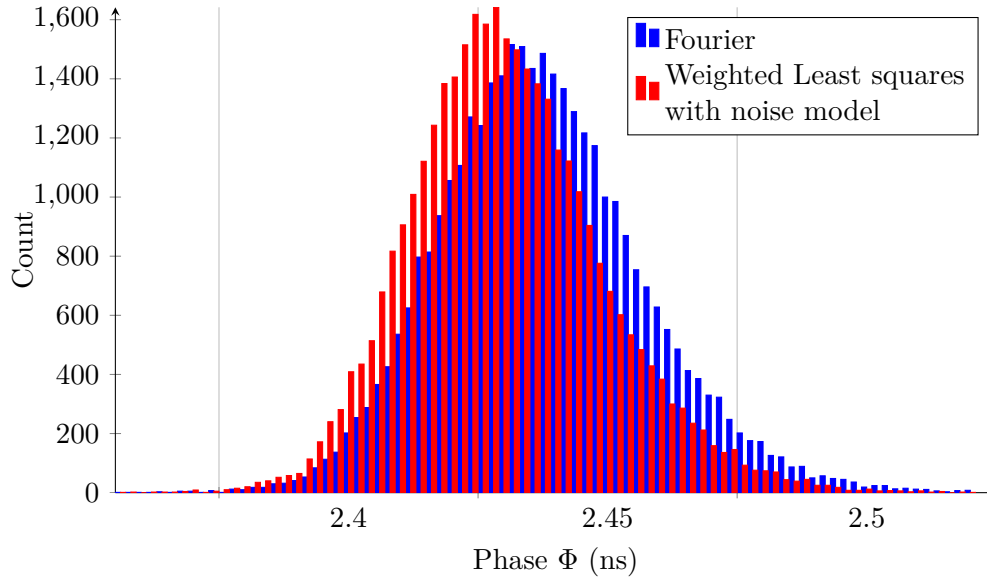


Figure 4.9: Phase histograms using the Fourier method and the weighted least squares method exploiting the estimated noise scale on a reference FD FLIM measurement of a plain fluorescein sample (see Figure 4.3.a).

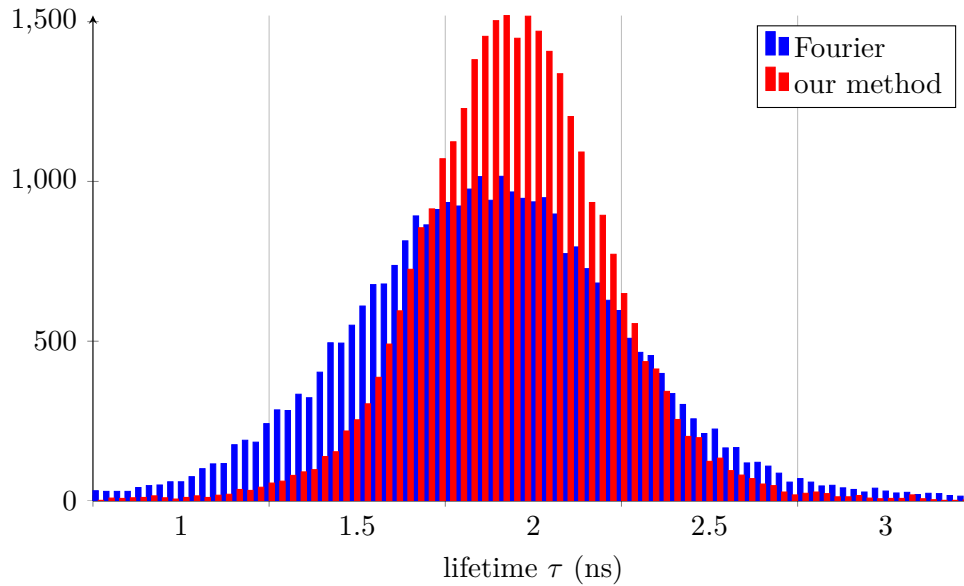
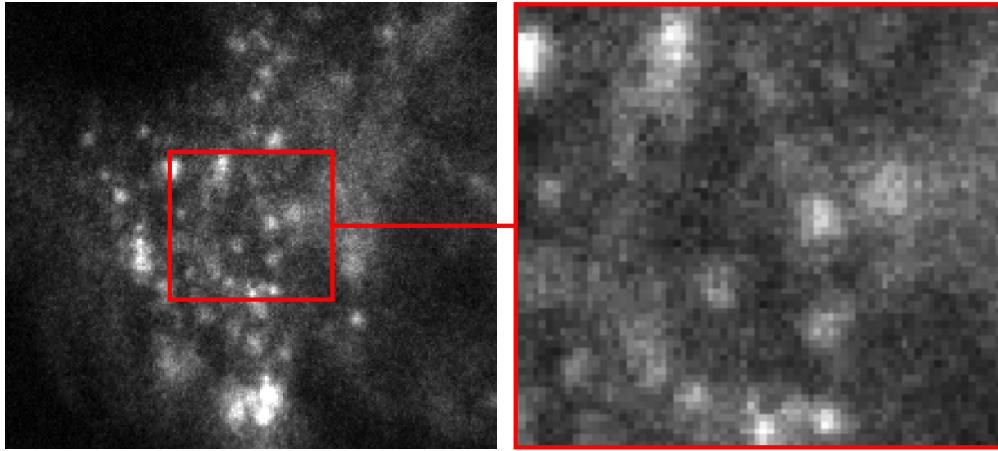
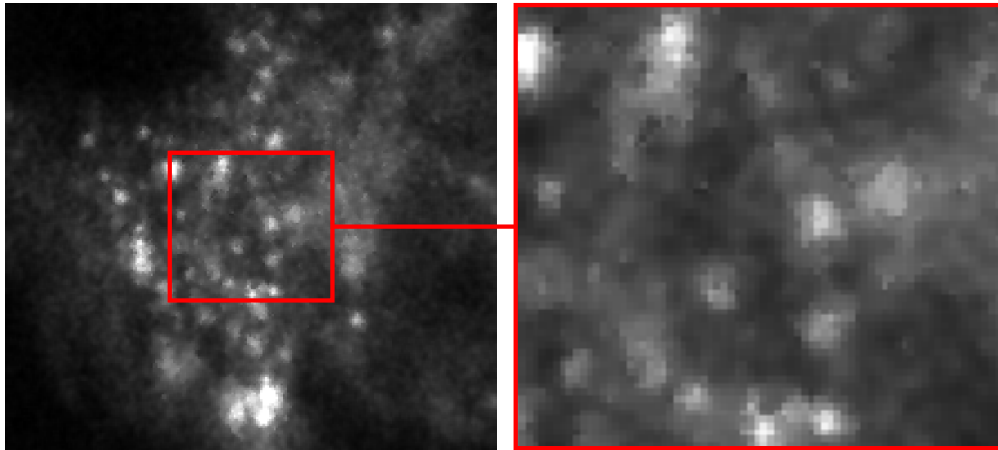


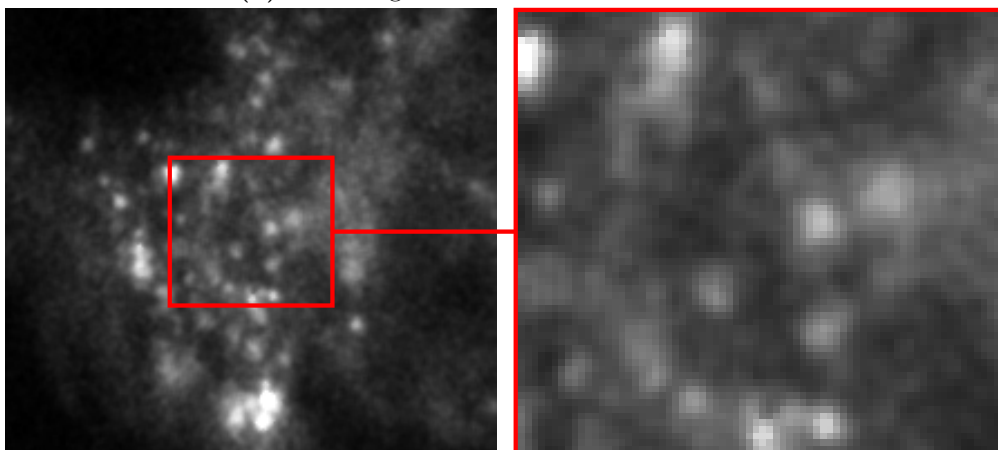
Figure 4.10: Lifetime histograms on the whole image control cells with GFP tagged receptor in live cell RPE1.



(a) Original FD FLIM image.



(b) Denoising with a constant noise variance.



(c) Denoising with the spatially adaptive noise variance.

Figure 4.11: Wiener filtering using the constant and spatially adaptive noise variances.

Based on the Bayesian framework presented in [Kervrann et al., 2007], we propose to investigate a more powerful method able to better capture patch-based distance statistics. We introduce an Approximate Bayesian Computing approach for the selection of “simulated” patches in the image (see Appendix B). In the patch selection step, the Euclidean distance is used to calculate the error between “simulated” and “observed” patches. We further use this patch collection to refine the distance function as in [Kervrann et al., 2007]. In this work, the authors modified the usual Euclidean distance used for patch comparison, yielding a filter which is better parametrized and with a higher performance. They assumed the normalized distance between $\sqrt{n} \times \sqrt{n}$ patches to follow a chi-square distribution with n degrees of freedom. However, the chi-square distribution is mainly valid for white Gaussian noise and non-overlapping patch pairs. Accordingly, we propose a more general distribution to extend the chi-square distribution which is the Gamma distribution as suggested in [Kervrann, 2010]. The resulting *Gamma NL-means filter* is given by the following expression:

$$\hat{I}_{GNL}(\mathbf{x}) = \frac{\sum_{\mathbf{y} \sim U_r(\mathbf{x})} \left(\frac{\|S_I(\mathbf{y}) - S_I(\mathbf{x})\|^2}{2 \text{Var}[I(\mathbf{x})]} \right)^{k-1} e^{-\frac{\|S_I(\mathbf{y}) - S_I(\mathbf{x})\|^2}{2\beta \text{Var}[I(\mathbf{x})]}} I(\mathbf{y})}{\sum_{\mathbf{y} \sim U_r(\mathbf{x})} \left(\frac{\|S_I(\mathbf{y}) - S_I(\mathbf{x})\|^2}{2 \text{Var}[I(\mathbf{x})]} \right)^{k-1} e^{-\frac{\|S_I(\mathbf{y}) - S_I(\mathbf{x})\|^2}{2\beta \text{Var}[I(\mathbf{x})]}}} \quad (4.17)$$

where the set of variables $\mathbf{y} \sim U_r(\mathbf{x})$ in the sum are uniformly drawn from a ball of radius r . The proposed noise variance model is incorporated to normalize the inter-patch distance. The parameters k and β controlling the Gamma distribution are estimated by using the moment method given a large set of normalized distances computed from pairs of patches in the noisy input image. A typical result of the performance of the patch-based filter ($r = 7$ pixels and 7×7 patches) is presented in Figure 4.12d.

This filter has been compared to state-of-the-art denoising algorithm tailored for Poisson-Gaussian noise. We first denoised our images using BM3D [Dabov et al., 2007] after a General Anscombe transform for variance stabilization assuming a mixed Poisson-Gaussian noise. Before applying BM3D, we use the exact unbiased inverse stabilization transform described in [Makitalo and Foi, 2013]. Since ICCD is not addressed by these authors, these methods suppose a linear dependency between local intensity and noise variance. As plotted in Figure 4.7, the linear model is a good approximation on the considered intensified sequence. We also filtered our images with ND-SAFIR [Boulanger et al., 2010] where the Poisson-Gaussian noise variance is estimated and also used to weight down the inter-patch distance in recent versions.

Compared to our filter, BM3D has not a significant impact on the resulting image; we plan to take spatial dependency into account in the BM3D noise variance model. ND-SAFIR performs better but creates piecewise constant areas contrary to the proposed *Gamma NL-means filter*.

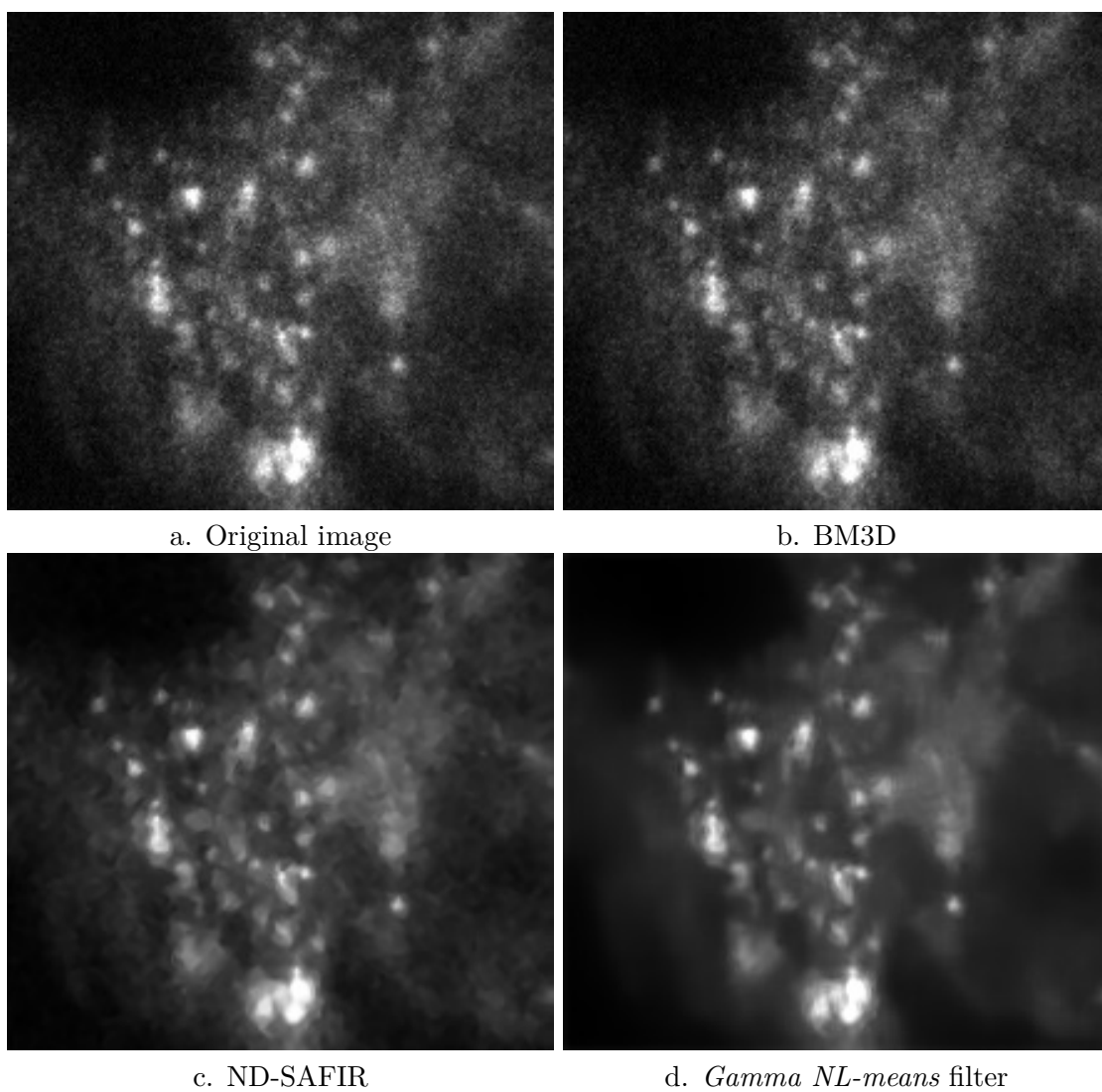


Figure 4.12: Comparisons of several denoising algorithms.

5 Fluorescence lifetime estimation on moving endosomes in FD FLIM

One of the advantage of FD FLIM over time domain techniques is the speed of operation that puts time lapse measurements of fluorescence lifetime on dynamic sample within reach. However, in the conventional methods presented in Section 3.2.2 as well as the approach proposed above, the fluorescent objects are supposed to be static. If a FD FLIM measurement can be acquired in tenth of milliseconds [Lajevardipour and Clayton, 2013; P. C. Schneider, 1997; Holub et al., 2001], intracellular processes can present a wide range of time scales, from the microsecond down to the nanoseconds [Tinoco and Gonzalez, 2011]. As a result, motions can occur on living cells during the phase modulation. Figure 5.1 shows the impact of motions on the phase estimation. The lifetime mis-estimation results in a so-called doppler effect on the lifetime map as illustrated in Figure 5.2. The issue has been previously diagnosed in [Hanley et al., 2001] and further analyzed in [Lajevardipour and Clayton, 2013] where the impact of moving particle on lifetime variance is measured. However, to our knowledge, no method has been proposed to estimate the fluorescence lifetime on those moving structures.

In the context of an on-going biological experiment (see Chapter 6) we are interested in the measurement of FRET efficiency at the membrane and on the early endosomes. In this section, we thus propose a statistical framework for robust lifetime estimation on moving endosomes in order to provide a corrected reconstruction of the lifetime map. To alleviate complexity while taking into account the correlation of parameters, we propose an iterative estimation procedure where the estimation of lifetime parameter and the movement parameter are decoupled. The proposed method need only two, non-critical, input parameters : an upper-bound for the object number and the diffracted endosome size in pixel (7×7 is a typical choice, scale may vary on microscope magnification).

The remainder of this chapter is organized as follows. The intensity model for the dynamical endosome is first laid out in Section 5.1. The joint estimator is then presented in Section 5.2, first the iterative aspect, followed the by object detection and tracking for initialization. Finally in Section 5.3, we test our method on simple simulation and experimental sequences. As their can be no ground truth for fluorescence lifetime of a few endosomes in experimental sequence, we compared the motion compensation aspect of our method with two competing algorithms chosen because they share common methodologies.

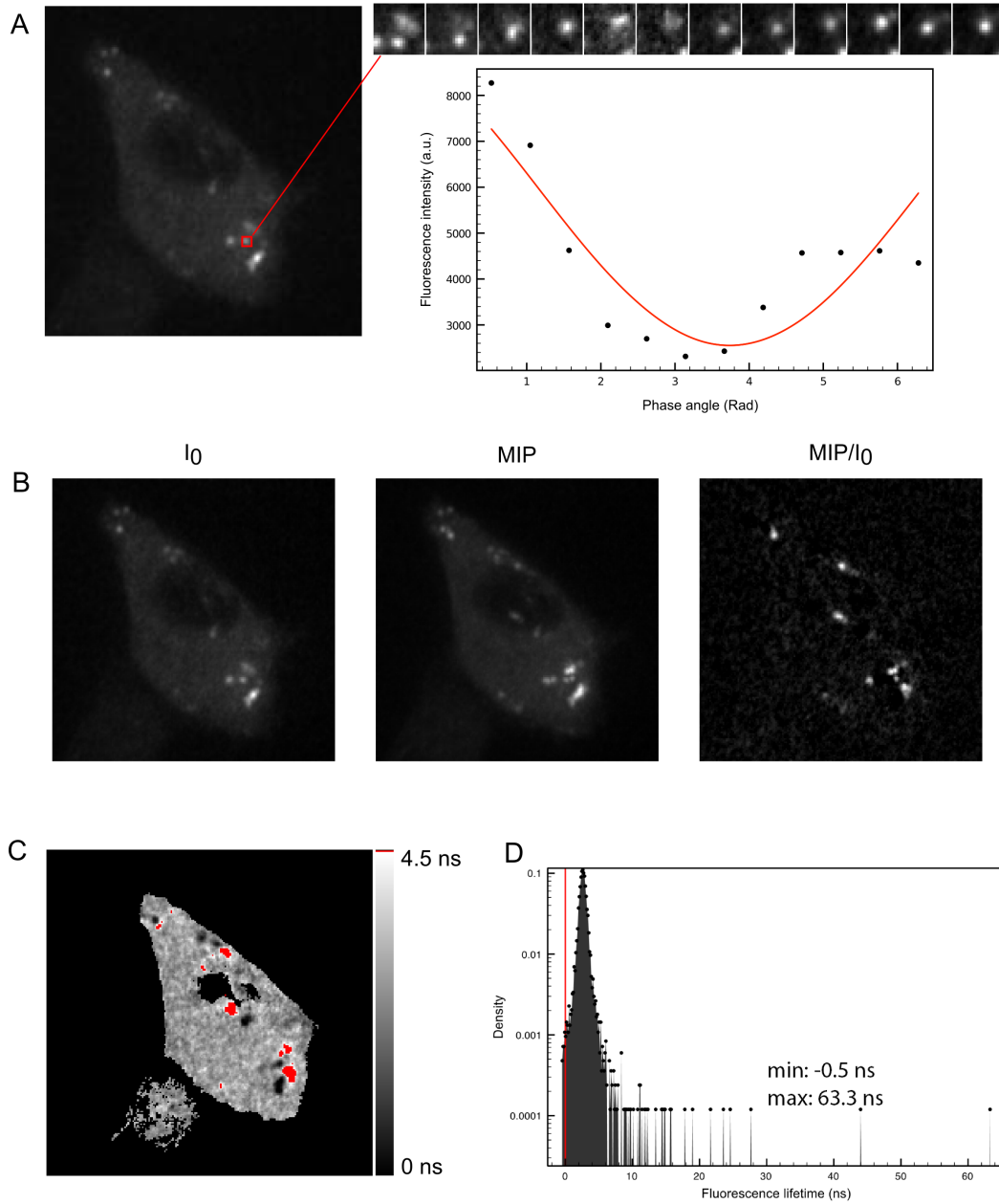


Figure 5.1: Visualization of sub-cellular structure motions during image acquisition and effect on the FLIM images. A: Example of image sequence with moving sub-structures (shown as series of zoomed thumbnails) and of modulation signal S_θ with sine fitting in red. B: Global estimation of motion by maximum intensity projections (MIP) and ratio with initial intensity I_0 (right). C: Reconstructed lifetime image showing outliers in red. D: Distribution of lifetime values in the reconstructed lifetime map in C. showing extreme, non physical (negative or too high) values.

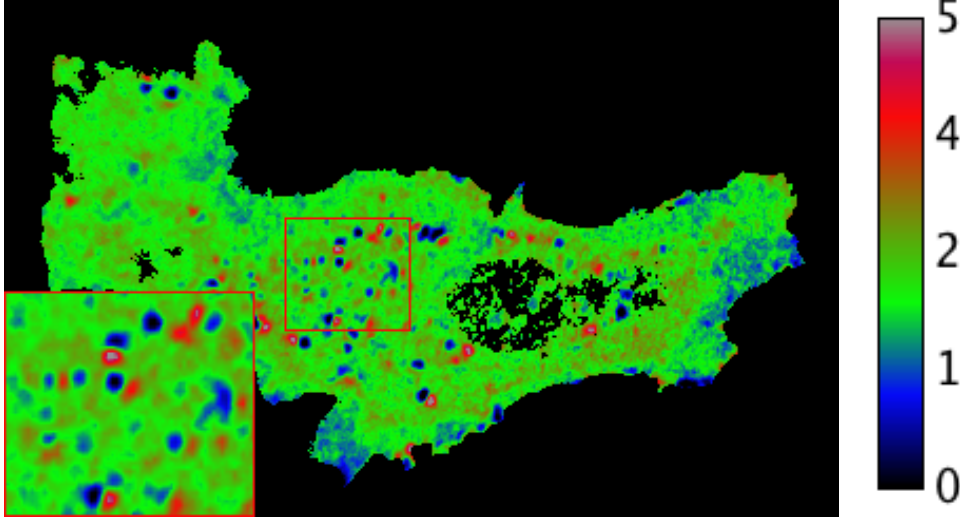


Figure 5.2: “Doppler effect” on lifetime measurement (in nanoseconds) due to motion (see Figure 3.7).

5.1 Modeling spatial and temporal variations

In order to model the lifetime of a moving particle, we propose a parametrization of both spatial and temporal intensity variations of a sub-resolved object. In our approach the microscope point spread function (PSF), corresponding to a Bessel function, is approximated as a Gaussian function as it is a common practice in spot detection literature [Smal et al., 2010]. Secondly, as the confocal equipment is not rigorously stigmatic the signal is composed of a background and a pinpoint vesicle before microscope diffraction. The background follows the model (9.34) due to the membrane imaging and/or cytoplasmic fluorescence. Finally, the background is assumed to be smooth over the PSF support.

More formally, let $I(k)(\mathbf{x})$ be the intensity on frame k at location $\mathbf{x} \in \Omega$ (pixel grid), we have:

$$\begin{aligned} I(k)(\mathbf{x}) &= S_{\theta_b}(k)(\mathbf{x}) + S_{\theta_0}(k)G_\gamma(\mathbf{x} - \mathbf{x}_0(k)) + \varepsilon(k)(\mathbf{x}) \\ &= S_{\theta_b}(k)(\mathbf{x}) + \left[C_{S_0} + A_{S_0} \cos\left(\frac{2\pi k}{K} + \Phi_{\tau_0}\right) \right] G_\gamma(\mathbf{x} - \mathbf{x}_0(k)) + \varepsilon(k)(\mathbf{x}) \end{aligned} \quad (5.1)$$

where $S_{\theta_0}(k)$ is the vesicle mean intensity parametrized by $\theta_0 = (C_{S_0}, A_{S_0}, \Phi_{\tau_0})^T$ as in (9.34), $S_{\theta_b}(k)(x)$ is the spatially varying background signal parametrized by $\theta_b(\mathbf{x}) = (C_{S_b}(x), A_{S_b}(\mathbf{x}), \Phi_{\tau_b}(\mathbf{x}))^T$, $G_\gamma(\mathbf{x})$ is a Gaussian function of variance γ^2 describing the shape of the vesicles and centered on the origin, $\mathbf{x}_0(k)$ is the vesicle location on frame k , ε is the noise introduced by the ICCD noise, described in Chapter 4.

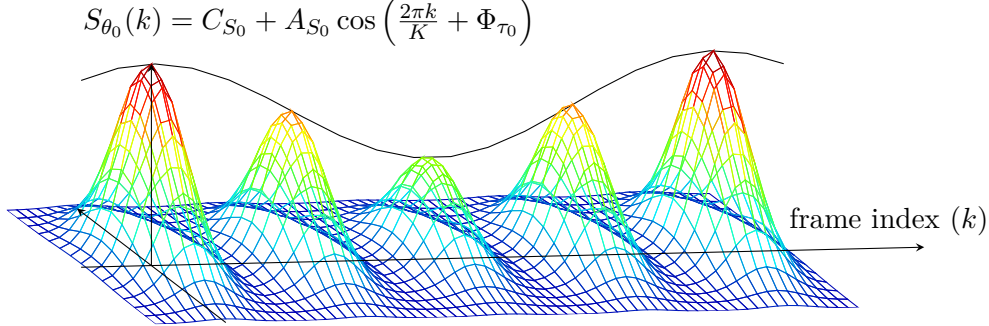


Figure 5.3: Moving vesicle model.

5.2 Vesicle parameter estimation

This section presents the estimation procedure of the decay time τ_0 for each detected vesicle. In this procedure, the vesicle location $\mathbf{x}_0(k)$ and shape γ and the lifetime parameter vector θ_0 are jointly estimated. This optimization problem is implemented by successive and alternative minimization of criteria with respect to $(\mathbf{x}_0(k), \gamma)$ and to θ_0 until $|\frac{\theta_0^n - \theta_0^{n+1}}{\theta_0^n}| \leq \delta$ with n the iteration number and δ a constant (set to 10^{-6} in our experiments). Our algorithm is illustrated in Figure 5.4 for the sake of clarity.

5.2.1 Iterative minimization procedure

5.2.1.1 Sinusoid parameter prediction

Given a collection of displacements $\hat{\mathbf{x}}_0^n(k)$ and a scale γ^n for a vesicle at iteration n of our algorithm. The parameter vector θ_0 controlling the sinusoidal signal is estimated by minimizing a weighted least squares criterion similar to (4.15). At iteration n , we have:

$$\hat{\theta}_0^n = \underset{\theta_0}{\operatorname{argmin}} \sum_{k \in [1, K]} \sum_{\mathbf{x} \in W(\hat{\mathbf{x}}_0^n(k))} \frac{(I(k)(\mathbf{x}) - S_{\theta_0}(k)G_{\gamma^n}(\mathbf{x} - \hat{\mathbf{x}}_0^n(k)))^2}{\operatorname{Var}[I(k)(\mathbf{x})]} \quad (5.2)$$

where $W(\hat{\mathbf{x}}_0^n(k))$ is a 7×7 window centered at $\hat{\mathbf{x}}_0^n(k)$. At each iteration, lifetime parameters θ_0 are initialized as follows :

- C_{S_0} takes the mean of the set $\left\{ \frac{I(k)(\mathbf{x})}{G_{\gamma^n}(\mathbf{x} - \hat{\mathbf{x}}_0^n(k))} \right\}_{k \in [1, K], \mathbf{x} \in W(\hat{\mathbf{x}}_0^n(k))}$
- $A_{S_0}^n$ takes the maximum value of the set $\left\{ \frac{I(k)(\mathbf{x})}{G_{\gamma^n}(\mathbf{x} - \hat{\mathbf{x}}_0^n(k))} \right\}_{k \in [1, K], \mathbf{x} \in W(\hat{\mathbf{x}}_0^n(k))}$
- $\Phi_{\tau_0}^n = \Phi_{M_0} - \Phi_E + \arctan(\omega_E \tau_{EGFP})$ where τ_{EGFP} is the fluorophore lifetime measured without FRET (e.g. 2.5 ns for the EGFP) and $(\Phi_{M_0} - \Phi_E)$ is obtained by calibration.

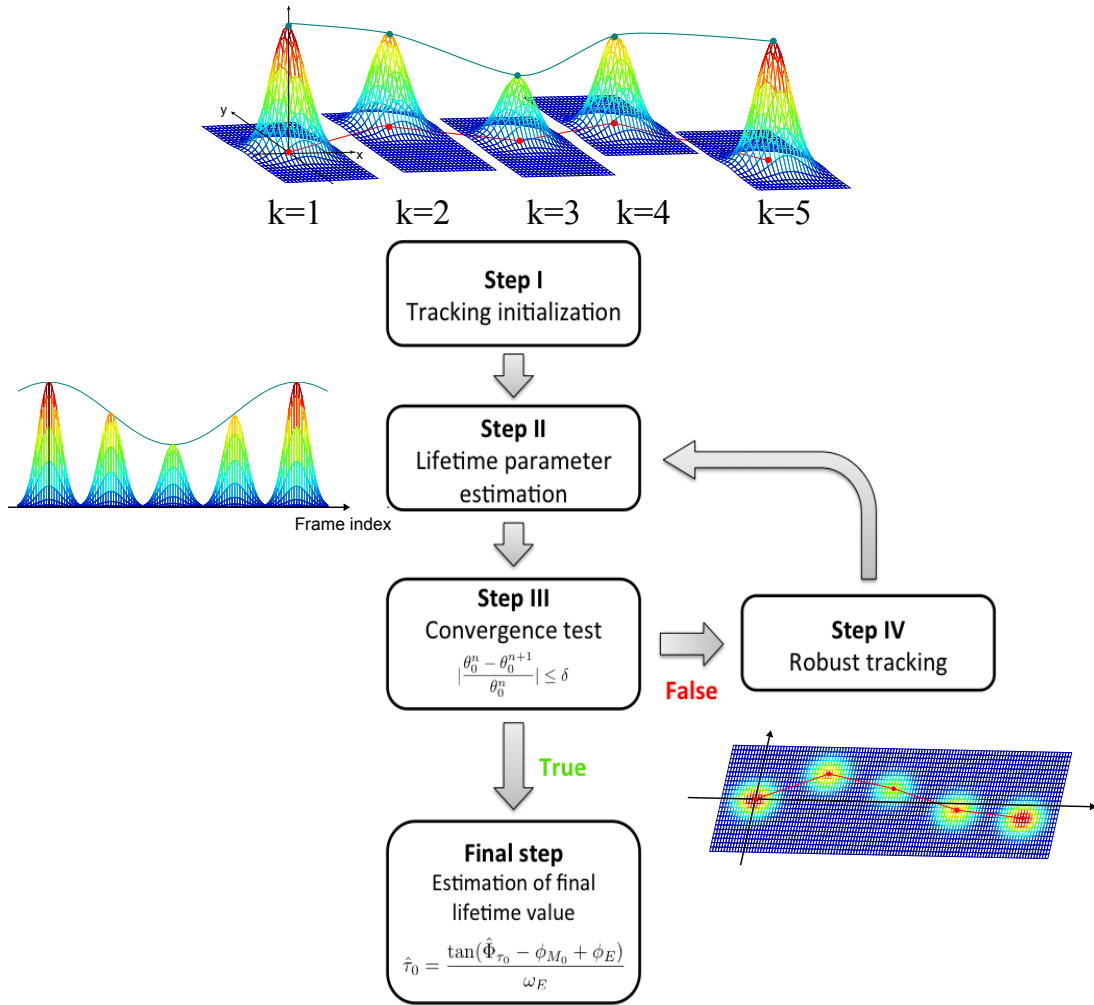


Figure 5.4: Iterative and alternative procedure for fluorescence lifetime estimation on moving endosomes.

5.2.1.2 Robust local motion estimation

At iteration $n + 1$ of the algorithm, the motion parameters $\mathbf{x}_0^{n+1}(k)$ are estimated for each vesicle over the K frames given the parameter $\hat{\theta}_0^n$ controlling the sinusoidal. Tracking is performed frame-by-frame by minimizing a robust error function:

$$(\hat{\mathbf{x}}_0^{n+1}(k), \hat{\gamma}^{n+1}) = \underset{(\mathbf{x}_0(k), \gamma)}{\operatorname{argmin}} \sum_{\mathbf{x} \in W(x_0(k))} \rho_\eta \left(I(k)(\mathbf{x}) - S_{\hat{\theta}_0^n}(k) G_\gamma(\mathbf{x} - \mathbf{x}_0(k)) \right).$$

The function ρ is a influence function chosen along a scale parameter $\eta = \lambda \sigma_{res}(k)$ in order to weight down outliers during the minimization process. Experiments show that the Leclerc's influence function defined as $\rho_\eta(r) = 1 - e^{-r^2/\eta^2}$ gives more stable results even if no significant difference is noticeable with other M-estimators (e.g. Tukey Bi-weighted or German-McClure). The scale parameter $\sigma_{res}(k)$ is defined for each frame as [Rousseeuw et al. \[1987\]](#):

$$\sigma_{res}(k) = 1.4826 \frac{\operatorname{median}_{i \in [1, |W(\hat{x}_0(k))|]} |r_i - \operatorname{median}_{i \in [1, |W(\hat{x}_0(k))|]} r_i|}{|W(\hat{x}_0(k))|} \quad (5.3)$$

where $\{r_i\}_{i \in [1, |W(\hat{x}_0(k))|]}$ is the set of residuals of estimation introduced in (9.8) when using the L^2 -norm as influence function which is equivalent to a least mean squares estimation. We note that the background is not taken into account in this Gaussian fitting. Indeed the motion estimator demonstrated better performances in very noisy conditions on real data without the background modeling, probably because of the reduced number of parameters. For each frame, the parameters estimation is initialized with the estimate on the previous frame i.e. $\gamma(k + 1) = \gamma^{n+1}(k)$, $\mathbf{x}_0(k + 1) = \hat{\mathbf{x}}_0^{n+1}(k)$ for $k \in [1, K - 1]$ and $\mathbf{x}_0(0) = \mathbf{x}_0^n(0)$, $\gamma(0) = \gamma^n(0)$ for the first frame.

5.2.2 Initialization

5.2.2.1 Object detection and initialization

Particles are detected on the first frame only using a two-step approach. First, pixels are classified as potential particle pixels using a gradient-based measure. The measure used in this study is based on the so-called structure tensor [\[Rao, 1990\]](#) or second-moment matrix, whose elements are estimated by convolving the image with the first derivative of the Gaussian kernel ($\sigma=1$ pixel). This can be done computationally very efficiently thanks to the separability of the Gaussian kernel. The tensor is integrated within a small window (typically 7×7 pixels) and the resulting smallest eigenvalue is used as classification measure. The N particle positions are selected as the pixels having the highest scores for the classification measure while respecting a distance of 7 pixels between these highest measures. Here, N represents a coarse overestimation of the expected number of particles set as a parameter of the algorithm. In the second step of the algorithm, the initially detected locations are further analyzed in order to discriminate between correct and

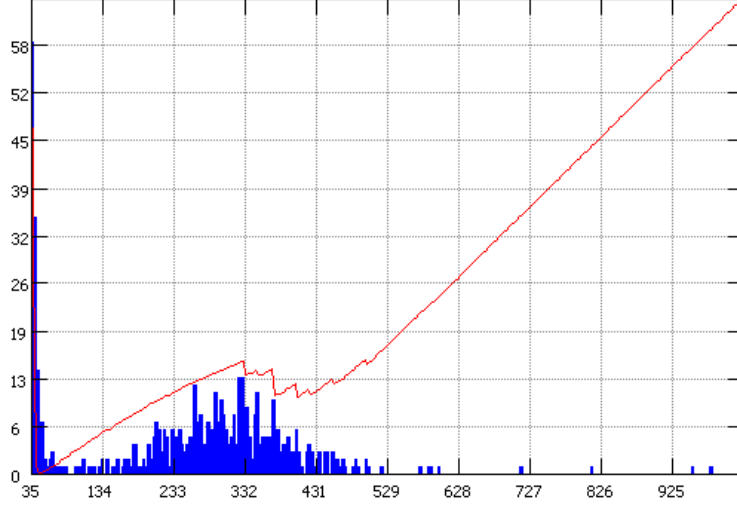


Figure 5.5: Matusita distance in red estimated on each bin of the histogram of the spot candidate scores.

spurious detections. This is done by computing the threshold that best separates the two populations in terms of their scores for the classification measure. The optimal threshold m is estimated from the histogram of the scores by minimizing the Matusita distance [Matusita, 1956]:

$$\hat{m} = \operatorname{argmin}_m \left(\sum_{i=m_{\min}}^m \left(\sqrt{H(i)} - \max_{k \in [m_{\min}, m]} \sqrt{H(k)} \right)^2 + \sum_{i=m}^{m_{\max}} \left(\sqrt{H(i)} - \max_{k \in [m, m_{\max}]} \sqrt{H(k)} \right)^2 \right) \quad (5.4)$$

Pixels with values above that threshold are taken as the true particle positions, up to pixel precision. A refinement of the detected particle positions is performed in the next stage.

5.2.2.2 Trajectory initialization

In order to initialize the iteration described in Section 5.2.1, each particle detected on the first frame is first tracked over the K frames of the FD FLIM measurement. This motion estimation is also carried out locally and without *a priori* on intensity variation. To do so, a local robust Gaussian fitting algorithm [Anderson et al., 1992] is applied to

estimate $\mathbf{x}_0^0(k)$ and γ^0 :

$$(\hat{\mathbf{x}}_0^0(k), \hat{\gamma}^0) = \underset{(\mathbf{x}_0(k), \gamma, a, b)}{\operatorname{argmin}} \sum_{\mathbf{x} \in W(\mathbf{x}_0(k))} \rho_\eta(I(k)(\mathbf{x}) - (aG_\gamma(\mathbf{x} - \mathbf{x}_0(k))) + b).$$

For each frame $k \in [1, K]$, the parameter estimation is initialized with the position and shape estimate on the previous frame, local background and local maximum for amplitude. For the first frame, positions are initialized with the position estimated using our spot detector.

We have been proposing this initialization method as a vesicle tracker for the particle tracking challenge organized by E. Meijering and J-C Olivo-Marin recently published in [Chenouard et al., 2014]. We took part in the vesicle scenario. Our algorithm is not a tracking method *per se* but a lifetime estimation that compensate for local motion. Accordingly, we did not expect our method to be able to compete with global methods that optimize the set of associations between particles previously detected on each frame (see Part II). However, thanks to our robust framework, our algorithm is ranked number 2 out of 14 methods in localization precision (RMSE on detected particle). The only notable difference of our approach on the detection aspect is the M-estimation and competing method that propose simple Gaussian fitting ranked lower.

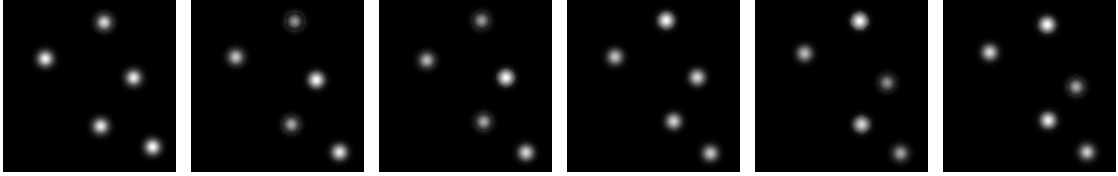
5.3 Lifetime map reconstruction results

A lifetime map corrupted by motion is reconstructed by estimating lifetime on the background (Section 4.3.1), and then imposing a patch of size $\hat{\gamma}$ and value $\hat{\tau}_0$ at location $\hat{x}_0(0)$ for each vesicle on the background lifetime map. As a particle motion produces artifacts on the whole trajectory, we propose a basic inpainting technique based on two-dimensional interpolation to fill the gap. We first illustrate our lifetime reconstruction and motion estimation on simple simulations, we then highlight our results on real samples.

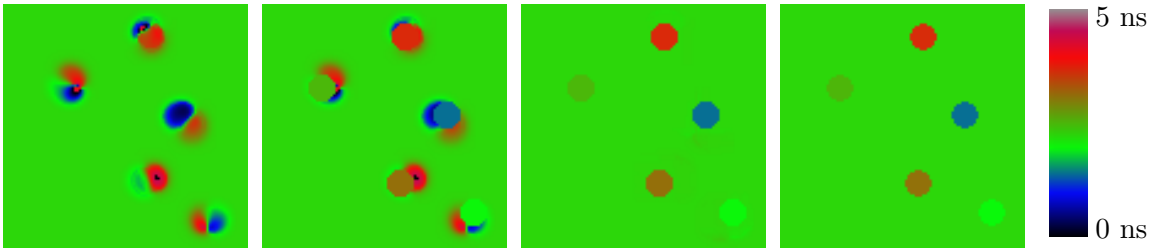
5.3.1 Lifetime map reconstruction on synthetic data

To illustrate the reconstruction of artifacts due to motion only, we applied our algorithm on simulations (see Figure 5.6) where the lifetime estimate is only affected by the vesicle motion without additional noise. The tracking is performed without issue, while parameter estimation takes 7 to 8 iterations to converge. The precision is about 10^{-6} after the first iteration, on this simple example and additional iterations are not necessary.

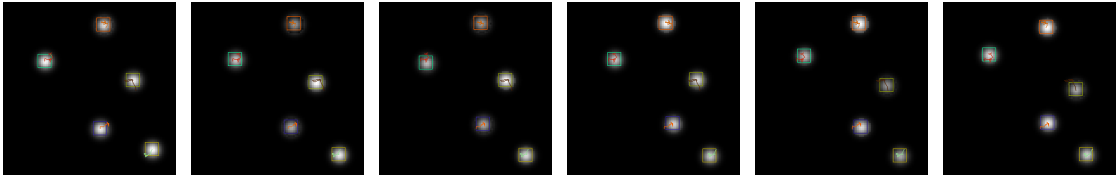
We tested the impact of our iterative approach on more challenging data. Those new simulations are based on our intensity model presented in Section 5.1 and the noise model presented in Section 4.2. Background is simulated with an experimental vesicle-free sample and cytoplasmic fluorescence is simulated in the background with constant parameter θ_b . Vesicle intensities follow (9.28) and motions are limited to a



(a) Simulated noise free FD FLIM measurement presenting 5 moving vesicles (6 frames out a 12 frames simulation). Each vesicle present a different lifetime and thus a difference phase delay in intensity. The differences in phase delay has been artificially increased for the purpose of illustration. The very high intensity gradient has been adapted for visualization purpose.



(b) Motion-induced artifacts. (c) lifetime τ estimated on each vesicle. (d) Basic inpainting. (e) Ground truth.



(f) Motion estimation results after our iterative process. Parameters converge after four to eight iterations.

Figure 5.6: Simulating motion impact on lifetime map and reconstruction. **a)** Simulated sequence with 5 vesicles exhibiting free Brownian motion modeled by a normal law for displacement with a standard deviation of 2 pixels (contrast has been enhanced for visualization). **b)** The estimated lifetime map on this FD FLIM measurement with the doppler effect footprint. **c)** Patches taking the value of the estimated fluorescence lifetime are added on the initial vesicle detection locus. The patch size is set to three times the size of the estimated spot scale **d)** A simple inpainting algorithm is applied to correct secondary artifacts for cosmetic purpose. **e)** True lifetime simulated on background and vesicles **f)** Motion estimation carried out during the iterative process.

Iteration n	0	1	2	3
Tracking mean error (pixel)	0.240	0.121	0.081	0.080
Lifetime mean error (ns)	0.387	0.248	0.247	0.247

Table 5.1: Convergence of tracking and lifetime errors is reached after 3 iterations on 30 simulated vesicles and 95 % of vesicle tracked.

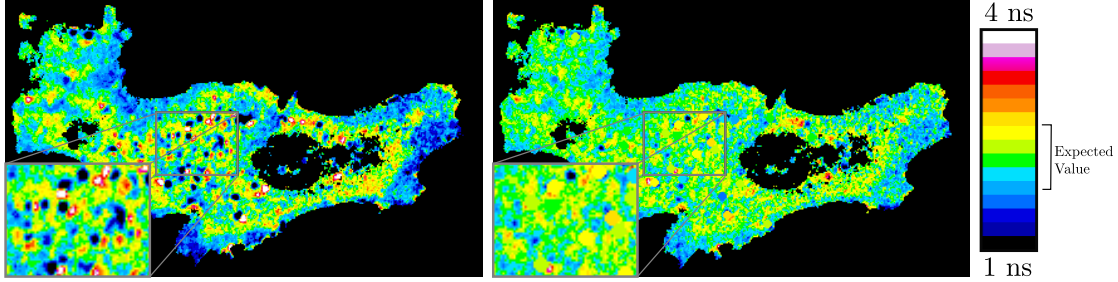


Figure 5.7: Left: Lifetime map using Fourier decomposition. Dark blue and red spots are unrealistic values due to organelle movements. Right: lifetime map reconstruction using our method.

two-pixel displacement. The non-stationary Gaussian noise parameters are estimated on the stack and then imposed on synthetic vesicles. Table 5.1 shows the convergence of lifetime and motion parameter on simulated vesicles.

5.3.2 Endosome tracking accuracy in experimental conditions

We tested our reconstruction on living epithelial cells presenting GFP-tagged receptors, acquisitions that are further described in Chapter 6. We highlight the result of our reconstruction method on experimental samples in Figure 5.7. However, it is very challenging to assess the precision of the estimated endosome fluorescence lifetime on experimental samples. Nevertheless, the lifetime parameter is closely related to the quality of the displacement estimate, and we can much easily measure the quality of motion tracking. To test our algorithm in experimental conditions, 30 moving spots localizing the GFP-tagged receptors have been imaged with our FD FLIM setup and manually tracked using the MJtrack software [Smal et al., 2010]. In order to highlight the effect of the proposed intensity modeling, we first compared the performances of our method against a frame-by-frame Gaussian fitting [Anderson et al., 1992]. This simple method reuses the estimated position on the previous frame as an initialization for spot fitting. In order to compare our approach with a more competitive method, we also tracked those vesicles with the probabilistic particle tracker described in [Genovesio et al., 2006] and implemented in the ICY software [de Chaumont et al., 2012]. This multiple particle tracking algorithm detects spots using an undecimated wavelet transform [Olivo-Marin, 2002] on each frame before building tracks frame-by-frame. For each frame pair, the correspondences between the two sets of detections are optimized thanks to Brownian

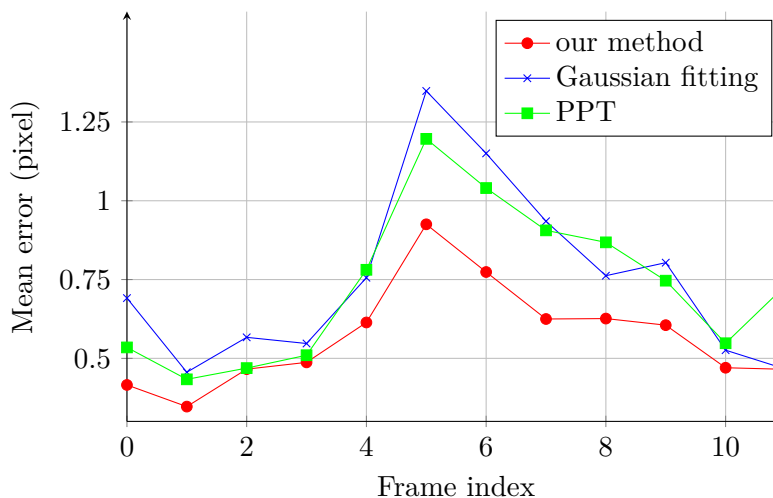


Figure 5.8: Mean localization error using Gaussian fitting [Anderson et al., 1992], Probabilistic particle tracking [Genovesio et al., 2006] and our method on fluorescently tagged RX protein in living epithelial cells. Endosomes have been tracked by hand using the MJtrack software [Smal et al., 2010].

motion modeling and combinatorial optimization. This method is extensively described and tested along other particle tracking techniques in Part II. To address the problem of intensity variations that we modeled in our method, images are normalized using the Midway equalization method described in [Angelini et al., 2007].

The detector proposed in [Olivo-Marin, 2002] cannot adapt to local changes of SNR. As a result, the lowest SNR images that are normalized by our histogram equalization present an higher number of detected objects due to noise artifacts. However, as particles are sparsely localized in our experimental data-set, the three compared algorithms manage to track the 30 particles on the entire stack of 12 frames. The mean localization errors are represented in Figure 5.8 and the tracking of our method is visually illustrated in Figure 5.9. As one could expect, the localization errors occur as the signal-to-noise ratio drops at lower intensities. Thanks to our thorough intensity modeling, our method presents a more precise spot localization throughout the whole sequence, a difference that intensifies on more noisy images.

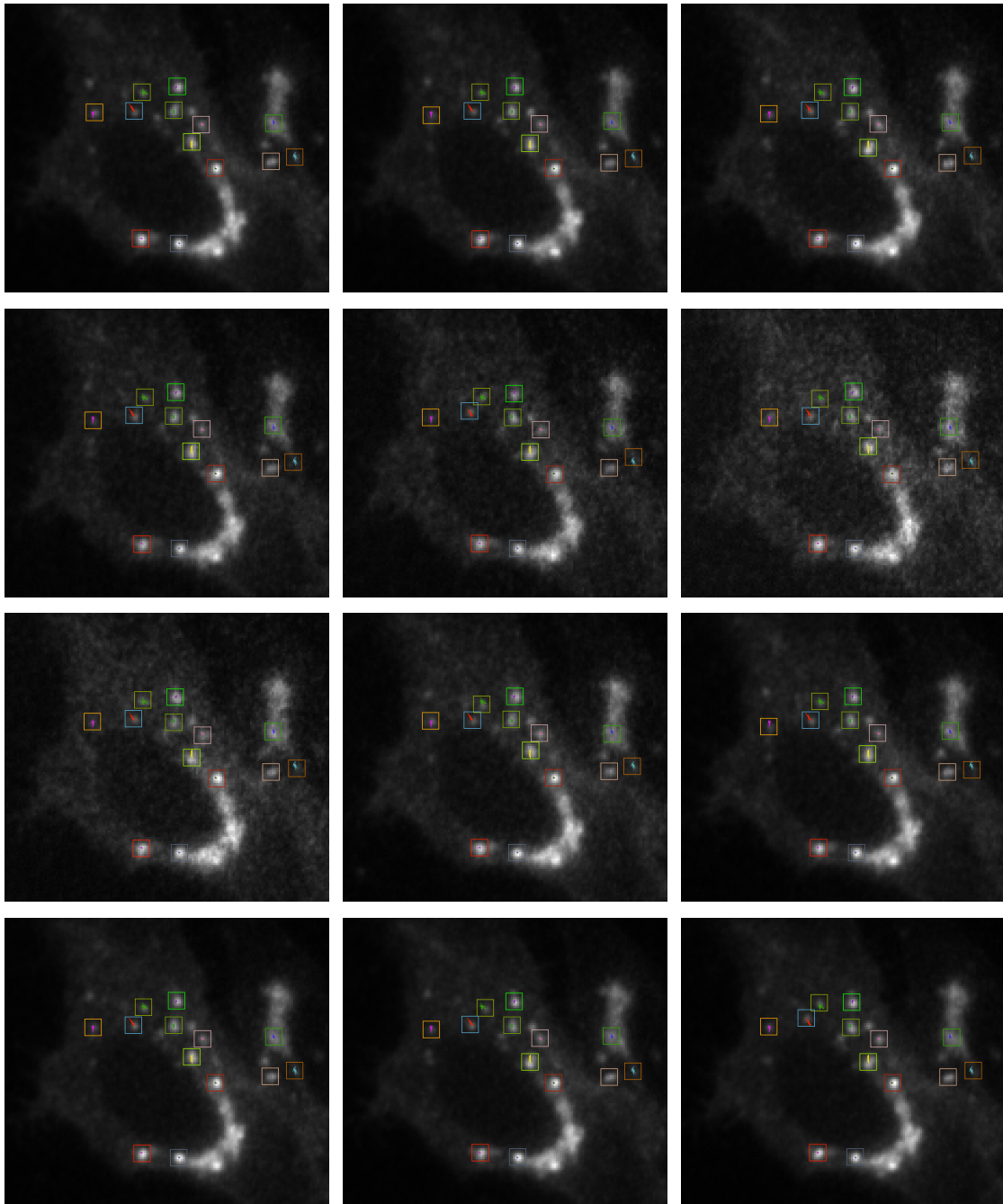


Figure 5.9: An example of GFP-tagged receptor tracking on a 12 frames stack (images have been normalized for visualization purpose). The data points presenting the highest localization error coincide with the noisier images presented in the second line.

6 Application to protein interaction analysis at the membrane and during endocytosis

Our collaborators in the Ludger Johannes' team at Institut Curie (UMR 144) are interested in the signaling pathways triggered by the cytokine CX¹ in eukaryotic cells. The trafficking of this protein at the membrane triggers a signaling cascade inside the cell that eventually end in the nucleus where it provokes the transcription of genes involved in major diseases. The first step of this signaling cascade is known to be the association between the cytokine receptor RX and its associated kinase KX. However, the spatiotemporal localization of this interaction remains to be understood. In an experiment set up by the Ludger Johannes' team, the interaction between CX and RX are measured at different locations in space and time: at the membrane, in the endocytotic transport pathway, before and after injection of the cytokine.

6.1 Data acquisition

The methodology recommended to test such interactions is the FRET measurement efficiency (see Section 2.2) between RX and KX. Thanks to our motion compensation method, we can measure lifetime loss on dynamical structures such as trafficking endosomes as well as at the membrane. To trigger the FRET phenomenon on protein proximity, the RX donor protein has been tagged with GFP and the acceptor KX has been tagged with mCherry at different tagging sites. Experiments were conducted on epithelial cells (RPE1) using a confocal microscope with spinning disk setup (UMR 144 CNRS-PICT Institut Curie). The sub-resolved spot that are localized outside of the cluttered recycling compartment are the endosome of interest and the membrane is described by the cell background. The intensifier is a third generation from Lambert Instruments (model III8MD).

FRET efficiency can only be measured using relative lifetime loss. To that end, lifetime efficiency has been measured on GFP-tagged RX protein alone. Then to test the spatiotemporal localization of the RX-KX interaction and the effect of the cytokine CX, lifetime has been measured on GFP-tagged RX protein in the presence of its

¹Due to editorial conflicts, the name of protein involved in this study has been changed and the biological background of this study cannot be laid out.

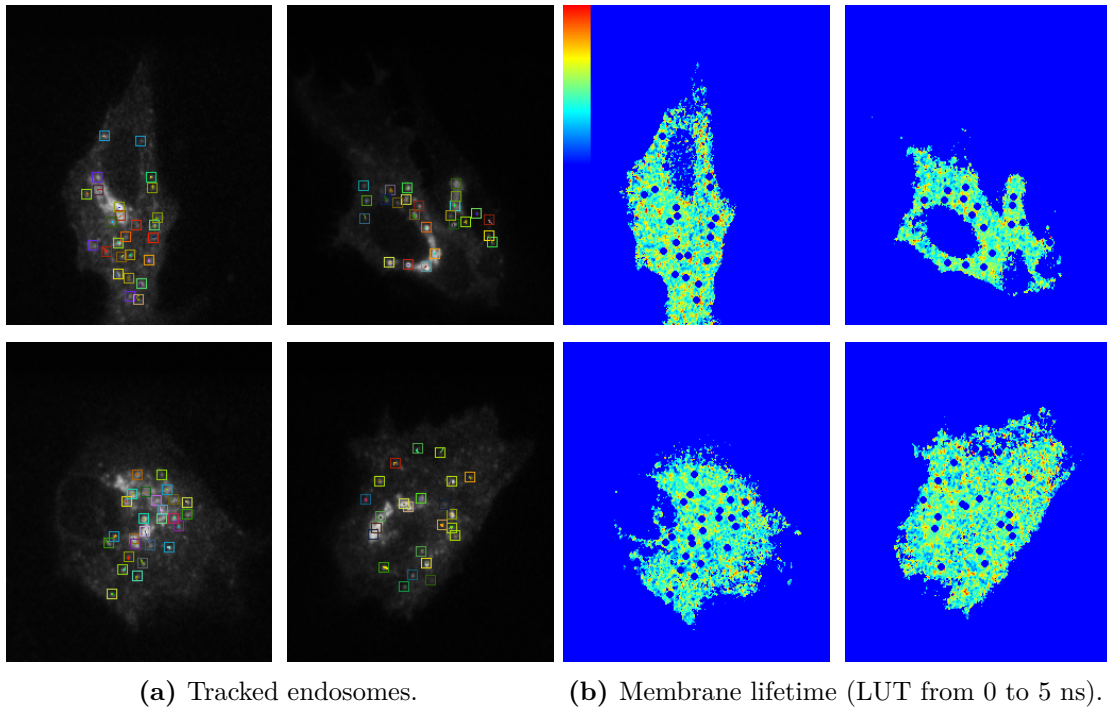


Figure 6.1: Tracked GFP-tagged RX on endosomes (left) and membrane lifetime map (right) in the absence of acceptor.

mCherry-tagged kinesin KX and the same donor-acceptor couple 15 minutes after CX treatment. In order to find the best tagging site for KX, the kinesin has been tagged on two different sites denoted mCherry-RX and RX-mCherry in what follows.

6.2 Data analysis

To differentiate the lifetime estimated on the early endosomes from the membrane, we exploit the lifetime estimated on tracked vesicles for the former and we automatically segment the cell background for the latter (see Figure 6.1). A summary of the lifetime measurement on the resulting five experiments is presented in Figure 6.2. The first conclusion we can draw is that the chosen site for tagging may have an impact on FRET efficiency. Indeed, both experiments in the mCherry-RX configuration show an higher lifetime loss.

As we could expect, adding an acceptor by tagging KX with mCherry results in a drop in measured lifetime across the whole cell. However, we also wish to probe if the FRET phenomena is more prominent on the membrane or the endosomes. In order to cope with inter-cellular variations, we have been measuring the differences between the mean

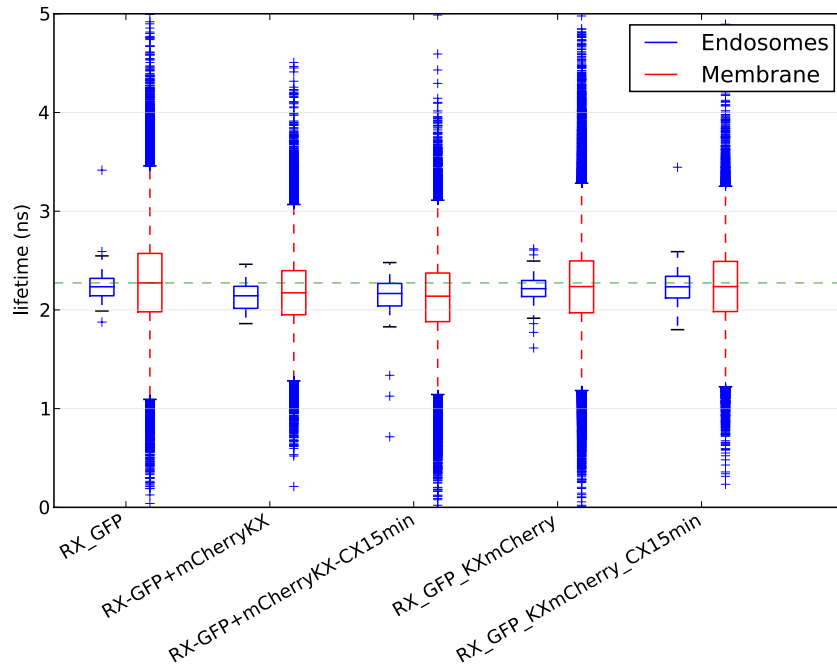


Figure 6.2: Lifetime distribution estimated on endosomes and the membrane in the five different experimental conditions.

endosomes lifetime and the mean membrane lifetime on each cell under study. On the 10 control cells that do not present mCherry-tagged KX (see Figure 6.1), the average difference is $+0.0099$ ns, meaning that the FRET phenomenon is slightly higher on the membrane. On the other hand, on the 13 cells presenting the mCherry-KX acceptor, the measured mean lifetime difference is -0.055 ns. This results may hint for a higher FRET on endosomes, and thus a RX-KX interaction localized at the endosomal level. However, a one-tail two-sample t -test that probes for the statistical significance of the shift between the two experimental conditions only gives a p-value of 0.07. This result hinders a conclusion on this relative lifetime loss shift.

This lack of statistical significance can be due to the phenotype inexistence, but it can also be due to the low number of endosomes on experimental sequences. Indeed, the number of detected endosomes measured between the control and acceptor treated cells drops from 10 per cell to 6 per cell. This difference is due to the high number of acquisitions that do not present endosomes in the second experiment. Similarly, the cells treated with the cytokine CX show a number of endosomes per cell dropping to 4, and a closer look shows numerous cells with acquisition induced artifacts (see Figure 6.4). We also measured a strong variability of the lifetime measured on the membrane with sometimes two lifetime populations across ten cells in the same experimental conditions

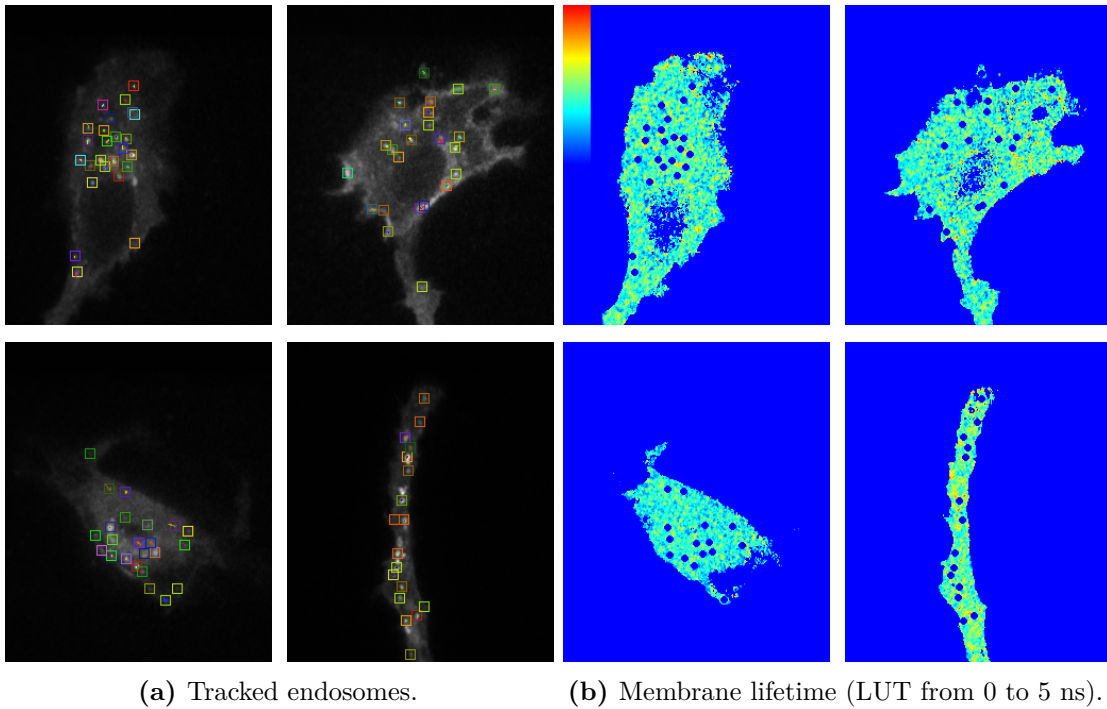


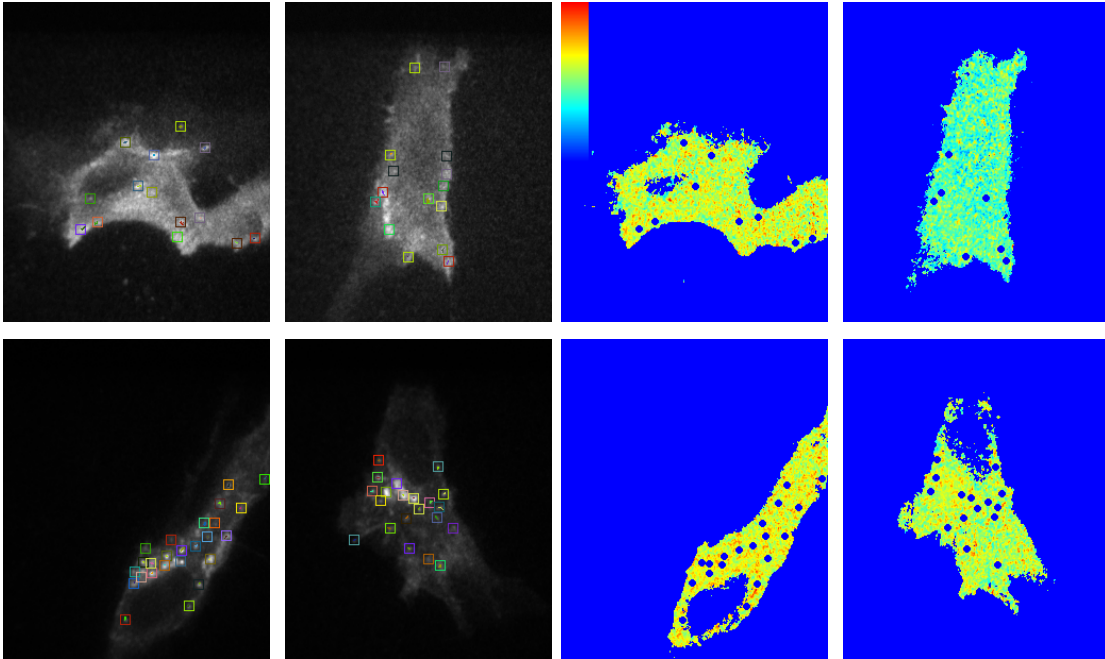
Figure 6.3: Tracked GFP-tagged RX on endosomes (left) and membrane lifetime map (right) in the presence of acceptor mCherry-KX.

(data not shown). Accordingly, further acquisitions are planned with our collaborators in order to investigate the significance of the endosomal FRET efficiency and to acquire better data after CX treatment.

6.3 Additional experiments

The spinning disk setup coupled with the cell morphological variation can provoke uncontrolled depth variation in the optical sectioning of the cell. This optical sectioning variation can hinder a constant measurement of the cell membrane fluorescence across the whole experiment as much as the imaging of endosomes. To address this problem, we propose to carry out the FD FLIM measurement with a TIRF microscope. Thanks to this technique, the cell can be imaged at a constant depth at the membrane level while still proposing a visualization of the early endosomes. Using this acquisition method, we hope to obtain a higher signal-to-noise ratio, a more consistent signal quality across the cells and more stationarity in lifetime measurement and spot detection under the same experimental conditions.

We also propose several strategies to improve the lifetime estimation specific to the



(a) GFP-tagged RX protein in endosomes (b) Membrane lifetime (LUT from 0 to 5 ns) without acceptor.

Figure 6.4: Tracked GFP-tagged RX on endosomes (left) and membrane fluorescence lifetime map (right) in the presence of acceptor mCherry-KX 15 minutes after CX injection. Among the KX-injected cells, only two cells present early endosomes that do not belong to the recycling compartment. Additionally the lifetime estimated on the membrane exhibits strong variations.

FD FLIM instrumentation on both endosomes and membrane. A modulated signal with a lower amplitude will present a higher noise stationarity that could be ignored or easily compensated. On the other hand, a very low sinusoidal amplitude does not allow for an accurate phase estimation. We propose to determine the best trade-off between the modulated signal amplitude and the lifetime estimation accuracy. To do so, we will use a plain fluorescein sample with known lifetime that will allow the estimator bias and covariance to be estimated empirically. Thanks to this strategy, we are hoping to reduce instrument induced noise in lifetime estimation.

In order to improve the tracking of endosomes, we will not randomize the recording order of the phase-modulation frames. This randomization was advised in [van Munster and Gadella Jr, 2004] to suppress the artifacts induced by photobleaching. If necessary, we will model photobleaching by combining the sinusoidal variation with an exponential decay. The LI-FLIM software [Lambert Instruments, 2010] includes a frame averaging by default to increase image intensity; we will deactivate this option to avoid over smoothing.

6 Application to protein interaction analysis at the membrane and during endocytosis

7 Conclusion

In the first part of this thesis, we have presented a dedicated signal processing method to reconstruct the fluorescein lifetime map corrupted by instrumental noise and intracellular motions in FD FLIM. A thorough study of the instrument-induced noise variance is first carried out to harness the strong heteroscedasticity that presents FD FLIM measurements. The ICCD noise footprint is thus presented. Our analysis shows that a correction is needed to cope with optical aberration. Apart from the application to fluorescence lifetime measurement, the advantages of our noise variance model is demonstrated with the help of two denoising algorithms. As the ICCD is a widespread instrument in low-light imaging, the associated methods could thus be useful in other fields. In addition, we proposed a fluorescence lifetime estimation method for dynamical analysis of endosomes inside the cell. Endosomes are detected on the first frame of the FD FLIM measurement. For each detected object, the lifetime and motion parameters are jointly estimated in an iterative and alternative fashion. On experimental sequences, the performance of the motion estimation is shown to outperform tracking algorithms that does not take the specific intensity model into account. The proposed methods are fully automatic and need only minimal and non-critical parameter setting.

Thanks to those contributions we are hoping to pave the way for fluorescence lifetime imaging microscopy on living cells presenting dynamical intracellular structures. In that sense, our method is applied on the biological experiment presented in the last chapter. The results hint for a higher protein interaction on the endosomes. From those data, we were able to point out some weakness in statistical significance and we propose the design of future acquisitions.

Two improvements could be envisaged for future work based on experimental requirements. To further improve the noise variance analysis, the next step is the study of the spatial correlation on the ICCD output. The estimation of multiple fluorescence lifetime on a pixel basis could be also interesting in the context of fluorophore with overlapping emission spectra. FD FLIM exploiting multiple frequencies have shown to be able to resolve multiple lifetimes [Gratton and Limkeman, 1983; Squire et al., 2000]. To evaluate the tracking method, more diversified intracellular structures should be considered. A few leads are already in this direction work, such as pixel soft classification between object and background.

More generally, the long-term goal is to perform time lapse FD FLIM measurement on a longer acquisition time. The motivation is to quantify protein interaction throughout for several cell cycles. If our method can already handle time lapse FD FLIM measurements,

the time between each measurement must be short enough for the local motion compensation to perform properly. By spacing out FD FLIM measurements, the reduced photo-toxicity and photo-bleaching would allow much longer time-lapse acquisitions. The motion estimation between each FD FLIM measurement should thus be carried out with multiple particle tracking method. Semi-global optimization strategies to optimize the set of trajectories needs then to be investigated. Part II presents a tracking algorithm suitable to cope with small and large displacements.

Appendices

A Derivation of the phase modulated signal for FD FLIM

This appendix presents the derivation of the model used to recover the fluorescence lifetime from an excited sample. Mono-exponential decay and simple sinusoidal excitation is assumed. We start by deriving the equation of the excited signal, then we explain in details the experimental method to estimate the fluorescence lifetime of a given sample. To our knowledge, this derivation has not been described to such a full extent before in the literature.

A.1 The excited signal

Let $E(t)$ and $I(t)$ be an emission signal and the response of a fluorescent molecule respectively at time t and let τ be the unknown lifetime. The excited fluorescent signal is given by

$$F(t) = E(t) * I(t) \quad (\text{A.1})$$

where $*$ denotes the convolution operator. Assume a mono-exponential decay and a simple sinusoidal excitation of the following form:

$$E(t) = E_0[1 + M_E \sin(\omega t + \phi_E)], \quad (\text{A.2})$$

$$I(t) = I_0 e^{-t/\tau} \quad (\text{A.3})$$

where I_0 denote the intensity at time $t = 0$. It follows that

$$\begin{aligned} F(t) &= \int_0^\infty E(t-t')I(t')dt' \\ &= E_0 I_0 \left(\int_0^\infty e^{-t'/\tau} dt' + M_E \int_0^\infty \sin(\omega(t-t') + \phi_E) e^{-t'/\tau} dt' \right) \\ &= E_0 I_0 (C + M_E B(t)) \end{aligned}$$

such that

$$C = \int_0^\infty e^{-t'/\tau} dt' = \tau$$

and

$$\begin{aligned}
B(t) &= \int_0^\infty \sin(w(t-t') + \phi_E) e^{-\frac{t'}{\tau}} dt' \\
&= \left[-\tau \sin(w(t-t') + \phi_E) e^{-\frac{t'}{\tau}} \right]_0^\infty - w\tau \int_0^\infty \cos(w(t-t') + \phi_E) e^{-\frac{t'}{\tau}} dt' \\
&= \tau \sin(wt + \phi_E) - \left(\left[-w\tau^2 \cos(w(t-t') + \phi_E) e^{-\frac{t'}{\tau}} \right]_0^\infty + (w\tau)^2 \int_0^\infty \sin(w(t-t') + \phi_E) e^{-\frac{t'}{\tau}} dt' \right) \\
&= \tau \sin(wt + \phi_E) - w\tau^2 \cos(wt + \phi_E) - (w\tau)^2 B(t).
\end{aligned}$$

Hence, we have

$$\begin{aligned}
B(t) &= \frac{\tau}{1 + (w\tau)^2} (\sin(wt + \phi_E) - w\tau \cos(w\tau + \phi_E)) \\
&= \frac{\tau}{1 + (w\tau)^2} \left(\sin(wt + \phi_E) - \frac{\sin(\arctan(w\tau)) \cos(w\tau + \phi_E)}{\cos(\arctan(w\tau))} \right) \\
&= \frac{\tau}{\cos(\arctan(w\tau))(1 + (w\tau)^2)} (\cos(\arctan(w\tau)) \sin(wt + \phi_E) - \sin(\arctan(w\tau)) \cos(w\tau + \phi_E)) \\
&= \frac{\tau}{\cos(\arctan(w\tau))(1 + (w\tau)^2)} \sin(wt + \phi_E - \arctan(w\tau)).
\end{aligned}$$

Finally, we obtain

$$F(t) = E_0 I_0 \tau \left(1 + \frac{1}{\cos(\arctan(w\tau))(1 + (w\tau)^2)} \sin(wt + \phi_E - \arctan(w\tau)) \right) \quad (\text{A.4})$$

$$= F_0 [1 + M_F \sin(\omega t + \phi_E - \arctan(\omega\tau))] \quad (\text{A.5})$$

where $M_F = \frac{1}{\sqrt{1+(w\tau)^2}}$ and $F_0 = E_0 I_0 \tau$ (as in [Holub, 2003]).

This result shows that the fluorescence response of the sample induces a phase delay and an amplitude decrease in the excited signal which is coherent with physical intuition.

A.2 Lifetime estimation

As we control the frequency of the emission signal, (9.15) shows that the phase and amplitude of the signal yield the lifetime τ (using a calibration reference measurement to retrieve ϕ_E). Actually, the experimental frequency in such experiment is too high for the phase to be directly measurable on a CCD sensor. To overcome this problem, it is usual to modulate the detection sensitivity with an other sinusoidal signal $G(t)$ (see (9.9)):

$$G(t) = G_0 [1 + M_G \sin(\omega t + \phi_G)]. \quad (\text{A.6})$$

In the homodyne case, we use the same frequency as the original signal. The result of this modulation then yields to:

$$\begin{aligned}
 D(t) &= G(t)F(t) \\
 &= F_0G_0[1 + M_F M_G \sin(\omega t + \phi_G) \sin(\omega t + \phi_E - \arctan(\omega\tau)) \\
 &\quad + \sin(\omega t + \phi_E - \arctan(\omega\tau)) + \sin(\omega t + \phi_G)] \\
 &= F_0G_0[1 + M_F M_G \cos(\phi_E - \arctan(\omega\tau) - \phi_G) \\
 &\quad + \cos(2\omega t + \phi_E - \arctan(\omega\tau) + \phi_G) \\
 &\quad + \sin(\omega t + \phi_E - \arctan(\omega\tau)) \\
 &\quad + \sin(\omega t + \phi_G)] \\
 &\approx F_0G_0[1 + M_F M_G \cos(\phi_G - \Phi_E + \arctan(\omega\tau))].
 \end{aligned}$$

This approximation comes from the low-pass behavior of the CCD camera. The measured signal is then time-independent. One solution to recover the value $\arctan(\omega\tau)$ is to tune ϕ_G the following way :

$$\phi_G = \phi_{G_0} + \frac{2\pi k}{K}. \quad (\text{A.7})$$

Thus, we obtain K samples (K must be chosen > 3) defined as:

$$D(k) = F_0G_0[1 + M_F M_G \cos(\phi_{G_0} + \frac{2\pi k}{K} - \phi_E + \arctan(\omega\tau))]. \quad (\text{A.8})$$

The observations $D(k)$ can be then fitted with cosine function (using various methods including Fourier decomposition and robust regression methods) to estimate the parameter controlling (9.35), most notably the phase $\Phi = \phi_{G_0} - \phi_E + \arctan(\omega\tau)$ and amplitude ratio $M_F M_G = M_G(1 + (\omega\tau)^2)^{-1/2}$. We thus have to estimate the lifetime, provided we can calibrate the optical setup to measure $\phi_{G_0} - \phi_E$ and M_G . To do so, a FD FLIM measurement of reference sample is with known lifetime τ_{ref} is acquired in the same condition. By fitting the $D_{ref}(k)$ on cosine function, we obtain an estimate for the reference phase $\widehat{\Phi}_{ref}$ yielding :

$$(\widehat{\phi_{G_0} - \phi_E}) = \widehat{\Phi}_{ref} - \arctan(\omega\tau_{ref}) \quad (\text{A.9})$$

and

$$\widehat{M}_G = \widehat{M}_F \widehat{M}_{G_{ref}} \sqrt{1 + (\omega\tau_{ref})^2} \quad (\text{A.10})$$

Finally the phase lifetime is given by:

$$\widehat{\tau}_\phi = \frac{1}{\omega} \tan(\widehat{\Phi} - \widehat{\Phi}_{ref} + \arctan(\omega\tau_{ref})) \quad (\text{A.11})$$

and the modulation lifetime is as follows:

$$\hat{\tau}_M = \frac{1}{\omega} \sqrt{\left(\frac{\widehat{M}_F \widehat{M}_G}{\widehat{M}_F \widehat{M}_{Gref} \sqrt{1 + (\omega \tau_{ref})^2}} \right)^2 - 1}. \quad (\text{A.12})$$

B Gamma NL-means and approximate Bayesian Computation

In this appendix, we present the Gamma NL-means-based denoising algorithm. The approach inspired from the Approximate Bayesian Computation (ABC) framework [Beaumont et al., 2002; Marjoram et al., 2003], is especially adapted to complex situations where the posterior cannot be easily derived or computed. We exploit empirical noise statistics and propose a distance learning framework to adapt to different conditions. This is particularly relevant for images contaminated by heterogeneous sources of noise.

B.1 Bayesian interpretation of NL-means

Consider a gray-scale image $I = (I(\mathbf{x}))_{\mathbf{x} \in \Omega}$ defined over a bounded domain $\Omega \subset \mathbb{R}^2$ and $I(\mathbf{x}) \in \mathbb{R}_+$ is the noisy observed intensity at pixel $\mathbf{x} \in \Omega$. Assume that the image I is a noisy version of an unknown image u , that is $I = u + noise$. Define a $\sqrt{n} \times \sqrt{n}$ observed patch $S_I(\mathbf{x})$ at pixel x as: $S_I(\mathbf{x})(\mathbf{t}) \triangleq I(\mathbf{x} + \mathbf{t})$, $\forall \mathbf{t} \in [-\frac{\sqrt{n}-1}{2}, \dots, \frac{\sqrt{n}-1}{2}]^2$. The NL-means at pixel \mathbf{x} is weighted average of all gray values in the entire image. Formally, we have [Buades et al., 2005]:

$$\hat{I}_{NL}(\mathbf{x}) = \frac{1}{Z(\mathbf{x})} \sum_{\mathbf{y} \in \Omega} \exp\left(-\frac{\|S_I(x) - S_I(y)\|_2^2}{h^2}\right) I(\mathbf{y}) \quad (\text{B.1})$$

and $Z(\mathbf{x})$ is a normalizing factor. The weights express the amount of similarity ($\|\cdot\|_2$ denotes the Euclidean distance) between the n -dimensional image patches $S_I(\mathbf{x})$ and $S_I(\mathbf{y})$ of each pair of pixels \mathbf{x} and \mathbf{y} involved in the computation. For the sake of simplicity, we omitted in (B.1) the choice of a weighted Euclidean norm over the patches as described in [Buades et al., 2005]. The decay parameter h^2 acts as a filtering parameter. The range of the search space can be as large as the whole image but, in practice, it is necessary to restrict the computation of weights to semi-local neighborhoods.

In the line of work of [Buades et al., 2005; Kervrann et al., 2007], we describe a more recent interpretation of NL-means in the Bayesian setting [Louchet, 2008]. Define a prior on patches $\mathbf{z} \in \mathbb{R}^n$ from the noisy image I . A simple histogram is given by $p(\mathbf{z}) = \frac{1}{|\Omega|} \sum_{\mathbf{y} \in \Omega} \mathbf{1}[\mathbf{z} = S_I(\mathbf{y})]$ where $\mathbf{1}[\cdot]$ denotes the indicator function. The Bayesian estimate $\hat{S}_u(\mathbf{x})$ of a patch $S_u(\mathbf{x})$ with L_2 -risk and prior p on patches is given by the

posterior expectation $\widehat{S}_u(\mathbf{x}) = \mathbb{E}_p[S_U(\mathbf{x})|S_I(\mathbf{x})]$, i.e.

$$\widehat{S}_u(\mathbf{x}) = \int \overbrace{p(\mathbf{z}|S_I(\mathbf{x}))}^{\text{posterior}} \mathbf{z} d\mathbf{z} = \int \overbrace{p(\mathbf{z})}^{\text{prior}} \overbrace{p(S_I(\mathbf{x})|\mathbf{z})}^{\text{likelihood}} \mathbf{z} d\mathbf{z}.$$

In the case of zero-mean white Gaussian noise (variance σ^2),

$$\widehat{S}_u(\mathbf{x}) = \frac{1}{Z(\mathbf{x})} \int p(\mathbf{z}) e^{-\frac{\|S_I(\mathbf{x})-\mathbf{z}\|_2^2}{2\sigma^2}} \mathbf{z} d\mathbf{z}. \quad (\text{B.2})$$

Given $p(\mathbf{z})$ as defined above and switching the sums, we get

$$\widehat{S}_u(\mathbf{x}) = \frac{1}{Z'(\mathbf{x})} \int \sum_{\mathbf{z} \in \mathbb{R}^n} \mathbf{1}[\mathbf{z} = S_I(\mathbf{y})] e^{-\frac{\|S_I(\mathbf{x})-\mathbf{z}\|_2^2}{2\sigma^2}} \mathbf{z} d\mathbf{z}. \quad (\text{B.3})$$

For a given \mathbf{y} , a patch \mathbf{z} yielding a non-zero term can only be $\mathbf{z} = S_I(\mathbf{y})$. Finally, after central projection [Salmon and Strozecki, 2012], we get $\widehat{I}_{NL}(\mathbf{x})$ (see (B.1)). NL-means is therefore a posterior expectation and the prior model is based on the empirical histogram of patches taken in the input noisy image. In the next section, we consider more general likelihood models and priors.

B.2 Approximate Bayesian Computation NL-means filtering

B.2.1 Principles of ABC rejection method

One of the basic problem in Bayesian statistics is the computation of the posterior for general forms of noise distributions. If the posterior density cannot be computed explicitly or is time consuming, we usually resort to stochastic simulation to generate samples for the posterior. The commonly-used approach is the rejection method but, more recently, Beaumont et al. [Beaumont et al., 2002] described a generalization of the usual rejection method in the domain of genetics.

Formally, assume data \mathcal{D} generated from a model determined by λ whose prior is denoted $p(\lambda)$. The so-called ABC method is as follows [Beaumont et al., 2002; Marjoram et al., 2003]:

1. Generate λ from $p(\cdot)$;
2. Simulate \mathcal{D}' from the model with parameter λ ;
3. Calculate a distance $\rho(\mathcal{D}, \mathcal{D}')$ between \mathcal{D}' and \mathcal{D} , accept λ if $\rho(\mathcal{D}, \mathcal{D}') \leq \delta$, and return to 1.

As $\delta \rightarrow \infty$, accepted observations come from the prior. When $\delta \rightarrow 0$, this rejection algorithm is exact and accepted observations are independent and identically distributed from the posterior distribution $p(\lambda|D)$. Nevertheless, most of samples are rejected if we set $\delta = 0$. Then, this approach requires the setting of δ and the selection of a suitable metric $\rho(\cdot)$.

The next step is to calculate expectations of the form $\mathbb{E}(\lambda|D) = \int p(\lambda|D) \lambda d\lambda$ where the expectation is taken with respect to the posterior distribution of λ . The simplest way to approach this is to draw samples $\{\lambda_i\}_{i=1, \dots, N}$, from $p(\lambda|D)$ using the previous algorithm and then approximate using the sum $N^{-1} \sum \lambda_i$. However, a more stable estimate can be obtained by weighting the λ values with the posterior. Consequently, all values of λ are included in the the sum and there is no rejection step. This is a direct extension of the estimate given in Beaumont et al. [Marjoram et al., 2003] which used Epanechnikov kernels to weight each value of λ .

B.2.2 Patch-based ABC method

The interpretation of ABC given above allows us to revisit previous analyzes of the NL-means in the Bayesian setting. The objective is to restore pixel x given an observed patch $S_v(x)$. Denote λ the unknown scalar intensity value at a given pixel whose whose prior $p(\lambda)$ is assumed to be uniform in the range $[0, \dots, \lambda_M]$ where λ_M is the maximum intensity value. Consider the ABC procedure following the previous guidelines in the case of zero-mean white Gaussian noise:

1. Generate $\lambda \sim U[0, \dots, \lambda_M]$;
2. Find a pixel value $I(\mathbf{y})$ in the entire image such that $I(\mathbf{y}) = \arg \min_{\mathbf{y}' \in \Omega} |I(\mathbf{y}') - \lambda|$ and apply a central retro-projection to get a patch $S_I(\mathbf{y})$;
3. Calculate the error $\epsilon(x, y) = \frac{\|S_I(\mathbf{y}) - S_I(\mathbf{x})\|_2^2}{2\sigma^2}$ between the “simulated” patch $S_I(\mathbf{y})$ and the “observed” patch $S_I(\mathbf{x})$ at pixel \mathbf{x} , compute $\pi(\epsilon(x, y))$ and return to 1.

Here $\pi(\cdot)$ denotes the unknown probability density function of the error term. Instead of uniformly drawing independent samples in the n -dimensional space, Step 2 is expected to generate more plausible artificial data, “closer” to the observed data. Note that Step 2 amounts to uniformly drawing a patch in the entire image domain.

B.2.3 Data-driven density learning

For most cases, we will expect $\epsilon(x, y)$ to have one mode located at 0. In the Gaussian case and non-overlapping patches, the errors are not centered at 0 but are expected to follow a chi-square distribution χ_n^2 with n degrees of freedom. Yet, for overlapping patches, it is established that the error is the sum of three independent χ_n^2 variables: $\epsilon(x, y) = z_1 + 2z_2 + 3z_3$ such as $z_1 \sim \chi_{n-p}^2$, $z_2 \sim \chi_{2p-n}^2$ and $z_3 \sim \chi_{n-p}^2$ where $\frac{n}{2} < p < n$ controls

the rate of overlapping. This is explicitly true for sliding windows in one-dimensional signals and we have $\mathbb{E}[\epsilon(x, y)] = 2n$ and $\text{Var}[\epsilon(x, y)] = (12n - 4p)$.

In the case of variable and multiple overlappings in 2D, a general form for the distribution of the error cannot be obtained. Nevertheless, it is established in [Feiveson and Delaney, 1968] that the sum of weighted chi-squares variables can be approximated by a Gamma distribution controlled essentially by two parameters k and β . Consequently, we have experimentally investigated this idea of approximating the empirical density $\pi(\cdot)$ of errors by fitting Gamma distributions using the moment method, yielding the following algorithm.

B.2.4 Gamma NL-means (GNL-means)

The proposed ABC-based Gamma NL-means is based on the following stochastic two-step procedure:

Step 1: Data-driven density learning

1. Draw uniformly $\pi r^2 |\Omega|$ pairs of patches $(S_I(\mathbf{x}), S_I(\mathbf{y}))$ in the entire noisy image I such as $\|\mathbf{x} - \mathbf{y}\|_2 \leq r, r > 0$ and compute the empirical density $\pi(\cdot)$ of errors $\epsilon(x, y) = \|S_I(\mathbf{y}) - S_I(\mathbf{x})\|_2^2 / (2\sigma^2)$;
2. Estimate the Gamma distribution parameters k and β using the moment method, i.e. by fitting the empirical mode $= (k - 1)\beta$ and variance $= k\beta^2$ of the density.

Step 2: ABC-based denoising

$$\hat{I}_{GNL}(\mathbf{x}; k, \beta) = \frac{1}{C(\mathbf{x})} \sum_{\mathbf{y} \sim U_r(\mathbf{x})} (\epsilon(x, y))^{k-1} e^{-\frac{\epsilon(x, y)}{\beta}} I(\mathbf{y}) \quad (\text{B.4})$$

where the set of N variables $\mathbf{y} \sim U_r(\mathbf{x})$ in the sum are uniformly drawn from a ball of radius r (same value as in Step 1) centered at pixel \mathbf{x} and $C(\mathbf{x})$ is normalization constant.

The computational time of the GNL-means is of about 80s on a 512×512 image and C++ implementation on an Intel Core i7 64-bit CPU 2.4GHz. Performances of the GNL-means are first demonstrated on real images in confocal imaging combined with frequency domain fluorescence lifetime imaging (FD FLIM) (see Section 4.3.2).

Part II

Tracking heterogeneous transports in a dense intracellular environment

Introduction

The quantification of intracellular dynamics is a fundamental task to understand mechanisms such as protein assembly and trafficking, intracellular signaling or pathogens invasion as much as cell scale phenomena like morphogenesis, mitosis or cell migration. As time lapse microscopy and increasing resolution in modern microscopy generates a huge amount of data, automatic quantification of motion is required to understand biological dynamics, mechanisms and processes [Meijering et al. \[2006\]](#). The diversity of possible motion types in a single experiment, the possible rarity of transient events call for a per-object method in order to unbiasedly measure the individual behaviors.

During the last decade, several algorithms have been tailored to cope with different types of cellular and subcellular motion down to Brownian single molecule behavior. One of the remaining big challenges in this area of methodological development has been the tracking of extremely heterogeneous movements of objects in crowded scenes. In our first preliminary work, we evaluated the performances of several state-of-the-art algorithms in complex scenario including dense populations of diffusing particles, which suddenly change to directed motion. A typical cellular scenario with this property is the jerky motion of vesicles and viruses switching between cytoplasmic diffusion and motor-mediated, sudden displacements. These switches are particularly challenging to detect because they occur rarely. The presence of numerous neighboring candidates in the expected range of particle motion makes the tracking ambiguous and induces false positives. Limiting the ambiguity by reducing the search range, on the other hand, is not an option, as this would increase the rate of false negatives. This very interesting problem has been brought to our attention during a three-month laboratory visit in the Danuser lab. The tracking problem amounted to quantify extremely rare and sudden active transport of vimentin along the cytoskeleton while the rest of dense population of protein undergo a confined diffusion.

In this work, we first propose an original review of the multiple particle tracking (MPT) algorithms proposed in the literature. The most common strategies put forward to face the MPT challenges in bioimaging are presented. Throughout this technical review, a large focus is made on heterogeneous type of motions and particle density. Accordingly, we reserve a significant part to the methods that model various dynamics in a single trajectories such as the Interacting Multiple Modeling [[Blom and Bar-Shalom, 1988](#); [Genovesio et al., 2006](#)] or the u-track algorithm [[Jaqaman et al. \[2008\]](#)]. In this context, we propose a mathematical formulation to the dynamical filter proposed in u-track. To the best of our knowledge, this is the first time such an effort is made for this widespread

tracking software in bio-imaging. From this review, we conclude that no method in the literature is designed to detect abrupt transitions from diffusive transport to fast active transport in a dense population of particle.

Building on the u-track platform we propose here a new, interacting multiple model smoother that exploits recursive tracking in multiple rounds in forward and backward temporal directions in order to achieve convergence of the instantaneous speed estimate time-point-by-time-point. This allows us to estimate fast transitions from freely or confined diffusive to directed motion. To avoid false positives we complemented recursive tracking with a robust inline estimator of the adaptive search radius for assignment (a.k.a. gating). We tested our method on simulation to measure the influence of density and motion switching probability. In biological applications, our algorithm allows us to quantify the extremely small percentage of motor-driven movements of intermediate filament precursor particles along microtubules in a dense field of unbound particles. We also show in experimental data sets of virus trafficking that our algorithm can cope with up to a strong reduction in recording frame rate without losing tracking performance relative to methods relying on fast sampling.

Contributions:

- Literature review:
 - Description of the u-track algorithm in a mathematical framework as a Generalized Pseudo Bayesian filter of order 1
 - A focus on particle density and motion heterogeneity.
 - Systematic classification into six key features to evaluate strengths and weaknesses of related works.
- A new tracker design for dense condition and heterogeneous types of motion:
 - Interacting Multiple Modeling smoother fusing forward and backward tracking for dynamic modeling with low computational overhead.
 - Adaptive search radius online estimation scheme exploiting recursive tracking and adapting to the detected local motion type.
- Performance validation:
 - Our method out-performs competitive particle tracking methods on the targeted problematic on simulated data.
 - Our method out-performs competitive particle tracking methods in a variety of less sophisticated scenario on simulated data.
 - Study of the vimentin trafficking on the cytoskeleton measure very rare and sudden transition in the dynamics.
 - Our method is proven to be more robust to acquisition speed reduction on virus sequences.

Disambiguation: particle tracker and particle filters

The present manuscript makes an extensive use of the word “particle”. Most of the time, it is used to designate the target of the tracker, i.e. a vesicle or a molecule that appears diffracted in a fluorescence microscopy sequence. However, the word “particle” seldomly refers to the particle filtering technique where particles are used to represent a posterior probability. In such case, the context clearly precises it.

8 Quantifying transport heterogeneity in living cells

To introduce our main study, this section gives a short overview of fundamental dynamical processes inside the cell. We shortly describe the foundation for intracellular passive and active transports, and we describe the biological origins of the heterogeneous dynamics that are observable in the cell.

We then present the challenges related to the estimation of the parameters controlling dynamics on sub-resolved molecules. We discuss the influence of parameter heterogeneity and moving target density.

Finally, we present a typical case studying of challenging dynamic quantification experiment, namely the detection of rare motor-mediated motion in a crowded population of unit length filament of vimentin. This study has been the starting point for the design of our new tracker for multiple particle motion analysis.

8.1 Dynamical models in living cell

It has been established for a while that protein trafficking was only due to diffusion inside the cytoplasm [Agutter et al., 1995], and if simple thermal agitation does actually represent a non-negligible proportion of molecular motions inside the cell, trafficking mechanisms are much more complex.

8.1.1 Passive transport

The first dynamical event that has been observed in the cell is the aforementioned diffusion or Brownian motion. The diffusion phenomenon has been described by Robert Brown in the early 19th after his observation of the stochastic motion of pollen particles. It has been later demonstrated that this motion is due to the thermal agitation in the medium resulting in shocks between molecules and causing stochastic trajectories (see Figure 8.1). The propagation function of a pure Brownian motion with n degrees of freedom is described by the following probability distribution function:

$$p(\mathbf{x}, t|\mathbf{x}_0) = \frac{1}{(4\pi Dt)^{\frac{n}{2}}} e^{-\frac{(\mathbf{x}-\mathbf{x}_0)^\top(\mathbf{x}-\mathbf{x}_0)}{4Dt}}. \quad (8.1)$$

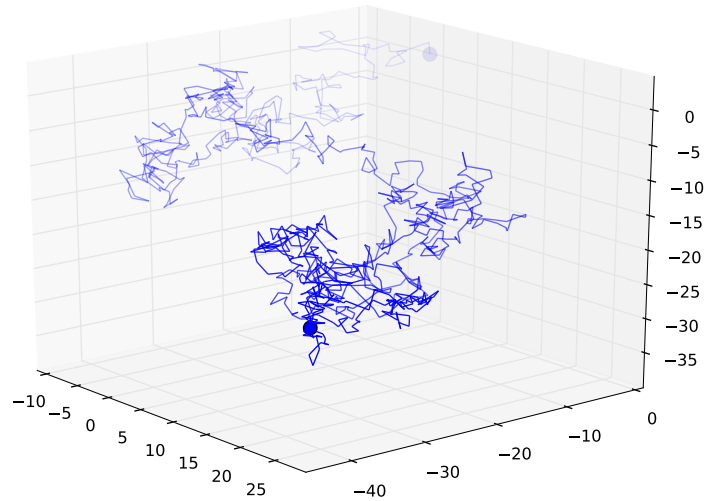


Figure 8.1: Trajectory of a single molecule undergoing Brownian motion in three dimensions. Segment color strength indicates temporal progression.

The mean squared displacement (MSD) is also often used since it yields a simple form to describe diffusion. By integrating 9.5 over time we obtain and the mean squared displacement:

$$\langle \|\mathbf{x}(t) - \mathbf{x}(0)\|^2 \rangle = 2nDt \quad (8.2)$$

where D is the diffusion coefficient which depends on object size, medium viscosity and temperature. Inside the cell, diffusive dynamics are a key component in short distance transportation. Diffusion triggers the connectivity for signal transduction and is involved in reaction-diffusion system during embryonic development.

8.1.2 Active transport

An other dynamical process that has been heavily studied in the past decade is the motor-mediated transport of molecules. Primarily supported by actin filament and microtubule networks, it ensures spatial organization and temporal synchronization in the intracellular mechanisms and structures. At the microscopical level, the observed displacement is not stochastic and presents a locally constant speed v along the cytoskeleton. The particle MSD can be straightforwardly described by the following equation [Saxton, 1994a]:

$$\langle \|\mathbf{x}(t) - \mathbf{x}(0)\|^2 \rangle = v^2 t^2. \quad (8.3)$$

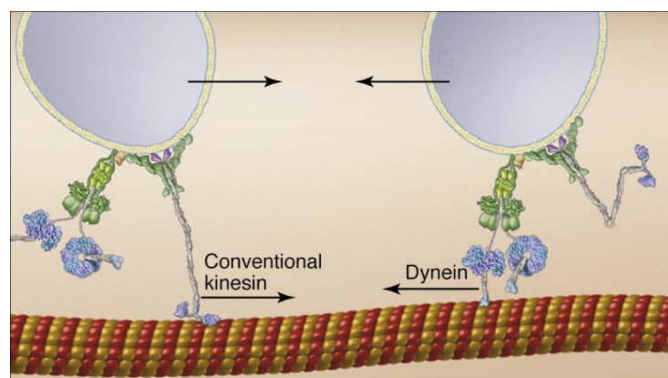


Figure 8.2: Motor-mediated vesicular transport along the microtubule network (source: [Vale, 2003]).

Motor-mediated transport is involved in numerous dynamical events in the cell: large membrane organelles transport (e.g. Golgi, mitochondria and nucleus), vesicular mediated transportation that takes part in protein secretion from the endoplasmic reticulum (protein assembly) to the Golgi apparatus (protein sorting) and then to the membrane as well as endocytic pathways, cytoskeletal filaments dynamics, intracellular signaling, cell migration and transportation of a subset of mRNAs [Vale, 2003]. The motor toolbox involved in such transportation is specific to each cytoskeleton component. Motors moving towards the microtubule plus-end are the kinesin family. As illustrated in Figure 8.2, they are used for transporting vesicular cargoes. They also have a role in chromosome segregation, anterograde axonal transport and protein secretion pathways. Motors moving in the opposite direction towards the microtubule minus-end belong to the dynein family. They present a more complex structure. The role of the dynein encompasses retrograde axonal transport mitotic, spindle positioning, nuclei positioning, mRNA localization, intermediates filament transport and endocytic pathways. The motor operating along actin filaments is the myosin protein. It is primarily associated to cellular attachments, contraction and migration.

8.1.3 Heterogeneous transport

In experimental conditions, the strict classification presented above rarely holds. The complexity of internal structures and molecular processes in the living cell influences the molecular dynamics and prevents the systematic application of pure Brownian or directed motion modeling. This section gives a few examples of heterogeneous transports. The two first types are extensions of the Brownian diffusion model to subdiffusion, active diffusion or uniform flow. The third one is the particle switching between active and Brownian transports or active transport regime. This frequent dynamical scenario is the

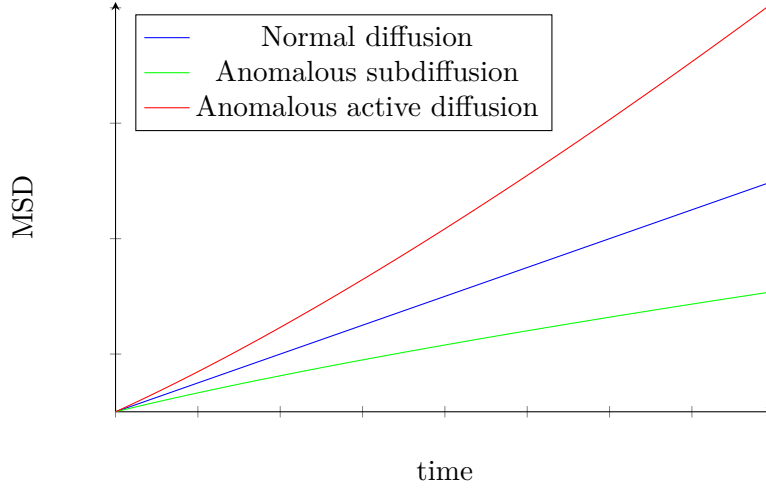


Figure 8.3: Simulation of anomalous subdiffusion and active diffusion as a function of time.

main transport type of interest in the present study.

In the Brownian diffusion case, intracellular clutter can cause anomalous diffusion resulting in MSD measurements that differ from the theory (see Figure 8.3). On the one hand, cytoskeleton density will hinder the free displacement of the particle resulting in a non-linear evolution of the MSD below the theoretical expectation, a phenomena called subdiffusion (green curve in Figure 8.3). On the other hand, the cytoskeleton elasticity combined with thermal bending can contribute to active diffusion which will result in higher MSD measurements than predicted by a normal diffusion process (red curve in Figure 8.3) [Caspi et al., 2002; Brangwynne et al., 2009].

Heterogeneous transports have also been used by Qian et al. [1991] and Kusumi et al. [1993] to describe the random diffusion of protein in a uniform flow at the membrane. The dynamic is thus described as a Brownian motion on top of a directed displacement bearing the following probability distribution:

$$p(\mathbf{x}, t | \mathbf{x}_0) = \frac{1}{(4\pi Dt)^{\frac{n}{2}}} e^{-\frac{(\mathbf{x}-\mathbf{x}_0-vt)^\top (\mathbf{x}-\mathbf{x}_0-vt)}{4Dt}} \quad (8.4)$$

and associated mean squared displacement:

$$\langle \|\mathbf{x}(t) - \mathbf{x}(0)\|^2 \rangle = 2nDt + v^2 t^2. \quad (8.5)$$

Finally, a frequent intracellular scenario is the jerky motion of vesicles or virus switching between cytosolic diffusion and motor-mediated displacements. Such dynamics have been described as the “conveyor belt” model in [Saxton, 1994a], that is a combination of active and passive transports described earlier. This model has also been used in

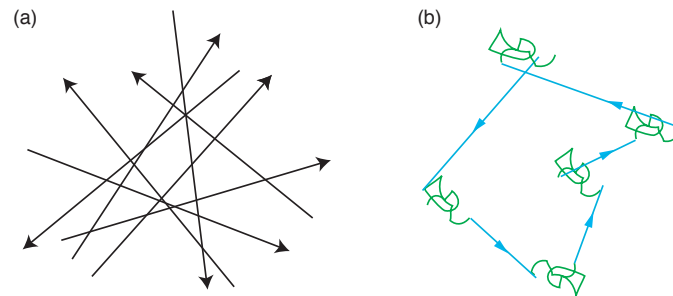


Figure 8.4: Heterogeneous motion model on a disordered cytoskeleton network (a) and associated vesicle trajectory undergoing switches between confined diffusion and directed motion (see [Bressloff and Newby, 2013]).

[Bressloff and Newby, 2013] to describe motor-transported particle transitions from a cytoskeleton network to an other (see Figure 8.4). A non-exhaustive list of biological events described by such a model includes: intermediate filaments protein transport along the cytoskeleton as described in [Pralhad et al., 1998] and in the present work, axon neurofilament transportation by fast motors in an intermittent and asynchronous fashion [Wang and Brown, 2001; Li et al., 2012], viral infection that intermittently exploits endosomal directed transport to reach the nucleus (e.g. HIV) [Lagache et al., 2009] or protein diffusion in the mesh of actin microfilaments network [Bressloff and Newby, 2013].

8.2 Challenges of intracellular particle transport quantification in fluorescence microscopy

To analyze the role of specific proteins in intracellular trafficking and signaling pathways of the living cell, a fundamental task is the identification of the different motion models described above and the estimation of the parameters controlling them. Before introducing our problematic in the next section, we discuss the challenges faced by the quantification of intracellular motion in fluorescence microscopy. Those challenges stem from the inherent limitations of fluorescence microscopy as much as the intracellular phenotypes under study.

8.2.1 Fluorescence microscopy limitations

Due to the resolution limit in light microscopy (200 nm) and the small size of the molecule under study ($\approx 0.2 \mu\text{m}$), the imaged molecule appears diffracted. As a result, its appearance is more dependent on the microscope characteristic point spread function than the object itself. This raises the advantages that the particle can easily be modeled

and detected as far as signal intensity is sufficient [Smal et al., 2010]. However, this raises the issue that molecules cannot be characterized by their appearances. This can trigger ambiguities in trajectories estimation especially in a dense population of particles.

Other challenges stem from the illumination dose limitation due to photodamages. For a given illumination dose and acquisition time, the experimenter can adjust the acquisition frequency to optimize motion quantification. The first option is to increase the acquisition frequency. The particles thus show little frame-by-frame displacements, making motion estimation an easier task only limited by spatial density. However, this high frame rate decimates the available illumination per image. The higher image quantity comes at the cost of signal quality because of the light sensor sensitivity in low-light conditions. The lower signal-to-noise will thus hinder the detection of particles. As we will detail in our review section, several efforts have been described in the literature to improve tracking in low light conditions [Godinez et al., 2011; Smal et al., 2008a; Godinez et al., 2009; Aguet et al., 2013; Chenouard et al., 2013]. Another possibility for the experimenter consists in reducing the acquisition frequency. This results in brighter objects, alleviating the detection issue. However, in this case, motion quantification can be more difficult depending on the phenotypes under study.

8.2.2 Challenging intracellular phenotypes

A living cell time lapse acquisition can present thousands of proteins in one image. In the case of fluorescence staining techniques or tagging of very dense population of proteins, the different fluorophores can not even be differentiated from each other. In this case, single particle tracking is not possible and only semi-local approaches such as correlation technique (STICS) or even optical flow methods can estimate homogeneous parameters in the image such as diffusion constant or uniform flows [Fortun et al., 2013]. Otherwise the estimation of single particle trajectories is preferred. In this context, the density is not an issue *per se*. The motion quantification challenge arises from the combination of dense population, objects mean squared displacement and acquisition speed. Indeed, large apparent displacements combined with spatial density trigger numerous ambiguities due to particle similarity. We name this ratio “spatiotemporal density” in what follows.

Additional challenges in protein motion estimation is the sudden trajectory apparitions and terminations as well as transient disappearances. In some scenarios, proteins can also merge and split, adding to ambiguity with trajectory apparitions and terminations in the neighborhood.

Those various challenges can be harnessed thanks to the dynamical homogeneity of particle trajectories. As detailed in our review effort (see Chapter 9), large apparent displacements can be predicted by analyzing the measured time points. To detect trajectories termination a local search radius can also be estimated [Genovesio et al., 2006; Jaqaman et al., 2008; Liang et al., 2010; Winter et al., 2012]. However, as discussed above, dynamical heterogeneity is a widespread behavior in the cell. Motion type

switching combined with low temporal resolution results in unpredictable transitions in space and time from confined diffusion to large active transport. In the biological experiment described in the following section, those transitions are extremely rare in a dense population of particles.

In the next Chapter we will detail the various strategies that helped taking up those challenges. Before that, the next section describes the motion quantification problem that justified our focus on heterogeneity and spatiotemporal density.

8.3 A challenging case study: dense intermediate filament network dynamics analysis

I had the opportunity to work on intermediate filament (IF) of vimentin production within Gaudenz Danuser's lab in Harvard Medical School (Boston, U.S.A.) during a three month laboratory visit. We discovered a very interesting tracking challenge while studying the support of the IF network formation. The heterogeneity of motion types, molecular density and the rarity of events of interest called for a original approach on multiple particle tracking based on a thorough study of existing algorithm strengths and weaknesses.

The biological background of this specific study is briefly presented in this section. We introduce the tracking challenges that arose from the preliminary quantification experiment and motivated the research activity in multiple particle tracking methods.

8.3.1 Intermediate filament network

The IFs network is part of the cytoskeleton with the actin filaments and microtubules (see Figure 8.5). While microtubules are known for their resistance to compression, and actin microfilaments for their weaker bounds, IFs characteristics are high flexibility, high stretching ability and strong bound. They have a supportive role to reinforce the cell and help to maintain the position and integrity of various organelles and to provide anchorage within the cytoplasm [Goldman et al., 2008; Herrmann et al., 2007]. Vimentin is the most widely distributed of all IF proteins. It can be found in fibroblasts, leukocytes, and blood vessel endothelial cells.

As opposed to actin filament and tubulin complex polymerization mechanisms, IF assembled themselves under simple conditions [Eriksson et al., 2009]. It has been proven that vimentin IF form in three phases as illustrated in Figure 8.6. The first step is completed within seconds as vimentin associates laterally in four octamers that form into 60 nm Unit Length Filament (ULF) (Figure 8.6.A). Much slowly, ULFs longitudinally anneal into IF (Figure 8.6.B) in a second step. Growing IF can also fuse end-to-end (Figure 8.6.C). Finally, IF diameter reduction suggests IFs maturation [Herrmann et al., 2007].

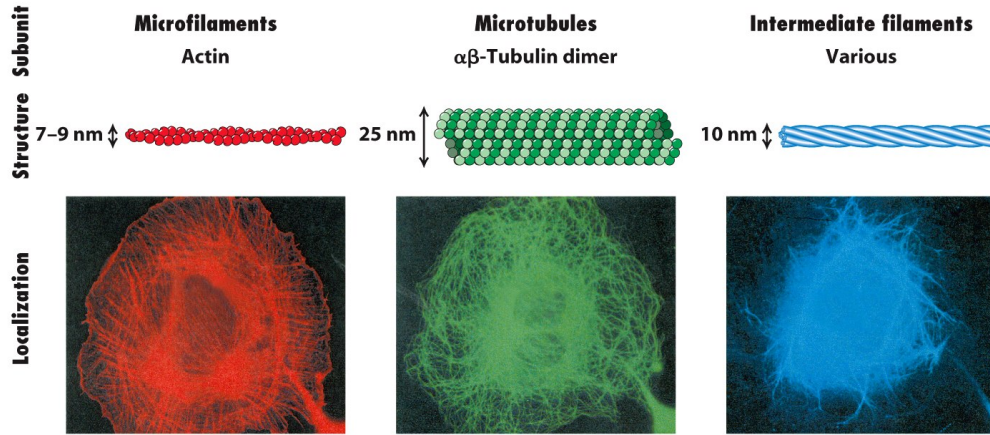


Figure 17-2
Molecular Cell Biology, Sixth Edition
© 2008 W. H. Freeman and Company

Figure 8.5: The three fundamental networks forming the cytoskeleton (source: from [Lodish, 2008]).

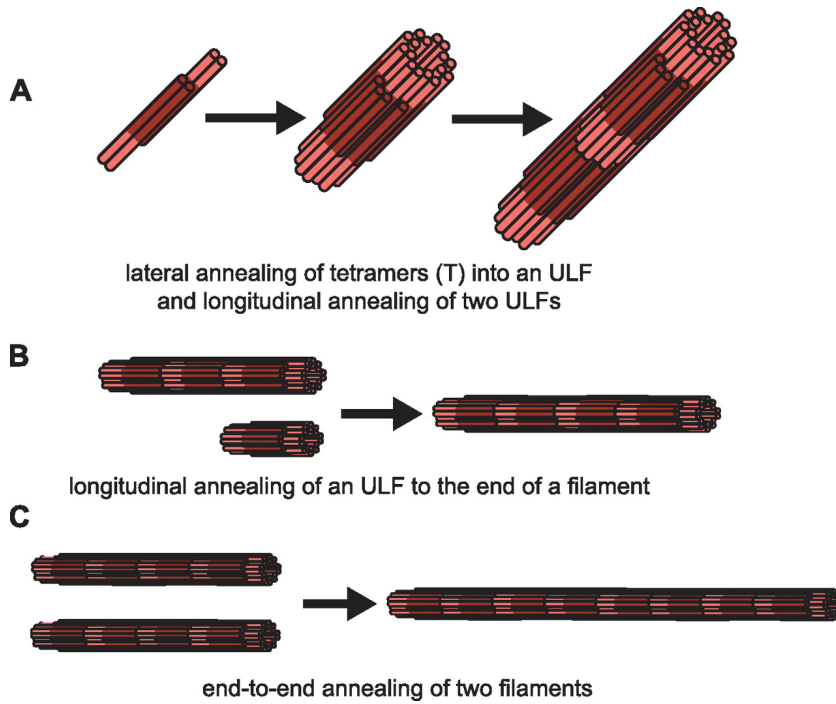


Figure 8.6: Intermediate filament (IF) formation (source: from [Kirmse et al., 2007]).

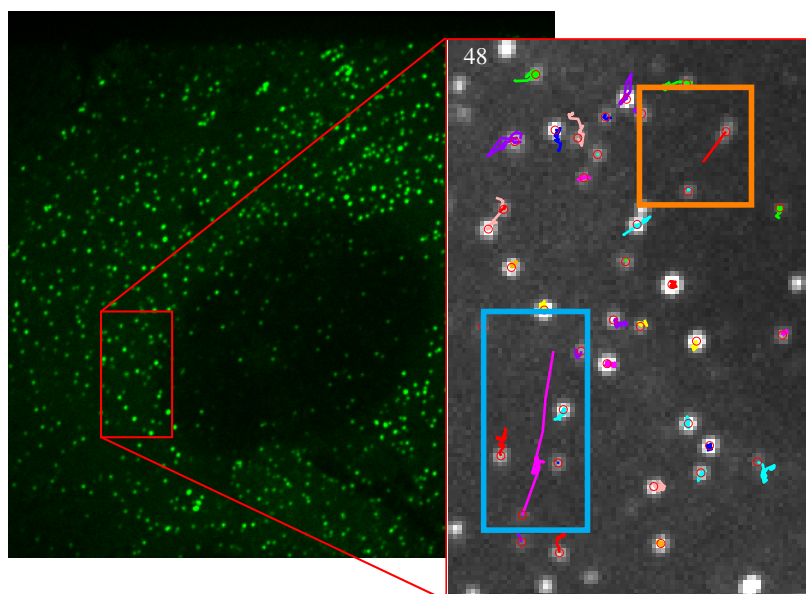


Figure 8.7: Vimentin motility seems to present a large proportion of confined Brownian motion and rare, sudden, motor-mediated transport. Vimentin null epithelial cell (cell line SW13) transfected with ULF of vimentin Y117L mutant fused to GFP. Image acquired with a spinning disk confocal microscope with a 100x objective zoom 1.5 (Numerical Aperture 1.4, pixel size $0.10905 \mu\text{m}/\text{pixel}$). Colored Tracks have been computed with an advanced u-track parametrization. This quantification is not perfect as demonstrated in Figure 8.8. However, u-track manages to highlight a large directed motion in a dense population of Brownian moving particles.

8.3.2 Unit length filament (ULF) dynamics analysis

While the IF network formation process has been extensively studied [Herrmann et al., 2007], a few studies have already been dedicated to vimentin motility and structural support [Pralhad et al., 1998; Yoon et al., 1998]. More than ten years ago, Pralhad et al. [1998] already stated that “a single [vimentin ULF] often [displays] vibrational movements for a short period of time, followed by a burst of rapid unidirectional movement”. Additionally, an inhibition in vimentin motility after nocodazole treatment was already observed in this work, hinting for a transport along the microtubule network. However, the Material and Methods Section cites the use of “Measure Distance” Metamorph function for quantification, hinting for a semi-manual quantification of motion. Furthermore, the resulting tracks put forward in this study are spatially sparse inside the cells while the highlighted acquisition in the same work are crowded.

Recently, Professor Gelfand in NorthEastern University proposed a similar experiment to investigate the support for the longitudinal annealing of ULF (see Figure 8.6.B and C). Having evidences that vimentin could bind to actin and microtubules during

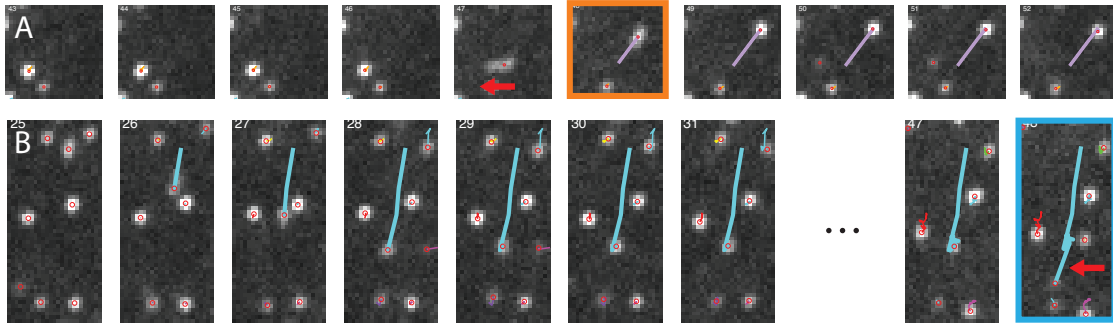


Figure 8.8: U-track best effort in dense spatiotemporal conditions does not retrieve motion type switching correctly. A) Vimentin ULF presents a fast directed motion between two stationary Brownian states (orange detail in Figure 8.7). The tracking algorithm misses the brutal transition pointed by the red arrow. B) The ULF undergoes a direct motion and then switches to a confined Brownian motion scheme (blue detail in Figure 8.7). The u-track algorithm produces a false positive, pointed by the red arrow, due to the strong inertia of the stochastic filtering.

longitudinal annealing, researchers in his lab treated epithelial cells with latrunculin and nocodazole separately to probe various contributions of the cytoskeleton component. The polymerization of actin (induced by latrunculin) or microtubule (induced by nocodazole) should indeed yield an inhibition in motor-mediated displacement if one of those hypothesis is verified. Visually, the experimenter could observe the motor-mediated motions described by [Prahlad et al. \[1998\]](#) in control cells. However, approximately three fast motions per minute were observable in the control cells (see Figure 8.7) on a population of thousands of ULF, while the aforementioned study claim 50% of directed motions. Thus, if visual assessment of dynamics is already known as a weak experimental procedure, the events rarity in the data reproduced several times within the Gelfand lab makes it even more fragile, making the use of a automatic tracker mandatory. The important vesicle density and motion type heterogeneity (see Figure 8.7) places this quantification experiment in the most challenging part of the quantification we proposed in Section 8.2. Not surprisingly, the Gelfand lab struggled to quantify this dynamics using on-the-shelf automatic tracking algorithm. The Gelfand’s lab thus sought for the Danuser’s lab expertise in that domain.

The u-track algorithm [[Jaqaman et al., 2008](#)] is a robust multiple particle tracking method that has been developed specifically for biological dynamics quantification in the Danuser’s lab and has been exploited for numerous collaborations ever since. U-track is a very versatile tracker, and we configured it thoroughly to detect the sub-resolved ULF and quantify the above-described dynamics. The detection of those spot-shaped ULF has not been a challenge thanks to the work of [Aguet et al. \[2013\]](#), and the large majority of jiggling ULF probably bound to the cytoskeleton were easily tracked. The results were much different on the motor-mediated motions described above. U-track best effort does not manage to retrieve the rare transitions from confined diffusion to fast

directed motion which are very difficult to predict because of the strong spatiotemporal density (see Figure 8.8). As we will show in our technical review, this is an issue with all state-of-the-art tracking algorithm design. Augmenting artificially the search radius is not a solution, as the density will cause numerous false positives as illustrated in Figure 8.9. Additionally, u-track implementation of directed motion estimation can induce additional false positives in crowded scenes (see Figure 8.7). This is due to a characteristic of this stochastic filtering scheme that I also investigated during my stay in the Danuser's lab. The literature study and numerical experiments I carried out as a visiting scholar and that will be detailed in the following sections proved those preliminary results to be worth the design of a new algorithm and tracking concepts.

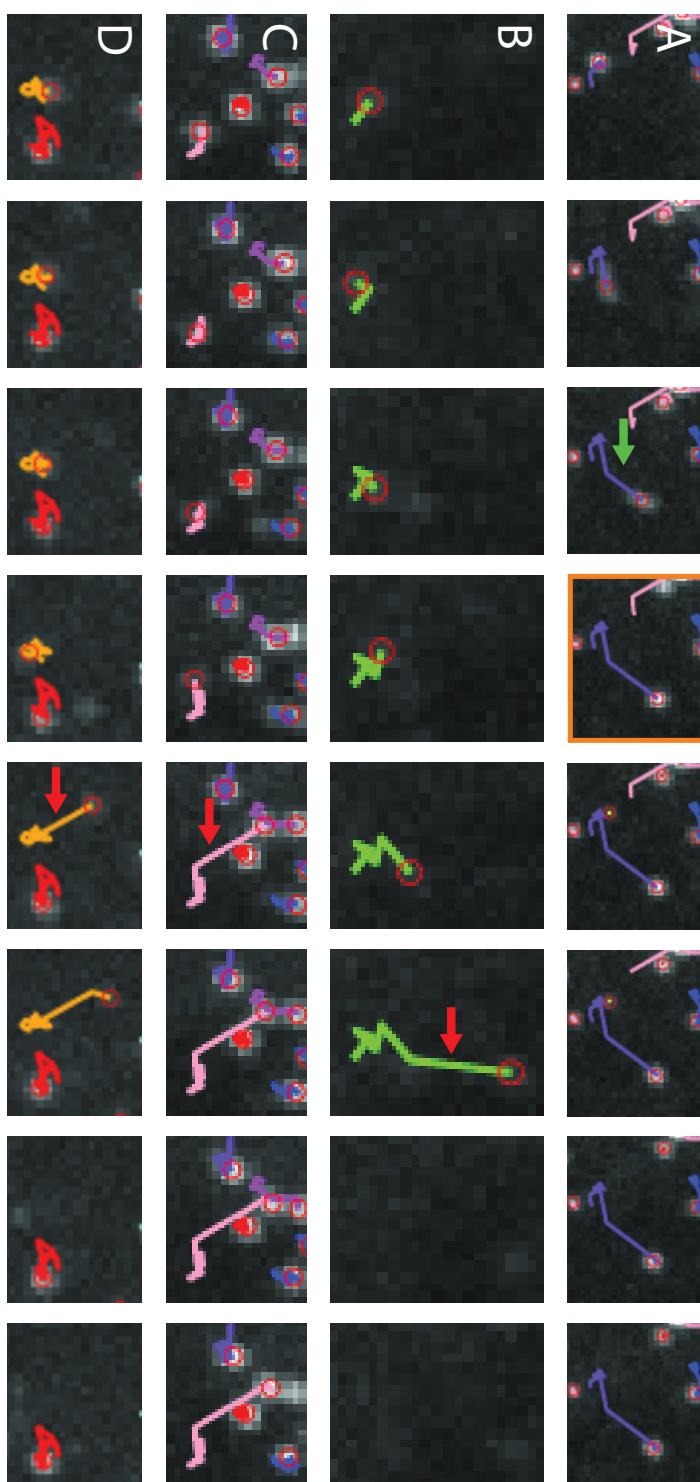


Figure 8.9: Artificially augmenting the search radius upper bound produces numerous false positives in the sequence. A) Search radius manual increase allows the tracking of brntal transitions from Brownian to directed motion that were not possible with a more restrictive setup. B,C,D) On the other hand, multiple false positives appear on the whole sequence.

9 Technical review of particle tracking algorithms

Automatic tracking algorithms were originally proposed for applications in aerospace or street surveillance [Bar-Shalom, 1990]. This literature has naturally inspired the various algorithms proposed for multiple particle tracking (MPT) in bio-imaging. However, no method described in other fields is able to address in a common framework all of the challenges and issues that are specific to intracellular motion quantification in fluorescence microscopy [Kalaidzidis, 2007]:

- Bleaching and phototoxicity hinder the excitation dose which lower the signal quality and acquisition speed.
- Spatiotemporal density due to spatial density of particles combined with low acquisition speed.
- Stochastic nature of particle motions, multiple types of dynamics and switching behaviors.
- Sudden apparitions and terminations of particle trajectories.
- Transient disappearances of particles causing **gaps** in the tracks. Gaps are due to temporary out-of-focus displacements in confocal or TIRF microscopy or object mis-detection caused by potentially low light conditions.
- High number of particles triggering high computational cost.
- High degree of similarity of isotropically shaped target profiles.
- Particle merging and splitting events that can result from particles that are too close to be resolved by the microscope (also called **particle coalescence**), or physical molecular interaction.

Therefore tracking multiple particles in bio-imaging has been an open problem over the past decades [Gelles et al., 1988; Meijering et al., 2006; Kalaidzidis, 2009].

In a nutshell, intracellular object trackers can be roughly divided into two groups of methods [Godinez et al., 2009]:

- The first category gathers two-step methods relying on object detection followed by an association step to find the optimal linking cost between sets of detections.

A large number of challenges faced by the quantification of intracellular dynamics observed in live cell microscopy has been tackled by those methods. Assignment in a group of particles which are close together is handled by combinatorial assignment [Jaqaman et al., 2008; Sbalzarini and Koumoutsakos, 2005; Racine et al., 2006; Chenouard et al., 2009; Magnusson and Jaldén, 2012]. Multiple transport types inside the cell have been analyzed using Bayesian filtering techniques [Genovesio et al., 2006; Jaqaman et al., 2008]. Temporary disappearances or object mis-detections are recovered by either considering link cost minimization on a group of frames [Sbalzarini and Koumoutsakos, 2005; Chenouard et al., 2013; Sergé et al., 2008] or on the whole sequence [Racine et al., 2006; Magnusson and Jaldén, 2012], or by a second linking step applied on tracklets [Jaqaman et al., 2008]. Some methods also propose to iterate successive detection and tracking steps to locally refine spot localization [Sergé et al., 2008].

- The second category of trackers does not rely on such a two-step approach. Object detection is performed on a per-track basis (instead of per-frame) and directly inferred from image data to solve ambiguous situations thanks to particle filtering or joint probabilistic data association (JPDA) [Smal et al., 2008a; Godinez et al., 2009; Smal et al., 2008b; Sergé et al., 2008]. This second category has been designed to cope with other challenging scenarios, especially low dose imaging presenting low signal-to-noise ratios.

In either frameworks, merging and splitting of vesicles can also be addressed in a post-processing step [Jaqaman et al., 2008; Feng et al., 2011], or as a single pass, within the link cost minimization [Racine et al., 2006; Magnusson and Jaldén, 2012].

As suggested in the previous chapters, a big challenge in this area is related to motion heterogeneity in crowded scenes. Yet, a frequent cellular scenario with this property is the jerky motion of vesicles and viruses switching between cytoplasmic diffusion and motor-mediated, fast displacements [Saxton, 1994b; Bressloff and Newby, 2013]. As illustrated in Figures 9.1 and 9.2, these switches are particularly challenging to detect since they are not predictable spatially or temporally and they occur in a dense spatiotemporal context of otherwise homogeneous population of particles. As we shall see will in this review, existing approaches that model motion heterogeneity are not designed to cope with rapid transitions from Brownian to directed motion that are not predictable (see Figure 9.1). Increasing the search radius is not the solution as it can generate false positives in such dense conditions. The u-track algorithm [Jaqaman et al., 2008] manages to recover a part of the directed motion (see Figure 9.1)) thanks to a adaptive initialization of speed estimate (see Section 9.3). Nonetheless, Figure 9.2 displays the downside of such inertia as the same algorithm produces false positives in the same sequence.

To improve this tracking approach, we propose an original analysis of fifteen algorithms chosen for their performances and originality in the literature. We consider six criteria for classification:

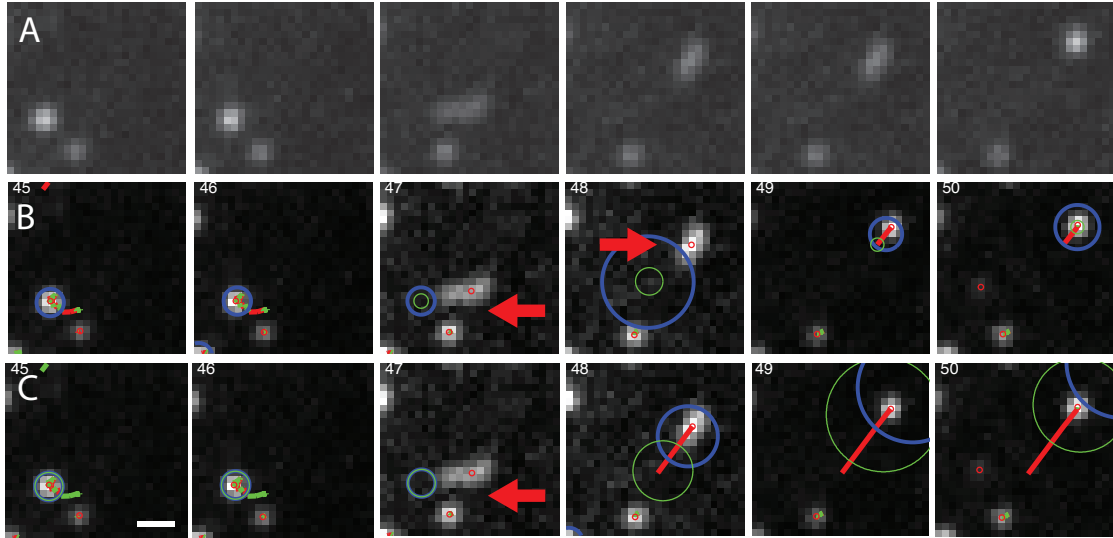


Figure 9.1: Particles presenting motion type switching are challenging to track. **A)** An example of heterogeneous motion type on a single track (detail). The ULF of vimentin presents a fast directed motion between two Brownian states. **B)** An IMM based algorithm, similar to [Genovesio et al., 2006] (supporting an forward-backward initialization step) does not retrieve the direct segment, only the Brownian sections are correctly tracked. An artificial increase of the search radius is not possible without an important number of false positives in the whole sequence. **C)** The u-track algorithm will allow to retrieve a part of the direct motion segment thanks to the Kalman Filter initialization routine and speed transmission. In this algorithm, the search radius has the same size for Brownian and directed motion hypothesis. **Color code:** Red and Green segments represent the detected types of displacement, which can be directed or Brownian respectively. Blue and Green circles represent the search radius associated with directed and Brownian motions respectively. The position of the search radius reflects the predicted localization (scale bar is $0.5 \mu m$, acquisition frequency is 1Hz).

1. As heterogeneous dynamical modeling is a major problem in our study, we extensively describe the ability of the methods that have been put forward to model diffusion, active transport and heterogeneous motions.
2. We review the linking cost optimization scheme used to estimate the best set of assignments between detections at different temporal levels: from consecutive frames, groups of frames or at the whole sequence level.
3. The spatial gating parameter estimation (a.k.a. search radius) is an other crucial issue when dealing with crowded scenes and unpredictable transitions.
4. The similarity distance used to build the cost function also deserves a separated discussion.

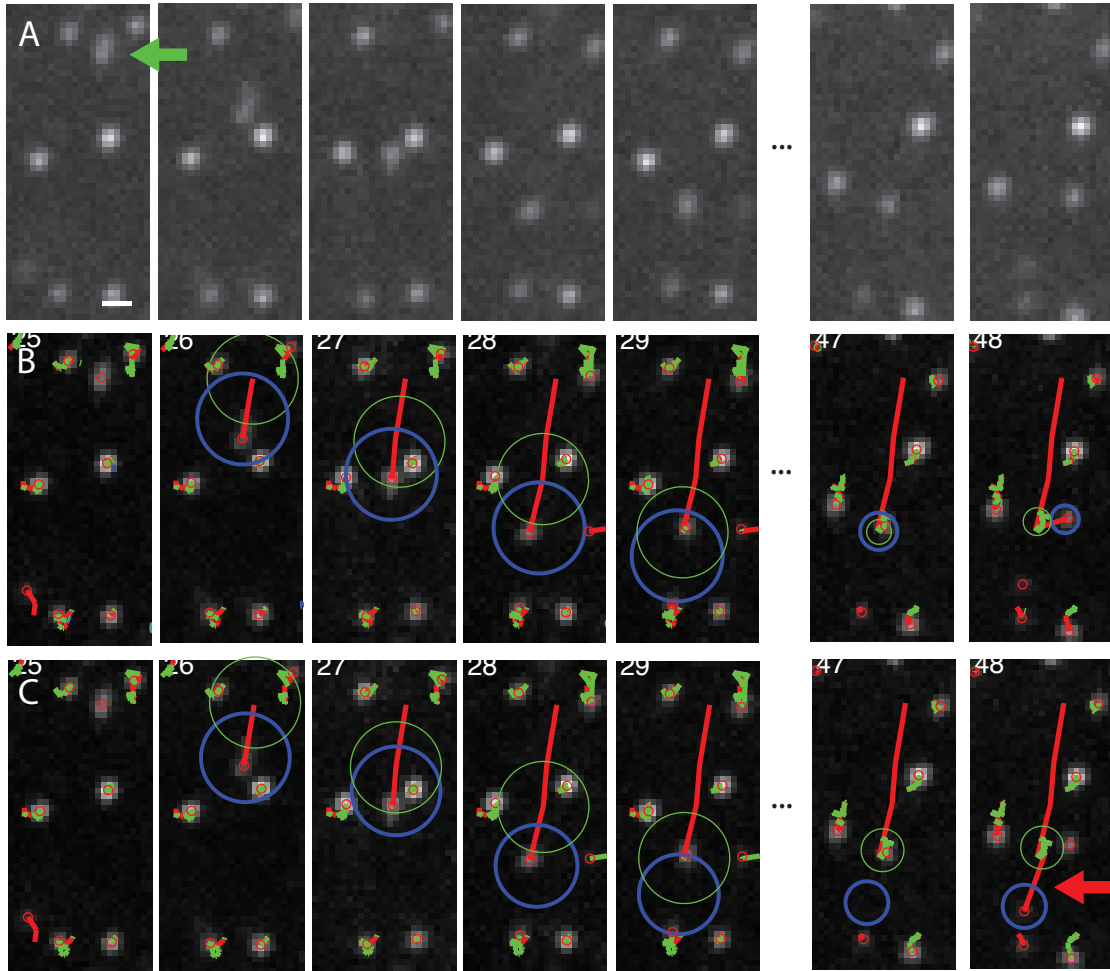


Figure 9.2: An example of motion heterogeneity in more dense conditions. **A)** The ULF move fast and switch to a confined Brownian motion. **B)** An IMM based algorithm produces a correct track, switching to a Brownian motion scheme. The merging of Kalman filters posterior results in an adaptive estimation of the speed that quickly converges to zero. **C)** The u-track algorithm produces a false positive due to the strong inertia of the stochastic filter. This figure shows an example of u-track convergence to a single speed for the track. Accordingly, the Kalman filter constantly “looks” in the general direction of the trajectory. **Color code:** Red and Green segments represent the detected types of displacement, which can be directed or Brownian respectively. Blue and Green circles represent the search radius associated with directed and Brownian motions respectively. The position of the search radius reflects the predicted localization (scale bar is $0.5 \mu m$, acquisition frequency is 1Hz).

5. Gap closing ability that fills “gaps” in tracks caused by transient disappearances or mis-detections.
6. The detection of particle merging or splitting events is crucial for molecule interaction analysis.

In this framework, we emphasize on their respective strengths and weaknesses at tracking heterogeneous motions in dense conditions. This will help to understand the limits of the methods described in the literature and suggest possible improvements. Finally, it is worth noting that a contribution of this review is the description of the u-track algorithm with statistical and probabilistic tools. This software is indeed widely used for various applications in MPT because of its robustness and flexibility. While the original publication focused mainly on the linear assignment problem, cost function design and experimental results, we describe in this review the dynamics modeling and gating method after a thorough analysis of the algorithm.

The outline of the Section is as follows. We first report the previous review efforts in the literature and we explain our positioning (see Section 9.1). As motion modeling and track termination/apparition are among the highest hurdles in our study, particle detection methods are briefly described (see Section 9.2). The six key criteria that allow for a complete description of each tracker in the literature are then discussed (see Sections 9.3 to 9.8). We conclude this study with a Table that uniquely summarize the numerical strategies put forward in fifteen algorithms chosen for their performances in biological imaging and originality (see Section 9.9).

9.1 Previous review effort

In [Meijering et al., 2012], the authors proposed a classification and a comparison of cell and particle tracking software, a majority of the related methods being also presented in this review. This valuable study allows an overview of particle tracking software to provide the end-users with a comprehensive comparison of the software availability and ability (cell, particle, 2D or 3D tracking ...) and to label the algorithm class as: “manual”, “semi-automatic” and “automatic”. In this section we will precise this aspect focusing essentially on “automatic” trackers. We discuss the flexibility of several trackers from a more technical point of view. As in [Meijering et al., 2012], we present a summarizing table at the end of this Chapter. However, we propose a more technical classification since we analyse underlying approximations, modelings and optimization solutions.

Kalaidzidis [2009] and Kalaidzidis [2007] also proposed a technical comparison of tracking algorithms. In this review, the author proposed a general description of tracking algorithms followed by a short discussion about applications to bio-imaging. In our

review effort, we also focus on the ability of algorithms to track particles with temporally varying dynamical models.

Finally, in sight of the 2012 ISBI conference, Erik Meijering and Jean-Christophe Olivo-Marin came up with a challenge in order to objectively compare state-of-the-art MPT methods on four simulated scenarios. The proposed simulated benchmarks are diffusing vesicles, microtubule plus-TIPs presenting directed motions, receptors exhibiting heterogeneous motions and finally three-dimensional diffusion of viruses. Each scenario were declined in low (100 particles/ 512×512 pixels) to high (1000 particles/ 512×512) particle density, and signal-to-noise ratios ranging from very low dose imaging (SNR 1) to the highest quality (SNR 7). Most of the challenge participants, fourteen teams in total, contributed to the MPT field. Those studies are also reported in our review. However, a few teams adapted algorithms primarily dedicated to track cells, aircrafts or even submarines¹. We also took up this challenge with a slight adaption of the local tracker presented in Section 5.2.2. Our modest contribution was suboptimal by design (no optimization at the frame scale, no motion modeling), and was submitted to highlight the impact of robust Gaussian fitting. Nevertheless, our detection reached the second position in detection RMSE on the “vesicle” experiment (the only one for which we submitted results). Detail on the implementation can found in Part I of this manuscript. The MPT algorithm we present in the current study is much more advanced tracking wise, but this study started long after the challenge was ended. As the recent publication associated to the challenge [Chenouard et al., 2014] was still in the reviewing process as we prepared this work, we did not exploit the simulated benchmark in our experiments.

It is worth noting that the competing methods were specifically designed given a specific training dataset provided by the organizers. As a result, a large set of submitted methods were conceptually very different from the original publications which served as starting points [Sbalzarini and Koumoutsakos, 2005; Smal et al., 2008b; Godinez et al., 2011]. Consequently, no specific probabilistic tracker (JPDA, Particle filters) was competing. The take-away message given by the organizers was fourfold: i) there is not a unique method that outperforms any others for a given scenario; ii) as expected, the methods that make use of multiple time points using Kalman filtering, multiple hypothesis tracking or gap closing perform better than the the others; iii) all the best performing methods use dedicated motion model to adapt to known dynamics for each dataset; iv) the methods that proved sufficient design flexibility to adapt to each scenario performed better.

In [Meijering et al., 2012], the underlying techniques are described in the Supplemental Method Section but only the tracking results are compared. In the present review, we propose a more technical comparison based on modeling and tracking strategies. While

¹When describing the work of Magnusson and Jaldén [2012] in our review, we actually refer to the adaptation to MPT that has been proposed for this challenge, as the original algorithm was designed for cell tracking.

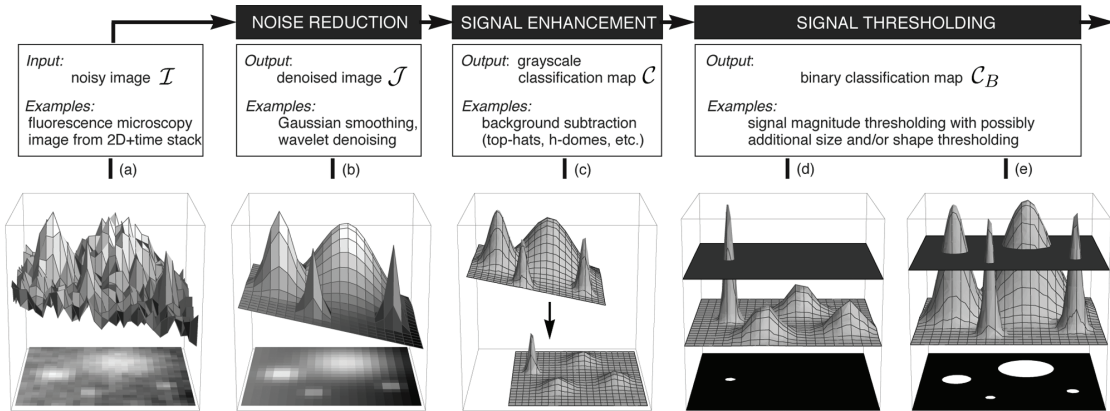


Figure 9.3: Object detection framework including noise reduction, signal enhancement and thresholding (source from: [Smal et al., 2010]).

experimenting with our method, we experimentally compared the methods that were designed for our targeted issue, i.e. those able to adapt to heterogeneous motion. Those methods consider multiple models to describe the dynamics in the literature and are implemented in the the best performing methods in the challenge. As in our study, the u-track performances were experimentally compared in the challenge. However, the competing implementation of u-track (independently developed from u-track designers) was not fair since it did not make use of the u-track multiple motion modeling.

9.2 Particle detection

It has been shown in an extensive review [Smal et al., 2010] that a variety of methods perform well for a wide range of signal-to-noise ratios. For $\text{SNR} > 3$, the general framework described by Smal et al. [2010] starts with an image pre-processing for noise reduction and object enhancement by using median, wavelet-based or Laplacian-of-Gaussian filters. The candidate spot coordinates are then selected using local-maxima localization or thresholding. Finally, the center coordinates of spots can be estimated using Gaussian model fitting or intensity centroid localization (see Figure 9.3 for an overview). For lower dose imaging, some authors advise to focus on machine learning-based methods to obtain more satisfying results.

As motion modeling and termination detection are the main issues in this study and detection can be performed independently, particle detection will not be described further. We refer the reader to the following works for an overview of spot detection methods [Cheezum et al., 2001; Thomann et al., 2002; Henriques et al., 2010; Smal et al., 2010].

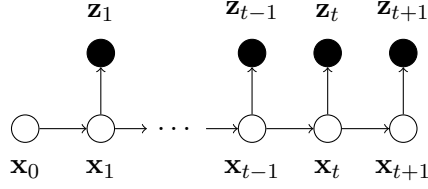


Figure 9.4: Dependency graph of a Hidden Markov process applied to the state \mathbf{x}_t and measure \mathbf{z}_t , $\forall t \in \mathbb{N}$.

9.3 Dynamics modeling

9.3.1 Bayesian filtering

Bayesian filtering has been applied in a large number of studies of dynamical system. While the parameters of a system evolve over time, sensors give a projection of this system by providing a limited, noisy and sometimes sparse measurements of the system state. By modeling the system state as a Hidden Markov Model, Bayesian filtering analyses measurement over time in order to provide an estimation of the system parameters. In this Section, we describe Bayesian filtering applied to the study of intracellular object dynamics. This includes Kalman filtering, multiple modeling and particle filtering.

In the Bayesian filtering framework, we assume an evolution model which is generally a Markov process of 1^{st} or 2^nd order. Denoting by \mathbf{x}_t and \mathbf{z}_t respectively the hidden state and the observation at time t and assuming a 1^{st} order Markov model, we have:

$$p(\mathbf{x}_{t+1}|\mathbf{x}_{1:t}) = p(\mathbf{x}_{t+1}|\mathbf{x}_t) \quad (9.1)$$

where $\mathbf{x}_{1:t} = \{\mathbf{x}_1, \dots, \mathbf{x}_t\}$. The filtering distribution $p(\mathbf{x}_{t+1}|\mathbf{z}_{1:t})$ (posterior distribution) obeys the following recursion rule if we assume a conditionally independent observation process:

$$p(\mathbf{x}_{t+1}|\mathbf{z}_{1:t+1}) \propto p(\mathbf{z}_{t+1}|\mathbf{x}_{t+1}) \int_{\mathbf{x}_t} p(\mathbf{x}_{t+1}|\mathbf{x}_t)p(\mathbf{x}_t|\mathbf{z}_{1:t})d\mathbf{x}_t \quad (9.2)$$

and $\mathbf{z}_{1:t} = \{\mathbf{z}_1, \dots, \mathbf{z}_t\}$. The recursion requires the specification of a dynamic model describing the state evolution $p(\mathbf{x}_{t+1}|\mathbf{x}_t)$ and the likelihood function of the data. A Hidden Markov Model, as illustrated in Figure 9.4, is entirely described by a prior distribution $p(\mathbf{x}_0)$, a transition probability $p(\mathbf{x}_{t+1}|\mathbf{x}_t)$ (from \mathbf{x}_t to \mathbf{x}_{t+1}) and the likelihood function $p(\mathbf{z}_t|\mathbf{x}_t)$. The aim of the recursive filtering is to estimate the *a posteriori* distribution $p(\mathbf{x}_{t+1}|\mathbf{z}_{1:t+1})$. A two-step approach (prediction and updating) is recommended to compute the filtering density:

Prediction step The prediction step, also known as process update, makes use of an evolution model to predict the probability distribution $p(\mathbf{x}_{t+1}|\mathbf{z}_{1:t})$ at time $t + 1$ given all

measurements till time t . The relationship between the measurements and the evolution model is given by the Chapman-Kolmogorov equation:

$$p(\mathbf{x}_{t+1}|\mathbf{z}_{1:t}) = \int p(\mathbf{x}_{t+1}|\mathbf{x}_t)p(\mathbf{x}_t|\mathbf{z}_{1:t})d\mathbf{x}_t. \quad (9.3)$$

Update (or filtering) step When a measurement is available at time $t + 1$, the predicted probability distribution is updated in one step, also called sensor update. An recursive expression for probability distribution $p(\mathbf{x}_{t+1}|\mathbf{z}_{1:t+1})$ is obtained from the Bayes' rule:

$$\begin{aligned} p(\mathbf{x}_{t+1}|\mathbf{z}_{1:t+1}) &= \frac{p(\mathbf{z}_{t+1}|\mathbf{x}_{t+1})p(\mathbf{x}_{t+1}|\mathbf{z}_{1:t})}{p(\mathbf{z}_{t+1}|\mathbf{z}_{1:t})} \\ &= \frac{p(\mathbf{z}_{t+1}|\mathbf{x}_{t+1})p(\mathbf{x}_{t+1}|\mathbf{z}_{1:t})}{\int p(\mathbf{z}_{t+1}|\mathbf{x}_{t+1})p(\mathbf{x}_{t+1}|\mathbf{z}_{1:t})d\mathbf{x}_{t+1}} \end{aligned} \quad (9.4)$$

where the denominator is a normalization term. The two-step optimal filter is only a conceptual solution, since the multidimensionality of the integral prevents the calculation of the analytical solution in most cases. However, different methods have been proposed in the literature to solve (9.3) and (9.4) with appropriate approximations. Assuming linearity and Gaussianity of the model, the Kalman filter provides the optimal solution. Similarly, an optimal solution is provided by the Grid-based Method [Doucet et al., 1998] under the assumption of a discrete state space and finite number of states. Suboptimal methods like Extended Kalman filters [Bar-Shalom, 1987], Unscented Kalman filter [Julier et al., 1995], and particle filters [Isard and Blake, 1996; Arulampalam et al., 2002] have been proposed to approximate the posterior density in more general cases, that is when linearity or Gaussianity cannot be assumed. In what follows, we discuss these probabilistic formulations applied to dynamics analysis of intracellular objects. We focus on three general modeling frameworks: Kalman filtering [Kalman and others, 1960], extension to interacting multiple models [Bar-Shalom et al., 2004] and particle filtering [Arulampalam et al., 2002].

9.3.2 Kalman Filtering

It is established that Kalman filtering [Kalman and others, 1960] provides the optimal estimation of the state of a linear stochastic process. In single molecule tracking [Genovesio et al., 2003; Briquet-Laugier et al., 1999], the vector state \mathbf{x}_t at time t usually represents the position and speed of the target (or object) or an equivalent description (modeled here in 2D for simplicity, a 3D model deriving straightforwardly):

$$\mathbf{x}_t = (x_t, y_t, dx_t, dy_t)^\top. \quad (9.5)$$

The filtering problem can be described by the following equation system:

$$\mathbf{x}_{t+1} = \mathbf{F}\mathbf{x}_t + \mathbf{w}_t \quad (9.6)$$

$$\mathbf{z}_{t+1} = \mathbf{H}\mathbf{x}_{t+1} + \mathbf{v}_t \quad (9.7)$$

where the transition matrix \mathbf{F} represents the motion type, usually expressed as:

$$\mathbf{F} = \begin{pmatrix} 1 & 0 & 0 & 0 \\ 0 & 1 & 0 & 0 \\ 0 & 0 & 0 & 0 \\ 0 & 0 & 0 & 0 \end{pmatrix} \quad \text{or} \quad \mathbf{F} = \begin{pmatrix} 1 & 0 & 1 & 0 \\ 0 & 1 & 0 & 1 \\ 0 & 0 & 1 & 0 \\ 0 & 0 & 0 & 1 \end{pmatrix} \quad (9.8)$$

for Brownian and directed motion. The matrix \mathbf{H} is an observation matrix projecting from the state space to the measurement space. The variable \mathbf{w}_t and \mathbf{v}_t represent respectively the model noise and the measurement noise assumed to be zero-mean independent white noise with covariance matrices \mathbf{Q}_t and \mathbf{R}_t . In Bayesian sequential estimation with the aforementioned hypothesis, the filtering distribution $p(\mathbf{x}_{t+1}|\mathbf{z}_{1:t+1}) \sim \mathcal{N}(\hat{\mathbf{x}}_{t+1}, \hat{\mathbf{P}}_{t+1})$ can be computed recursively as derived in [Anderson and Moore]. The prediction step yields:

$$\bar{\mathbf{x}}_{t+1} = \mathbf{F}\hat{\mathbf{x}}_t \quad (9.9)$$

$$\bar{\mathbf{P}}_{t+1} = \mathbf{F}\hat{\mathbf{P}}_t\mathbf{F}^\top + \mathbf{Q}_t \quad (9.10)$$

followed by the update step when a new measurement \mathbf{z}_{t+1} is available:

$$\mathbf{K}_{t+1} = \frac{\bar{\mathbf{P}}_{t+1}\mathbf{H}^\top}{\mathbf{H}\bar{\mathbf{P}}_{t+1}\mathbf{H}^\top + \mathbf{R}_{t+1}} \quad (9.11)$$

$$\hat{\mathbf{P}}_{t+1} = (\mathbf{I} - \mathbf{K}_{t+1}\mathbf{H})\bar{\mathbf{P}}_{t+1} \quad (9.12)$$

$$\hat{\mathbf{x}}_{t+1} = \bar{\mathbf{x}}_{t+1} + \mathbf{K}_{t+1}(\mathbf{z}_{t+1} - \mathbf{H}\bar{\mathbf{x}}_{t+1}) \quad (9.13)$$

where \mathbf{K}_{t+1} is the adaptive Kalman gain applied to the measured innovation ($\mathbf{z}_{t+1} - \mathbf{H}\bar{\mathbf{x}}_{t+1}$) and \mathbf{I} denotes the identity matrix. Updated at each time step, the gain represents the inertia of the Kalman filter. Low prediction errors (w.r.t. measurement errors) will lead to a low value for the gain and strong inertia as the filter follows the prior model. Conversely, for high prediction errors, the estimate is very close to the measurement. Let us note that in a large number of tracking algorithms, combinatorial assignment algorithms are used to associate the predicted state $\bar{\mathbf{x}}_{t+1}$ with the “best” measurement considering the entire set of detections. Accordingly, the measurement \mathbf{z}_t does not depend only on \mathbf{x}_t and (9.15) is considered as an approximation.

9.3.3 Multiple dynamical model filtering

A single Kalman filter cannot take into account the variety of intracellular transportation. Moreover, a general constant speed model is not reactive enough to deal with abrupt temporal changes [Genovesio et al., 2006]. To handle different dynamics, tracking methods for maneuvering targets [Blom and Bar-Shalom, 1988; Bar-Shalom et al., 2004] use N Kalman Filters with different transition matrices:

$$\mathbf{x}_{t+1} = \mathbf{F}^{\theta_{t+1}}\mathbf{x}_t + \mathbf{w}_{t+1}^{\theta_{t+1}} \quad (9.14)$$

$$\mathbf{z}_{t+1} = \mathbf{H}^{\theta_{t+1}}\mathbf{x}_{t+1} + \mathbf{v}_{t+1}^{\theta_{t+1}}, \quad (9.15)$$

where $\theta_t \in \Lambda = \{1, \dots, N\}$ and $\theta_{1:t} = \{\theta_1, \theta_2, \dots, \theta_t\}$ is the sequence of model indexes to be estimated and assumed to follow an homogeneous Markov process, $\mathbf{F}^{\theta_{t+1}}$ is the transition matrix associated to the dynamical model $\theta_{t+1} \in \Lambda$. The same association applies for the other Kalman filtering notations presented Section 9.3.2. Each possible sequence for $\theta_{1:t}$ should be considered to filter the state parameter optimally as:

$$p(\mathbf{x}_{t+1}, \mathbf{z}_{1:t+1}) = \sum_{\theta_1 \in \Lambda} \sum_{\theta_2 \in \Lambda} \cdots \sum_{\theta_{t+1} \in \Lambda} p(\mathbf{x}_{t+1}, \mathbf{z}_{1:t+1}, \theta_1, \dots, \theta_{t+1},) \quad (9.16)$$

$$\propto \sum_{\theta_1 \in \Lambda} \sum_{\theta_2 \in \Lambda} \cdots \sum_{\theta_{t+1} \in \Lambda} p(\theta_{1:t+1} | \mathbf{z}_{1:t+1}) p(\mathbf{x}_{t+1} | \theta_{1:t+1}, \mathbf{z}_{1:t+1}) \quad (9.17)$$

The parameter space describing $\theta_{1:t}$ is exponentially increasing with time. Accordingly, this model “history” [Bar-Shalom et al., 2004] would require an exponentially growing number of Kalman filters to estimate the *a posteriori* distribution. A common approximation proposed in the literature is to consider the last $N \in \mathbb{N}$ possible modes as:

$$p(\mathbf{x}_{t+1}, \mathbf{z}_{1:t+1}) \approx \sum_{\theta_{t+1} \in \Lambda} p(\theta_{t+1} | \mathbf{z}_{1:t+1}) p(\mathbf{x}_{t+1} | \theta_{t+1}, \mathbf{z}_{1:t+1}), \quad (9.18)$$

implemented as N competing Kalman filters, that is

$$p(\mathbf{x}_{t+1} | \mathbf{z}_{1:t+1}, \theta_{t+1}) \sim \mathcal{N}(\mathbf{x}_{t+1}; \hat{\mathbf{x}}_{t+1}^{\theta_{t+1}}, \hat{\mathbf{P}}_{t+1}^{\theta_{t+1}}). \quad (9.19)$$

Finally the moments of the Gaussian mixture yields the expectation and covariance of the overall posterior at time step $t + 1$:

$$\hat{\mathbf{x}}_{t+1} = \sum_{\theta_{t+1} \in \Lambda} p(\theta_{t+1} | \mathbf{z}_{1:t+1}) \hat{\mathbf{x}}_{t+1}^{\theta_{t+1}} \quad (9.20)$$

$$\hat{\mathbf{P}}_{t+1} = \sum_{\theta_{t+1} \in \Lambda} p(\theta_{t+1} | \mathbf{z}_{1:t+1}) \left(\hat{\mathbf{P}}_{t+1}^{\theta_{t+1}} + \|\hat{\mathbf{x}}_{t+1}^{\theta_{t+1}} - \hat{\mathbf{x}}_{t+1}\|^2 \right). \quad (9.21)$$

In the application to multiple intracellular target tracking, the predictions provided by Kalman filters are used in the linking cost optimization procedure. Two works [Genovesio et al., 2006; Jaqaman et al., 2008] have been proposing different approaches to motion heterogeneity modeling. In [Genovesio et al., 2006], the Interacting Multiple Model estimator introduced in [Blom and Bar-Shalom, 1988] is first proposed. It is well characterized and it is now widespread in the MPT literature. The u-track method [Jaqaman et al., 2008] has not been described formally with mathematical justification. In this Section, we show that this algorithm can be interpreted as a Generalized Pseudo Bayesian filter of order 1. We also describe in detail the implementation of the u-track algorithm to give further insights into its performance.

9.3.3.1 Generalized Pseudo Bayesian of order 1

In the u-track algorithm [Jaqaman et al., 2008], a thorough reverse engineering analysis shows that the algorithm is similar to the Generalized Pseudo Bayesian algorithm of order one (GPB1). This algorithm has primarily been described by Ackerson and Fu [1970] and is refereed in [Tugnait, 1982; Bar-Shalom et al., 2004]. In this modeling approach, the Gaussian mixture described by (9.18) is directly exploited by Kalman filters. Accordingly, the overall posterior described by $\hat{\mathbf{x}}_t$ and $\hat{\mathbf{P}}_t$ in (9.19) is considered as the current filtered estimate for each dedicated Kalman filters. Each filter obeys to (9.9) and (9.11) with different transition matrices. The probability $p(\theta_t|\mathbf{z}_{1:t}), \forall \theta_t \in \Lambda$ can then be derived recursively as:

$$p(\theta_{t+1}|\mathbf{z}_{1:t+1}) = p(\mathbf{z}_{t+1}|\mathbf{z}_{1:t}, \theta_{t+1}) \sum_{\theta_t \in \Lambda} p(\theta_{t+1}|\theta_t)p(\theta_t|\mathbf{z}_{1:t}). \quad (9.22)$$

In practice, u-track does not consider model “history” to estimate the current dynamical model probability. Only the most probable model is kept in the posterior:

$$\begin{cases} p(\theta_{t+1}|\mathbf{z}_{1:t+1}) = 1 & \text{if } \theta_{t+1} = \underset{\theta_{t+1} \in \Lambda}{\operatorname{argmax}} \left(\mathcal{N}(z_{t+1}; H\bar{\mathbf{x}}_{t+1}^{\theta_{t+1}}, H^{\theta_{t+1}}\bar{P}_{t+1}^{\theta_{t+1}} {}^t H^{\theta_{t+1}} + R_t^{\theta_{t+1}}) \right) \\ p(\theta_{t+1}|\mathbf{z}_{1:t+1}) = 0 & \text{else} \end{cases} \quad (9.23)$$

Hence, only the Kalman filter associated to the most probable model is updated. Using this approximation, GPB1 algorithm can operate every filtering cycle with N prediction steps and only one Kalman filter that operates full recursion. This can reduce significantly the computational complexity.

9.3.3.2 Interacting multiple model

In the Interacting Multiple Model estimator (IMM) [Blom and Bar-Shalom, 1988], a recursive estimation of the dynamical model transition probability is exploited to increase the amount of information available from the model “history” while using only N Kalman filters. The N Kalman filters estimate the respective posteriors from a mixture of Gaussians which is an alternative to the overall posterior (9.18). The “mixing” of the Gaussian distributions is controlled by the estimated transition probabilities. This method has been primarily designed for the detection of smooth transitions in aircraft dynamics between cruising (directed displacement) and maneuvering (Brownian model or constant acceleration model). It was exploited to track multiple particles in bio-imaging for the first time in [Genovesio et al., 2006]. This method is now widespread in the field of MPT [Feng et al., 2011; Rezatofghi et al., 2012; Chenouard et al., 2014]. In this section, we briefly describe this algorithm.

Each probability $p(\mathbf{x}_{t+1}|\theta_{t+1}, \mathbf{z}_{1:t+1})$ in (9.18) is further decomposed to point out the model transition from the dynamic model at time t to the future dynamic model at time

$t + 1$ [Blom and Bar-Shalom, 1988]:

$$p(\mathbf{x}_{t+1}, \mathbf{z}_{1:t+1}) = \sum_{\theta_{t+1} \in \Lambda} p(\theta_{t+1} | \mathbf{z}_{1:t+1}) \frac{p(\mathbf{z}_{t+1} | \mathbf{x}_{t+1}, \theta_{t+1})}{p(\mathbf{z}_{t+1} | \mathbf{z}_{1:t}, \theta_{t+1})} p(\mathbf{x}_{t+1} | \theta_{t+1}, \mathbf{z}_{1:t}) \quad (9.24)$$

$$= \sum_{\theta_{t+1} \in \Lambda} p(\theta_{t+1} | \mathbf{z}_{1:t+1}) \frac{p(\mathbf{z}_{t+1} | \mathbf{x}_{t+1}, \theta_{t+1})}{p(\mathbf{z}_{t+1} | \mathbf{z}_{1:t}, \theta_{t+1})} \int p(\mathbf{x}_{t+1} | \mathbf{x}_t, \theta_{t+1}) p(\mathbf{x}_t | \mathbf{z}_{1:t}, \theta_{t+1}) d\mathbf{x}_t. \quad (9.25)$$

The last term $p(\mathbf{x}_t | \mathbf{z}_{1:t}, \theta_{t+1})$ represents the probability of the state \mathbf{x}_t given a possible future dynamical model θ_{t+1} . It can be further derived as

$$p(\mathbf{x}_t | \mathbf{z}_{1:t}, \theta_{t+1}) \propto \sum_{\theta_t \in \{1 \dots N\}} p(\mathbf{x}_t | \mathbf{z}_{1:t}, \theta_t) p(\theta_t | \theta_{t+1}, \mathbf{z}_{1:t}). \quad (9.26)$$

For a given dynamical model index $\theta_t \in \Lambda$, the associated Kalman filter yields:

$$p(\mathbf{x}_t | \mathbf{z}_{1:t}, \theta_t) \sim \mathcal{N}(\mathbf{x}_t; \hat{\mathbf{x}}_t^{\theta_t}, \hat{\mathbf{P}}_t^{\theta_t}). \quad (9.27)$$

Accordingly, the integral in (9.25) can be interpreted as a Kalman state prediction, and each member of the sum can be interpreted as a sensor update of a Kalman filter associated to the model θ_{t+1} (see (9.4)). In other words, before estimating the filtered state at time $t + 1$ with the Kalman filter associated to model θ_{t+1} , the Gaussian mixture (9.19) is reconditioned as [Blom and Bar-Shalom, 1988]:

$$p(\mathbf{x}_t | \mathbf{z}_{1:t}, \theta_{t+1}) \sim \mathcal{N}(\mathbf{x}_t; \tilde{\mathbf{x}}_t^{\theta_{t+1}}, \tilde{\mathbf{P}}_t^{\theta_{t+1}})$$

where

$$\tilde{\mathbf{x}}_t^{\theta_{t+1}} = \sum_{\theta_t \in \{1 \dots N\}} p(\theta_t | \theta_{t+1}, \mathbf{z}_{1:t}) \hat{\mathbf{x}}_t^{\theta_t} \quad (9.28)$$

$$\tilde{\mathbf{P}}_t^{\theta_{t+1}} = \sum_{\theta_t \in \{1 \dots N\}} p(\theta_t | \theta_{t+1}, \mathbf{z}_{1:t}) \left(\hat{\mathbf{P}}_t^{\theta_t} + \|\hat{\mathbf{x}}_t^{\theta_t} - \tilde{\mathbf{x}}_t^{\theta_{t+1}}\|^2 \right). \quad (9.29)$$

The probability $p(\theta_t | \theta_{t+1}, \mathbf{z}_{1:t})$ can be derived using the Bayes' rule as [Bar-Shalom et al., 2004]:

$$p(\theta_t | \theta_{t+1}, \mathbf{z}_{1:t}) \propto p(\theta_{t+1} | \theta_t, \mathbf{z}_{1:t}) p(\theta_t | \mathbf{z}_{1:t}), \quad (9.30)$$

$$= p(\theta_{t+1} | \theta_t) p(\theta_t | \mathbf{z}_{1:t}). \quad (9.31)$$

The probability $p(\theta_t | \mathbf{z}_{1:t}), \forall \theta_t \in \Lambda$ is computed as in (9.22).

9.3.3.3 Implementations of multiple modeling algorithms

The differences between the algorithms proposed in [Genovesio et al., 2006] and in [Jaqaman et al., 2008] reside in their implementation as much as the underlying theory. A combination of three aspects must be taken into account to understand the differences highlighted in Figures 9.1 and 9.2.

The first aspect is the initialization step. In order to set a prior for the initialization of the Kalman filter speed, u-track performs three rounds of tracking in forward and backward directions by reversing the temporal order of the image sequence. The IMM algorithm that we have re-implemented for illustration and experimental results also supports this strategy.

An other specificity of u-track is the unusual transition matrix used to model the Brownian state:

$$\mathbf{F} = \begin{pmatrix} 1 & 0 & 0 & 0 \\ 0 & 1 & 0 & 0 \\ 0 & 0 & 1 & 0 \\ 0 & 0 & 0 & 1 \end{pmatrix}. \quad (9.32)$$

This representation means that the speed vector $(dx_t, dy_t)^\top$ in the state parameter is entirely transmitted by the Brownian Kalman filter as far as the estimated gain is low.

Finally, u-track does not merge estimates. As a result, if a particle stays in a Brownian state and follows this model, it will present a low gain and the temporal filter will let the speed estimate unfiltered. This speed estimate will be unchanged even if it is not realistic in the current situation.

The consequence of these three implementation details is that the estimates $\hat{\mathbf{x}}_t$ can converge on a single vector $(\widehat{dx}_t, \widehat{dy}_t)^\top$ during the three rounds of tracking, even if motion type switches have been detected. This modeling actually increases robustness when an object undergoes a directed displacement in a unique direction or slowly changes before switching to a Brownian walk. Figure 9.1B shows that u-track converges on a single displacement for the track and can estimate a segment of the directed motion. On the same data, a more classical IMM, even with the improved initialization, is only able to recover the Brownian segments. Figure 9.2 highlights the limitations of such an approach. The strong inertia of the filter and the unique speed estimation result in important false positives in dense and heterogeneous conditions. In our new tracking method, we will combine the two approaches to benefit from IMM flexibility and good convergence properties of u-track.

9.3.4 Particle filtering

When the linear and/or Gaussian assumptions do not hold, particle filtering [Arulampalam et al., 2002] allows us to estimate the posterior density $p(\mathbf{x}_{t+1} | \mathbf{z}_{1:t+1})$. Particle filters

represent the posterior by a finite set of N_p particles \mathbf{x}_{t+1}^m and associated weights w_{t+1}^m as:

$$p(\mathbf{x}_{t+1}|\mathbf{z}_{1:t+1}) = \sum_{m=1}^{N_p} w_{t+1}^m \delta(\mathbf{x}_{t+1} - \mathbf{x}_{t+1}^m) \quad (9.33)$$

where $\sum_{m=1}^{N_p} w_{t+1}^m = 1$. The particles can be chosen carefully from the importance function $\mathbf{x}_{t+1}^m \sim q(\mathbf{x}_{t+1}|\mathbf{x}_t^m, \mathbf{z}_{t+1})$ allowing for an efficient representation of the posterior. The updating of weights is then as follows:

$$w_{t+1}^m = w_t^m \frac{p(\mathbf{z}_{t+1}|\mathbf{x}_{t+1}^m)p(\mathbf{x}_{t+1}^m|\mathbf{x}_t^m)}{q(\mathbf{x}_{t+1}|\mathbf{x}_t^m, \mathbf{z}_{t+1})}. \quad (9.34)$$

The default choice consists in taking $q(\mathbf{x}_{t+1}|\mathbf{x}_t^m, \mathbf{z}_{t+1}) = p(\mathbf{x}_{t+1}|\mathbf{x}_t)$ (bootstrap filter). An estimate $\hat{\mathbf{x}}_{t+1}$ can then be obtained using the minimum mean square estimator as in [Smal et al., 2008a] yielding $\hat{\mathbf{x}}_{t+1} = \sum_{m=1}^{N_p} w_{t+1}^m \mathbf{x}_{t+1}^m \approx \mathbb{E}[x_{t+1}|z_{1:t+1}]$.

The exponential complexity due to the simultaneous tracking of several objects combined with the tendency of the particle filter to coalesce on one single mode can be problematic if the object number is too large [Smal et al., 2008a]. To circumvent this issue, mixture of particles [Smal et al., 2008a; Yoon et al., 2008] and independent particle filters [Godinez et al., 2009], have been proposed. Moreover, these techniques use image intensity to define measurements. For instance, patch-based distance between a Gaussian model and image data is generally adopted. Detection is carried out online on a per-track basis and proved to be robust to low dose imaging conditions and in the case of highly spatially and temporally varying background. Nevertheless, as particle filter based methods present a high computational cost [Smal et al., 2008b] and the objects (spots) look very similar [Godinez et al., 2009], these probabilistic approaches are often applied in sparse and noisy scenario as in [Smal et al., 2008a; Godinez et al., 2009]. Note that motion heterogeneity modeling has been recently combined with particle filtering in [Yang et al., 2012] to estimate “stop-and-go” dynamics of growing axons.

9.3.5 Other statistical methods

In a recent paper, Winter et al. [2012] proposed an original approach to quantify the directed axonal transport without stochastic filtering. Let $L_{0,t}$ be the track set at time t . Each possible trajectory up to time $t + W$ is built (typically W is set to 6 in the experiment). In this set, the i th track is described by the length l_i , the set of intensities $\{I_{0,i}, \dots, I_{T+W,i}\}$ and the set of local speeds $\{dx_{0,i}, \dots, dy_{T+W,i}\}$ and $\{dy_{0,i}, \dots, dy_{T+W,i}\}$. The cost of the i th track is thus computed based on speed, intensity and track length as a weighting cue:

$$C(i) = l_i \left(\frac{\text{Var}_{t \in \{0..T+W\}} [I_{t,i}]}{\text{mean}_{t \in \{0..t+W\}} [I_{t,i}]} + \frac{\text{Var}_{t \in \{0..T+W\}} [\sqrt{dx_{t,i}^2 + dy_{t,i}^2}]}{\text{mean}_{t \in \{0..t+W\}} [\sqrt{dx_{t,i}^2 + dy_{t,i}^2}]} \right) \quad (9.35)$$

Contrary to filter-based methods, this estimator exploits past and future measurements and thus could potentially handle unpredictable switching. However the speed estimate is not temporally locally adaptive, leading an over-smoothing of the speed estimation.

Finally, a large collection of other methods relies on the Euclidean distance or Mahalanobis distance with global covariance parameter to capture Brownian motion [Bonneau et al., 2004; Sbalzarini and Koumoutsakos, 2005; Racine et al., 2006; Sergé et al., 2008; Liang et al., 2010; Magnusson and Jaldén, 2012].

9.3.6 Conclusion

The flexibility and simplicity of multiple Kalman filtering is the best trade-off between precision and computational cost. This statement made on theoretical basis is confirmed by the algorithm chosen by the participants of the MPT challenge organized for ISBI 2012 (and recently published [Chenouard et al., 2014]). Particle filtering is more general and more flexible, but also computationally demanding; it cannot easily handle several hundreds of targets in dense conditions. The usual issue of filter-based motion modeling is that they do not exploit the whole dataset. Accordingly, the related methods cannot predict sudden changes of direction. More recently, Winter et al. [2012] have proposed an interesting approach to profit from past and future measurements. This method handles only directed motions, but the cost function could be adapted to piecewise stationary dynamics. However this method requires to compute a cost for every physically possible track. The temporal window must be reduced to lower the computational demand, but one would then loose the temporal perspective. In our method, we propose a stochastic smoothing approach on dynamic modeling exploiting each measurement in the sequence while keeping a computationally efficient per-track basis.

9.4 Linking cost optimization

A prior dynamical model can be used to predict object positions at different time steps, but the optimal assignment between the set of predictions and measurements must also be estimated. The so-called linking problem is formulated as the minimization of an objective energy of the following form:

$$L_{T_e, T_s} = \underset{\{C_{t,ij} \in \{0,1\}\}}{\operatorname{argmin}} \sum_{t=T_s}^{T_e} \sum_{i=1}^{N_t} \sum_{j=1}^{N_{t+1}} C_{t,ij} d(\bar{\mathbf{x}}_{t,i}, \mathbf{z}_{t+1,j}) \quad (9.36)$$

$\mathbf{z}_{t+1,j}$ is the j th detected spot at time $t + 1$.

$\bar{\mathbf{x}}_{t,i}$ is the prediction at time $t + 1$ associated with the i th detection at time t .

N_t is the number of detected spots at time t .

T_s and T_e denote respectively the beginning and the end of the temporal window used for linking cost minimization.

$C_{t,ij} \in \{0, 1\}$ is a binary variable indicating the presence of a link ($C_{t,ij} = 1$) or the absence ($C_{t,ij} = 0$) between the detected targets i and j at time t and $t + 1$.

$d(\cdot)$ is a similarity measure to evaluate the correspondence between predictions and measurements.

We add a flexible constraint on assignment to model particle appearance, linking, disappearance, merging and splitting:

$$\begin{aligned} \sum_{j \in N_{t+1}} C_{t,ij} &\leq 2, \quad \forall i \in N_t, \quad \forall t \in \{T_s, \dots, T_e\}, \\ \sum_{i \in N_t} C_{t,ij} &\leq 2, \quad \forall j \in N_{t+1}, \quad \forall t \in \{T_s, \dots, T_e\}. \end{aligned} \quad (9.37)$$

Due to the computational complexity, no optimization method attempts to estimate the whole track set as a single combinatorial problem (see [Racine et al., 2006] for a seldom effort). Instead, the parameter space of possible associations is gated in space and time. In order to gate the parameter spatially, most of the algorithms straightforwardly use a search radius generally set by the user (see Section 9.5). The strategies used for temporal gating are more diversified, ranging from single frame-to-frame association [Jaqaman et al., 2008; Genovesio et al., 2006; Smal et al., 2008b; Sergé et al., 2008; Godinez et al., 2009; Rezatofghi et al., 2012; Smal et al., 2008a; Liang et al., 2010; Winter et al., 2012], optimization on a group of frames [Sbalzarini and Koumoutsakos, 2005; Chenouard et al., 2013; Feng et al., 2011] to more global optimization techniques [Racine et al., 2006; Magnusson and Jaldén, 2012]. Those different optimization strategies have an important impact on the intrinsic properties of linking algorithms. The number of objects that can be handled is limited for some of them [Kalaidzidis, 2009]. Those design choices also define the ability to close gaps in tracks due to object mis-detection or temporary disappearance, to detect track termination and creation or to handle merging and splitting of tracks.

In this section we give an overview of possible strategies, starting from the naive Nearest Neighbors up to the more complex MHT based algorithm. We also propose a short description of three ad-hoc methods that stands out in the MPT literature.

9.4.1 Nearest Neighbor assignment

A Nearest Neighbor-based method for frame-to-frame assignment has been proposed by Genovesio et al. [2006]. Let N_t be the number of detections at time t . A similarity measure list is computed for each possible association: $\{d(\bar{\mathbf{x}}_{t,i}, \mathbf{z}_{t+1,j}) / (i, j) \in [1, N_t] \times [1, N_{t+1}]\}$.

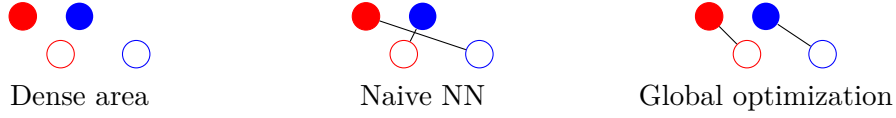


Figure 9.5: Naive Nearest-Neighbor assignment and global optimization. Filled circles represent detection $\mathbf{z}_{t+1,i}$, outlined circles represent associated prediction $\bar{\mathbf{x}}_{t,i}$.

Furthermore, This list is sorted, and the $\min(N_t, N_{t+1})$ shortest links that satisfy a threshold set by the user are selected. This method is “sub-optimal in a global sense” as noticed by the authors. Indeed, in the case of particles close to each other, this method is not sophisticated enough to match particles properly (see Figure 9.5). However it allows the detection of track appearances and disappearances which correspond respectively to the predictions and measurements that have not been assigned.

9.4.2 Linear programming in a bi-partite detection graph

In order to improve the frame-to-frame linking method, [Sbalzarini and Koumoutsakos \[2005\]](#) have proposed an approach formulated as a transportation problem, as already described in [\[Hitchcock, 1941\]](#). Given a set of links $L_{T_s, T_{s+1}}$, assignments are initialized using a Nearest Neighbor approach similar to [\[Genovesio et al., 2006\]](#); then possible re-assignments for each link are evaluated until the minimum cost is reached. Additionally, to handle temporary disappearances of the tracked object, [Sbalzarini and Koumoutsakos \[2005\]](#) proposed to estimate multiple link sets $L_{T_s, T_{s+r}}$ separately. For each detection at time T_s , the best association among the $r \in \{2, 3\}$ link sets is selected. As a link between two non temporally consecutive detections can be selected against consecutive detections, the algorithm is efficient to handle short disappearances. The disadvantage is that it can also bypass a detection in a track, or create false positives due to target crossing paths. In order to model appearance, disappearance and gap closing, dummy (also called virtual) detections have been introduced.

To address the temporal suboptimality issue, the link set is optimized both spatially and temporally in [\[Jaqaman et al., 2008\]](#) using a two-step approach. The spatial optimization is performed on each pair of frames resulting in track segments (or tracklets). The temporal optimization associates tracklets that are likely to stem from the same trajectory but corrupted by transient disappearances or mis-detections. Both steps rely on a sparse graph model representation and require the use of the shortest-path algorithm [\[Jonker and Volgenant, 1987\]](#). To avoid irremediable false positive linking due to the lack of temporal perspective in the first step, the authors proposed to set an upper bound on the search radius.

9.4.3 Probabilistic methods

While those methods select the most likely measurement at each time step, joint probabilistic data association (JPDA) [Bar-Shalom, 2000; Fortmann et al., 1980; Blackman and House, 1999] iteratively maintains the probability distribution for each possible assignment, assuming a fix number of tracks. Several strategies have been put forward to handle track creations and terminations for a limited number of bio-image sequences [Smal et al., 2008b; Godinez et al., 2011; Rezatofghi et al., 2012]. At each frame, the best set of assignments can be determined using an exhaustive review of possible hypothesis inside the same track gate [Sergé et al., 2008]. This method can be computationally expensive [Kalaidzidis, 2009] though, in theory, this could be achieved more efficiently using linear programming algorithm [Blackman and House, 1999]. To handle short disappearances, trajectories are maintained during a few frames using virtual detections. The track is considered terminated after a fix number of frames without assignment candidate within the track gate. Those methods can solve ambiguous scenarios like nearby tracks that coalesce and temporarily result in a single detection. However, dense scenarios associated with numerous disappearances would trigger high computational cost and cannot perform better than the aforementioned methods [Kalaidzidis, 2009].

Some recent works exploit particle filtering to implement tracking in the Bayesian framework [Godinez et al., 2009; Smal et al., 2008a] as presented in Section 9.3.4. As the measurement is the whole image, there is no explicit linking cost optimization as described by (9.36). In a paper focused on probabilistic and deterministic approaches by [Godinez et al., 2009], the authors concluded that the best performing methods rely on independent particle filters. In the case of close predictions (i.e. Euclidean distance is inferior to a given threshold) when the *a posteriori* distribution is not unimodal, a local optimization scheme and a graph-based model are proposed to handle interactions. Godinez et al. [2009] use the same method as described in [Sbalzarini and Koumoutsakos, 2005] to deal with close spot assignment. This work hints that probabilistic tracking appears especially suitable to challenging detection and estimation of a low number of targets; deterministic combinatorial algorithm are required to tackle density.

9.4.4 Multiple Hypothesis Tracking

To go beyond simple frame-to-frame association, multiple hypothesis tracking (MHT) methods have been proposed to optimize the linking set by considering all possible tracks on the entire sequence using linear programming algorithms [Reid, 1979; Blackman, 2004]. Nevertheless, the exponentially growing computational complexity is a limiting factor for applications in biological imaging. They are typically designed for tracking twenty objects at most [Kalaidzidis, 2009; Liang et al., 2010]. In a recent paper [Chenouard et al., 2013], the authors proposed a contribution to address this issue by reducing the parameter space using a tow-fold strategy: i) the sequence is first divided into groups of

frames (up to five frames); ii) all the possible tracks are clustered spatially in order to take advantage of sparsity. To do so, two tracks are considered in the same cluster if they share a common detection inside their track gates. The computational cost is thus shown to increase linearly with the image size and frame number. However, in dense spatiotemporal conditions, even restricted gatings do not always allow for tracks clustering. Increasing linearly, spatiotemporal density is likely to increase the exponentially computational complexity.

In order to handle short disappearances, virtual detections are inserted as association candidates at each time step. All possible tracks cost are estimated with stochastically filtering. For each cluster, the optimal track set is finally estimated using a linear programming algorithm. The method is demonstrated to outperform competing methods in low SNR conditions and sparse scenarios.

9.4.5 Three ad-hoc assignment methods

Other authors proposed original approaches to address the linking cost optimization problem. These approaches are based on different concepts but produce very satisfying results in many applications. In this section, we detail three representative algorithms.

In [Winter et al., 2012], the authors proposed a method appropriate for specific applications such as the tracking of axonal transport presenting a constant speed and no transient disappearances. The link set L_{T_e, T_e+1} is optimized on a frame-to-frame basis but a given temporal window $[T_e, T_e + W]$ is used to estimate the local velocity. Instead of using a traditional stochastic filter, costs are assigned to each possible track extension using a least mean squares estimation of the local speed of each possible tracklet in the group of frames $[T_e, T_e + W]$ (Section 9.3.5). Hence, the best track set is selected using a minimum spanning tree passing by every detection. The link set L_{T_e, T_e+1} between the first two frames is finally selected and the process is iterated at time $T_e + 1$. The minimum spanning tree algorithm handles efficiently merging and splitting but gap closing is not possible and termination can be confounded with merging.

Racine et al. [2006] proposed an ambitious method that optimizes the link set in a single optimization step. The track set is initialized using a frame-to-frame Nearest Neighbor procedure. Simulated annealing algorithm is then used to estimate the global minimum of the objective energy. The method can also handle merging and splitting. Recently, a extension has been proposed to handle gap closing in the particle tracking challenge [Chenouard et al., 2014]. Yet, incorporating constant speed or heterogeneous motion models cannot be implemented in this framework [Racine et al., 2006] so that the algorithm cannot stray from homogeneous diffusion scenarios. Additionally, no theoretical and empirical study is provided to characterize the link set estimate convergence toward the optimal solution. The authors propose to use the method as a starting point for manual validation by an expert biologist.

In [Magnusson and Jaldén, 2012], the authors aim at optimizing the whole track set

with a greedy algorithm in a track-by-track fashion. At each iteration, a track is randomly selected in the graph of physically possible links and added dynamically to the estimated track set using the Viterbi shortest path algorithm. This track is selected if it increases the likelihood of the track set, otherwise, it is rejected. If selected, the track is evaluated and compared with the current track set. In case of conflict, the conflicting track is removed and re-inserted following the Viterbi principle. The method [Magnusson and Jaldén, 2012] is spatially greedy while the large majority of methods described above are temporally greedy as they concatenate spatially optimized link set. As mentioned by the authors, this method does not reach the global optimum (as it is probably the case in [Racine et al., 2006]), though it is very efficient computationally. No specific dynamical modeling is proposed, though the cost of each added track could be estimated by stochastic filtering.

9.4.6 Conclusion

Picking a link set optimization scheme largely depends on the data at hand. Noisy data with unreliable detections ($\text{SNR} < 2$) call for probabilistic methods where detection can be performed on a per-track basis. While testing for a general trend in object dynamics, global though suboptimal method are also an interesting lead [Racine et al., 2006]. Otherwise, reliable detection and the need for precision call for a graph-based optimization on a limited number of frames coupled with a gap closing step. The computational complexity can then guide the decision toward a bipartite detection graph-based optimization, or a more complex MHT based algorithm. In the recent particle tracking challenge [Chenouard et al., 2014] only deterministic methods are proposed (unlike JPDA or particle filtering) and the authors underline that competing methods that use several time steps for optimization seem to perform better.

9.5 Estimation of spatial gating parameter

The spatial gating parameter is not only useful to reduce computational complexity, it is also decisive to handle track terminations. The cost for track termination is generally defined as [Blackman and House, 1999]:

$$C_{i0} = \beta(1 - P_D P_G) \quad (9.38)$$

where P_D denotes the probability of detection, P_G denotes the probability that this detection is found into the track gate and β is related to the expected termination rate. Those parameters are chosen empirically by the user and are not spatially and temporally adaptive. Accordingly, prior dynamical modeling is the more satisfying solution for track termination or temporary disappearance detection. Most gating methods are controlled by the global covariance parameter of prediction errors. The global covariance can

be either specified by the user [Sergé et al., 2008; Sbalzarini and Koumoutsakos, 2005; Godinez et al., 2009], trained offline from simulations [Magnusson and Jaldén, 2012] or estimated from data [Racine et al., 2006]. In crowded scene presenting heterogeneous types of motion, the high probability of false positives due to mis-detections of track termination requires a locally adaptive search radius. In [Genovesio et al., 2006] and [Jaqaman et al., 2008], the authors proposed to limit the search radius C based on the covariance matrix Q_t that models the process noise of the temporal stochastic filter. Assuming a normal distribution, the search radius is then based on a p -value [Genovesio et al., 2006], or an equivalent heuristic [Jaqaman et al., 2008] of the following form:

$$C = \lambda(2\mathbf{H}^t\hat{\mathbf{Q}}_t\mathbf{H})^{\frac{1}{2}} \quad (9.39)$$

The covariance matrix is derived from $\text{Var}[\mathbf{z}_{1:t} - \mathbf{H}\bar{\mathbf{x}}_{1:t}]$, which performs well for long tracks that individually present homogeneous behaviors.

In a more marginal note, an isotropic search radius is preferred over an anisotropic shape in [Jaqaman et al., 2008]. Actually, the mixing of the prediction error in the x , y and possibly z directions allows for a more robust estimate of the search radius on short tracks.

As we shall in our experiments, we can improve this estimation algorithm by specifying a search radius estimator which adapts to motion type switching detection.

9.6 Similarity measure

As shown in Table 9.1, several methods use more than one coordinate to measure the distance between predictions and measurements. A frequent additional cue is intensity. For example, let us consider two vesicles moving at different depth and acquired on the same image by a confocal microscope. On this two-dimensional projection, the two vesicles might appear very close from each other. As they will present different intensities on the focal plane, the intensity distance can indeed help lifting the ambiguity. But intensity can also be a misleading cue. Indeed, the depth of an object can rapidly change and rapid motion can strongly modify the intensity. Additionally, balancing the different contributions between spatial and appearance proximity is not an easy task. Intensity must thus be used with care for specific applications as in [Liang et al., 2010], or to lift ambiguities on merging detection as in [Jaqaman et al., 2008].

Along the same line, the geometry of the target should be used carefully. The first reason is that the scale of sub-resolution depends on the optical microscope and cannot help to discriminate two particles. However, in practice, particle motions have a high impact on vesicle appearance. In the case of locally constant motion such as microtubule plus-TIP tracking, geometry becomes an interesting cue (see Figure 9.6), but abrupt change in dynamical behaviour can strongly modify the shape of the tracked object (see first row in Figure 9.1.A). One could argue that if shape is not a descriptor for a

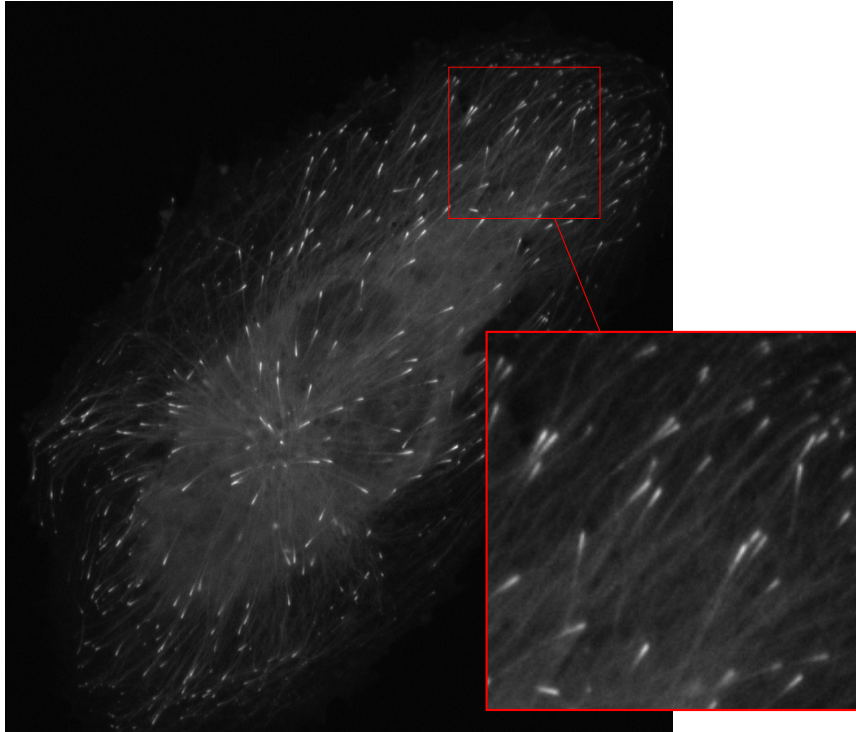


Figure 9.6: Tracking of comet-shaped EB1 protein marking microtubule plus-TIP (courtesy of the Danuser Lab). In this imaging use-case, object shape is a very valuable cue for tracking.

single spot, it could give a prior for motion estimation. This is true, but spots that are close to each other and not discriminated by the detector, can also present such an elongated intensity footprint. In practice, we thus recommend to use shape only for specific scenarios such as plus-TIPs tracking or axon extremities tracking [Yang et al., 2012].

A measure of perceivability has also been proposed in the literature. It has been first introduced by [Sergé et al. \[2008\]](#) to model the probability of blinking of quantum dots. The blinking probability allows lifting the ambiguity between partially and completely turned off particles. This probabilistic representation is also needed because the computational scheme cannot handle gap closing. In the recent effort of [Chenouard et al. \[2013\]](#), the probability of the perceivability is embedded in a Bayesian framework. As the MHT method evaluates every possible track combination and every possible gap size in a given temporal window, tracks that contain a lot of dummy detections could be preferred over similar tracks that present more consistency. Instead of using an arbitrary set cost for linking virtual detection, the perceivability measure promotes tracks that are built with

less dummy variables. The built tracks contain a low number of false detections² and present a high consistency.

One should also note the important difference between the Euclidean distance and the Mahalanobis distance defined as:

$$D_M(\mathbf{x}, \mathbf{y}) = (\mathbf{x} - \mathbf{y})^\top \Sigma^{-1} (\mathbf{x} - \mathbf{y}). \quad (9.40)$$

The latter is of course appealing when dealing with heterogeneous diffusion constant or process noise in experimental sequences. Though the use of the Mahalanobis distance should be restricted to long tracks as covariance mis-estimation could induce important bias in the resulting distance estimate.

To conclude, the only universal cue for similarity measure in sub-resolution object tracking is thus the spatial coordinates supported by an accurate modeling of the particle dynamics. Other cues can also be used efficiently to handle specific biological problems [Liang et al., 2010] or to adapt to the specificity of the algorithm [Chenouard et al., 2013].

9.7 Gap closing

A gap is a missing sample in an expected continuous track. Such a gap can be caused by several factors: transient motions out of the focus plan in confocal or TIRF microscopy, spot mis-detection due to low-dose imaging and finally transient coalescence of spots that cannot be discriminated. We recall briefly here the three categories of strategies used to tackle missing particles in the literature.

The first strategy, introduced by Sbalzarini and Koumoutsakos [2005], consists in optimizing the link set over multiple frames. Virtual detections are introduced to formally represent the missing samples in the trajectory. As in [Chenouard et al., 2013], these methods can only fill short gaps (up to four or five frames).

In the probabilistic framework [Sergé et al., 2008; Smal et al., 2008a,b; Godinez et al., 2009], the absence of detection inside the track gate does not immediately trigger track termination. A parameter controlling the particle blinking probability can be iteratively updated at each time step to make the good decision. Finally, the track is considered terminated after a fix number of frames without assignment of candidates. Contrary to the previous method, this approach is not robust to transient false detection in a target gate.

The third strategy implemented by Jaqaman et al. [2008] and also recommended by Chenouard et al. [2013] consists in handling gap closing in a post-processing step. In [Jaqaman et al., 2008], the linear programming algorithm [Jonker and Volgenant, 1987] is re-used using tracklets instead of detections, thus handling the gap closing in

²In this paper the probability of false detection is determined by the user. It can vary in space and time to take bleaching and intracellular structures into account. One could also use the confidence measure stemming from spot detector.

polynomial time. The tracklet extremities are first classified into two motion categories (directed and Brownian) using an asymmetry metric [Huet et al., 2006], and the motion parameter (diffusion parameter or speed) are locally re-estimated. This local motion model determines the probability of the presence of a gap before or after the tracklet. The gap length also weights down this probability distribution in an empirical fashion. As in the linking cost optimization step, the u-track algorithm uses a search radius based on the local motion to gate the parameter space.

9.8 Merging and splitting

There is two sources of merging and splitting events that an algorithm can detect. Some events are due to biological interactions between molecules or vesicles. Others are due to the resolution limit of the microscope, when the detector cannot resolve multiple neighboring particles. The former are detected to quantify a biological process inside the cell, while the latter must be detected to measure complete tracks. When detection-induced mergings occur, they are often transient and a gap closing scheme can be sufficient to links partial trajectories. In the case of biology-induced merging or splitting, a specific scheme must be designed to evaluate the underlying biology processes.

In the global link set optimization-based methods [Racine et al., 2006; Magnusson and Jaldén, 2012] merging and splitting are systematically considered along with bi-partite link without specific cost. In [Smal et al., 2008a; Godinez et al., 2009], particle filter coalescence is considered to detect merging events. In [Jaqaman et al., 2008; Feng et al., 2011], events are detected as a post-processing step using position, speed and intensity of track segment to measure similarities. In cluttered conditions, the metric used to detect such events will strongly affect the detection of track creation and termination. As a result, using either online or offline merge and split detection, it is important to decorrelate the track estimation step from the merging and splitting detection . It should be achieved with dedicated parameters and models.

9.9 Conclusion & Table

Based on this review, we analyzed fifteen algorithms and methods. We systematically classified those algorithms using eight criteria, adding two criteria to the six already listed and previously detailed (see Table 9.1):

- Dynamics modeling (diffusion, constant speed or heterogeneous transport).
- Optimization algorithms for linking predictions and measurements (linear programming, ...).
- Temporal windowing for fast optimization.
- Spatial gating for optimal matching (manual, global or local covariance).

- Similarity measure for correspondence.
- Gap closing for track continuity.
- Merging and splitting for adaptivity.
- Sequential tracking for the on-the-fly analysis.

As the time scale for experiment can be weeks or even months in quantitative biology, MPT algorithms design should favor quality over computational efficiency. Online MPT algorithms are thus not required and offline trackers are more appropriate as they exploit all the data set. However, the computational time must be predictable and be kept reasonable to allow an optimal parametrization of algorithm. MPT algorithms should then ideally be designed to bear a linear complexity with respect to frame number, the track number and the particle spatiotemporal density.

Paper	Dynamics	Minimization	temp. window	Scale and Gating
Sergé et al. [2008]	Diffusion	Exhaustive hypothesis comp.	2	Manual
Jaqaman et al. [2008]	Diffusion, Constant speed, Switching	Linear programming	2	Filter covariance
Magnusson and Jaldén [2012]	Diffusion	Enhanced Viterbi algorithm	Global	Trained
Genovesio et al. [2006]	Diffusion, Constant speed, Switching	Nearest Neighbor	2	Filter covariance
Sbalzarini and Koumoutsakos [2005]	Diffusion	Linear programming	2,3 or 4	Manual
Godinez et al. [2009]	Diffusion	PF + Linear programming	2	Manual
Racine et al. [2006]	Diffusion	Simulating Annealing	Global	Global covariance
Rezatofighi et al. [2012]	Diffusion, Constant speed, Switching	Exhaustive hypothesis comp.	2	Manual
Smal et al. [2008a]	Diffusion, Constant speed	Particle filtering	2	Filter covariance
Liang et al. [2010]	Diffusion	Linear programming	2	Trained
Smal et al. [2008b]	Constant speed	Not specified	2	Manual
Feng et al. [2011]	Diffusion, Constant speed, Switching	Linear programming	4,5,6	Manual
Chenouard et al. [2013]	Diffusion, Constant speed, Switching	Linear programming	up to 5	Filter covariance
Winter et al. [2012]	Constant speed	Minimum spanning tree	up to 6	Manual
Godinez et al. [2011]	Diffusion	Exhaustive hypothesis comp.	2	Filter covariance
Paper	Similarity measure	Gap closing	Merge Split	Online tracking
Sergé et al. [2008]	Mahalanobis (coord., int.), Perceivability	Yes	No	Yes
Jaqaman et al. [2008]	Euclidean (coord., int. for merging/splitting)	Yes	Yes	No
Magnusson and Jaldén [2012]	Euclidean (coord.)	Yes	Yes	No
Genovesio et al. [2006]	Mahalanobis (coord.)	No	No	Yes
Sbalzarini and Koumoutsakos [2005]	Euclidean dist. (coord., int.)	Yes	No	Yes
Godinez et al. [2009]	Patch based distance (coord,int,sigma)	Yes	Yes	Yes
Racine et al. [2006]	Mahalanobis (coord.,int)	No	Yes	No
Rezatofighi et al. [2012]	Mahalanobis (coord., int)	Yes	No	Yes
Smal et al. [2008a]	Patch based distance (coord.,int.,sigma)	Yes	Yes	Yes
Liang et al. [2010]	Mahalanobis (coord., int.)	No	No	No
Smal et al. [2008b]	Euclidean (coord.)	No	No	Yes
Feng et al. [2011]	Euclidean (coord.)	Yes	Yes	Yes
Chenouard et al. [2013]	Mahalanobis (coord.), Perceivability	Yes	No	No
Winter et al. [2012]	Weighted cost (speed, int., Track length)	No	Yes	Yes
Godinez et al. [2011]	Mahalanobis (coord.,Int.,sigma)	No	No	Yes

Table 9.1: Comparison of 15 algorithms chosen in the literature for their impact in quantitative biology, performances and originality.

10 Iterative u-track

Our study shows that state-of-the-art algorithms in the Bayesian framework are able to model diffusive, active and heterogeneous motions efficiently. Moreover, thanks to the use of combinatorial algorithm to handle linking cost optimization, state-of-the-art algorithms can also tackle scenarios that are made ambiguous by spatiotemporal density. However, the combination of large apparent displacements, particle density and unpredictable transitions in transport type (heterogeneity) can severely impact the tracking performances.

First, heterogeneity requires the ability to accurately detect abrupt changes in the particle dynamics to lift the ambiguities in dense conditions. However, as explained in the previous chapter, a stochastic filter cannot estimate the brutal transitions from Brownian to directed motion resulting in false negatives (see Figure 9.1). Advances in combinatorial optimization such as MHT based trackers [Chenouard et al., 2013; Liang et al., 2010] or more global methods [Racine et al., 2006] are valuable since they improve those results but are yet limited. Indeed, those approaches are independent from the cost applied to each possible track. Using a different similarity cue (intensity or shape) is also appropriate to lessen the density in the parameter space but only in some specific application as explained in the previous chapter. In this chapter, we propose a stochastic smoothing approach to interacting multiple modeling of dynamics. We can forecast rapid transitions and estimate the track speed at each time point. Each displacement is predicted by considering the past and future measurements without using a temporal window larger than two time points for linking cost optimization.

Secondly, the spontaneous apparition and terminations of trajectories in a dense environment can generate false positives and negatives (see Figure 8.9 and 9.2). Accordingly, the search radius gating parameter plays an important role and must be reactive to adapt the local transport type and possible transition. In our approach, we exploit the detected motion type to adapt the search radius locally. We also exploit the iterative characteristic of our method to obtain a convergent estimate for the search radius.

We build our algorithm over the u-track platform because of its design modularity. Additionally, it is well designed to handle large number of objects and complex dynamics. The frame-to-frame linking step is not computationally prohibitive while MHT based method complexity tends to grow exponentially with density. As the gap closing is decorrelated from the frame-to-frame optimization, longer gaps can be computed with a lower impact on computational cost than a single step optimized on a larger temporal

window. Finally, the per-track gating estimation approach and multiple motion modeling makes this tracker attractive for our challenging study.

Finally we assess the performances of our method on synthetic and biological data. In the controlled framework of simulated data, our method is compared with multiple model filtering algorithms: IMM-based tracker (similar to [Genovesio et al., 2006]) and u-track GPB1 implementation [Jaqaman et al., 2008]. We first test heterogeneous scenarios such as increasing probability of abrupt transitions combined with increasing particle density or increasing active transport velocity within an heterogeneous track. More general scenarios are tested such as mixture of trajectories that undergo exclusively free, confined diffusion or directed motion. We also demonstrate the performances of our method in the case of directed motions with stationary direction and varying velocities. On biological data, the challenging vimentin study is successfully analyzed. Furthermore, we highlight the robustness of our method with respect to acquisition speed reduction in experimental conditions using fluorescence imaging of viruses.

10.1 Iterative Interacting Multiple Model (IIMM) Method

To improve the detection of abrupt changes from a dynamical regime to an other in a track, it seems natural to exploit past and future measurements and thus increasing the amount of information about the dynamics of the quantified trajectory. Concretely, while a transition from confined diffusion to directed motion (see Figure 9.1) is challenging to detect in dense conditions, the same transition is much easier to recover in reverse temporal order (backward tracking) since it becomes a directed to confined Brownian motion (see Figure 9.2). To exploit this strategy, we first propose an Interacting Multiple Model that proves sufficient flexibility to detect the less challenging transitions. Additionally one wants to fuse forward and backward tracking method in order to recover more challenging transitions. We thus propose an iterative framework that exploits tracking and forward and backward temporal directions to converge on a single speed estimate by time point as illustrated in Figure 10.1. The new algorithm is thus an iterative interacting multiple model smoother (IIMM). This method presents the flexibility of IMM filtering while keeping the converging ability of the u-track approach to dynamic model.

At each tracking round $k + 1$, the estimated state posterior $p(\mathbf{x}_{t+1,k+1}, \mathbf{z}_{1:T})$ is modeled as a mixture of predictions provided by the last N Kalman filters (see (9.18)) and the overall posterior estimated at the previous tracking round as:

$$p(\mathbf{x}_{t+1,k+1}, \mathbf{z}_{1:T}) \approx \sum_{\theta_{t+1,k+1} \in \Lambda} p(\theta_{t+1,k+1} | \mathbf{z}_{1:t+1}) p(\mathbf{x}_{t+1,k+1} | \theta_{t+1,k+1}, \mathbf{z}_{1:t+1}) \quad (10.1) \\ + p(\hat{\theta}_{t+1,k} | \mathbf{z}_{t+1:T}) p((2\mathbf{H} - \mathbf{I})\mathbf{x}_{t+1,k} | \hat{\theta}_{t+1,k}, \mathbf{z}_{t+1:T})$$

Similarly to the IMM derivation (see Section 9.3.3.2), and unlike the original u-track design (see Section 9.3.3.1), the state probability considering a single mode is further

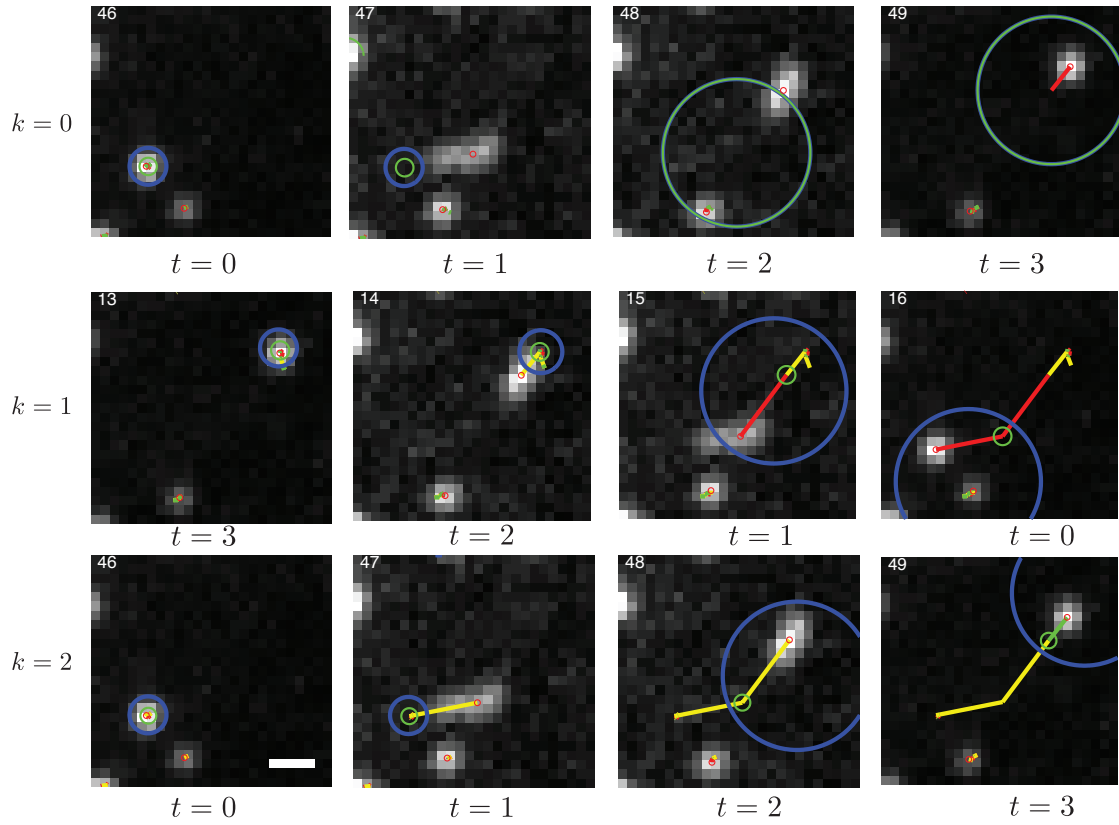


Figure 10.1: Convergence of speed estimation at the time point scale. Red links represent directed prediction selection, Green links represent Brownian prediction and Yellow represent prediction stemming from the previous tracking round. A small tracklet motion is easily retrieved during the first tracking round; it serves as a track initialization for the following track rounds (scale bar is $0.5 \mu m$, acquisition frequency is 1Hz).

derived as:

$$\begin{aligned}
p(\mathbf{x}_{t+1,k+1}|\theta_{t+1,k+1}, \mathbf{z}_{1:t+1}) &= \frac{p(\mathbf{z}_{t+1}|\mathbf{x}_{t+1,k+1}, \theta_{t+1,k+1})}{p(\mathbf{z}_{t+1}|\mathbf{z}_{1:t}, \theta_{t+1,k+1})} p(\mathbf{x}_{t+1,k+1}|\theta_{t+1,k+1}, \mathbf{z}_{1:t}) \\
&= \frac{p(\mathbf{z}_{t+1}|\mathbf{x}_{t+1,k+1}, \theta_{t+1,k+1})}{p(\mathbf{z}_{t+1}|\mathbf{z}_{1:t}, \theta_{t+1,k+1})} \\
&\quad \times \int p(\mathbf{x}_{t+1,k+1}|\mathbf{x}_{t,k+1}, \theta_{t+1,k+1})p(\mathbf{x}_{t,k+1}|\mathbf{z}_{1:t}, \theta_{t+1,k+1})d\mathbf{x}_t.
\end{aligned} \tag{10.2}$$

IMM-based methods have been primarily designed to detect slow maneuvers of aircrafts at high acquisition frequency [Blackman and House, 1999]. Those methods are well designed for smooth transitions from cruising, modeled by directed motion, and a maneuvering aircraft, modeled by Brownian motion or a more precise acceleration model. Clearly, the IMM algorithm reconditions the overall posterior before the next Kalman filtering cycle. This “mixing” [Blackman and House, 1999] exploits the estimated transition probability $p(\theta_{t,k+1}|\theta_{t+1,k+1}, \mathbf{z}_{1:t})$ (see (9.28) and (9.29)). The low temporal resolution that can be used in fluorescence microscopy does not allow the observation of such a smooth transitions. The switches from motor-mediated motion to local jiggling or Brownian diffusion is chemically triggered and observed as an instantaneous process. In order to take into account the abrupt transitions, we propose the following approximation that does not require the transition probability $p(\theta_{t,k+1}|\theta_{t+1,k+1}, \mathbf{z}_{1:t})$:

$$p(\mathbf{x}_{t,k+1}|\mathbf{z}_{1:t}, \theta_{t+1,k+1}) \sim \mathcal{N}(\hat{\mathbf{x}}_{t,k+1}; \mathbf{x}_{t,k+1}^{\theta_{t+1,k+1}}, \hat{\mathbf{P}}_{t,k+1}^{\theta_{t+1,k+1}}) \tag{10.3}$$

Given (10.3), the integral in (10.2) can be interpreted an update step in the recursive Kalman filter. We thus simplify the IMM mixing with N independent Kalman filters updated independently and individually from $(\hat{\mathbf{x}}_{t,k+1}^{\theta_{t+1,k+1}}, \hat{\mathbf{P}}_{t,k+1}^{\theta_{t+1,k+1}})$. It follows that the estimated prior of a given Kalman filter is not influenced by other transport type probabilities as this is the case in (9.28).

Following (10.1), the filtered state at the current tracking round $k + 1$ competes with the state probability filtered by the previous tracking round $(\hat{\mathbf{x}}_{t+1,k}^{\theta_{t+1,k}}, \hat{\mathbf{P}}_{t+1,k}^{\theta_{t+1,k}})$. At the temporal update step, only the prediction with the highest likelihood is considered in the assignment graph to be optimized using the shortest-path algorithm presented in [Jonker and Volgenant, 1987]. The sensor update is then carried out for each filter upon the measurement selected by the combinatorial assignment algorithm. The complete algorithm implementation is summarized in a flowchart in Figure 10.2. This approach can also be interpreted as an iterative forward-backward filtering-based smoother, as described in [Fraser and Potter, 1969], applied to IMM filtering.

As in the u-track platform, $K = 3$ tracking rounds are performed to obtain a converging estimation of the speed. We thus obtain a converging speed estimation time point by time point as illustrated in Figure 10.1, instead of speed per track on the former algorithm.

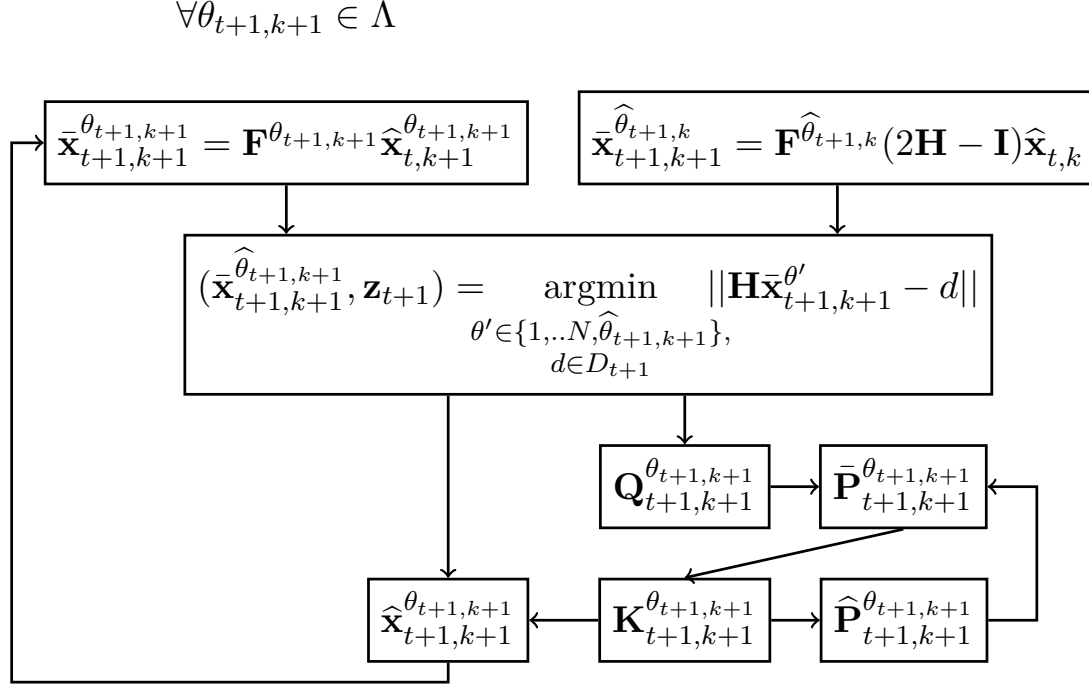


Figure 10.2: Overview of our tracking algorithm at tracking round $k+1$. Let D_{t+1} be the detection (measurement) set at time $t+1$. For each measurement, the closest prediction $\bar{\mathbf{x}}_{t+1,k+1}^{\hat{\theta}_{t+1,k+1}}$ is selected by the among predictions made by N Kalman filters at round $k+1$ and the estimated posterior at round k . The graph-based combinatorial algorithm [Jonker and Volgenant, 1987] estimates the optimal assignment $(\bar{\mathbf{x}}_{t+1,k+1}^{\hat{\theta}_{t+1,k+1}}, \mathbf{z}_{t+1})$ between the closest prediction and detections for every track. Once the best measurement is assigned to the track, this measurement is used to update each Kalman filter variable independently.

In this example, the vimentin undergoes very confined Brownian motion followed by a sudden motor-mediated motion (experimental results showed that the support of such displacement are microtubules). Such transitions could not be detected by usual Kalman filtering without manually extending the search radius, rising the false positive probability on the whole sequence. Our scheme iteratively estimates the whole direct transition between two stationary confined diffusion regimes.

10.2 On-line iterative estimation of gating parameter

As discussed in Section 9.5, locally adaptive gating is required in spatiotemporal dense conditions combined with heterogeneous particle behaviors to accurately detect track apparitions and terminations. We benefit from the iterative behavior of our algorithm

to improve the estimation of the search radius. First, we save memory by adapting the classic online process noise estimator [Stengel, 1986] to our problem. At each time step, the parameters $(m_{t,k}, n_{t,k}, M_{t,k})$ are updated as:

$$\bar{\mathbf{z}}_{t+1} = \mathbf{z}_{t+1} - \mathbf{H}\bar{\mathbf{x}}_{t+1,k} \quad (10.4)$$

$$n_{t+1,k} = n_{t,k} + 1 \quad (10.5)$$

$$m_{t+1,k} = m_{t,k} + \frac{\bar{z}_{t+1} - m_{t,k}}{n_{t+1,k}} \quad (10.6)$$

$$M_{t+1,k} = M_{t,k} + (\bar{z}_{t+1} - m_{t+1,k})^\top (\bar{z}_{t+1} - m_{t+1,k}) \quad (10.7)$$

where $n_{t+1,k} \in \mathbb{N}$ is the number of prediction errors iteratively incremented, $m_{t+1,k} \in \mathbb{R}$ is the associated mean and $M_{t+1,k} \in \mathbb{R}$ is the sum of squares of differences from the mean. The process noise variance is thus given by:

$$\mathbf{H}\hat{\mathbf{Q}}_{t+1,k} = \frac{M_{t+1,k}}{n_{t+1,k}}. \quad (10.8)$$

This method can converge towards a single spatial process noise variance estimation for the whole track (as demonstrated in Figure 10.3). However, this is not sufficient in our heterogeneous use case.

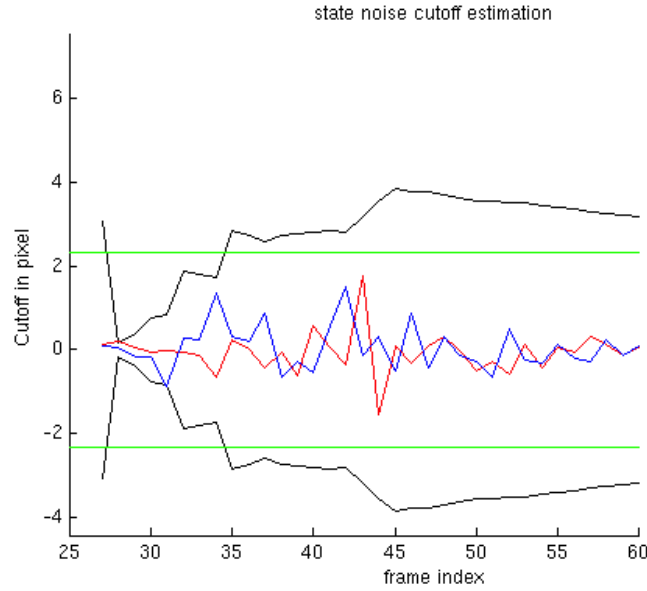
The transition from directed to Brownian motion can favor on over-estimation of the search radius. To adapt to those rapid transitions, we propose to maintain a parameter set $(m_{t,k}^0, n_{t,k}^0, M_{t,k}^0)$ dedicated to Brownian motion on each track. When a motion type switch from directed to Brownian displacement is detected by the IIMM, i.e. when the prediction of the Brownian Kalman filter is the most probable, the triplet $(m_{t,k}, n_{t,k}, M_{t,k})$ is reset to $(m_{t,k}^0, n_{t,k}^0, M_{t,k}^0)$. Finally, we exploit the iterative properties of our algorithm to make the search radius estimation more robust. On track apparition, or when a prediction from the previous tracking round is selected against the current IMM filter prediction, we use the noise estimation variable from the previous tracking round:

$$(m_{t,k+1}, n_{t,k+1}, M_{t,k+1}) = (m_{t,k}, n_{t,k}, M_{t,k}). \quad (10.9)$$

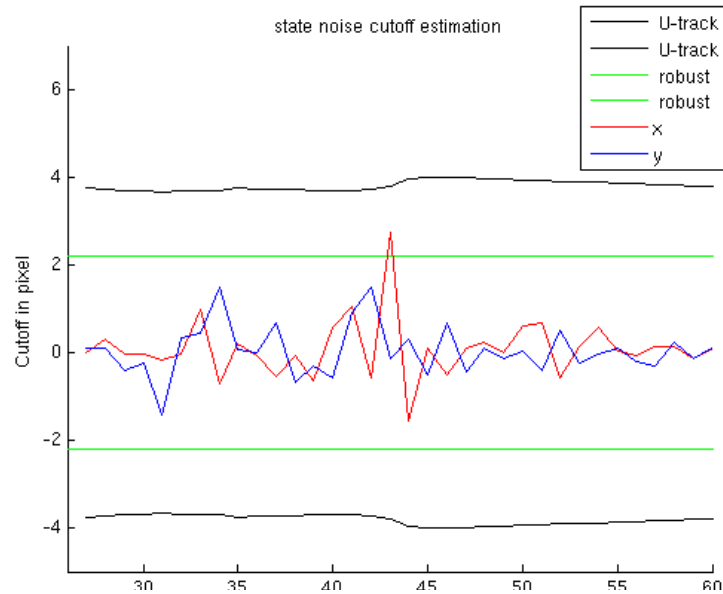
We thus obtain a process-noise estimate that is adapted to each dynamical sub-regime in a track. We also avoid a search radius underestimation due to the converging predictions of our IIMM filter.

10.3 Tracking performances on synthetic data

In this Section we demonstrate the performance of our algorithm on synthetic data in connection with the vimentin case study, that is the tracking of particles presenting heterogeneous motion in a dense environment. We show that our algorithm performs very well compared to competing methods in this specific scenario as well as others, more homogeneous, dynamics quantification studies.



(a) U-track needs a few frames to calibrate the noise process.



(b) Online iterative cut-off estimation that exploits backward and forward tracking to smooth estimates.

Figure 10.3: U-track cut-off estimation and online iterative estimation on the last forward tracking round. Red and Blue lines represent the prediction errors in x and y . The Green line describes the median of absolute deviation scaled by a factor 3; it gives the scale of the prediction residuals. The Black line is the cut-off estimated by u-track.

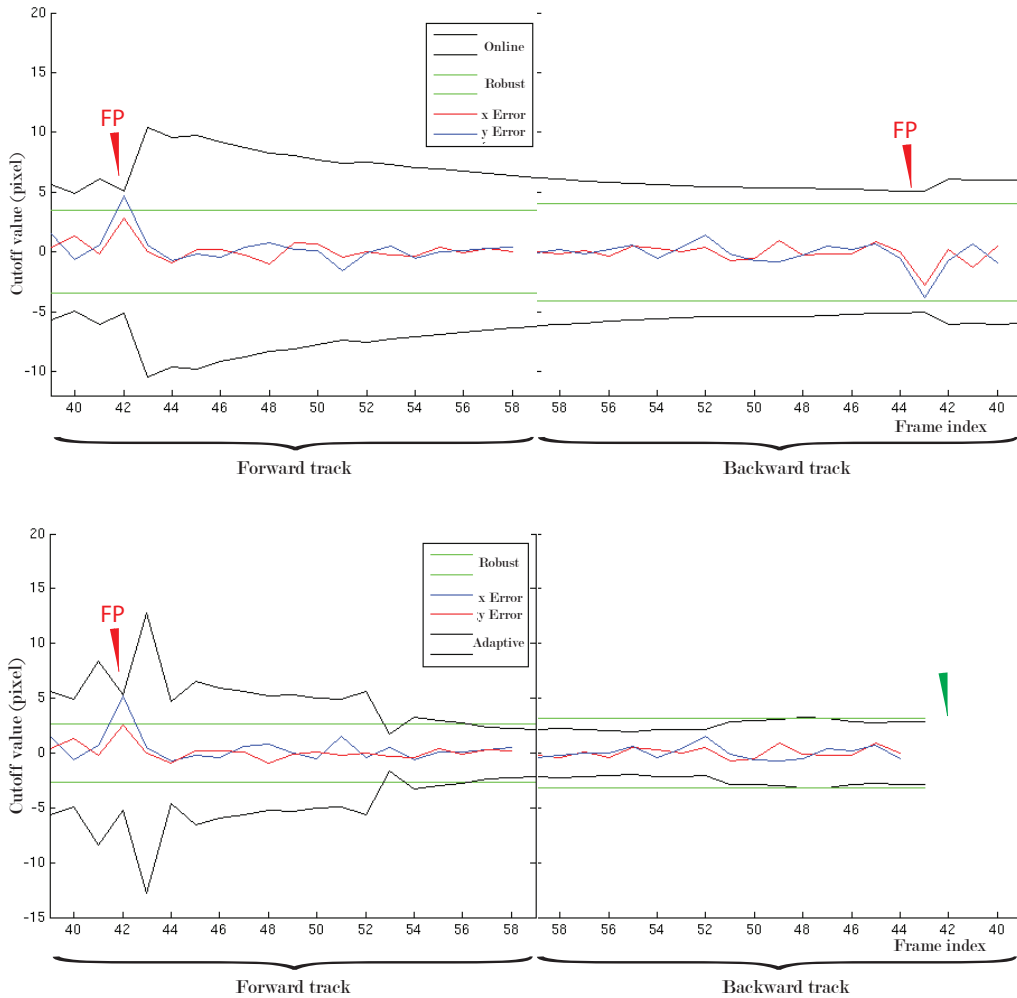


Figure 10.4: Impact of noise adaptation on linking cut-off for a single track. In this example, the low number of data points on the first few frames results in a weak estimate of the search radius leading to a false positive. Above, the process noise is computed using the iterative online estimator [Stengel, 1986]. As the method is not locally adaptive, it exploits all the prediction errors (Red and Blue lines) and repeats the tracking errors during backward tracking. Below, the process noise is computed using our method. By finally estimating the Kalman Filter process noise, we provide an accurate end of track time point on the backward tracking. The subsequent forward tracking does not repeat the previous mistakes (data not shown).

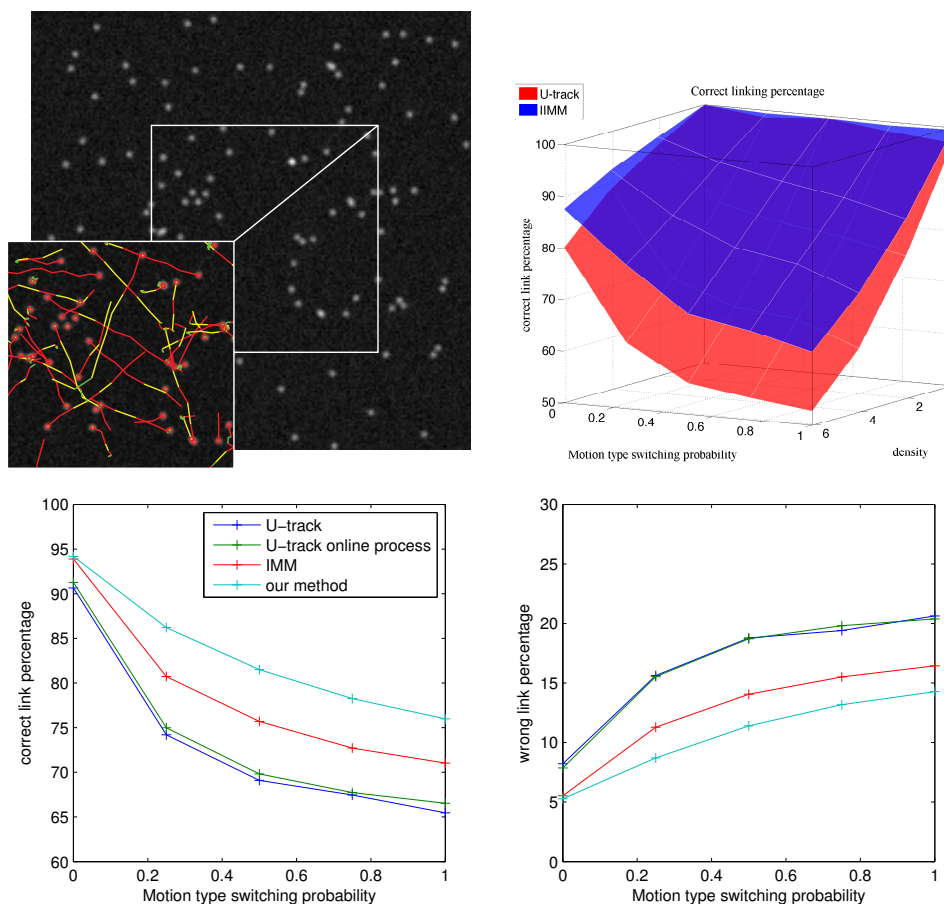


Figure 10.5: **A)** Example of track simulation presenting a density of $1 \text{ spot}/\mu\text{m}^2$. **B)** Correct linking percentage with respect to density and motion type switching probability. Our method outperform u-track by 15% in the hardest case. **C)** True positive and false positive ratio on the same simulation with a density of $3 \text{ spots}/\mu\text{m}^2$ comparing our method with u-track, u-track with an online process noise estimator and an IMM algorithm with forward-backward initialization.

10.3.1 Tracking performances on heterogeneous dynamics in a dense intracellular environment

This simulated data is mainly described by two parameters: heterogeneity and density. Heterogeneity is modeled by the probability of having a motion type switching between confined Brownian and directed displacement at a given time point. Each simulated track starts with confined Brownian motion with a 2D diffusion coefficient uniformly distributed ranging from 0.05 to $2.5 \mu\text{m}/\text{image}$ (0.1 to 4 pixels) and a confinement radius with a uniform distribution ranging from 0.25 to $1.75 \mu\text{m}$ (0.5 to 2 pixels). The directed

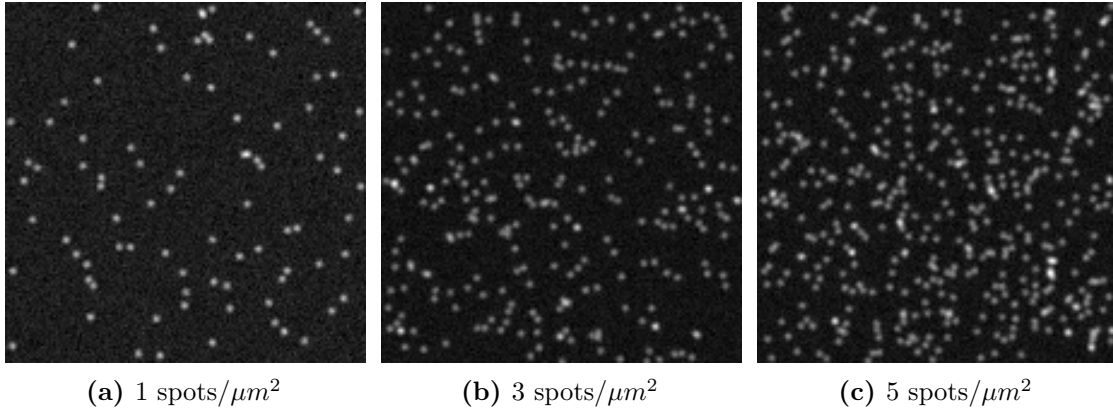


Figure 10.6: Display of several simulated densities.

segment speed follows a uniformly random distribution bounded by $0.5 \mu\text{m}/\text{image}$ (10 pixels/image) in a $10 \mu\text{m}$ by $10 \mu\text{m}$ image (200×200 pixels), though the speed value is fixed for every directed segment. The track length is a realization of a Gaussian variable $L \sim \mathcal{N}(50, 20)$ for every experiment. Each sequence is composed of 500 frames. To control density, the number of detected objects ranges from 1 to 6 spots/ μm^2 (see Figure 10.6). In order to evaluate the motion estimation only, the simulated position is directly used without the detection step. Those results are thus valid for different types of tracked objects.

We compared our method with the original u-track algorithm, the u-track algorithm with additional support for our online gating parameter estimation algorithm and a IMM algorithm similar to the work of [Genovesio et al. \[2006\]](#). The IMM we re-implemented supports a combinatorial optimization scheme and a forward-backward scheme for Kalman filters initialization to provide a fair comparison. A three dimensional graph illustrates the impact of both density and heterogeneity in Figure 10.5.B. This Figure shows only the differences between u-track and our method for clarity. Results in Figure 10.5.C highlight that the superiority of our method increases with motion probability while performances are similar for confined motion (motion switching probability set to 0). While density increases, our method faces a 15% drop in performances while other methods can lose up to 25% percent of correct linking percentage.

Thanks to the process noise variance online estimation scheme, the measured computational overhead is only 10% in the worst case compared with u-track. It is negligible compared with the IMM implementation.

10.3.2 Evaluation the gating parameter estimation

We also assess independently the performance of our adaptive gating parameter estimator on the same simulations. As shown in Figure 10.4, the process noise estimation error is

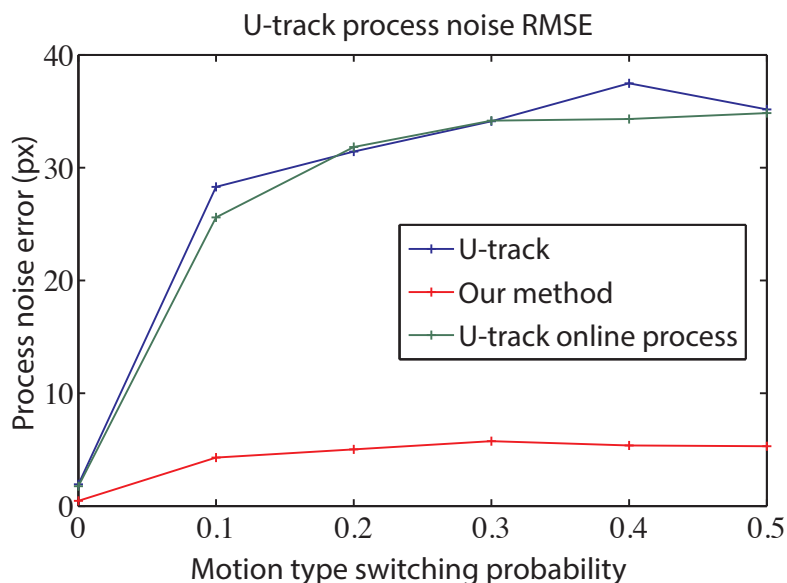


Figure 10.7: Process noise estimation error on simulation wrt motion switching probability: 0 means pure Brownian motion, 0.5 means a rate of 50% chances to switch to direct or Brownian motion. Vesicle density is set to 3 spots/ μm^2 . Our method is compared with process-noise variance estimation on the whole track up to time t (u-track) and an online and iterative though non adaptive process noise variance estimation (u-track online process).

dramatically reduced, even when the target maneuver is completely unpredictable due to motion type switching. One can note that the use of an online variance estimator that takes advantage of forward-backward tracks has little impact on process noise estimation error. This shows that our adaptive scheme has a decisive impact on gating parameter estimation (see Figure 10.7).

10.3.3 Sensibility to transition speed

We tested our algorithm against the amount of unexpected switch in dynamics combined with density. However, an other interesting challenge is the velocity involved in those switching. We have been testing, using the same simulations, the robustness of our tracker with respect to speed of motor-mediated displacement that occurs instantaneously after a long period of confined displacement. We show in Figure 10.8 that our method outperforms competing methods in this scenario. The speed varies from 0 to 0.5 $\mu\text{m}/\text{image}$ (0 to 10 pixels/image) and the density is set to 3 spots/ μm^2 .

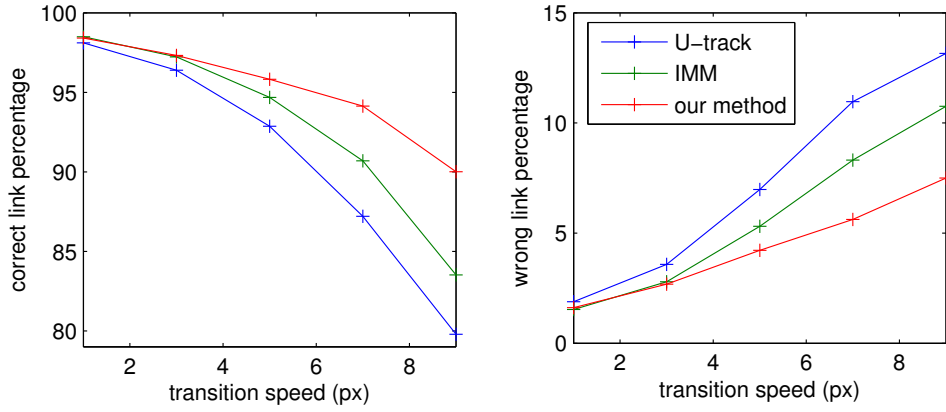


Figure 10.8: Correct linking and false positive percentage wrt transition speed.

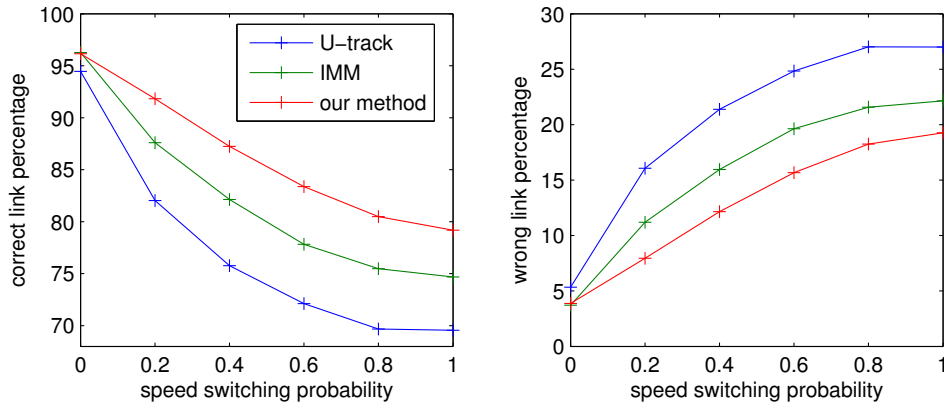


Figure 10.9: Correct linking and false positive percentage wrt speed switching probability.

10.3.4 Sensibility to speed variation

We have also tested our method on additional simulated cases out of the original scope. An interesting study is the ability to adapt to speed variation in a single direction. The multiple intracellular structures in the cell can indeed have a strong impact on vesicular-mediated transportation; the vesicles move with variable velocities in real data. To test this scenario, we tested our method on simulated objects moving at varying speed in a fixed direction chosen randomly. The speed varies from 0.05 to 0.5 $\mu\text{m}/\text{image}$ (1 to 10 pixels/image) and the density is set to 3 spots/ μm^2 . In those sequences our method outperforms u-track by 10%, showing its versatility (see Figure 10.9).

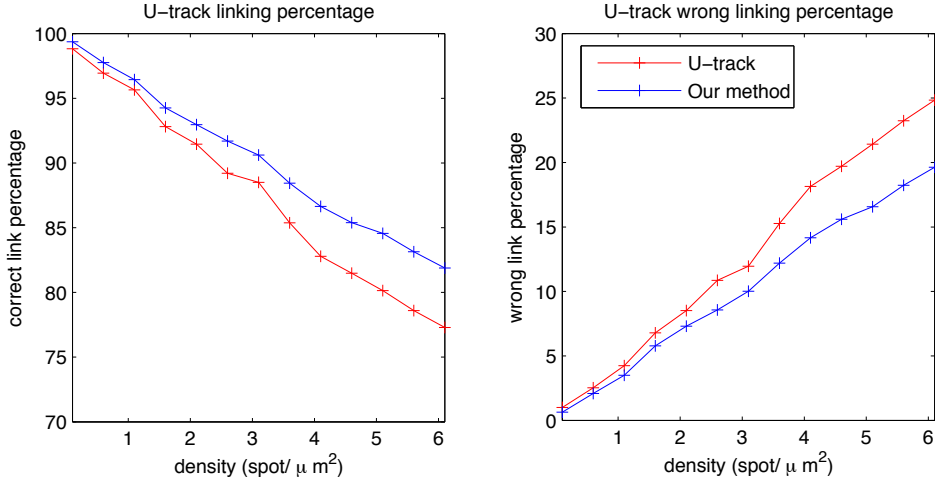


Figure 10.10: The same simulation scheme used for u-track training has been tested and the performance of our method (KF iter in this figure) compared with the u-track algorithm. The probabilities of confined diffusion, free diffusion, directed are 0.5, 0.4 and 0.1 respectively.

10.3.5 Motion type heterogeneity with individual stationarity: non regression test

We saw in the previous section that our method outperforms IMM-based and GPB1-based method on trajectories exhibiting non-stationary behavior. To prove that our algorithm performs well for many case studies, from simple to complex scenarios, we performed a non regression test using the original training data used to test the u-track algorithm. Those simulations consist in a mix of confined diffusion (50%), free diffusion (40 %) and direct motions (10%) with fixed speed and slowly changing directions. The confinement radius ranges from 0.2 to 2 pixels. The diffusion coefficient ranges from 0.1 to 4 pixels/image. The speed ranges is from 4 to 10 pixels/imag. The mean trajectory length is 50 frames. Each sequence is composed of 500 frames.

10.3.6 Computational time overhead

Finally, we measured the computational time and the relation to density. Experiment has been carried out with the simulations described in the previous section. As above, detection is not taken into account. We can see that the complexity grows linearly with density in both cases. Our approach presents a higher complexity due to the independent Kalman Filters and the iterative characteristic. However, our online variance estimation keeps computational complexity overhead to 10%.

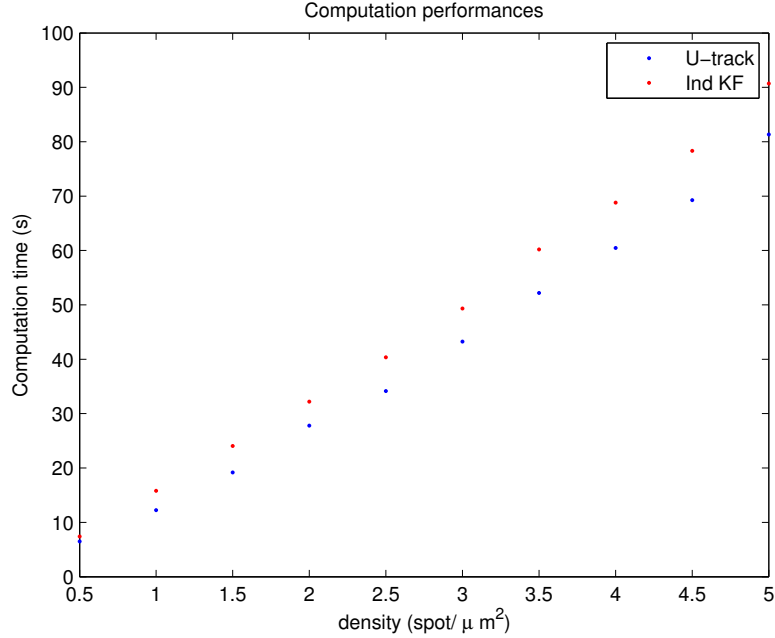


Figure 10.11: Computation time measured on the tracking alone (no detection). Mixture of confined diffusion (50%), free diffusion (40 %) and direct motions (10%). Computation overhead is around 10% with respect to u-track. The complexity grows linearly with density.

10.4 Motion quantification results on experimental data

This algorithm has primarily been designed to quantify specific behaviors of intra-cellular objects that could not be estimated by state-of-the-art algorithms (see Figure 9.1,9.2). In this Section we present the biological interpretation that can be drawn by the application of our new algorithm on unit length filament of vimentin dynamics. We also show that our algorithm is more robust to frame rate reduction, opening the way for a better image signaling quality while keeping a robust quantification of dynamics.

10.4.1 Detection method

To quantify dynamical process inside the cell, one needs a set of measurements for estimating object locations. We focus in our experimental results on the detection of sub-resolved objects (vesicle, viruses ...) that appear as blurred spots in the image. In a cluttered environment, accurate detection is crucial. False positives can indeed influence the track termination detection and, on the other hand, too few detections can hinder motion modeling accuracy. To ensure a high quality of detection, we tested our algorithm with a state-of-the-art detector, using a recent algorithm proposed by [Aguet et al., 2013]

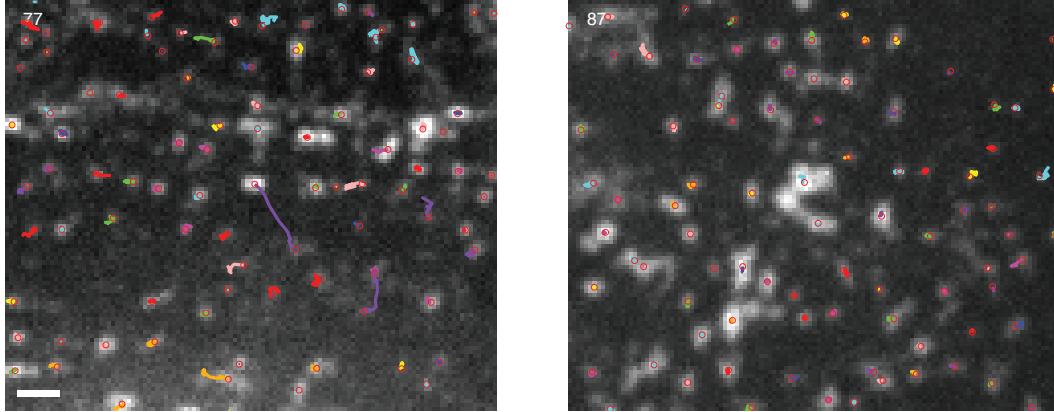
(see Appendix C for a detailed description). This new spot detector has proven a robust design and was heavily tested on experimental sequences. We describe this detector for completeness. This will give the reader an example of a typical and well design detection framework that combines linear filtering, robust local maxima detection and model fitting as reviewed in [Smal et al., 2008a].

10.4.2 Vimentin is bound to microtubules

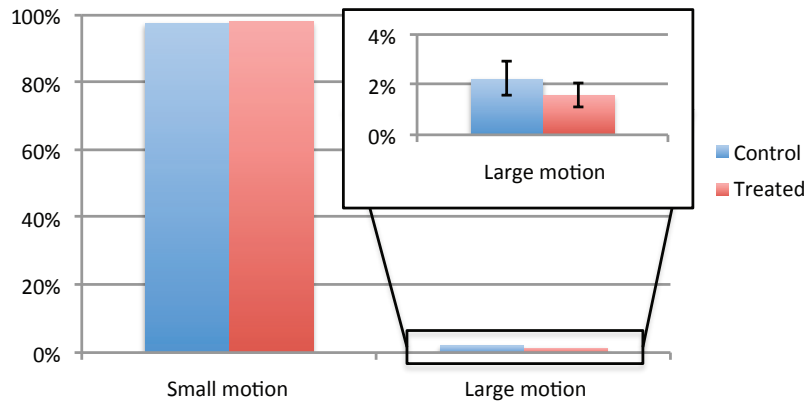
A biological experiment has been performed in the Gelfand Lab to measure the relationship between vimentin intermediate filament (IF) polymerization with other components of the cytoskeleton, namely the actin and microtubule networks. A detailed background of this biological experiment is given Section 8.3. To quantify the interaction between unit length filament of vimentin and the microtubule network, the cells were treated with nocodazole. If the hypothesis that vimentin is bound to microtubule is true, control cell should exhibit few motor-mediated motions and a large number of confined Brownian motions while the treated cell should present a reduction in the directed motion proportion. As shown in Figure 10.12, our algorithm allows us to quantify such a tiny difference with a very significant p -value of 0.0088 using a one-sided two-samples t -test. After careful parametrization, we manage to obtain with u-track a five-fold p -value of 0.045 with the same test on the same data. Also, Figure 10.13 demonstrate that control cells present a consistently larger number of large directed motions, the threshold can range from 2 pixels to 10 pixels (max). Those results are in accordance with preliminary studies published in [Prahlad et al., 1998].

10.4.3 Robustness against acquisition speed reduction

Tracker robustness against low frame-rate is crucial in biological imaging. It allows for a reduction of the excitation to reduce light inducing damage on the sample and permitting longer acquisitions. Also for a given illumination dose and acquisition time, a lower acquisition speed allows a better signal-to-noise ratio. To assess the performance of our tracker, we used data from a previous experiment on viruses [Burckhardt et al., 2011]. To quantify those motions, new protocols needed to be designed. Those virus required to be heavily labeled in ordered to obtain a sufficient signal while keeping a very high acquisition speed. Thanks to the high acquisition frequency (30Hz) of those sequences, viruses motion estimation is not a hard task. This allows us to consider the original track as a ground truth and artificially reducing the frame rate to test the robustness of the tracker. In Figure 10.14, we plot the number of correct tracks versus the decimation factor. The performances of our tracker reduce linearly while the performances of the u-track algorithm drop quadratically with a 12% difference. Figure 10.4.3 illustrates those measurements showing that our method can estimate entire tracks with fewer errors on a 50-fold decimation while u-track is not able to estimate the complete trajectory.



(a) Control cells highlight rare active transports (b) Nocodazole treated cells present only among confined Brownian motion.



(c) Histograms of large motion. A large motion is above the 99.9 percentile of the speed estimated on the control cell (t -test p -value=0.0088).

Figure 10.12: A. Control cell. B. After nocodazole treatment, the ULF should exhibit a decrease of its large motions proportion. C. A threshold for detecting large motion is estimated using the 99.9 percentile of the speed estimated. A t -test on the whole experiment gives a p -value of 0.0088. Imaging with spinning disk confocal microscope. Acquisition speed is set to 1 Hz for a minute. Scale bar is 1 μ m.

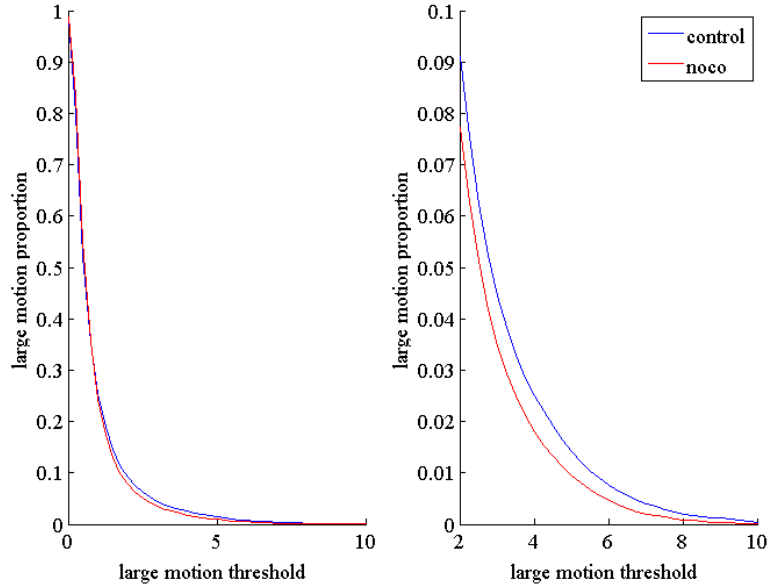


Figure 10.13: Evolution of large motion count with large motion threshold for control and treated cells. This is equivalent to a inverted cumulative histogram for the estimated velocities.

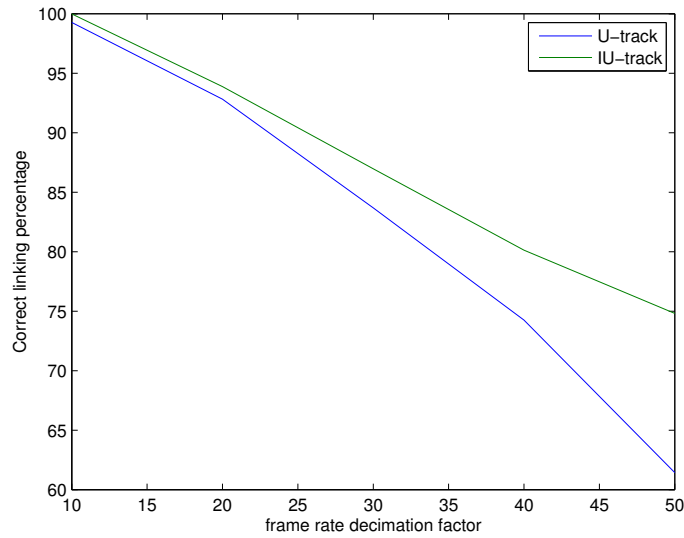


Figure 10.14: Error rate of u-track and iu-track wrt frame-rate decimation on a virus tracking experiment [Burckhardt et al., 2011]. Frame-rate is artificially reduced to test the robustness of our tracker.

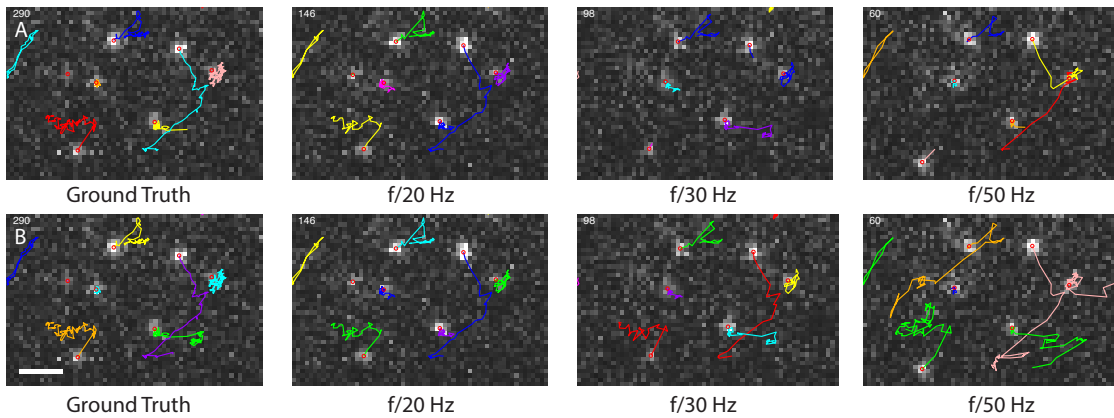


Figure 10.15: Viruses tracking inside the cell [Burckhardt et al., 2011]. Frame-rate is artificially reduced to test the robustness of our tracker. On this example, we observe that u-track break point is around a 30-fold decimation while our improvement exhibits a single error at a 30-fold decimation (longer tracks on the last experiment are due to lower frame rate but represent real tracks). Imaging with spinning disk confocal microscope. Acquisition speed is set to 30 Hz. Scale bar is $0.9 \mu m$.

11 Conclusion

In this work, we have first carried out a review of the multiple particle tracker algorithms proposed in the literature. We mainly focus on their ability to track heterogeneous intracellular motions and transports in spatiotemporal dense conditions induced by acquisition limitations. This problem is interesting because heterogeneous transports are very wide spread inside the cell. Additionally, limitations in fluorescence microscopy, spatial density of particles in the cell and potentially large displacements produce ambiguities in the formation of trajectories. In our review dedicated to this challenging problem, we put the emphasis on dynamical modeling, more specifically on multiple dynamical model filtering. In this context, we have proposed a statistical and probabilistic formulation for the u-track [Jaqaman et al., 2008] multiple dynamical model estimator. To the best of our knowledge, it is the first time that such a description is proposed for this algorithm widely used in biology and bio-imaging. This filter is very similar to the Generalized Pseudo Bayesian of order 1, which was not clear in the literature. Also, we put it in perspective with the well known Interacting Multiple Modeling [Blom and Bar-Shalom, 1988]. Based on this review, we showed that no multiple particle tracking algorithm is designed to retrieve unpredictable transition from Brownian to large directed displacements. Recent advances in multiple particle tracking such as MHT [Reid, 1979; Chenouard et al., 2013] recommend to exploit several frames and time points for tracking, but no solution is given to identify rapid transitions in motion types.

Based on this analysis, we have proposed an iterative interacting multiple model smoother that tracks particles in forward and backward directions until convergence of the local speed estimates. This method retrieves abrupt switches in the particle behavior that an usual temporal filter cannot forecast. We have also proposed a new adaptive search radius to improve gating of possible assignments and to better detect terminations in cluttered environment. Our method has been evaluated on simulated data and is demonstrated to outperform previous filters based on multiple modeling in heterogeneous and dense conditions. Simulations also show that our algorithm outperforms those competing methods on non-heterogeneous scenarios such as particles exhibiting varying velocities. On experimental sequences, our method identifies very small differences in vimentin heterogeneous dynamics with a better statistical significance than u-track. We also shown that our tracker is more robust toward low acquisition frame-rate. Those results could pave the way to longer quantification experiment in bio-imaging that has been previously been prevented by photo-damages and limitations of tracking algorithms.

Future works in the tracking area will be two-fold. We will first focus on application

to a wider range of problematics. Numerous collaborations and exciting challenges requiring object tracking are envisaged in the Danuser lab. We also hope that the expertise developed in tracking would make possible the collaborative design of motion quantification experiments with microscopists and biologists. A possible project is to optimize the quality of trajectories with minimal photo-damages. The second focus will be on methodological issues. In the short-term, we plan to investigate more the influence of iteration on speed and trajectory accuracy. If the advantages of this technique has been visually assessed, we did not analyse the actual role of iteration in the work. In the mid-term, the use of our IIMM smoother in the context of MHT is a very appealing approach. Short gaps could be then efficiently filled using our iterative scheme.

Appendices

C Particle detection in experimental conditions

C.1 Modeling

In the work of [Aguet et al. \[2013\]](#), the image model $M(\mathbf{x})$ on position $\mathbf{x} \in \Omega$ (pixel grid) of a particle is:

$$M(x, A, \sigma, \mu, C) = AG_{\sigma, \mu}(\mathbf{x}) + C + \xi(\mathbf{x}) \quad (\text{C.1})$$

where $A \in \mathbb{R}^+$ is the spot amplitude, $G_{\sigma, \mu}(\cdot)$ is a Gaussian function with standard deviation σ and mean μ that approximates the microscope PSF and $\xi(x) \sim \mathcal{N}(0, \sigma_r)$ with $\sigma_r \in \mathbb{R}^+$ denotes the standard deviation of the read-out noise. The scale σ that describes the Gaussian function is a characteristic of the acquisition setup and thus constant throughout the whole image. This precise model allows particle location estimation using least-square-based single or mixture model fitting. The main challenge addressed by the authors is the localization of the candidate positions for spot fitting.

C.2 Significant local maxima detection

A classic approach to detect probable locii for particle is to determine the local maxima on a filtered image [[Smal et al., 2010](#)]. The filter (e.g. Laplacian-of-Gaussian filtering) reduces noise and enhances object of interest. An issue is that all noise-induced signal variation that have been blurred out by the filter, can also result in a local maxima. One could perform a statistical test on least squares fitted residuals individually for each local maxima, but this is computationally inefficient at best and often untractable. To solve this problem, [Aguet et al. \[2013\]](#) proposed to estimate the amplitude A and background level C for each pixel and then test for the statistical significance of those estimation for each pixel on the whole image. The authors show that this is possible using simple linear filtering of the image, provided that the standard deviation σ is known (or estimated off-line as detailed Section C.4). This lightweight filtering process alleviates the computational constraint while still testing every single pixel on the image for the presence of a particle.

Let us consider an objective function $f(A, C)$ to be minimized at each location $\mathbf{x}_0 \in \Omega$

on the pixel grid Ω :

$$f(A, C) = \sum_{\mathbf{x} \in W} (AG_{\sigma,0}(\mathbf{x}) + C - I(\mathbf{x}_0 - \mathbf{x}))^2, \quad \forall \mathbf{x}_0 \in \Omega \quad (\text{C.2})$$

where W of size $8 \times \sigma$ is a spatial window centered on zero. By differentiation, we have:

$$\begin{cases} \frac{\partial f}{\partial A}(A, C) = \sum_{\mathbf{x} \in W} 2G_{\sigma,0}(\mathbf{x})(AG_{\sigma,0}(\mathbf{x}) + C - I(\mathbf{x}_0 - \mathbf{x})) = 0 \\ \frac{\partial f}{\partial C}(A, C) = \sum_{\mathbf{x} \in W} 2(AG_{\sigma,0}(\mathbf{x}) + C - I(\mathbf{x}_0 - \mathbf{x})) = 0 \end{cases} \quad \forall \mathbf{x}_0 \in \Omega \quad (\text{C.3})$$

which finally yields an estimate for the amplitude $\hat{A}(\mathbf{x}_0)$ and the background level $\hat{C}(\mathbf{x}_0)$:

$$\begin{cases} \hat{A}(\mathbf{x}_0) = \frac{(I * G_{\sigma,0})(\mathbf{x}_0) - \overline{G_{\sigma,0}}(I * \mathbf{1}_W)(\mathbf{x}_0)}{n\overline{G_{\sigma,0}^2} - n\overline{G_{\sigma,0}}^2}, \\ \hat{C}(\mathbf{x}_0) = \frac{(I * \mathbf{1}_W)(\mathbf{x}_0) - n\overline{G_{\sigma,0}}\hat{A}(\mathbf{x}_0)}{n} \end{cases} \quad (\text{C.4})$$

where $G_{\sigma,0}$ is the Gaussian kernel of size $8 \times \sigma$ and $\overline{G_{\sigma,0}}$ the mean value, n is the number of pixels in W and $\mathbf{1}_W$ is a summation filter over W .

To determine if the amplitude $\hat{A}(\mathbf{x}_0)$ stems from a particle, [Aguet et al. \[2013\]](#) proposed to test for the statistical significance of the estimated amplitude with respect to the background local variations. First, a local threshold that discriminates non-significant amplitudes is estimated based on the local background noise variance. Secondly, a t -test is carried out to assert which amplitudes are significantly below the given local threshold. The background variance σ_r^2 is estimated using the estimated residuals¹:

$$\hat{\sigma}_r^2 = \frac{\sum_{\mathbf{x} \in W} (\hat{A}G_{\sigma,0}(\mathbf{x}) + \hat{C} - I(\mathbf{x}_0 - \mathbf{x}))^2}{n - 1} \quad (\text{C.5})$$

which can also be interpreted as a linear filtering over the whole image. Thanks to the normal assumption $\xi(\mathbf{x}) \sim \mathcal{N}(0, \sigma_r)$, one can measure the probability that a realization of the background is above a given threshold T using the Gauss error-function:

$$\alpha = \frac{1}{2} \left(1 - \operatorname{erf} \left(\frac{T}{\sqrt{2}\sigma_r} \right) \right). \quad (\text{C.6})$$

By fixing the p -value α that describes the desired sensitivity of the detector, we obtain a local threshold estimate defined as:

$$T = \sqrt{2}\sigma_r \operatorname{erf}^{-1}(1 - 2\alpha) \quad (\text{C.7})$$

¹As one can note, this equation is slightly different from the proposed formula in [\[Aguet et al., 2013\]](#) and the associated code. Further discussions with the authors ruled the latter a mistake that has little consequence on the rest of the derivation and results validity.

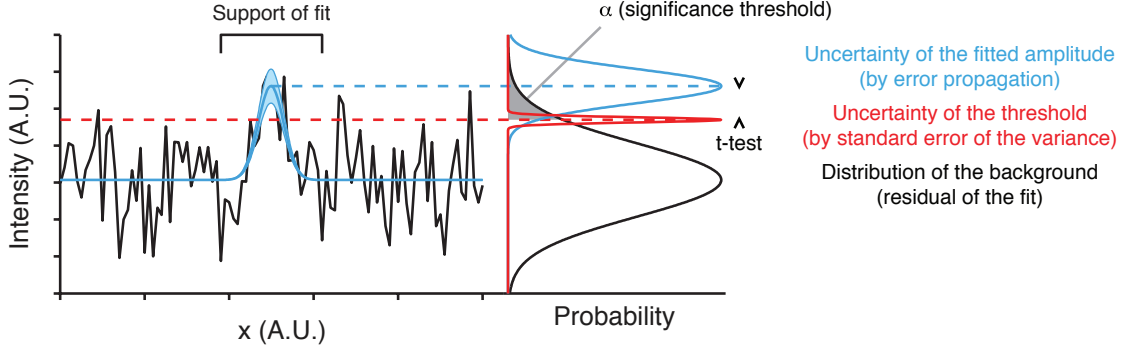


Figure C.1: One dimensional illustration of σ_r (black), σ_A (in blue) and σ_T (in red) and t -test that assert the statistical significance of the estimated amplitude (illustration courtesy of François Aguet).

A low p -value (e.g. $\alpha = 0.01$) thus results in a high threshold and a high rejection rate of amplitude induced by noise or weaker signal. Once this threshold has been estimated, the uncertainty on \hat{A} is exploited to test for the statistical significance of the hypothesis $H_0 : \hat{A} \leq T$ using a t -test. The unbiased estimator for σ_A assuming $A \sim \mathcal{N}(\hat{A}, \sigma_A)$ and $C \sim \mathcal{N}(\hat{C}, \sigma_C)$ gives:

$$\sigma_A = \sqrt{\frac{\sum_{\mathbf{x} \in w} (\hat{A} G_{\sigma,0}(\mathbf{x}) + \hat{C} - I(\mathbf{x}_0 - \mathbf{x}))^2}{n-3}} \sum_{\mathbf{x} \in W} G_{\sigma,0}(\mathbf{x})^2 \quad (\text{C.8})$$

and the standard error σ_t for the threshold T is approximated by:

$$\sigma_T \approx \frac{\sigma_r}{\sqrt{(n-1)}} \text{erf}^{-1}(1-2\alpha). \quad (\text{C.9})$$

As a clear illustration of the physical meaning of σ_r , σ_A and σ_T has been proposed in [Aguet et al., 2013]. We reproduce the illustration for sake of clarity in Figure C.1. We can thus calculate the one-sided, two sample t -test statistic:

$$t = \frac{\hat{A} - T}{\sqrt{\frac{\sigma_A^2 + \sigma_T^2}{n}}} \quad (\text{C.10})$$

Finally, for the whole image, the comparison $\text{tcdf}(t) \leq \alpha$ where tcdf denote the Student's cumulative distribution gives a mask of significance for each pixel as illustrated in Figure C.2.

C.3 Model fitting

For each local maxima on the Laplacian-of-Gaussian filtered image that coincide with the mask of significance of a 2D Gaussian model or Gaussian mixture is fitted to estimate

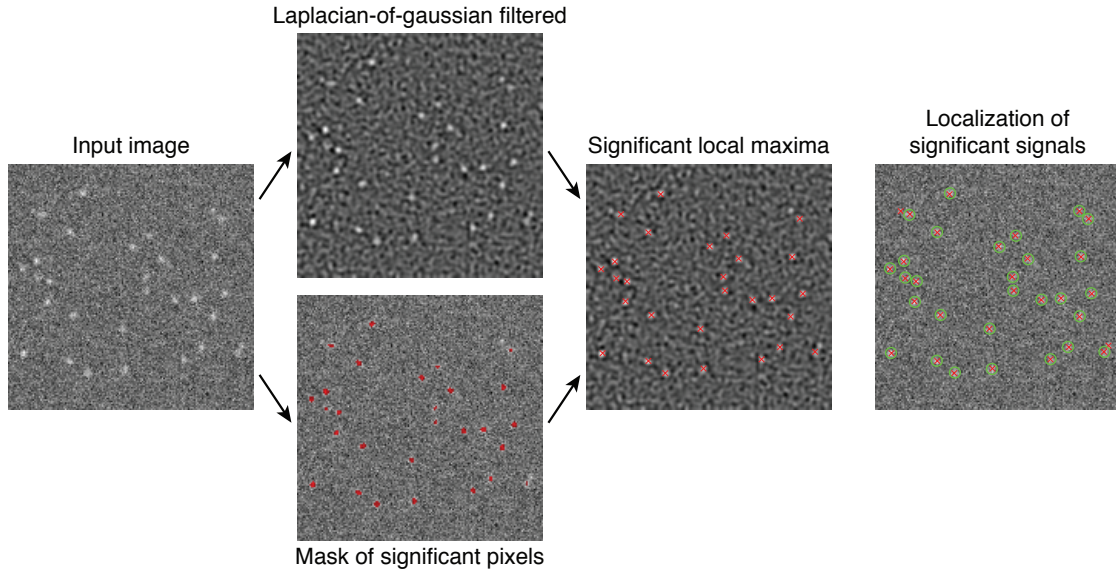


Figure C.2: Detection workflow as described in [Aguet et al., 2013].

$(A, \mu, C, \sigma)^t$ on a sub-resolved level. This estimation is carried out solving a non linear least square problem thanks to the Levenberg–Marquardt algorithm provided by the GSL. The t -test described above is performed again to test for other spurious detections after the first pixel-resolved approximation. If a mixture of Gaussian is used, a similar F-test is carried out to check the most significant number of modes. As u-track handles well merging and splitting thanks to its dedicated post-processing step and similarity cost, we stick to single Gaussian fitting estimation and thus select false positive to a minimum.

C.4 PSF scale estimation

The standard deviation σ characteristic of the 2D Gaussian PSF is estimated as a pre-processing step. The detection algorithm above is applied using a rough approximation σ_0 (which is a constant set to $\sigma_0 = 1.5$ pixel). Using Gaussian mixture modeling on the distribution of estimated σ , we select the PSF scale as the most probable mode.

12 General conclusion

The dynamic and heterogeneity inherent to every bio-physical process is now observable thanks to time-lapse fluorescence microscopy techniques. Quantitative microscopy consists in the measurement of those complex phenotypes. The challenges faced by quantitative biology originate from the instrumentation as much as on the phenotypes under study. In this manuscript, we have presented two projects that attempt to tackle some of those challenges by modeling those phenomena and estimating the parameters that control them.

Our first contribution opens the way to the measurement of fluorescent lifetime on dynamical structures *in vivo*. Frequency domain FLIM (FD FLIM) is arguably the most suitable technique for fluorescence lifetime imaging on living cell. However, transient intracellular motions can still happen during acquisition. The conventional Fourier transform, widely used for lifetime estimation with this technology, does not take those motions into account, neither it adapts to the specific noise footprint of the FD FLIM measurement. We have thus presented a dedicated signal processing method that reconstructs the fluorescein lifetime map corrupted by instrumental noise and intracellular motions in FD FLIM. Potentially low intensities in FD FLIM measurements require the use an Intensified CCD. While this technology enables the detection of very low photon counts, it also induces a very specific noise footprint. A thorough study of the noise variance model induced by the ICCD was first carried out to harness the strong heteroscedasticity that present FD FLIM measurements. Further analyses have shown that a model correction is needed to cope with optical aberrations in the ICCD. The noise model and the estimation of the associated parameter is first applied to the estimation of fluorescence lifetime. The performances of our noise variance model are further demonstrated using the well-known Wiener filter and a new patch-based algorithm for denoising images. This study is also relevant in other fields where the ICCD is exploited (military, astronomy). We then introduce a fluorescence lifetime estimation method for moving endosomes in the cell. For each particle detected in the FD FLIM measurement, the lifetime and motion parameters are jointly estimated locally in an iterative and alternative fashion. As the lifetime parameters control sinusoidal variation of the intensity, we use this intensity model to further improve motion compensation. On experimental sequences, endosome localization error is shown to be reduced by this modeling. The localization error is shown to be lower than a wide-spread wavelet-based detection method. The proposed methods are fully automatic and need only minimal and non-critical parametrization.

Our second contribution pushes the envelope in intracellular dynamics quantification. The second part of this manuscript describes our contribution to the tracking of multiple particles presenting heterogeneous transports in dense conditions. We focus here on unpredictable transitions between different types of transportation in a single trajectory. A frequent intracellular scenario with this property is the switching between confined diffusion in the cytosol and motor-mediated active transport in random directions. We first propose a review of the tracking methods proposed in the literature for sub-resolved particle tracking with an emphasis on motion heterogeneity and density. We show that those algorithms are not designed to retrieve unpredictable transitions between Brownian and directed displacements. We propose in this manuscript a study and a classification of the related works in this area. Our contribution is the description of the u-track algorithm in the adapted Bayesian framework. While this software is widely used in quantitative biology for its robustness and performances, the detail of the dynamical modeling has not been disclosed. To allow for an objective comparison of the different approaches for multiple dynamics filtering, we show here that the u-track algorithm is similar to a Generalized Pseudo Bayesian of order 1. We also present the implementation details that explain the observed experimental behavior in u-track and competing methods. After the conclusion we draw, we have proposed two adaptations to improve the tracking of heterogeneous types of motion in dense conditions. We first introduced an iterative interacting multiple model smoother. In a nutshell, this method fuses forward and backward tracking to improve the detection of abrupt transitions between diffusing and directed motion. Upon this improvement, we proposed a locally adaptive estimator for the tracker search radius. Our approach has been tested on simulations. We show that our method outperforms competing methods in the targeted scenario, but also on more homogeneous types of dynamics challenged by density. On experimental sequences, we manage to quantify the rare switching between confined diffusion and motor-mediated dynamics of unit length filament of vimentin. We also highlight the resistance of our method toward a reduction in temporal resolution.

Those contributions lie at the heart of the on-going effort by the community in signal processing and computer vision in quantitative fluorescence microscopy: on the one hand the modeling and correction of the instrumental impact, on the other hand the modeling and quantification of cellular phenotypes.

As detailed in the conclusion of each part, both methods can be further improved. However the short-term effort is focused on the application to biological problematics. In FD FLIM we planned additional experiments to further probe the spatiotemporal localization of a receptor interaction with its kinase. The long-term goal of this experiment is to measure fluorescence lifetime on a longer time scale in order to measure the evolution of the local FRET efficiency during the whole endocytic process. To handle complex or large motions that could happen in between FD FLIM acquisitions, our new tracking algorithm could be used. Also, our effort on multiple particle tracking will be directly exploited at the beginning of my upcoming post-doc to measure abortion rates in clathrin

mediated endocytosis. As the multiple particle tracking has been shown to improve u-track performances on u-track training data, this method will be widely available through a new release of the u-track algorithm.

I am now convinced by the essential place of the computational expert in modern biology. The collaboration between the different expertise in bio-chemistry, microscopy and data analysis pave the way to the advent of ambitious techniques that inject the model very early in the experimental process (in speckle microscopy the modeling is taken into account from the fluorescent tagging step). This configuration allows pushing the boundaries on the quantity and quality of the data extracted from living cells. The development of data processing methods in synchronization with the biological problematic at stake is beneficial for the biologist community as well as the computational community. It ensures the quality and completeness of the data. It ensures fast feedback and efficiency of efforts. It encourages the design of robust and flexible computation methods that can have a large impact in other fields. It proposes extremely interesting challenges, a large part of which remains to be explored.

List of Figures

0.1	α -tubuline marqué par la EGFP (GFP amélioré). a) cette chimère localise les microtubules (b) la EGFP est attaché au N-terminus de la α -tubuline. La partie intérieur de la structure cylindrique de la GFP est responsable du phénomène de fluorescence (source: Zeiss).	16
0.2	Comparaison schématique des microscopies à champ large et confocale typiquement utilisées pour l'étude du vivant (source [Vonesch et al., 2006]).	17
0.3	Un exemple de mesure FD FLIM pour $K = 6$ signaux de modulation. Le contraste a été augmenté artificiellement pour améliorer la visualisation. Les molécules fluorescentes permettent de localiser le récepteur IFNAR1 marqué en GFP sur des cellules épithéliales (RPE1).	19
0.4	Résidus obtenus au sens des moindres carrés après estimation du modèle paramétrique décrivant le comportement sinusoïdal de la modulation de phase (voir (0.1)). Les résidus sont tracés pour l'ensemble de la mesure (Figure 3.4). La variation d'amplitude des résidus met en évidence une forte hétéroscédasticité. Estimation effectuée sur un microscope confocal "spinning disk" avec un intensificateur II18MD (Lambert Instruments).	20
0.5	"Effet Doppler" induit par le mouvement des endosomes sur les mesures de temps de vie de l'ordre de quelques nanosecondes (séquence 0.3).	21
0.6	Processus de formation de l'image formation dans un CCD intensificateur de troisième génération.	22
0.7	Gain expérimental non-stationnaire en FD FLIM. Représentation de la variance calculée sur une mesure de référence FD FLIM de 12 images acquises avec un microscope confocal.	23
0.8	Histogrammes de phase comparant les résultats obtenus avec la méthode de Fourier et la méthode des moindres carrés pondérés par l'échelle du bruit estimée.	24
0.9	Erreurs moyennes de localisation. La méthode "Gaussian Fitting" [Anderson et al., 1992] est analogue à notre méthode, mais sans prise en compte de modèle d'intensité sinusoïdale. La méthode PPT est une méthode plus avancée combinant détection, puis calcul des trajectoires selon le principe du filtrage stochastique [Genovesio et al., 2006]. Les résultats sont obtenus sur des protéines RX marquées GFP et suivies manuellement (cellules épithéliales).	26

0.10	RX protéine marquée GFP sur les endosomes (gauche) et temps de vie à la membrane (droite) en l'absence d'accepteur.	27
0.11	Distribution de temps de vie estimés au niveau des endosomes et à la membranes (voir détails Section 6.1 à la page 113).	28
0.12	Convergence des estimations de vitesse à l'échelle du point de temps lors d'un changement de brutal dynamique. Avant l'image # 46, la particule de vimentine présente un mouvement Brownien confiné prolongé. Elle se déplace brutalement le long du cytosquelette pour retrouver un état Brownien confiné prolongé dès l'image # 49. Les traits rouges représentent la détection de déplacement dirigés, les traits verts représente la détection d'un mouvement Brownien et les traits jaunes représentent la prédiction issue du calcul à l'itération précédente.	32
0.13	Erreurs d'estimation de la variance du bruit caractérisant le processus mesuré sur simulations en fonction de la probabilité de changement de type de transport (0 indique un déplacement purement Brownien confiné, 0.5 indique une chance sur deux de transiter vers un mouvement dirigé à chaque point de temps). Notre méthode (en rouge) est sept fois plus précise que l'estimateur u-track (en bleu). De plus, une simple estimation récursive de la variance, prenant en compte les mesures d'erreur issues du calcul à l'itération précédente, met en évidence l'intérêt de notre méthode basée sur l'algorithme u-track (en vert). L'adaptivité et l'agilité de l'algorithme de suivi sont assurées par la mise en place de plusieurs filtres.	33
0.14	Pourcentage de vrais positifs (et faux positifs sur le graphique de droite) sur données simulées en fonction de la densité et de la probabilité de changement de type de transport (0 indique un déplacement purement Brownien confiné, 0.5 indique une chance sur deux de transiter vers un mouvement dirigé à chaque point de temps). Comparaison des performances avec notre méthode u-track et avec un filtrage IMM. La densité est fixé à 3 spots par micromètre carré sur l'exemple à gauche et sur les résultats à droite. Notre approche présente une amélioration de 15% par rapport à u-track sur le scénario le plus complexe.	34
0.15	(a) & (b) Exemple de suivi de filaments unitaires de vimentine sur une cellule témoin (à gauche) et traitée au nocodazole. (c) Proportion de mouvement d'amplitude importante avant et après traitement au nocodazole. Un mouvement d'amplitude importante est défini comme le 99,9 percentile de la vitesse estimée localement par le filtre de Kalman. L'évaluation de la dynamique sur 6 cellules de contrôle et 6 cellules traitées (séquences de 100 images) met en évidence une différence significative pour une p -valeur de 0.0088 (t -test).	35

0.16	Suivi automatique de virus dans la cellule [Burckhardt et al., 2011]. La fréquence d'acquisition est artificiellement réduite pour tester la robustesse de l'algorithme.	36
1.1	Simplified Jablonsky diagram. The thick horizontal lines denote electronic energy levels. The thinner grey lines represents the various vibrational energy states. Straight arrows are associated with absorption or emission of a photon. Wavy arrows illustrate molecular internal conversions or non-radiative relaxation processes. Vertical upward arrows indicate the instantaneous nature of excitation processes.	48
1.2	Stokes shift for different species of GFP and some GFP mutation (adapted courtesy of Damien Maurel)	48
1.3	HeLa cells stained with antibody to actin (green), vimentin (red) and DNA (blue) (courtesy of EnCor Biotechnology)	49
1.4	α -tubulin labeled with GFP. a) this chimera localize to microtubule b) the EGFP is tagged on the N-terminus of the α -tubulin. The interior part of the barrel shape structure is responsible for the fluorescent phenomena (copyright Zeiss).	51
1.5	In stable transfection the vector DNA (red wave) pass through the cell and nuclear membranes and integrated into the host genome (black wave) where it is expressed sustainably. In transient transfection, the vector DNA is delivered into the nucleus but is not integrated into the genome. (adapted from [Kim and Eberwine, 2010])	52
1.6	Comparison of wide-field, scanning confocal and spinning disk confocal systems, with schematics for each. All systems are capable of being equipped for 3D and 4D data acquisition. Excitation beams are shown in green; emission beams, in blue. The differences between these systems mean that no single system is suited for every experiment. Typical system configurations are shown, and user modification and options allow great flexibility (source: from [Stephens and Allan, 2003]).	55
1.7	TIRF technique exploits the evanescent field to measure fluorescence at the plasma membrane (source: from [Stephens and Allan, 2003]).	56
1.8	Schematic representation of SPIM principle (source: from a scheme by Jan Krieger)	57
2.1	Jablonsky diagram: the thicker lines represent electronic energy levels and the thinner lines denote the various vibrational energy states. A timescale for the transition or a color is given as a an example when physically meaningful.	67
2.2	FRET efficiency evolution with the distance r between fluorophores ECFP and EYFP ($R_0=4.9$ nm).	69

2.3	FRET allows the measurement of structural dynamical events <i>in vivo</i> . . .	69
3.1	Representation of lifetime measurement and effect of a fluorescence lifetime loss in the time domain and frequency domain.	72
3.2	Example of typical TCSPC FLIM data. Total fluorescence intensity is shown in the center and corresponds to the sum of photon counts along the time axis at each pixel. The four side graphs correspond to time dependent photon counts in four different regions with variable sizes. By considering large regions, we observe an exponential fluorescence decay (see D). A: one pixel region; B and C: 3×3 patches at different locations; D: 15×15 patch and lifetime estimation by least mean squares fitting (commercial software).	73
3.3	Instrumental setup showing the different elements of the system and the corresponding signals for FD FLIM. $E(t)$ denotes the excitation light, $F(t)$ the fluorescence signal, $M_k(t)$ the detection modulation signal and S_θ is the resulting FD FLIM measurement.	74
3.4	An example of FD FLIM measurement with $K = 12$ phase-modulation signals. The sequence must read from the upper left to the lower right. Fluorescent structures localize receptors tagged with GFP in epithelial cells (RPE1). Contrast has been artificially enhanced on the image presenting low intensity for visualization purpose.	76
3.5	Principle of FD FLIM measurement post-processing A: Example of an image sequence showing the intensity variation (S_θ) at different phase shift values ($K=12$ values distributed on 2π radians). B: Example of signal S_θ observed at a given pixel (black dots) with a sine fitting curve (red). C: Fluorescence lifetime image reconstructed from the image sequence in B.	77
3.6	Residuals of least-squares estimates of the parameters controlling the sinusoidal described by the phase modulation images (see (9.34)). The residuals associated to each pixel in the whole stack presented Figure 3.4 are plotted. The residual amplitude variability highlights a strong heteroscedasticity (Spinning disk and an intensifier II18MD from Lambert Instruments).	79
3.7	Dynamical structures in FD FLIM (normalized details from Figure 3.4). . .	80
4.1	Image formation process in a third generation Intensified CCD.	83

4.2	Spatial non-stationarity induced by the ICCD on a background image (an acquisition in the absence of excitation on ICCD input). Spontaneous burst of photon in the intensified area highlights the sensitivity of the device (raw intensity is presented on the middle magnification and automatically highlighted in red in the right magnification)). The blue-squared area is not intensified and describe a much more stationary intensity footprint for the CCD.	86
4.3	Confirmation of the validity of the quadratic model from experimental measurements in a given local area of the II18MD from Lambert Instruments.	88
4.4	Horizontal profiles (after normalization) of noise variance and intensity on a single image. a) A simulated reference stack respecting the theoretical image formation highlights the expected equivalent symmetry between intensity and variance. b) On an experimental wide-field stack the curve highlights a dis-symmetry that is not compatible with a constant gain between intensity and variance. The variance is estimated using the median of absolute deviation on a 30×30 pixels square window.	89
4.5	Four different gains at four different locations computed from a FD FLIM reference stack of 13 frames acquired with a confocal setup (crosses represent measured variances, lines represent the theoretical noise model).	90
4.6	Variance vs spatial coordinates for $\lambda = 20000$ and $\epsilon = 10$ (a.i.u.) from a reference stack of 13 frames (FD FLIM confocal). In theory, the measured variance should form a horizontal plane with constant estimates.	91
4.7	Global parameter estimation from a wide-field FD FLIM sequence.	93
4.8	Variance prediction with added correction (red: noise variance model; blue: measured noise variance).	94
4.9	Phase histograms using the Fourier method and the weighted least squares method exploiting the estimated noise scale on a reference FD FLIM measurement of a plain fluorescein sample (see Figure 4.3.a).	97
4.10	Lifetime histograms on the whole image control cells with GFP tagged receptor in live cell RPE1.	97
4.11	Wiener filtering using the constant and spatially adaptive noise variances.	98
4.12	Comparisons of several denoising algorithms.	100
5.1	Visualization of sub-cellular structure motions during image acquisition and effect on the FLIM images. A: Example of image sequence with moving sub-structures (shown as series of zoomed thumbnails) and of modulation signal S_θ with sine fitting in red. B. Global estimation of motion by maximum intensity projections (MIP) and ratio with initial intensity I_0 (right). C: Reconstructed lifetime image showing outliers in red. D: Distribution of lifetime values in the reconstructed lifetime map in C. showing extreme, non physical (negative or too high) values.	102

5.2	“Doppler effect” on lifetime measurement (in nanoseconds) due to motion (see Figure 3.7).	103
5.3	Moving vesicle model.	104
5.4	Iterative and alternative procedure for fluorescence lifetime estimation on moving endosomes.	105
5.5	Matusita distance in red estimated on each bin of the histogram of the spot candidate scores.	107
5.6	Simulating motion impact on lifetime map and reconstruction. a) Simulated sequence with 5 vesicles exhibiting free Brownian motion modeled by a normal law for displacement with a standard deviation of 2 pixels (contrast has been enhanced for visualization). b) The estimated lifetime map on this FD FLIM measurement with the doppler effect footprint. c) Patches taking the value of the estimated fluorescence lifetime are added on the initial vesicle detection locus. The patch size is set to three times the size of the estimated spot scale d) A simple inpainting algorithm is applied to correct secondary artifacts for cosmetic purpose. e) True lifetime simulated on background and vesicles f) Motion estimation carried out during the iterative process.	109
5.7	Left: Lifetime map using Fourier decomposition. Dark blue and red spots are unrealistic values due to organelle movements. Right: lifetime map reconstruction using our method.	110
5.8	Mean localization error using Gaussian fitting [Anderson et al., 1992], Probabilistic particle tracking [Genovesio et al., 2006] and our method on fluorescently tagged RX protein in living epithelial cells. Endosomes have been tracked by hand using the MJtrack software [Smal et al., 2010].	111
5.9	An example of GFP-tagged receptor tracking on a 12 frames stack (images have been normalized for visualization purpose). The data points presenting the highest localization error coincide with the noiser images presented in the second line.	112
6.1	Tracked GFP-tagged RX on endosomes (left) and membrane lifetime map (right) in the absence of acceptor.	114
6.2	Lifetime distribution estimated on endosomes and the membrane in the five different experimental conditions.	115
6.3	Tracked GFP-tagged RX on endosomes (left) and membrane lifetime map (right) in the presence of acceptor mCherry-KX.	116
6.4	Tracked GFP-tagged RX on endosomes (left) and membrane fluorescence lifetime map (right) in the presence of acceptor mCherry-KX 15 minutes after CX injection. Among the KX-injected cells, only two cells present early endosomes that do not belong to the recycling compartment. Additionally the lifetime estimated on the membrane exhibits strong variations.	117

8.1	Trajectory of a single molecule undergoing Brownian motion in three dimensions. Segment color strength indicates temporal progression.	138
8.2	Motor-mediated vesicular transport along the microtubule network (source: [Vale, 2003]).	139
8.3	Simulation of anomalous subdiffusion and active diffusion as a function of time.	140
8.4	Heterogeneous motion model on a disordered cytoskeleton network (a) and associated vesicle trajectory undergoing switches between confined diffusion and directed motion (see [Bressloff and Newby, 2013]).	141
8.5	The three fundamental networks forming the cytoskeleton (source: from [Lodish, 2008]).	144
8.6	Intermediate filament (IF) formation (source: from [Kirmse et al., 2007]).	144
8.7	Vimentin motility seems to present a large proportion of confined Brownian motion and rare, sudden, motor-mediated transport. Vimentin null epithelial cell (cell line SW13) transfected with ULF of vimentin Y117L mutant fused to GFP. Image acquired with a spinning disk confocal microscope with a 100x objective zoom 1.5 (Numerical Aperture 1.4, pixel size 0.10905 $\mu\text{m}/\text{pixel}$). Colored Tracks have been computed with an advanced u-track parametrization. This quantification is not perfect as demonstrated in Figure 8.8. However, u-track manages to highlight a large directed motion in a dense population of Brownian moving particles.	145
8.8	U-track best effort in dense spatiotemporal conditions does not retrieve motion type switching correctly. A) Vimentin ULF presents a fast directed motion between two stationary Brownian states (orange detail in Figure 8.7). The tracking algorithm misses the brutal transition pointed by the red arrow. B) The ULF undergoes a direct motion and then switches to a confined Brownian motion scheme (blue detail in Figure 8.7). The u-track algorithm produces a false positive, pointed by the red arrow, due to the strong inertia of the stochastic filtering.	146
8.9	Artificially augmenting the search radius upper bound produces numerous false positives in the sequence. A) Search radius manual increase allows the tracking of brutal transitions from Brownian to directed motion that were not possible with a more restrictive setup. B,C,D) On the other hand, multiple false positives appear on the whole sequence.	148

9.1	<p>Particles presenting motion type switching are challenging to track. A) An example of heterogeneous motion type on a single track (detail). The ULF of vimentin presents a fast directed motion between two Brownian states. B) An IMM based algorithm, similar to [Genovesio et al., 2006] (supporting an forward-backward initialization step) does not retrieve the direct segment, only the Brownian sections are correctly tracked. An artificial increase of the search radius is not possible without an important number of false positives in the whole sequence. C) The u-track algorithm will allow to retrieve a part of the direct motion segment thanks to the Kalman Filter initialization routine and speed transmission. In this algorithm, the search radius has the same size for Brownian and directed motion hypothesis. Color code: Red and Green segments represent the detected types of displacement, which can be directed or Brownian respectively. Blue and Green circles represent the search radius associated with directed and Brownian motions respectively. The position of the search radius reflects the predicted localization (scale bar is $0.5 \mu m$, acquisition frequency is 1Hz).</p>	151
9.2	<p>An example of motion heterogeneity in more dense conditions. A) The ULF move fast and switch to a confined Brownian motion. B) An IMM based algorithm produces a correct track, switching to a Brownian motion scheme. The merging of Kalman filters posterior results in an adaptive estimation of the speed that quickly converges to zero. C) The u-track algorithm produces a false positive due to the strong inertia of the stochastic filter. This figure shows an example of u-track convergence to a single speed for the track. Accordingly, the Kalman filter constantly “looks” in the general direction of the trajectory. Color code: Red and Green segments represent the detected types of displacement, which can be directed or Brownian respectively. Blue and Green circles represent the search radius associated with directed and Brownian motions respectively. The position of the search radius reflects the predicted localization (scale bar is $0.5 \mu m$, acquisition frequency is 1Hz).</p>	152
9.3	<p>Object detection framework including noise reduction, signal enhancement and thresholding (source from: [Smal et al., 2010]).</p>	155
9.4	<p>Dependency graph of a Hidden Markov process applied to the state \mathbf{x}_t and measure $\mathbf{z}_t, \forall t \in \mathbb{N}$.</p>	156
9.5	<p>Naive Nearest-Neighbor assignment and global optimization. Filled circles represent detection $\mathbf{z}_{t+1,i}$, outlined circles represent associated prediction $\bar{\mathbf{x}}_{t,i}$.</p>	166
9.6	<p>Tracking of comet-shaped EB1 protein marking microtubule plus-TIP (courtesy of the Danuser Lab). In this imaging use-case, object shape is a very valuable cue for tracking.</p>	171

10.1	Convergence of speed estimation at the time point scale. Red links represent directed prediction selection, Green links represent Brownian prediction and Yellow represent prediction stemming from the previous tracking round. A small tracklet motion is easily retrieved during the first tracking round; it serves as a track initialization for the following track rounds (scale bar is $0.5 \mu m$, acquisition frequency is 1Hz).	179
10.2	Overview of our tracking algorithm at tracking round $k + 1$. Let D_{t+1} be the detection (measurement) set at time $t + 1$. For each measurement, the closest prediction $\hat{\mathbf{x}}_{t+1,k+1}^{\hat{\theta}_{t+1,k+1}}$ is selected by the among predictions made by N Kalman filters at round $k + 1$ and the estimated posterior at round k . The graph-based combinatorial algorithm [Jonker and Volgenant, 1987] estimates the optimal assignment $(\hat{\mathbf{x}}_{t+1,k+1}^{\hat{\theta}_{t+1,k+1}}, \mathbf{z}_{t+1})$ between the closest prediction and detections for every track. Once the best measurement is assigned to the track, this measurement is used to update each Kalman filter variable independently.	181
10.3	U-track cut-off estimation and online iterative estimation on the last forward tracking round. Red and Blue lines represent the prediction errors in x and y . The Green line describes the median of absolute deviation scaled by a factor 3; it gives the scale of the prediction residuals. The Black line is the cut-off estimated by u-track.	183
10.4	Impact of noise adaptation on linking cut-off for a single track. In this example, the low number of data points on the first few frames results in a weak estimate of the search radius leading to a false positive. Above, the process noise is computed using the iterative online estimator [Stengel, 1986]. As the method is not locally adaptive, it exploits all the prediction errors (Red and Blue lines) and repeats the tracking errors during backward tracking. Below, the process noise is computed using our method. By finally estimating the Kalman Filter process noise, we provide an accurate end of track time point on the backward tracking. The subsequent forward tracking does not repeat the previous mistakes (data not shown).	184
10.5	A) Example of track simulation presenting a density of $1 \text{ spot}/\mu\text{m}^2$. B) Correct linking percentage with respect to density and motion type switching probability. Our method outperform u-track by 15% in the hardest case. C) True positive and false positive ratio on the same simulation with a density of $3 \text{ spots}/\mu\text{m}^2$ comparing our method with u-track, u-track with an online process noise estimator and an IMM algorithm with forward-backward initialization.	185
10.6	Display of several simulated densities.	186

10.7	Process noise estimation error on simulation wrt motion switching probability: 0 means pure Brownian motion, 0.5 means a rate of 50% chances to switch to direct or Brownian motion. Vesicle density is set to 3 spots/ μm^2 . Our method is compared with process-noise variance estimation on the whole track up to time t (u-track) and an online and iterative though non adaptive process noise variance estimation (u-track online process).	187
10.8	Correct linking and false positive percentage wrt transition speed.	188
10.9	Correct linking and false positive percentage wrt speed switching probability.	188
10.10	The same simulation scheme used for u-track training has been tested and the performance of our method (KF iter in this figure) compared with the u-track algorithm. The probabilities of confined diffusion, free diffusion, directed are 0.5, 0.4 and 0.1 respectively.	189
10.11	Computation time measured on the tracking alone (no detection). Mixture of confined diffusion (50%), free diffusion (40 %) and direct motions (10%). Computation overhead is around 10% with respect to u-track. The complexity grows linearly with density.	190
10.12A.	Control cell. B. After nocodazole treatment, the ULF should exhibit a decrease of its large motions proportion. C. A threshold for detecting large motion is estimated using the 99.9 percentile of the speed estimated. A t -test on the whole experiment gives a p -value of 0.0088. Imaging with spinning disk confocal microscope. Acquisition speed is set to 1 Hz for a minute. Scale bar is 1 μm	192
10.13	Evolution of large motion count with large motion threshold for control and treated cells. This is equivalent to a inverted cumulative histogram for the estimated velocities.	193
10.14	Error rate of u-track and iu-track wrt frame-rate decimation on a virus tracking experiment [Burckhardt et al., 2011]. Frame-rate is artificially reduced to test the robustness of our tracker.	193
10.15	Viruses tracking inside the cell [Burckhardt et al., 2011]. Frame-rate is artificially reduced to test the robustness of our tracker. On this example, we observe that u-track break point is around a 30-fold decimation while our improvement exhibits a single error at a 30-fold decimation (longer tracks on the last experiment are due to lower frame rate but represent real tracks). Imaging with spinning disk confocal microscope. Acquisition speed is set to 30 Hz. Scale bar is 0.9 μm	194
C.1	One dimensional illustration of σ_r (black), σ_A (in blue) and σ_T (in red) and t-test that assert the statistical significance of the estimated amplitude (illustration courtesy of François Aguet).	200
C.2	Detection workflow as described in [Aguet et al., 2013].	201

Bibliography

- G Ackerson and K Fu. On state estimation in switching environments. *IEEE Transactions on Automatic Control*, 15(1):10–17, 1970.
- Francois Aguet, Costin N Antonescu, Marcel Mettlen, Sandra L Schmid, and Gaudenz Danuser. Advances in analysis of low signal-to-noise images link dynamin and AP2 to the functions of an endocytic checkpoint. *Developmental Cell*, 26(3):279–291, 2013. 00005.
- Paul S Agutter, PC Malone, and Denys N Wheatley. Intracellular transport mechanisms: a critique of diffusion theory. *Journal of Theoretical Biology*, 176(2):261–272, 1995.
- BDO Anderson and JB Moore. *Optimal Filtering. 1979*. Prentice-Hall, Englewood Cliffs, NJ.
- C.M. Anderson, G.N. Georgiou, IE Morrison, GV Stevenson, and R.J. Cherry. Tracking of cell surface receptors by fluorescence digital imaging microscopy using a charge-coupled device camera. *Journal of Cell Science*, 101(2):415, 1992.
- E. Angelini, J. Atif, and J. Delon. Detection of glioma evolution on longitudinal MRI studies. In *Biomedical Imaging (ISBI), 2007 IEEE International Symposium on*, Arlington (USA), 2007. IEEE.
- M Sanjeev Arulampalam, Simon Maskell, Neil Gordon, and Tim Clapp. A tutorial on particle filters for online nonlinear/non-Gaussian Bayesian tracking. *Signal Processing, IEEE Transactions on*, 50(2):174–188, 2002.
- D Axelrod, D E Koppel, J Schlessinger, E Elson, and W W Webb. Mobility measurement by analysis of fluorescence photobleaching recovery kinetics. *Biophysical Journal*, 16(9):1055–1069, September 1976. ISSN 0006-3495. URL <http://www.ncbi.nlm.nih.gov/pmc/articles/PMC1334945/>. 02060 PMID: 786399 PMCID: PMC1334945.
- Yaakov Bar-Shalom. *Tracking and Data Association*. Academic Press Professional, Inc., 1987.
- Yaakov Bar-Shalom. Multitarget-multisensor tracking: advanced applications. *Norwood, MA, Artech House, 1990, 391 p.*, 1, 1990.

- Yaakov Bar-Shalom. Multitarget-multisensor tracking: Applications and advances. Volume III. Norwood, MA, Artech House, Inc., 2000, 2000.
- Yaakov Bar-Shalom, X Rong Li, and Thiagalingam Kirubarajan. *Estimation with Applications to Tracking and Navigation: Theory Algorithms and Software*. John Wiley & Sons, 2004.
- M. A. Beaumont, W. Zhang, and D. J. Balding. Approximate Bayesian computation in population genetics. *Genetics*, 162:2025–2035, 2002.
- Wolfgang Becker, Bertram Su, and Axel Bergmann. Fast-acquisition multispectral FLIM by parallel TCSPC. volume 7183, pages 718305–718305–5, 2009. doi: 10.1117/12.807697. URL <http://dx.doi.org/10.1117/12.807697>. 00004.
- P. Bergamini, G. Bonelli, E. G. Tanzi, M. Uslenghi, L. Poletto, and G. Tondello. A fast readout and processing electronics for photon counting intensified charge-coupled device. *Review of Scientific Instruments*, 71(4):1841–1848, 2000. URL <http://scitation.aip.org/content/aip/journal/rsi/71/4/10.1063/1.1150545>.
- David J. S. Birch and Robert E. Imhof. Time-Domain Fluorescence Spectroscopy Using Time-Correlated Single-Photon Counting. In Joseph R. Lakowicz, editor, *Topics in Fluorescence Spectroscopy*, number 1 in Topics in Fluorescence Spectroscopy, pages 1–95. Springer US, January 1999. ISBN 978-0-306-43874-5, 978-0-306-47057-8. URL http://link.springer.com/chapter/10.1007/0-306-47057-8_1. 00167.
- Samuel Blackman and Artech House. *Design and Analysis of Modern Tracking Systems*. Boston, MA: Artech House, 1999. 02938.
- Samuel S Blackman. Multiple hypothesis tracking for multiple target tracking. *Aerospace and Electronic Systems Magazine, IEEE*, 19(1):5–18, 2004.
- Henk AP Blom and Yaakov Bar-Shalom. The interacting multiple model algorithm for systems with Markovian switching coefficients. *IEEE Transactions on Automatic Control*, 33(8):780–783, 1988.
- Frank Robbert Boddeke. *Quantitative fluorescence microscopy: autofocusing, z-axis calibration, image sensors, fluorescence lifetime imaging*. PhD thesis, Delft University Press, Delft, 1998.
- S. Bonneau, L. Cohen, and M. Dahan. A multiple target approach for single quantum dot tracking. In *Biomedical Imaging: Nano to Macro, 2004. IEEE International Symposium on*, page 664–667. IEEE, 2004.
- J. Boulanger, C. Kervrann, P. Bouthemy, P. Elbau, J.-B. Sibarita, and J. Salamero. Patch-based non-local functional for denoising fluorescence microscopy image sequences. *IEEE Transactions on Medical Imaging*, 29(2):442–454, 2010.

- Clifford P Brangwynne, Gijssje H Koenderink, Frederick C MacKintosh, and David A Weitz. Intracellular transport by active diffusion. *Trends in Cell Biology*, 19(9):423–427, 2009.
- Paul C Bressloff and Jay M Newby. Stochastic models of intracellular transport. *Reviews of Modern Physics*, 85(1):135, 2013.
- F. Briquet-Laugier, C. Boulin, and J.-C. Olivo-Marin. Analysis of moving biological objects in video microscopy sequences. In A. M. Frank and J. S. Walton, editors, *Society of Photo-Optical Instrumentation Engineers (SPIE) Conference Series*, volume 3642, pages 4–12, May 1999.
- A Buades, B Coll, and J.M. Morel. A review of image denoising methods, with a new one. *SIAM J. Multiscale Modeling and Simulation*. (2005), 4(2):490–530, 2005.
- Christoph J Burckhardt, Maarit Suomalainen, Philipp Schoenenberger, Karin Boucke, Silvio Hemmi, and Urs F Greber. Drifting motions of the adenovirus receptor CAR and immobile integrins initiate virus uncoating and membrane lytic protein exposure. *Cell host & microbe*, 10(2):105–117, 2011.
- Avi Caspi, Rony Granek, and Michael Elbaum. Diffusion and directed motion in cellular transport. *Physical Review E*, 66(1):011916, 2002.
- Michael K Cheezum, William F Walker, and William H Guilford. Quantitative comparison of algorithms for tracking single fluorescent particles. *Biophysical Journal*, 81(4):2378–2388, 2001.
- Nicolas Chenouard, Isabelle Bloch, and J-C Olivo-Marin. Multiple hypothesis tracking in microscopy images. In *Biomedical Imaging: From Nano to Macro, 2009. ISBI'09. IEEE International Symposium on*, page 1346–1349. IEEE, 2009.
- Nicolas Chenouard, Isabelle Bloch, and Jean-Christophe Olivo-Marin. Multiple hypothesis tracking for cluttered biological image sequences. *IEEE Transactions on Pattern Analysis and Machine Intelligence*, 2013.
- Nicolas Chenouard, Ihor Smal, Fabrice de Chaumont, Martin Maska, Ivo F. Sbalzarini, Yuanhao Gong, Janick Cardinale, Craig Carthel, Stefano Coraluppi, Mark Winter, Andrew R. Cohen, William J. Godinez, Karl Rohr, Yannis Kalaidzidis, Liang Liang, James Duncan, Hongying Shen, Yingke Xu, Klas E. G. Magnusson, Joakim Jaldén, Helen M. Blau, Perrine Paul-Gilloteaux, Philippe Roudot, Charles Kervrann, François Waharte, Jean-Yves Tinevez, Spencer L. Shorte, Joost Willemsse, Katherine Celler, Gilles P. van Wezel, Han-Wei Dan, Yuh-Show Tsai, Carlos Ortiz de Solórzano, Jean-Christophe Olivo-Marin, and Erik Meijering. Objective comparison of particle tracking methods. *Nature Methods*, 11(3):281–289, March 2014. ISSN 1548-7091. doi:

- 10.1038/nmeth.2808. URL <http://www.nature.com/nmeth/journal/v11/n3/full/nmeth.2808.html>. 00000.
- Anatole Chessel, François Waharte, Jean Salamero, and Charles Kervrann. A maximum likelihood method for lifetime estimation in photon counting-based fluorescence lifetime imaging microscopy. In *EUSIPCO-European Signal Processing Conference*, page 1–5, 2013. URL <http://hal.inria.fr/hal-00931631/>.
- Robert M. Clegg, T. W. Gadella, Jr., and Thomas M. Jovin. Lifetime-resolved fluorescence imaging. volume 2137, pages 105–118, 1994. doi: 10.1117/12.182715. URL <http://dx.doi.org/10.1117/12.182715>.
- José-Angel Conchello and Jeff W Lichtman. Optical sectioning microscopy. *Nature Methods*, 2(12):920–931, December 2005. ISSN 1548-7091, 1548-7105. doi: 10.1038/nmeth815. URL <http://www.nature.com/doifinder/10.1038/nmeth815>. 00354.
- K. Dabov, A. Foi, V. Katkovnik, and K. Egiazarian. Image denoising by sparse 3-D transform-domain collaborative filtering. *IEEE Transactions on Image Processing*, 16(8):2080–2095, 2007.
- Gaudenz Danuser. Computer vision in cell biology. *Cell*, 147(5):973–978, 2011. 00034.
- Fabrice de Chaumont, Stéphane Dallongeville, Nicolas Chenouard, Nicolas Hervé, Sorin Pop, Thomas Provoost, Vannary Meas-Yedid, Praveen Pankajakshan, Timothée Lecomte, Yoann Le Montagner, Thibault Lagache, Alexandre Dufour, and Jean-Christophe Olivo-Marin. Icy: an open bioimage informatics platform for extended reproducible research. *Nature Methods*, 9(7):690–696, July 2012. ISSN 1548-7091. doi: 10.1038/nmeth.2075. URL <http://www.nature.com/nmeth/journal/v9/n7/abs/nmeth.2075.html>. 00053.
- S. Delpretti, F. Luisier, S. Ramani, T. Blu, and M. Unser. Multiframe sure-let denoising of timelapse fluorescence microscopy images. In *5th IEEE International Symposium on Biomedical Imaging: From Nano to Macro, 2008. ISBI 2008*, pages 149–152, May 2008. doi: 10.1109/ISBI.2008.4540954.
- Arnaud Doucet, SJ Godsill, and C Andrieu. *On sequential simulation-based methods for Bayesian filtering*. Department of Engineering, University of Cambridge UK, 1998.
- K Dowling, S. C. W Hyde, J. C Dainty, P. M. W French, and J. D Hares. 2-D fluorescence lifetime imaging using a time-gated image intensifier. *Optics Communications*, 135(1–3):27–31, February 1997. ISSN 0030-4018. doi: 10.1016/S0030-4018(96)00618-9. URL <http://www.sciencedirect.com/science/article/pii/S0030401896006189>. 00065.

- John E Eriksson, Thomas Dechat, Boris Grin, Brian Helfand, Melissa Mendez, Hanna-Mari Pallari, and Robert D Goldman. Introducing intermediate filaments: from discovery to disease. *The Journal of Clinical Investigation*, 119(7):1763, 2009.
- A. H. Feiveson and F.C. Delaney. The distribution and properties of a weighted sum of chi squares. Technical Report NASA TN D-4575, National Aeronautics and Space Administration, Houston, Texas, May 1968.
- Linqing Feng, Yingke Xu, Yi Yang, and Xiaoxiang Zheng. Multiple dense particle tracking in fluorescence microscopy images based on multidimensional assignment. *Journal of Structural Biology*, 173(2):219–228, 2011.
- Thomas E Fortmann, Yaakov Bar-Shalom, and Molly Scheffe. Multi-target tracking using joint probabilistic data association. In *Decision and Control including the Symposium on Adaptive Processes, 1980 19th IEEE Conference on*, volume 19, page 807–812. IEEE, 1980.
- Denis Fortun, Chen Chen, Perrine Paul-Gilloteaux, François Waharte, Jean Salamero, and Charles Kervrann. Correlation and variational approaches for motion and diffusion estimation in fluorescence imaging. In *EUSIPCO-European Signal Processing Conference*, pages 1–5, September 2013. URL <http://hal.inria.fr/hal-00931408>.
- D Fraser and J Potter. The optimum linear smoother as a combination of two optimum linear filters. *IEEE Transactions on Automatic Control*, 14(4):387–390, 1969.
- A. Frenkel, MA Sartor, and MS Wlodawski. Photon-noise-limited operation of intensified CCD cameras. *Applied Optics*, 36(22):5288–5297, 1997.
- Theodorus WJ Gadella, Robert M. Clegg, and Thomas M. Jovin. Fluorescence lifetime imaging microscopy: Pixel-by-pixel analysis of phase-modulation data. *Bioimaging*, 2(3):139–159, 1994. URL [http://onlinelibrary.wiley.com/doi/10.1002/1361-6374\(199409\)2:3%3C139::AID-BI04%3E3.0.CO;2-T/abstract](http://onlinelibrary.wiley.com/doi/10.1002/1361-6374(199409)2:3%3C139::AID-BI04%3E3.0.CO;2-T/abstract).
- E. Gaviola. Ein fluorometer. Apparat zur messung von fluoreszenzabklingungszeiten. *Zeitschrift für Physik*, 42(11-12):853–861, 1927. URL <http://link.springer.com/article/10.1007/BF01776683>.
- Enrique Gaviola. Die abklingungszeiten der Fluoreszenz von Farbstofflösungen. *Annalen der Physik*, 386(23):681–710, 1926. URL <http://onlinelibrary.wiley.com/doi/10.1002/andp.19263862304/abstract>.
- Jeff Gelles, Bruce J Schnapp, and Michael P Sheetz. Tracking kinesin-driven movements with nanometre-scale precision. *Nature*, 331(6155):450–453, 1988.

- A. Genovesio, T. Liedl, V. Emiliani, W.J. Parak, M. Coppey-Moisan, and J.C. Olivo-Marin. Multiple particle tracking in 3-D+ t microscopy: method and application to the tracking of endocytosed quantum dots. *IEEE Transactions on Image Processing*, 15(5):1062–1070, 2006.
- Auguste Genovesio, Bo Zhang, and J-C Olivo-Marin. Tracking of multiple fluorescent biological objects in three dimensional video microscopy. In *Image Processing, 2003. ICIP 2003. Proceedings. 2003 International Conference on*, volume 1, page I–1105. IEEE, 2003.
- Ben N G Giepmans, Stephen R Adams, Mark H Ellisman, and Roger Y Tsien. The fluorescent toolbox for assessing protein location and function. *Science (New York, N.Y.)*, 312(5771):217–224, April 2006. ISSN 1095-9203. doi: 10.1126/science.1124618. 01525 PMID: 16614209.
- William J Godinez, Marko Lampe, Stefan Wörz, Barbara Müller, Roland Eils, and Karl Rohr. Deterministic and probabilistic approaches for tracking virus particles in time-lapse fluorescence microscopy image sequences. *Medical Image Analysis*, 13(2): 325–342, 2009.
- William J Godinez, Marko Lampe, Roland Eils, B Muller, and Karl Rohr. Tracking multiple particles in fluorescence microscopy images via probabilistic data association. In *Biomedical Imaging: From Nano to Macro, 2011 IEEE International Symposium on*, page 1925–1928. IEEE, 2011.
- Robert D Goldman, Boris Grin, Melissa G Mendez, and Edward R Kuczmarski. Intermediate filaments: versatile building blocks of cell structure. *Current Opinion in Cell Biology*, 20(1):28–34, 2008.
- E Gratton and M Limkeman. A continuously variable frequency cross-correlation phase fluorometer with picosecond resolution. *Biophysical Journal*, 44(3):315–324, December 1983. ISSN 0006-3495. URL <http://www.ncbi.nlm.nih.gov/pmc/articles/PMC1434839/>. 00481 PMID: 6661490 PMCID: PMC1434839.
- G. Grynkiewicz, M. Poenie, and R. Y. Tsien. A new generation of Ca²⁺ indicators with greatly improved fluorescence properties. *Journal of Biological Chemistry*, 260(6):3440–3450, March 1985. ISSN 0021-9258, 1083-351X. URL <http://www.jbc.org/content/260/6/3440>. 19783 PMID: 3838314.
- Mats GL Gustafsson. Nonlinear structured-illumination microscopy: wide-field fluorescence imaging with theoretically unlimited resolution. *Proceedings of the National Academy of Sciences of the United States of America*, 102(37):13081–13086, 2005. URL <http://www.pnas.org/content/102/37/13081.short>. 00842.

- Junyan Han and Kevin Burgess. Fluorescent Indicators for Intracellular pH. *Chemical Reviews*, 110(5):2709–2728, May 2010. ISSN 0009-2665, 1520-6890. doi: 10.1021/cr900249z. URL <http://pubs.acs.org/doi/abs/10.1021/cr900249z>.
- Q S Hanley, V Subramaniam, D J Arndt-Jovin, and T M Jovin. Fluorescence lifetime imaging: multi-point calibration, minimum resolvable differences, and artifact suppression. *Cytometry*, 43(4):248–260, April 2001. ISSN 0196-4763. 00083 PMID: 11260592.
- J Hedstrom, S Sedarous, and F G Prendergast. Measurements of fluorescence lifetimes by use of a hybrid time-correlated and multifrequency phase fluorometer. *Biochemistry*, 27(17):6203–6208, August 1988. ISSN 0006-2960. PMID: 3146345.
- Ricardo Henriques, Mickael Lelek, Eugenio F. Fornasiero, Flavia Valtorta, Christophe Zimmer, and Musa M. Mhlanga. QuickPALM: 3D real-time photoactivation nanoscopy image processing in ImageJ. *Nature Methods*, 7(5):339–340, May 2010. doi: 10.1038/nmeth0510-339. URL <http://www.nature.com/nmeth/journal/v7/n5/full/nmeth0510-339.html>. 00099.
- Harald Herrmann, Harald Bär, Laurent Kreplak, Sergei V Strelkov, and Ueli Aebi. Intermediate filaments: from cell architecture to nanomechanics. *Nature Reviews Molecular Cell Biology*, 8(7):562–573, 2007.
- M.A. Hink, T. Bisseling, and A.J.W.G. Visser. Imaging protein-protein interactions in living cells. *Plant Molecular Biology*, 50(6):871–883, 2002.
- Frank L. Hitchcock. The distribution of a product from several sources to numerous localities. *Math. Phys*, 20(1):224, 1941.
- O. Holub, M. J. Seufferheld, C. Gohlke, Govindjee, and R. M. Clegg. Fluorescence Lifetime Imaging (FLI) in Real-Time - a New Technique in Photosynthesis Research. *Photosynthetica*, 38(4):581–599, August 2001. ISSN 0300-3604, 1573-9058. doi: 10.1023/A:1012465508465. URL <http://link.springer.com/article/10.1023/A%3A1012465508465>.
- Oliver Holub. *Fluorescence lifetime imaging at video rate a new technique in photosynthesis research*. PhD thesis, Universitätsbibliothek, 2003. URL <http://opus.kobv.de/tuberlin/volltexte/2003/647/>.
- Erik FY Hom, Franck Marchis, Timothy K. Lee, Sebastian Haase, David A. Agard, and John W. Sedat. AIDA: an adaptive image deconvolution algorithm with application to multi-frame and three-dimensional data. *Journal of the Optical Society of America A*, 24(6):1580–1600, 2007. URL <http://www.opticsinfobase.org/abstract.cfm?uri=josaa-24-6-1580>. 00052.

- Robert Hooke and R. Waller. *The Posthumous Works of Robert Hooke, ... Containing His Cutlerian Lectures, and Other Discourses, Read at the Meetings of the Illustrious Royal Society. ... Illustrated with Sculptures. To These Discourses is Prefixed the Author's Life, ... Publish'd by Richard Waller.* Sam Smith, 1705. 00000.
- Sébastien Huet, Erdem Karatekin, Viet Samuel Tran, Isabelle Fanget, Sophie Cribier, and Jean-Pierre Henry. Analysis of transient behavior in complex trajectories: application to secretory vesicle dynamics. *Biophysical Journal*, 91(9):3542–3559, 2006. 00087.
- C. L. Hutchinson, J. R. Lakowicz, and E. M. Sevick-Muraca. Fluorescence lifetime-based sensing in tissues: a computational study. *Biophysical Journal*, 68(4):1574–1582, April 1995. ISSN 0006-3495. doi: 10.1016/S0006-3495(95)80330-9. URL <http://www.sciencedirect.com/science/article/pii/S0006349595803309>.
- Michael Isard and Andrew Blake. Contour tracking by stochastic propagation of conditional density. In *European Conference on Computer Vision—ECCV'96*, page 343–356. Springer, 1996.
- Khuloud Jaqaman, Dinah Loerke, Marcel Mettlen, Hirotaka Kuwata, Sergio Grinstein, Sandra L Schmid, and Gaudenz Danuser. Robust single-particle tracking in live-cell time-lapse sequences. *Nature Methods*, 5(8):695–702, 2008. 00278.
- Elizabeth A Jares-Erijman and Thomas M Jovin. FRET imaging. *Nature Biotechnology*, 21(11):1387–1395, November 2003. ISSN 1087-0156. doi: 10.1038/nbt896. 01039 PMID: 14595367.
- Roy Jonker and Anton Volgenant. A shortest augmenting path algorithm for dense and sparse linear assignment problems. *Computing*, 38(4):325–340, 1987.
- Simon J Julier, Jeffrey K Uhlmann, and Hugh F Durrant-Whyte. A new approach for filtering nonlinear systems. In *American Control Conference, 1995. Proceedings of the*, volume 3, page 1628–1632. IEEE, 1995.
- Yannis Kalaidzidis. Intracellular objects tracking. *European Journal of Cell Biology*, 86(9):569–578, 2007.
- Yannis Kalaidzidis. Multiple objects tracking in fluorescence microscopy. *Journal of Mathematical Biology*, 58(1-2):57–80, 2009.
- Rudolph Emil Kalman and others. A new approach to linear filtering and prediction problems. *Journal of Basic Engineering*, 82(1):35–45, 1960.
- Adel Kechkar, Deepak Nair, Mike Heilemann, Daniel Choquet, and Jean-Baptiste Sibarita. Real-time analysis and visualization for single-molecule based super-resolution microscopy. *PLoS ONE*, 8(4):e62918, April 2013. doi: 10.1371/journal.pone.0062918. URL <http://dx.doi.org/10.1371/journal.pone.0062918>. 00008.

- C Kervrann. Neighborhood filters and novel Bayesian approximations for non-local image regularization. In *SIAM Imaging Science*, Chicago, 2010.
- C. Kervrann, J. Boulanger, and P. Coupe. Bayesian non-local means filter, image redundancy and adaptive dictionaries for noise removal. In *Scale-Space and Variational Methods (SSVM'07)*, page 520–532, Ischia, Italy, 2007.
- Hee-Young Kim, Xiaolan Li, Christopher T. Jones, Charles M. Rice, Jean-Michel Garcia, Auguste Genovesio, Michael A. E. Hansen, and Marc P. Windisch. Development of a multiplex phenotypic cell-based high throughput screening assay to identify novel hepatitis C virus antivirals. *Antiviral Research*, 99(1):6–11, July 2013. ISSN 0166-3542. doi: 10.1016/j.antiviral.2013.04.020. URL <http://www.sciencedirect.com/science/article/pii/S0166354213001198>. 00002.
- Tae Kyung Kim and James H. Eberwine. Mammalian cell transfection: the present and the future. *Analytical and Bioanalytical Chemistry*, 397(8):3173–3178, August 2010. ISSN 1618-2642. doi: 10.1007/s00216-010-3821-6. URL <http://www.ncbi.nlm.nih.gov/pmc/articles/PMC2911531/>. 00039 PMID: 20549496 PMCID: PMC2911531.
- Robert Kirmse, Stephanie Portet, Norbert Mücke, Ueli Aebi, Harald Herrmann, and Jörg Langowski. A quantitative kinetic model for the in vitro assembly of intermediate filaments from tetrameric vimentin. *Journal of Biological Chemistry*, 282(25):18563–18572, 2007.
- Peter Kner, Bryant B. Chhun, Eric R. Griffis, Lukman Winoto, and Mats GL Gustafsson. Super-resolution video microscopy of live cells by structured illumination. *Nature Methods*, 6(5):339–342, 2009. URL <http://www.nature.com/nmeth/journal/v6/n5/abs/nmeth.1324.html>. 00200.
- Akihiro Kusumi, Yasushi Sako, and Mutsuya Yamamoto. Confined lateral diffusion of membrane receptors as studied by single particle tracking (nanovid microscopy). Effects of calcium-induced differentiation in cultured epithelial cells. *Biophysical Journal*, 65(5):2021–2040, 1993.
- T Lagache, E Dauty, and D Holcman. Physical principles and models describing intracellular virus particle dynamics. *Current Opinion in Microbiology*, 12(4):439–445, 2009.
- Alireza Lajevardipour and Andrew H. A. Clayton. The Effect of Translational Motion on FLIM Measurements-Single Particle Phasor-FLIM. *Journal of Fluorescence*, 23(4):671–679, March 2013. ISSN 1053-0509, 1573-4994. doi: 10.1007/s10895-013-1174-1. URL <http://link.springer.com/10.1007/s10895-013-1174-1>. 00000.

- Joseph R. Lakowicz and Henryk Szmajda. Fluorescence lifetime-based sensing of pH, Ca²⁺, K⁺ and glucose. *Sensors and Actuators B: Chemical*, 11(1–3):133–143, March 1993. ISSN 0925-4005. doi: 10.1016/0925-4005(93)85248-9. URL <http://www.sciencedirect.com/science/article/pii/0925400593852489>. 00000.
- J.R. Lakowicz and B.R. Masters. Principles of fluorescence spectroscopy. *Journal of Biomedical Optics*, 13:029901, 2008.
- Lambert Instruments. LI-FLIM Software, 2010. URL <http://www.lambertinstruments.com/download/software>.
- Jong-Sen Lee. Speckle analysis and smoothing of synthetic aperture radar images. *Computer Graphics and Image Processing*, 17(1):24–32, September 1981. ISSN 0146-664X. doi: 10.1016/S0146-664X(81)80005-6. URL <http://www.sciencedirect.com/science/article/pii/S0146664X81800056>. 00583.
- Yinyun Li, Peter Jung, and Anthony Brown. Axonal transport of neurofilaments: a single population of intermittently moving polymers. *The Journal of Neuroscience*, 32(2):746–758, 2012.
- Liang Liang, Hongying Shen, Pietro De Camilli, and James S Duncan. Tracking clathrin coated pits with a multiple hypothesis based method. In *Medical Image Computing and Computer-Assisted Intervention—MICCAI 2010*, page 315–322. Springer, 2010.
- Hai-Jui Lin, Petr Herman, and Joseph R. Lakowicz. Fluorescence lifetime-resolved pH imaging of living cells. *Cytometry Part A*, 52A(2):77–89, April 2003. ISSN 1552-4930. doi: 10.1002/cyto.a.10028. URL <http://onlinelibrary.wiley.com/doi/10.1002/cyto.a.10028/abstract>. 00098.
- J. Lippincott-Schwartz. Development and Use of Fluorescent Protein Markers in Living Cells. *Science*, 300(5616):87–91, April 2003. ISSN 00368075, 10959203. doi: 10.1126/science.1082520. URL <http://www.sciencemag.org/cgi/doi/10.1126/science.1082520>. 00852.
- J Lippincott-Schwartz, E Snapp, and A Kenworthy. Studying protein dynamics in living cells. *Nature reviews. Molecular cell biology*, 2(6):444–456, June 2001. ISSN 1471-0072. doi: 10.1038/35073068. 00908 PMID: 11389468.
- Harvey Lodish. *Molecular cell biology*. Macmillan, 2008.
- C. Louchet. *Variational and Bayesian models for image denoising : from total variation towards non-local means*. PhD thesis, University of Paris V, 2008.
- Matthias Machacek, Louis Hodgson, Christopher Welch, Hunter Elliott, Olivier Pertz, Perihan Nalbant, Amy Abell, Gary L. Johnson, Klaus M. Hahn, and Gaudenz Danuser.

- Coordination of Rho GTPase activities during cell protrusion. *Nature*, 461(7260): 99–103, September 2009. ISSN 0028-0836. doi: 10.1038/nature08242. URL <http://www.nature.com/nature/journal/v461/n7260/abs/nature08242.html>. 00311.
- Klas EG Magnusson and Joakim Jaldén. A batch algorithm using iterative application of the Viterbi algorithm to track cells and construct cell lineages. In *Biomedical Imaging (ISBI), 2012 9th IEEE International Symposium on*, page 382–385. IEEE, 2012.
- M. Makitalo and A. Foi. Optimal inversion of the generalized Anscombe transformation for Poisson-Gaussian noise. *IEEE Transactions on Image Processing*, 2(1):91–103, 2013.
- P. Marjoram, P. Molitor, V. Plagnol, and S. Tavaré. Markov chain Monte Carlo without likelihoods. *Proceedings of the National Academy of Sciences of the United States of America*, 100(26):15324–15328, 2003.
- Kameo Matusita. Decision rule, based on the distance, for the classification problem. *Annals of the Institute of Statistical Mathematics*, 8(1):67–77, 1956. URL <http://www.springerlink.com/index/455V4L8683Q4708G.pdf>. 00069.
- Erik Meijering, Ihor Smal, and Gaudenz Danuser. Tracking in molecular bioimaging. *Signal Processing Magazine, IEEE*, 23(3):46–53, 2006. 00159.
- Erik Meijering, Oleh Dzyubachyk, and Ihor Smal. Methods for cell and particle tracking. *Methods Enzymol*, 504(9):183–200, 2012.
- D M Miller and D C Shakes. Immunofluorescence microscopy. *Methods in Cell Biology*, 48:365–394, 1995. ISSN 0091-679X. 00210 PMID: 8531735.
- M. Minsky. Memoir on inventing the confocal scanning microscope. *Scanning*, 10(4): 128–138, January 1988. ISSN 1932-8745. doi: 10.1002/sca.4950100403. URL <http://onlinelibrary.wiley.com/doi/10.1002/sca.4950100403/abstract>. 00725.
- Desmond O’Connor. *Time-Correlated Single Photon Counting*. Academic Press, January 1984. ISBN 9780323141444. 02168.
- Jean-Christophe Olivo-Marin. Extraction of spots in biological images using multiscale products. *Pattern Recognition*, 35(9):1989–1996, 2002. URL <http://www.sciencedirect.com/science/article/pii/S0031320301001273>. 00206.
- Olympus America Inc. Olympus Microscopy Resource Center | Confocal Microscopy - Calcium Ion Probes, 2012. URL <http://www.olympusmicro.com/primer/techniques/confocal/applications/cameleons.html>.

- R. M. Clegg P. C. Schneider. Rapid acquisition, analysis, and display of fluorescence lifetime-resolved images for real-time applications. *Review of Scientific Instruments*, v.68, 4107-4119 (1997), 1997. ISSN 0034-6748. doi: 10.1063/1.1148354. 00095.
- Johan Philip and Kjell Carlsson. Theoretical investigation of the signal-to-noise ratio in fluorescence lifetime imaging. *Journal of the Optical Society of America A*, 20(2): 368–379, February 2003. doi: 10.1364/JOSAA.20.000368. URL <http://josaa.osa.org/abstract.cfm?URI=josaa-20-2-368>.
- Veena Prahlad, Miri Yoon, Robert D Moir, Ronald D Vale, and Robert D Goldman. Rapid movements of vimentin on microtubule tracks: kinesin-dependent assembly of intermediate filament networks. *The Journal of Cell Biology*, 143(1):159–170, 1998.
- D C Prasher, V K Eckenrode, W W Ward, F G Prendergast, and M J Cormier. Primary structure of the *Aequorea victoria* green-fluorescent protein. *Gene*, 111(2):229–233, February 1992. ISSN 0378-1119. 02147 PMID: 1347277.
- HSMP Qian, Michael P Sheetz, and Elliot L Elson. Single particle tracking. Analysis of diffusion and flow in two-dimensional systems. *Biophysical Journal*, 60(4):910–921, 1991.
- Victor Racine, Ariane Hertzog, Jacqueline Jouanneau, Jean Salamero, Charles Kervrann, and J-B Sibarita. Multiple-target tracking of 3D fluorescent objects based on simulated annealing. In *IEEE International Symposium on Biomedical Imaging: Nano to Macro*, page 1020–1023. IEEE, 2006.
- Sathish Ramani, Cédric Vonesch, and Michael Unser. Deconvolution of 3D fluorescence micrographs with automatic risk minimization. In *5th IEEE International Symposium on Biomedical Imaging: From Nano to Macro, 2008.*, page 732–735. IEEE, 2008. URL http://ieeexplore.ieee.org/xpls/abs_all.jsp?arnumber=4541100.
- A. Ravishankar Rao. *Computing oriented texture fields*. Springer, 1990. URL http://link.springer.com/chapter/10.1007/978-1-4613-9777-9_2. 00281.
- Donald Reid. An algorithm for tracking multiple targets. *IEEE Transactions on Automatic Control*, 24(6):843–854, 1979.
- Seyed Hamid Rezatofghi, Stephen Gould, Richard Hartley, Katarina Mele, and William E Hughes. Application of the IMM-JPDA filter to multiple target tracking in total internal reflection fluorescence microscopy images. In *Medical Image Computing and Computer-Assisted Intervention–MICCAI 2012*, page 357–364. Springer, 2012.
- P.J. Rousseeuw, A.M. Leroy, and J. Wiley. *Robust Regression and Outlier Detection*, volume 3. Wiley Online Library, 1987.

-
- J. Salmon and Y. Strozecki. Patch reprojections for Non-Local methods. *Signal Processing*, 92(2):477–489, 2012.
- Michael J Saxton. Single-particle tracking: models of directed transport. *Biophysical Journal*, 67(5):2110–2119, 1994a.
- Michael J Saxton. Single-particle tracking: models of directed transport. *Biophysical Journal*, 67(5):2110–2119, 1994b. 00062.
- Ivo F Sbalzarini and Petros Koumoutsakos. Feature point tracking and trajectory analysis for video imaging in cell biology. *Journal of structural biology*, 151(2):182–195, 2005.
- Arnaud Sergé, Nicolas Bertaux, Hervé Rigneault, and Didier Marguet. Dynamic multiple-target tracing to probe spatiotemporal cartography of cell membranes. *Nature Methods*, 5(8):687–694, 2008.
- O Shimomura, F H Johnson, and Y Saiga. Extraction, purification and properties of aequorin, a bioluminescent protein from the luminous hydromedusan, *Aequorea*. *Journal of Cellular and Comparative Physiology*, 59:223–239, June 1962. ISSN 0095-9898. 01576 PMID: 13911999.
- I. Smal, M. Loog, W. Niessen, and E. Meijering. Quantitative comparison of spot detection methods in fluorescence microscopy. *IEEE Transactions on Medical Imaging*, 29(2):282–301, 2010.
- Ihor Smal, Katharina Draegestein, Niels Galjart, Wiro Niessen, and Erik Meijering. Particle filtering for multiple object tracking in dynamic fluorescence microscopy images: Application to microtubule growth analysis. *IEEE Transactions on Medical Imaging*, 27(6):789–804, 2008a.
- Ihor Smal, Wiro Niessen, and Erik Meijering. A new detection scheme for multiple object tracking in fluorescence microscopy by joint probabilistic data association filtering. In *Biomedical Imaging: From Nano to Macro, 2008. ISBI 2008. 5th IEEE International Symposium on*, page 264–267. IEEE, 2008b.
- Brian L. Sprague, Chad G. Pearson, Paul S. Maddox, Kerry S. Bloom, E. D. Salmon, and David J. Odde. Mechanisms of microtubule-based kinetochore positioning in the yeast metaphase spindle. *Biophysical Journal*, 84(6):3529–3546, June 2003. ISSN 0006-3495. doi: 10.1016/S0006-3495(03)75087-5. URL [http://www.cell.com/biophysj/abstract/S0006-3495\(03\)75087-5](http://www.cell.com/biophysj/abstract/S0006-3495(03)75087-5). 00064.
- BQ Spring and RM Clegg. Image analysis for denoising full-field frequency-domain fluorescence lifetime images. *Journal of Microscopy*, 235(2):221–237, 2009.

- Squire, Verveer, and Bastiaens. Multiple frequency fluorescence lifetime imaging microscopy. *Journal of Microscopy*, 197(2):136–149, February 2000. ISSN 0022-2720, 1365-2818. doi: 10.1046/j.1365-2818.2000.00651.x. URL <http://doi.wiley.com/10.1046/j.1365-2818.2000.00651.x>. 00100.
- Robert F Stengel. *Optimal control and estimation*. Dover publications, 1986.
- David J. Stephens and Victoria J. Allan. Light Microscopy Techniques for Live Cell Imaging. *Science*, 300(5616):82–86, April 2003. ISSN 0036-8075, 1095-9203. doi: 10.1126/science.1082160. URL <http://www.sciencemag.org/content/300/5616/82.00632> PMID: 12677057.
- G. G. Stokes. On the Change of Refrangibility of Light. *Philosophical Transactions of the Royal Society of London*, 142:463–562, January 1852. URL <http://www.jstor.org/stable/108550>. 00000.
- Klaus Suhling, Paul M. W. French, and David Phillips. Time-resolved fluorescence microscopy. *Photochemical & Photobiological Sciences*, 4(1):13, 2005. ISSN 1474-905X, 1474-9092. doi: 10.1039/b412924p. URL <http://xlink.rsc.org/?DOI=b412924p>.
- D Thomann, DR Rines, PK Sorger, and G Danuser. Automatic fluorescent tag detection in 3D with super-resolution: application to the analysis of chromosome movement. *Journal of Microscopy*, 208(1):49–64, 2002.
- Ignacio Tinoco and Ruben L Gonzalez. Biological mechanisms, one molecule at a time. *Genes & Development*, 25(12):1205–1231, 2011.
- R Y Tsien. The green fluorescent protein. *Annual review of biochemistry*, 67:509–544, 1998. ISSN 0066-4154. doi: 10.1146/annurev.biochem.67.1.509. 04574 PMID: 9759496.
- Jitendra K Tugnait. Detection and estimation for abruptly changing systems. *Automatica*, 18(5):607–615, 1982.
- Ronald D Vale. The molecular motor toolbox for intracellular transport. *Cell*, 112(4):467–480, 2003.
- E.B. van Munster and T.W.J. Gadella Jr. Suppression of photobleaching-induced artifacts in frequency-domain FLIM by permutation of the recording order. *Cytometry Part A*, 58(2):185–194, 2004.
- Marco Vilela, Nadia Halidi, Sebastien Besson, Hunter Elliott, Klaus Hahn, Jessica Tytell, and Gaudenz Danuser. Fluctuation analysis of activity biosensor images for the study of information flow in signaling pathways. *Methods Enzymol*, 519:253–276, 2013. URL <http://www.hahnlab.com/downloads/protocols/2013-Meth-Enzym-Vilela-Danuser-fluctuation-analysis.pdf>. 00002.

-
- Cédric Vonesch, Francois Aguet, J-L Vonesch, and Michael Unser. The colored revolution of bioimaging. *Signal Processing Magazine, IEEE*, 23(3):20–31, 2006.
- Thomas Walter, Michael Held, Beate Neumann, Jean-Karim Hériché, Christian Conrad, Rainer Pepperkok, and Jan Ellenberg. Automatic identification and clustering of chromosome phenotypes in a genome wide RNAi screen by time-lapse imaging. *Journal of Structural Biology*, 170(1):1–9, April 2010. ISSN 10478477. doi: 10.1016/j.jsb.2009.10.004. URL <http://linkinghub.elsevier.com/retrieve/pii/S1047847709002731.00029>.
- Lei Wang and Anthony Brown. Rapid intermittent movement of axonal neurofilaments observed by fluorescence photobleaching. *Molecular Biology of the Cell*, 12(10):3257–3267, 2001.
- Mark R Winter, Cheng Fang, Gary Banker, Badrinath Roysam, and Andrew R Cohen. Axonal transport analysis using Multitemporal Association Tracking. *International Journal of Computational Biology and Drug Design*, 5(1):35–48, 2012.
- Huei-Fang Yang, Xavier Descombes, Charles Kervrann, Caroline Medioni, and Florence Besse. Tracking Growing Axons by Particle Filtering in 3D+t Fluorescent Two-Photon Microscopy Images. In *ACCV - Asian Conference on Computer Vision*, pages 272–283, Daejeon, Corée, République De, November 2012.
- Ji Won Yoon, Andreas Bruckbauer, William J Fitzgerald, and David Klenerman. Bayesian inference for improved single molecule fluorescence tracking. *Biophysical Journal*, 94(12):4932–4947, 2008.
- Miri Yoon, Robert D Moir, Veena Prahlad, and Robert D Goldman. Motile properties of vimentin intermediate filament networks in living cells. *The Journal of Cell Biology*, 143(1):147–157, 1998.
- Christophe Zimmer. From microbes to numbers: extracting meaningful quantities from images. *Cellular Microbiology*, 14(12):1828–1835, 2012.

ANNEXE 2 (Modèle dernière page de thèse)

VU :

Le Directeur de Thèse
(KERVRANN Charles)

VU :

Le Responsable de l'École Doctorale

VU pour autorisation de soutenance

Rennes, le

Le Président de l'Université de Rennes 1

Guy CATHELINÉAU

VU après soutenance pour autorisation de publication :

Le Président de Jury,
(Nom et Prénom)